Hierarchically Textured, Anti-Reflective, Self-Cleaning Glass for Solar PV Applications

A thesis presented to the University of Dublin, Trinity College

for the degree of Doctor of Philosophy

by

Eoin Cotter

Under the supervision of David McCloskey

Declaration

I declare that this thesis has not been submitted as an exercise for a degree at this or any other university and it is entirely my own work. I agree to deposit this thesis in the University's open access institutional repository or allow the Library to do so on my behalf, subject to Irish Copyright Legislation and Trinity College Library conditions of use and acknowledgement. I consent to the examiner retaining a copy of the thesis beyond the examining period, should they so wish (EU GDPR May 2018).

Eoin Cotter

26/03/2025

Abstract

The solar PV industry has grown enormously over the course of the last decade, owing largely to the reduction of the cost of solar modules. As solar panels have become cheaper, they have been deployed more on rooftops, often at suboptimal tilt and orientation. This leads to sunlight often striking the solar panels at glancing angles which can produce significant glare as well as loss of electrical output. Glare is unpleasant and is a cause for the rejection of solar PV installations in the planning system. The electrical losses due to reflection can reach 15% for solar panels in high latitude regions which are not oriented optimally. Soiling is another issue which typically leads to 3-5% losses to output in temperate climates (more without regular cleaning) and as much as 50% losses in arid regions with fine sand and dust. The problems of glare, reflection losses and soiling can all be addressed by modifying the top glass surface of a solar panel. I used COMSOL ray tracing simulations to predict good geometries for an anti-reflective textured surface. I then made range of bio-inspired hierarchically textured glass surface with microscale pits and nanoscale pillars. These modified glass surfaces showed a 3% improvement in light transmission at normal angle of incidence (out of a maximum of 4%) as well as an incidence angle modifier (IAM) that extends out to higher angles. The surfaces were also demonstrated to reduce glare, both by reducing the total amount of reflected light and increasing the reflective haze of that light. The surfaces with glass nanopillars were also super-hydrophilic (contact angle < 5 degrees) and I was able to show that the textured glass samples facilitate the removal of fine sand when a water droplet lands on the surface.

A large range of glass patterning techniques were considered, and I ultimately used hydrofluoric acid wet etching to produce the microscale pitted patterns and reactive ion dry etching to form the nanopillars. I decided to pattern glass directly instead of patterning a polymer film that could be retrofitted on a solar module. This was more challenging as there are limited patterning techniques suitable for glass. The superhydrophilic properties were achieved by texturing rather than chemically modifying the glass surface. By achieving anti-reflection and self-cleaning by texturing the glass surface my coating should be more robust than many alternative technologies.

Publications and Outputs

- Enhancing Efficiency and Lifetime of Photovoltaic Systems Through Passive Convective Cooling - Erik P. Soderholm; Eoin Cotter; David McCloskey - IEEE ITHERM San Diego - 2022 - 10.1109/iTherm54085.2022.9899647
- Analysis of energy, economic and environmental performance of solar water heaters for domestic hot water supply in northern European climate - Anandhi Parthiban, Eoin Cotter, David McCloskey – ECOS – 2023
- Room Temperature Fabrication of Macroporous Lignin Membranes for the Scalable Production of Black Silicon, Nadezda Prochukhan, Stephen A O'Brien, Arantxa Davó-Quiñonero, Anna Trubetskaya, Eoin Cotter, Andrew Selkirk, Ramsankar Senthamaraikannan, Manuel Ruether, David McCloskey, Michael A.Morris – Biomacromolecules – 2022
- Hierarchically Textured, Anti-Reflective, Super Hydrophilic Glass for Solar PV Applications – Written, not yet published – 2025
- Low Irradiance Losses of Photovoltaics in High Latitude Regions – Eoin Cotter, David McCloskey – NIL - 2021

Acknowledgments

First of all, I would like to give a huge thanks to my supervisor Prof. David McCloskey. I benefitted greatly from his guidance over the years. I always enjoyed our weekly meetings where my project as well as those of the other research group members were freely discussed. He provided many helpful and creative suggestions throughout the project.

Having spent the first half of my PhD doing computer simulations I had much to learn in the field of nanofabrication when it came to making my glass surfaces. Without the knowledge, advice and help of Chris Murray this would not have been possible. Working together we produced almost 100 textured glass samples, refining and optimizing and characterizing every step of the process. He did a huge amount of work.

I would also like to thank my friends and fellow research group members Eric Soderholm and Sayuj Sasidharan who taught me everything I know and more about COMSOL simulations. The other research group members Anandhi Parthiban, Evan Roy, Nishtha Shelly, Simon Gynn and Dilkhush Khicher, Kenny Yu and Simon Corbett all made my time in Trinity all the more enjoyable.

In 2022, 4th year astrophysics student Ross Brandon and I developed the MATLAB solar simulation, used to predict the improvement in yield for AR coatings. Riley Gatenby helped in making my nanoscale pillars using a reactive ion etching technique which he had developed. Luckily, he also managed to fix the ICP etch tool just in time to make my nanopillars before the deadline.

Many thanks also to the staff in CRANN and SNIAM in Trinity. Patrick Murphy, in particular, helped in making parts for the angle resolved reflectometer.

Outside of Trinity I would also like to thank my family Anne, Liam, Dónal and Niamh as well as my friends and housemates for their support as well as putting up with me talking about solar panels for years.

TABLE OF CONTENTS

Table of Figures

1 INTRODUCTION

1.1 MOTIVATION

At high latitudes the Sun's rays often strike the panels at a glancing angle which leads to significant reflection losses particularly in the winter months when the elevation angle of the Sun is low (in the Northern hemisphere). While reflection losses in absolute terms are greater in regions closer to the equator due to the larger solar insolation in relative terms reflection losses are of more important as you move closer to the Earths poles[1].

The significance of reflection losses becomes greater still as many PV installations, particularly roof mounted panels are not oriented optimally. The greatest reflection losses are for East/West mounted panels[2] at low tilt angles while panels on a tracker mount minimize reflective losses by staying at normal angle of incidence to the Sun. Although single and dual axis tracker systems can be employed to track the sun and reduce angle dependent reflection losses these systems are not always deployed due to high initial capital costs and operational costs, this is particularly the case for dual axis trackers[3]. Despite losses of 15-25% fixed tilt systems are still used in about half of solar farms worldwide[4].

The tilt angle of panels in a solar farm is often lower than the optimum for electricity production as panels set at high tilt angles cast long shadows and thus the panels cannot be densely spaced[5]. High tilt angles also increase the amount of wind loading which then requires more robust and costly mountings to protect the panels from strong gusts wind[6]. Loose spacing of solar panels wastes land which takes increasingly large share of the total cost of a solar farm as the cost of the solar modules falls while land prices increase. In Ireland solar panels are typically mounted at 25^o despite the optimum being 45^o due to the aforementioned reasons.

Glass has a reflectivity of 4% at normal angle of incidence in the optical range and this loss increases greatly at glancing angles. Thus the majority of commercially available solar panels come with an anti-reflective (AR) coating[7]. These coatings typically reduce the reflection losses by 75% or more at normal angle of incidence. Anti-reflection is achieved by introducing a low refractive index layer ideally of quarter optical wavelength thickness (for destructive interference). Unfortunately, there are very few solid materials that have a lower refractive index than glass (MgF_2 is an example) let alone the ideal refractive index of 1.22[8]. Low refractive index can instead be achieved by using a porous medium that has a low effective refractive index due to reduced density[9]. As per effective medium theory if the pores or other features are sub wavelength in scale light will interact with the coating air mixture as though it were a single medium with a low refractive index[10]. By increasing the porosity near the coating-air interface it is possible to create a graded AR coating with near perfect transmission[11].

SiO_2 is a popular AR coating material that can be deposited on the solar panel glass using a sol gel method that leaves a low-density porous structure with the desired refractive index. The hardness of these structures is in proportion to the porosity so there is a trade-off between longevity and low refractive index[12]. These coatings typically reduce reflective losses by 75% which translates to a 2-3% increase in output power for a PV system. There are however several problems with these AR coatings. The 3% transmittance improvement is at normal incidence while the improvement at glancing angles is smaller. The coatings also suffer greatly from abrasion and can lose half of their anti-reflective effect within two years. Figure 1-1 below shows a degraded AR coating. The main causes of AR coating degradation are sand impingement resulting from particles striking the glass at high speeds (relevant to sandstorms), abrasion due to brush bristles when the panels are being cleaned and abrasion resulting from sand particles lapping the surface during cleaning. Sand is the most abrasive form of soiling as the particles are made of quartz which has high hardness[13].

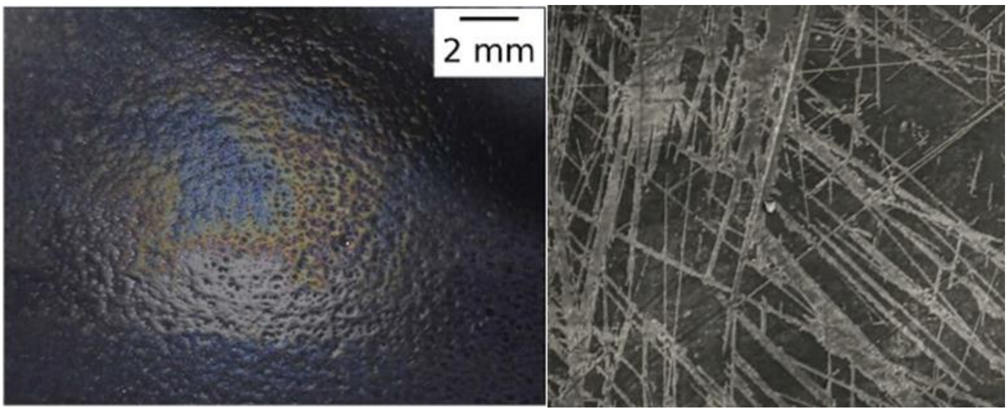

Figure 1-1: Scratched AR coatings: Left: the yellow regions indicate where the coating has reduced thickness, and the white shiny region is there the coating has come off completely. Image from Visual Characterization of Anti-Reflective Coating on Solar Module Glass, Todd Karin, IEEE 47th PVSC, 2020[13]. Right: an SEM image showing scratches on an AR coating as a result of two cleaning events with a brush[8].

Textured glass surfaces have two major advantages over conventional AR coatings. Firstly, they suppress reflection at glancing angles due to light trapping and secondly, they can be mechanically robust if the features are etched directly into the glass (subtractive process) rather than deposited on the glass surface (additive process). The concept of biomimetic surfaces such as the moth eye structure and the rose petal structure[14] has been applied to solar panels to enhance broad angle anti-reflection[15].

1.2 The Solar Industry

The use of solar power worldwide is set to increase significantly in the coming years due to the major reduction in solar PV module costs over the course of the last decade. The levelized cost of electricity (LCOE) for solar power has fallen from $ 0.378 per kWh in 2010 to $ 0.048 per kWh worldwide in 2021[15], which is an 87.3% decrease. The cost per kilowatt of installing photovoltaic capacity also fell to $ 800-950/kWh in 2021 from $ 4,700/kWh in 2010. At this price solar power has become competitive with onshore wind which has an LCOE of $ 0.033 per kWh and coal which has a LCOE of $ 0.055 per kWh for new plants[16] (excluding the external cost of CO2 emissions). By 2050 solar PV was expected to have the largest share of the renewable energy generation market and account for almost half of all electrical generation and 20% of all energy in general according to the IEA Net Zero by 2050 Roadmap[17]. This milestone has already been achieved by 2025 and the growth of the solar pv industry has consistently beaten predictions[18].

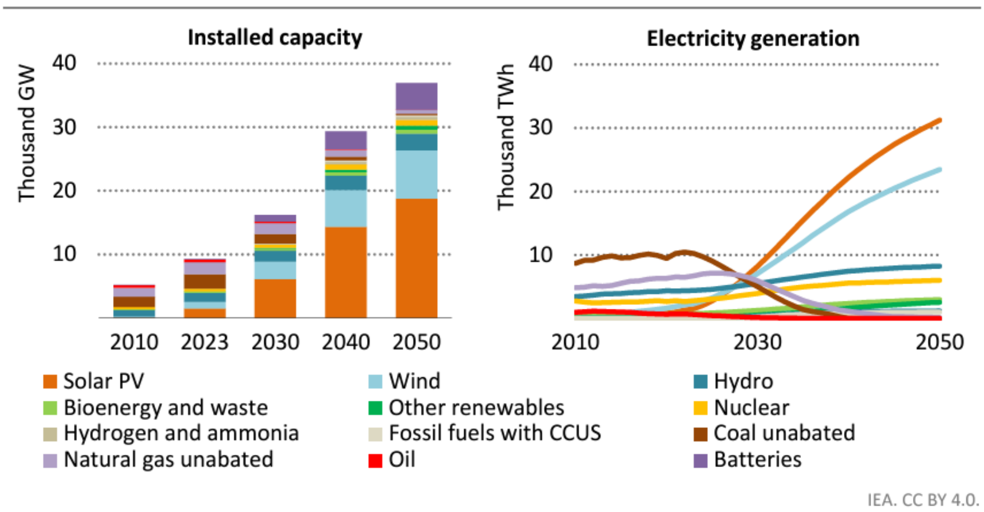

Figure 1-2: The solar PV industry. *Shows the installed capacity and electricity generation by source in the 2050 net zero scenario outlined by the IEA*[17]

It is now becoming increasingly viable for regions with lower solar irradiance such as Ireland, Britain, Scandinavia and Canada to deploy large scale commercial solar power as well as rooftop installations. Currently onshore wind farms are the dominant renewable electricity technology in these areas however there are limitations to grid penetration when using a single renewable technology due to the intermittent nature of both wind speed and solar irradiance both seasonally as well as over the course of the day. For example, in the Irish scenario, average wind speed is higher in the winter while solar irradiance is higher in the summer, thus these technologies can be seen as somewhat complementary rather than directly in competition with each other.

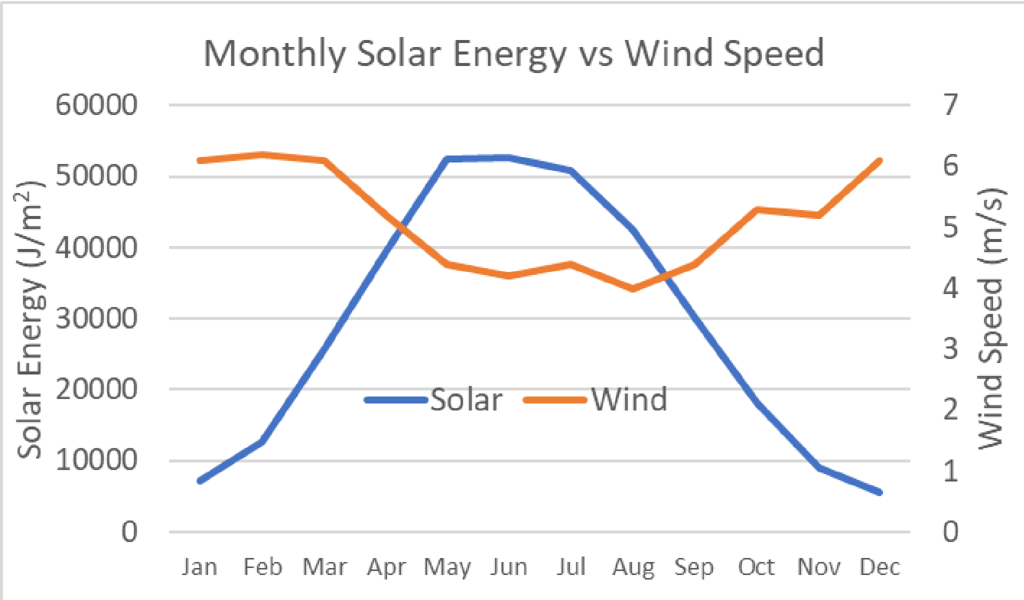

Figure 1-3: Wind power vs solar PV. The average monthly solar energy per meter squared versus the mean monthly wind speed. As can be seen mean wind speed is lower during the summer while the irradiance is higher at this time, thus wind power and solar power can be complimentary over the course of the year. The data is from the Dublin Airport weather station[19]

The large-scale deployment of renewables such as onshore and offshore wind turbines and solar PV modules both on commercial scale solar farms and rooftop installations will also have a significant effect on the electricity grid. Wind turbines generate AC power that is non-synchronous with the grid and thus it becomes increasing difficult to maintain a constant 50 or 60 Hz grid frequency[18] as wind power becomes a larger portion to total electricity generation[20]. Solar PV has the advantage that it does not even need grid connection, this is useful for deployment in remote areas of developing countries that may not have rural electrification.[21]

1.3 SOLAR CELL THEORY

A photodiode consists of a p-n junction, typically the base of the cell is p doped while an n type emitter layer is placed near the front of the cell. Incident photons are absorbed to form electron hole pairs and these carriers are separated by a built in electric field in the cell. As a result, electrons flow to the negative terminal and holes to the positive terminal resulting in an electric current[22].

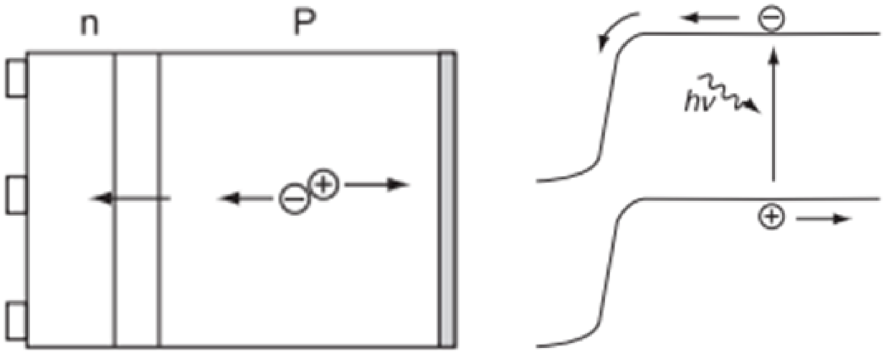

Figure 1-4: Solar cell diagram. The schematic on the left shows a solar cell the a p doped base and a n-type emitter layer at either end of the cell are metal contacts that carry the current away from the cell. The diagram on the right shows the band structure of the same solar cell with the built in electric field that accelerates the electrons to the terminal.[22]

The ideal solar cell can be represented by the Shockley solar cell equation,

$$I = I_{ph} - I_0 \left(e^{\frac{qV}{k_B T}} - 1 \right) \qquad 1.1$$

Where I_{ph} is the photocurrent and I_0 is the saturation current. In the dark (i.e. no photocurrent) the solar cell acts as a normal diode rectifier. The open circuit voltage i.e. the simplified case where the short circuit current I_{sc} and I_{ph} are equal, is given by,

$$V_{oc} = \frac{k_B T}{q} \, ln \left(1 + \frac{I_{ph}}{I_0} \right) \qquad 1.2$$

The open circuit voltage occurs where there is no current flowing between the terminals whereas the short circuit voltage occurs where the voltage between the terminals is zero. The maximum power produced by a solar cell is at the values of voltage V_m and current I_m on an I-V curve where the largest area can be drawn.

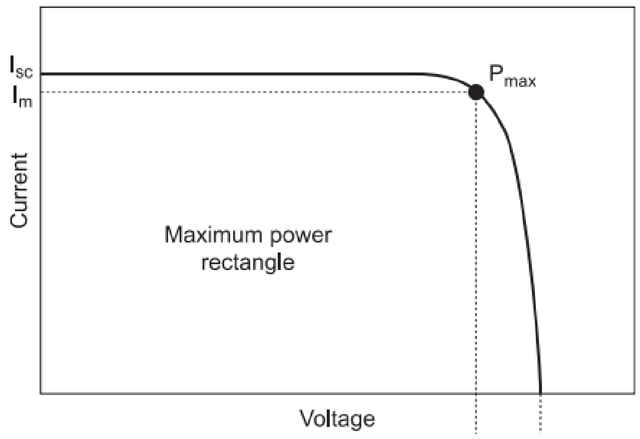

Figure 1-5: Maximum power point. *The power is maximised at a particular value of I_m and V_m that varies for different solar cells.*

The Fill Factor (FF) is a parameter which is given by,

$$FF = \frac{I_m V_m}{I_{sc} V_{oc}} = \frac{P_{max}}{I_{sc} V_{oc}} \quad 1.3$$

The usefulness of this factor is that it indicates the efficiency of the solar cell. A high fill factor corresponds with an I-V curve that is very close in shape to the maximum power rectangle, thus Figure 1-5 is a good example of a high fill factor device.

For real solar cells there is a series resistance and shunt resistance which reduces the maximum power output.

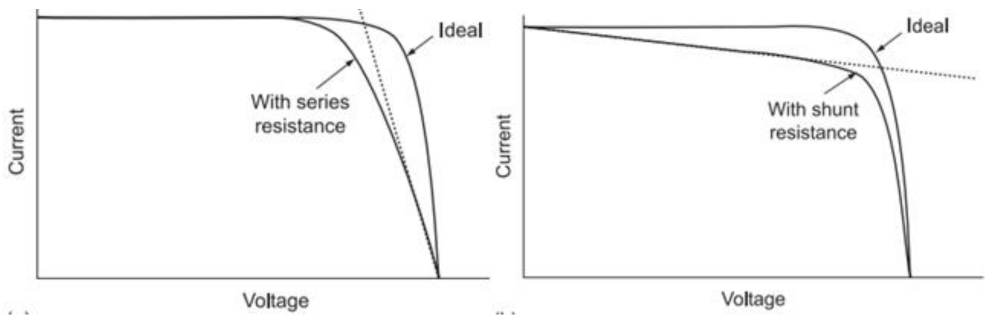

Figure 1-6: Shunt and series resistance. As can be seen in the two graphs the introduction of series and parallel resistance reduces maximum power while the open circuit voltage and short circuit current remain the same. Therefore, the non-ideal cell has a lower fill factor.

The quantum efficiency is the ratio of electrons (that contribute to the external current) to the number of photons that reach the solar cell. External quantum efficiency considers all photons that are incident on the cell while the internal quantum efficiency is for photons that actually enter the cell rather than get reflected at the surface. The photocurrent can be determined if the internal quantum efficiency is known.

$$I_{ph} = q \int_{(\lambda)} \phi(\lambda)\{1 - R(\lambda)\} IQE(\lambda) d\lambda \qquad 1.4$$

Where ϕ is the photon flux, R is the reflection coefficient and IQE is the internal quantum efficiency. All the variables are functions of the wavelength of the incident light. Low energy photons will not generate any electric power as they are below the bandgap of the solar cell semiconductor material and will not generate an electron hole pair, thus infrared light often passes to the back of the cell and is absorbed as heat. Photons with energies above the bandgap can form electron hole pairs but these are often lost to thermalization. As a result, photons with energies close to the band gap of the cell will generate the highest photocurrent[23].

The Shockley-Queisser limit gives the maximum theoretical efficiency for a single junction solar cell by assuming that every photon with an energy above the band gap produces a single electric charge[23].

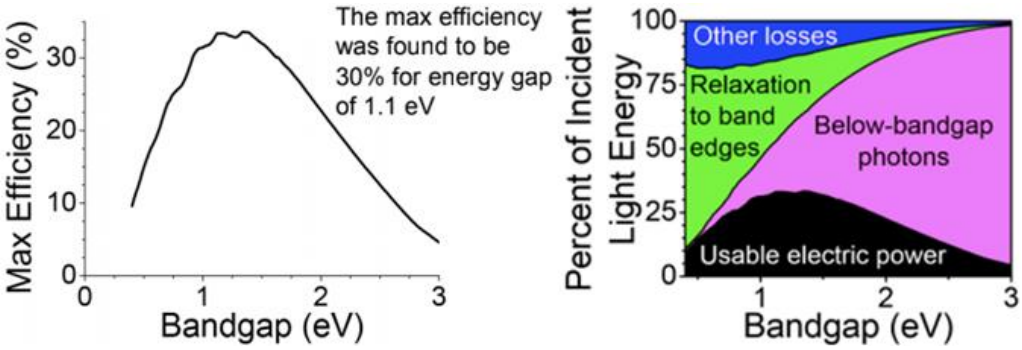

Figure 1-7: Shockley Queisser limit. *The band gap for silicon is 1.1 eV which is quite close to the band gap for maximum efficiency. Diagram on the right from Wikipedia*[24].

The assumptions of the Shockley Queisser limit are not real physical constraints, so it is possible to create a solar cell with higher efficiency. Potential ways to exceed the limit include the up-conversion of below band gap photons which would involve absorbing two low energy photons and emitting a single high energy photon. Quantum dots could achieve up-conversion as could non-linear optics although that would require very high light intensity and coherence. Hot electron capture would involve collecting the carriers generated by high energy photons that have excess kinetic energy before that energy is lost as heat[25].

1.4 SOLAR CELL AND MODULE DESIGN

Silicon based solar cells are the oldest of the solar cell designs and continue to have some of the best efficiencies. It is these cells that experienced a massive reduction in production cost in the 2010s as a result of economies of scale as well as reduced material use (thinner silver contacts and silicon wafers)[26]. Significant progress has been made in alternative PV designs such as perovskites, organic, dye sensitised, quantum dots and thin film. Figure 1-8 shows the progress over time for the various technologies.

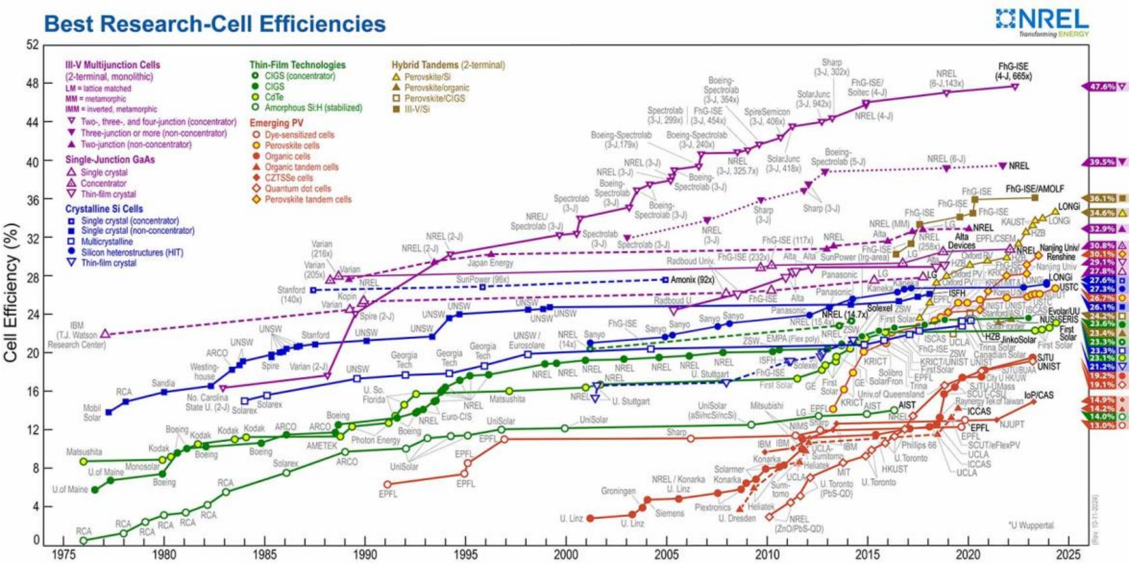

Figure 1-8: Solar cell state of the art. *The state of the art in solar cell design for various solar technologies, note that these are research grade cells and the commercial equivalents are less efficient*[27].

The multijunction solar cells are based upon a more complex and expensive design and thus are mainly suitable for specialized applications such as satellites, where solar power generation per unit weight or volume is a greater consideration than the cost of the solar cell itself.

Mono PERC Solar Cells: Passivated emitter and rear cell (PERC) have become increasingly common as a solar cell design in recent years. Recombination of carriers is particularly high at semiconductor interfaces due to the presence of lattice disruptions and dangling bonds. A back surface field is a highly doped layer at the rear of a cell that reduces surface recombination velocity. For a PERC cell, rather than the entire back of the cell being covered by a back surface field, only localised parts of the cell have a back surface field, and the remainder is covered with a passivation layer. This passivation layer reflects carriers from the back of the cell and reduces rear surface recombination. An added benefit is the increased reflection of infrared light from the cell which would otherwise increase the cell temperature[28].

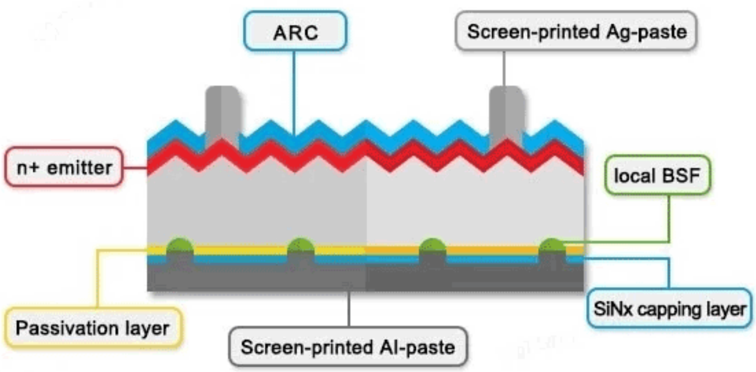

Figure 1-9: *The Mono PERC cell schematic. The aluminium oxide passivation layer covers most of the rear surface. Image ENF*[29]

The prefix Mono indicates that the cell design uses monocrystaline silicon rather than polycrystaline silicon or amorphous silicon. Monocrystaline silicon cells are more efficient due to the absence of grain boundaries that can act as recombination sites[30].

Bifacial Panel Design: Bifacial PERC solar cells are similar in design to regular PERCs however much of the rear aluminium paste is removed so that the device can receive light from both sides of the panel. Bifaciality is the ratio of power output from either side of the panel when both sides are exposed to the same amount of light. This ratio is typically 70%. Bifacial modules have a glass cover on either side which improves the structural strength and reduces the impact of thermal stress as the device is more symmetrical, the increased weight however adds to the mounting cost[31]. Typically, a polyolefin (POE) encapsulant is used rather than EVA (ethylene vinyl acetate) as it acts as a stronger barrier that prevents ions in the glass diffusing into the cell and causing potential induced degradation[32].

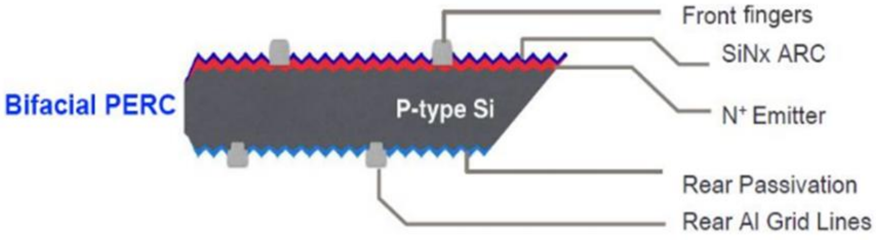

Figure 1-10: A Bifacial PERC schematic , with an aluminium grid at the rear rather than a full aluminium layer.[33] Note that the back of the cell is still textured to reduce reflection[31].

Solar Module Design: A solar panel consists of an array of solar cells connected both in series (to increase voltage) and in parallel (to increase current). This array of solar cells is encapsulated on both sides in a polymer layer such as EVA and then glass at the front and a plastic backsheet at the rear. Encapsulation is vital to protect the solar cells as well as the metal contacts from the elements, particularly water ingress. The encapsulant also protects the cells from mechanical damage either from sudden impacts or periodic stresses caused by thermal cycling and vibrations due to wind loading.

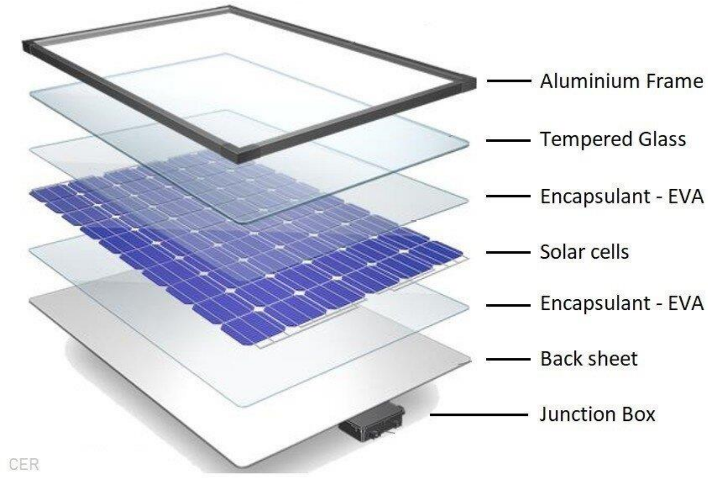

Figure 1-11: Solar module diagram. Shows the layers of a typical solar module, In the case of bifacial solar cells the backsheet is simply replaced with cover glass,. Image from Unbound Solar.[34]

The glass at the front on the module provides structural stability which is of particular importance for silicon solar cells which are brittle and thus vulnerable to bending. The front cover glass is typically between 2 and 3.2 mm in thickness to save weight and material cost but despite this the front cover glass makes up the largest contribution to the solar modules total weight. In the vast majority of cases low iron soda-lime tempered glass is used due to its low-cost relative to borosilicate glass and high strength.

In the case of thin film solar cells a plastic front cover can be used instead of glass due to the cells flexibility, this leads to significant weight savings and thus allows for a lighter and cheaper mounting structure, however a plastic front sheet will degrade when exposed to UV light from the sun giving the sheet a cloudy appearance and reducing optical transmission[35]. Fluoropolymers such as Ethylene Tetra Fluoro Ethylene (ETFE) do not degrade when exposed to UV radiation due to the strong C-F bonds however there in concern about using such materials on a large scale due to their non-biodegradable nature.[36]

1.5 SOLAR MODULE EFFICIENCY LOSS MECHANISMS

The efficiency of a solar panel as given by the manufacturer as measured under the standard test conditions of 1000 Wm^{-2} irradiance (AM 1.5 spectrum) at normal angle of incidence and 25^{o} C temperature. Such conditions are often not representative of regions with lower solar insolation as well as hot desert climates where the solar modules can reach temperatures greater than 100^{o} C. A loss breakdown can be seen in Figure 1-12.

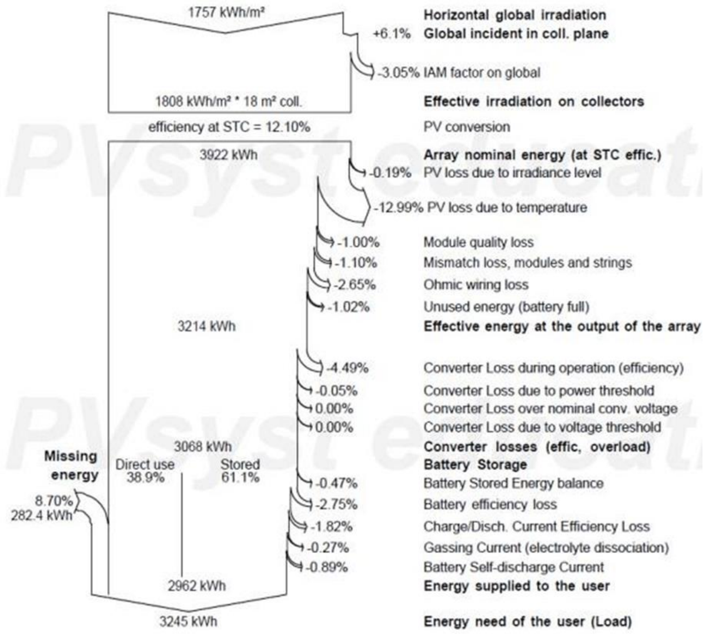

Figure 1-12: The breakdown of various losses in PVsyst. Inverter losses are a result of under sizing the inverter such that the maximum power is clipped on high irradiance days.[37]

Efficiency temperature coefficient: Solar cells ultimately convert heat from the sun into electrical energy and can thus be considered a heat engine. If the hot reservoir is the surface of the sun and the cold reservoir is the solar cell, then an increase in the cell temperature will reduce the Carnot efficiency of the cell[30]. This is, of course, a crude model as the energy transmitted between the reservoirs is in the form of radiation. A more accurate model relates the semiconductor band gap and temperature to the maximum power point voltage V_{MPP},

$$qV_{MPP} \approx E_g\left(1 - \frac{T_C}{T_H}\right) - k_B T_C \, ln\left(\frac{\Omega_{emit}}{\Omega_{abs}}\right) \qquad 1.5$$

Where the first term relates to the Carnot efficiency and the second term relates to the difference between the angle of absorption and emission (the greater emission angle increases entropy). Much of this voltage loss is due to radiative recombination which reduces the ratio of carrier generation to recombination. As the semiconductor temperature increases, the band gap gets narrower which reduces the cell voltage as can be seen in equation 1.5. Figure 1-13 below shows the various types of loss in a solar cell,

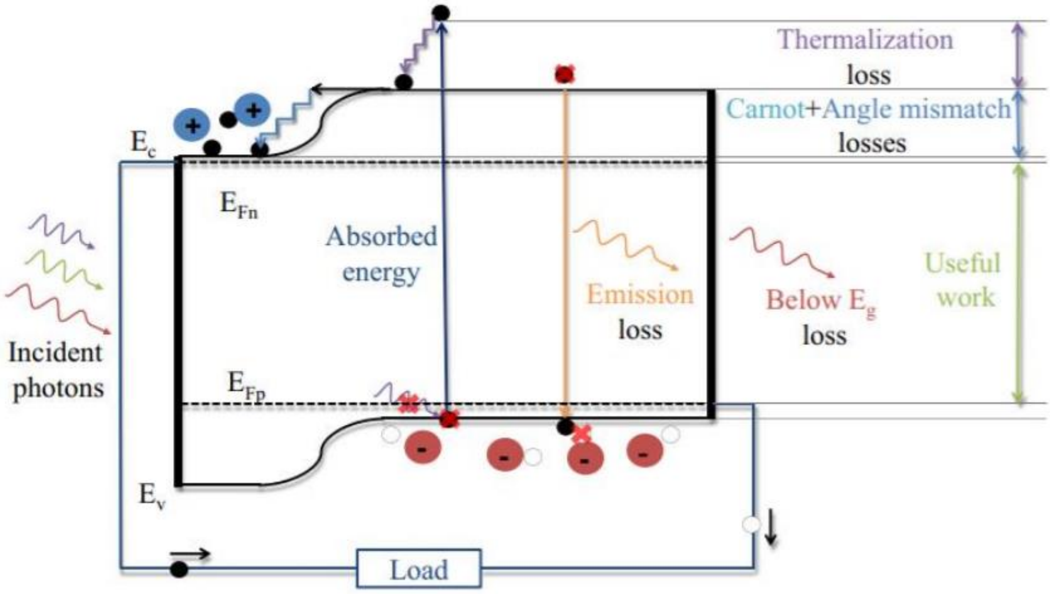

Figure 1-13: *Carnot model. Of particular interest are the Carnot, angle mismatch and emission losses as they are all functions of the cell temperature diagram from "Physics of the thermal behavior of photovoltaic devices"* [38].

The emission loss is described by the equation below,

$$E_g \frac{2\,\Omega_{emit}}{c^2 h^3} \int_{E_g}^{\infty} \frac{E^2}{e^{\frac{E - qV_{MPP}}{k_B T_C}}} dE \qquad 1.6$$

where only photon energies above the band gap are considered. The emission increases with temperature as can be seen in the integral. The angle mismatch losses and Carnot losses below are caused by the charge carriers losing their kinetic energy when they reach the cell junction and thus the cell voltage is reduced. As with emission these terms are also temperature dependent,

$$k_B T_C \, ln\left(\frac{\Omega_{emit}}{\Omega_{abs}}\right) J_{MPP} \qquad 1.7$$

$$E_g \left(\frac{T_C}{T_H}\right) J_{MPP} \qquad 1.8$$

Unlike the emission loss these losses are linear with respect to temperature. As the emission loss is a relatively small component of the temperature coefficient the temperature coefficient can be reasonably approximated as a constant within the relevant range of solar panel temperatures[38].

Thermal Degradation: There are several mechanisms by which the lifetime of a solar panel can be reduced due to elevated temperatures. Over time, metal atoms from the panel contacts can migrate into the cell which reduces the shunt resistance as a conducting bridge is formed in the device[39]. A short-circuited cell is quickly destroyed due to the high current. Cyclical thermal stress can also cause the panel to crack although the presence of several busbars creates redundancy and allows most of the panel to continue operation[31].

The EVA encapsulate layer between the glass and solar cell can also degrade, especially after UV absorbers have leached out of the polymer, and as diffusion is temperature dependent the rate of degradation is greater at higher temperatures[40]. Potential induced degradation is another solar panel failure mechanism where ions in the glass (sodium) can get through the encapsulant and diffuse into the solar cell. A negative bias voltage to the cell can cause gas bubbles to form at the metalization silicon interface due to electrochemical reactions[39].

Solar cell efficiency under low light conditions: The rated solar panel efficiency assumes an irradiance of 1000 Wm^{-2} however at lower irradiances this efficiency is reduced[41]. The solar cell efficiency can be expressed in terms of the fill factor by the following equation,

$$\eta = \frac{v_{oc} i_{sc} FF}{GA} \qquad 1.9$$

Where G is the irradiance and A is the panel area. The open circuit voltage is given by,

$$v_{oc} = V_{oc,STC}\left(1 + \frac{\beta}{100} \cdot \Delta T + a\, ln\left(\frac{G}{G_{STC}}\right)\right) \qquad 1.10$$

Where β is the temperature coefficient for the open circuit voltage and *a* is the irradiance correction factor (0.06). G_{STC} is the irradiance under standard conditions i.e. 1000 Wm^{-2}. The short circuit current as a function of irradiance is,

$$i_{sc} = \frac{I_{sc,STC}\left(1 + \frac{\alpha}{100} \cdot \Delta T\right) G}{G_{STC}} \qquad 1.11$$

Where α is the temperature coefficient of the short circuit current. By subbing equations 1.9 and 1.10 into equation 1.11 the efficiency can be expressed as a function of the irradiance[41] as shown in equation 1.12. The loss in efficiency at low irradiance has been demonstrated experimentally (see Figure 1-14) and is especially significant at very low irradiation values[42].

$$\eta = \frac{V_{oc,STC}\left(1 + \frac{\beta}{100} \cdot \Delta T + a\, ln\left(\frac{G}{G_{STC}}\right)\right) \frac{I_{sc,STC}\left(1 + \frac{\alpha}{100} \cdot \Delta T\right) G}{G_{STC}} FF}{GA} \qquad 1.12$$

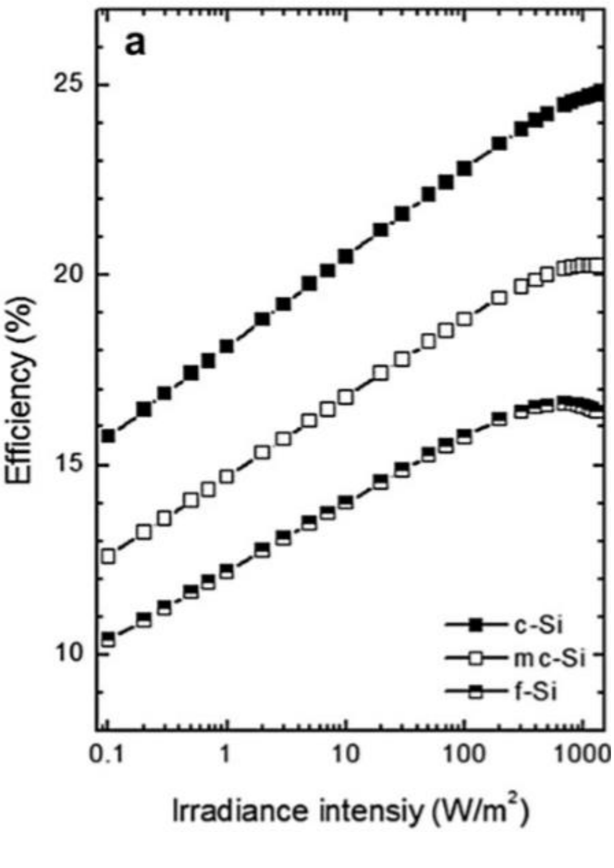

Figure 1-14: Low light losses. Efficiency of monocrystalline, polycrystalline and amorphous silicon solar cells. Note that the irradiance axis is on a log_{10} scale so the drop in efficiency only becomes severe at very low irradiance values. Daytime solar insolation in Ireland can fall to 100 Wm^{-2} during overcast conditions so this effect is still significant[42].

Shunt and Series Resistance Losses: Series resistance comes from the finite carrier mobility in the solar cell as well as resistance in the metal contacts and resistance at the metal semiconductor interface.

Under standard operating conditions the shunt resistance plays only a minor role as the much lower series resistance provides a more favourable path for the electric current. At low light levels, the effect of the shunt resistance becomes increasingly important. As the light intensity decreases, the bias point and current through the solar cell also decreases, and the equivalent resistance of the solar cell may begin to approach the shunt resistance. When these two resistances are similar, the fraction of the total current flowing through the shunt resistance increases, thereby increasing the fractional power loss due to shunt resistance. Consequently, under cloudy conditions, a solar cell with a high shunt resistance retains a greater fraction of its original efficiency than a solar cell with a low shunt resistance[43].

Annual energy losses as a result of low shunt resistance can be as high as 10% particularly for older solar cell designs[44]. The primary cause of low shunt resistance are defects in the manufacturing process such as leakage currents around the edge of the cell or defects in the bulk silicon that provides a current path through the cell. The total solar cell current is the photocurrent I_L minus the recombination rate and the short circuit current.

$$I = I_L - I_0 exp\left[\frac{qV}{nk_BT}\right] - \frac{V}{R_{SH}} \qquad 1.13$$

In equation 1.13 I_0 is the saturation current, the recombination rate is dependent on temperature T and voltage V while R_{SH} is the shunt resistance.

Reflection: Reflection at an interface can be understood by applying the Fresnel equations below,

$$R_s = \left|\frac{n_1 \cos\theta_i - n_2 \cos\theta_t}{n_1 \cos\theta_i + n_2 \cos\theta_t}\right|^2 \qquad 1.14$$

$$R_p = \left|\frac{n_1 \cos\theta_t - n_2 \cos\theta_i}{n_1 \cos\theta_t + n_2 \cos\theta_i}\right|^2 \qquad 1.15$$

Where θ_i is the incident angle and θ_t the refracted angle, R_s and R_p are the s and p polarized reflectivity respectively and n_1 and n_2 are the reflective indexes at the interface of the two media. In the case of unpolarized light, such as direct sunlight the total reflection is the average of R_s and R_p. The two main causes of reflection are large differences in the refractive index between the two media that form an interface and large angles of incidence. The incidence angle modifier IAM is the normalized reflection loss as a function of angle, it is a useful metric when comparing the reflectivity of different surfaces.

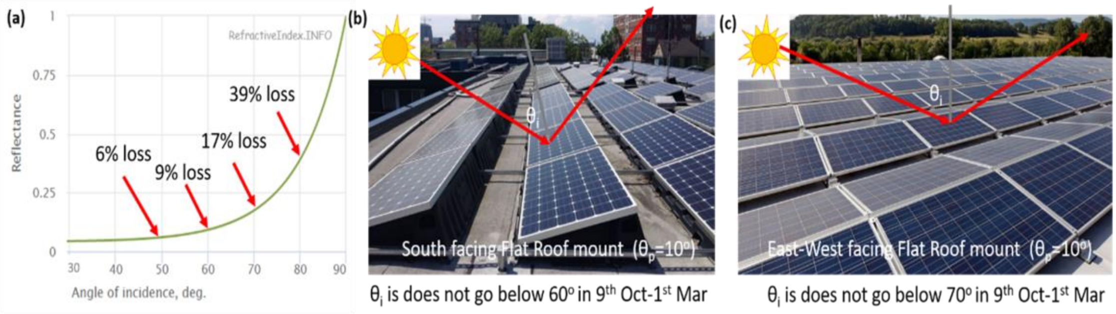

Figure 1-15: Incidence Angle Modifier (IAM) is useful when considering reflection losses at glancing angles.

Electrical Losses: Inverter losses result from the fact that solar panels generate DC power which must be converted to AC power for most applications and the inverters that utilize power electronics are not 100% efficient. Under ideal conditions expensive commercial scale inverters operate at 99% efficiency however this is when the panels are operating at their maximum power point, maximum power point trackers MPPTs periodical alter the operating voltage to ensure they are operating the voltage that produces the most power. Under cloudy conditions where the solar irradiance can change rapidly the maximum power point fluctuates and the MPPTs cannot keep up. Thus in reality inverter losses are higher than the manufacturers specifications[45].

Mismatch losses occur due to variation in performance of solar panels in an array. These variations are a result of manufacturing defects as well as non-uniform rates of degradation, soiling on some panels may also be greater than on others (e.g. bird droppings on some panels and not others). Thus the maximum power point of each solar panel will be slightly different. This problem can be tackled with micro-inverters such that each panels has its own small inverter but this increases the initial capital cost[44].

Cable losses are a result of Joule heating ($P = I^2R$) in the cables and thus high currents are not desirable. To minimise these losses cable length should be minimized and the cable should be thick to reduce electrical resistance and well insulated so they can operate at voltages of up to 1.5 kV[13].

1.6 Glint and Glare

Glint is defined as a brief, momentary flash of bright light, typically resulting from the reflection of sunlight off a moving surface. A common example is the transient solar reflection from a moving vehicle. In contrast, glare refers to a continuous and sustained source of bright light, generally associated with stationary objects. Due to the slow relative motion of the sun, these objects reflect sunlight for a prolonged duration, making glare a more persistent visual phenomenon. The fundamental distinction between glint and glare lies in their temporal characteristics. Standard industry glare analysis tools evaluate glare on a minute-by-minute basis, classifying solar reflections predominantly as "glare" rather than "glint" due to their extended duration.

The ocular effects of solar glare can be categorized into three levels of increasing severity. The first level denotes a low potential for inducing after-images or flash blindness. The second level indicates a moderate likelihood of temporary after-images. The third and most severe level represents a high potential for retinal burns, which may cause permanent ocular damage. These classifications assume a typical blink response from the observer. However, the potential for retinal burns from PV glare is negligible, as photovoltaic (PV) modules do not concentrate reflected sunlight.[46]

Glare is more broadly defined as a visual condition characterized by excessive contrast or an improper distribution of light sources, resulting in discomfort, visual impairment, or a reduced ability to discern details and objects. Low-angle reflections are a primary cause of glare and pose significant hazards to drivers and pilots. Additionally, glare is a source of discomfort for nearby residents, often leading to increased local opposition to solar PV installations. High levels of glare typically arise from sunlight reflecting off flat, smooth surfaces such as water, glass, or other materials with high specular reflectivity. Although water and glass exhibit lower overall reflectance than surfaces like snow, concrete, or foliage, they can generate significantly more glare at specific angles due to the specular nature of their reflections (glass and water often have smooth surfaces). This occurs when specular reflection projects an image of the sun directly into an observer's field of vision. The chart below (Figure 1-16) presents a hazard plot for a PV array.

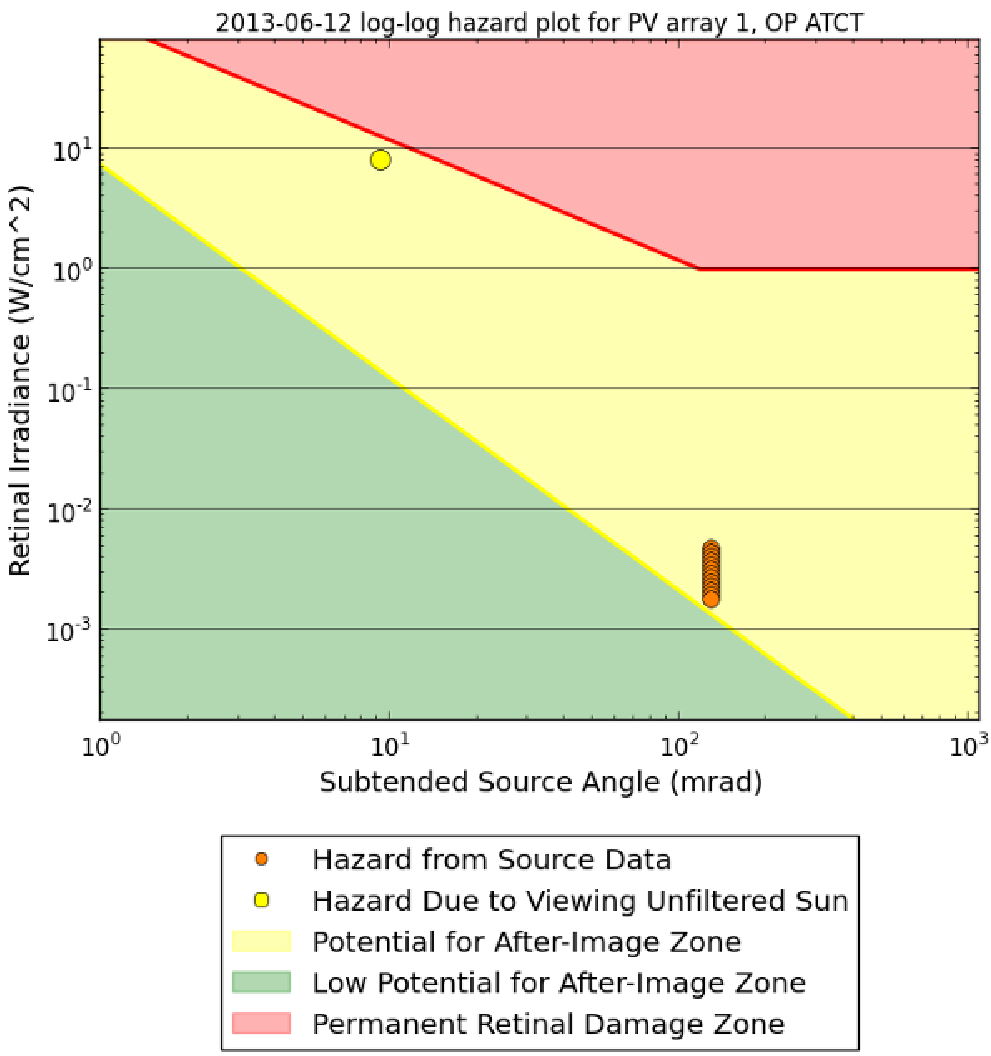

Figure 1-16: Glare plot. Shows a typical solar glare hazard plot. In this case the glare is over three orders of magnitude less intense than looking directly at the sun but is still within the zone of were there is potential for eye damage, in any case this glare is unpleasant and undesirable[46].

Reflections from PV panels can impair visibility, particularly when they produce sustained after-images. Empirical studies indicate that a reflected intensity of 7 W/m^2 is sufficient to induce an after-image lasting between four and twelve seconds. This magnitude of reflection accounts for only one to two percent of typical solar irradiance at a given location, which generally ranges between 800 and 1000 W/m^2. A critical factor influencing PV panel reflectance is the angular relationship between the module surface and the incident sunlight. A panel that absorbs 90 percent of direct sunlight may still reflect up to 60 percent when its orientation deviates from direct solar alignment. This phenomenon is particularly pronounced for low-tilt panels during sunrise and sunset, as noted by Yellowhair (2015).[47] The commonly cited assertion that PV panels reflect less than five percent of sunlight is only valid when the panels are positioned directly toward the sun. For fixed-mount panels, this condition is met only briefly each day, highlighting the variability of reflectance with solar position.

Glare can be supressed by a roughened surface that diffuses the reflected light[48]. Commercially available solutions include sandblasted glass, or textured glass however these have the drawbacks of reduced transmission and thus lower energy yield as well as increasing the surface area on the solar panel which enhances soiling. Another solution is a biomimetic surface with light trapping qualities which is what I have done for this thesis. Figure 1-17 below from Phytonics shows how these textured surfaces can suppress glare by reducing total reflection and diffusing the remaining reflected light.

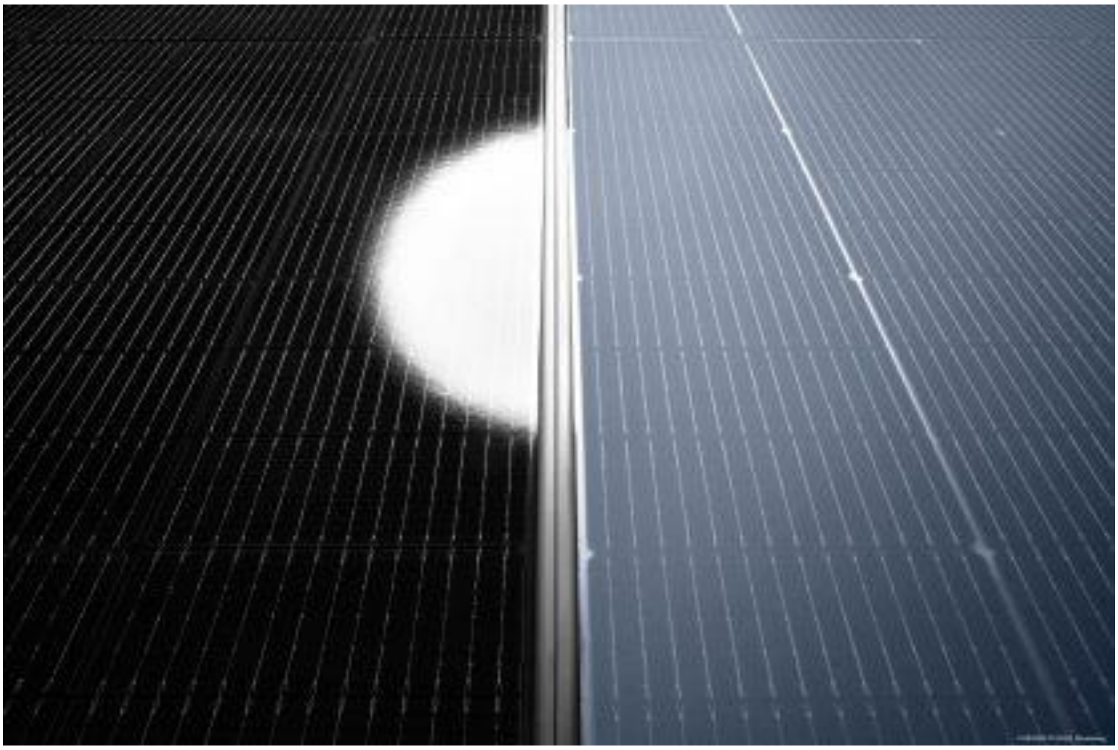

Figure 1-17 Anti-glare coating. This figure compares an ordinary solar panel with a porous silica AR coating with another solar panel with a biomimetic rose petal pattern imprinted onto a polymer layer. This Anti-glare surface was produced by Phytonics, which is a spin-off from the Karlsruhe Institute of Technology (KIT)[14]

1.7 SOILING

Soiling is a major problem for the PV industry as the accumulation of dirt on a solar panel surface can often reduce power output by a third, particularly in sandy regions. In the worst case power generation drops to zero as the panel it totally covered in sand, snow or dirt[49]. Soiling is so significant that it is considered worthwhile to use cleaning methods that are sufficiently abrasive to remove most anti-reflection coatings from the modules cover glass if it means reliable removal of the dirt. Thus, as the outer layer of a solar module it is important that any proposed AR coating helps reduce soiling or at the very least does not enhance soiling.

Soiling losses usually follow a sawtooth pattern as contaminants gradually accumulate until a rainfall or cleaning event occurs and the level of soiling is reset albeit somewhat higher as some soiling is permanent[50]. A substantial amount of rain is required to actually remove the soiling, and without active washing, the PV energy output can be reduced 20% to 40% during typical weather conditions in the Southwest United States[50].

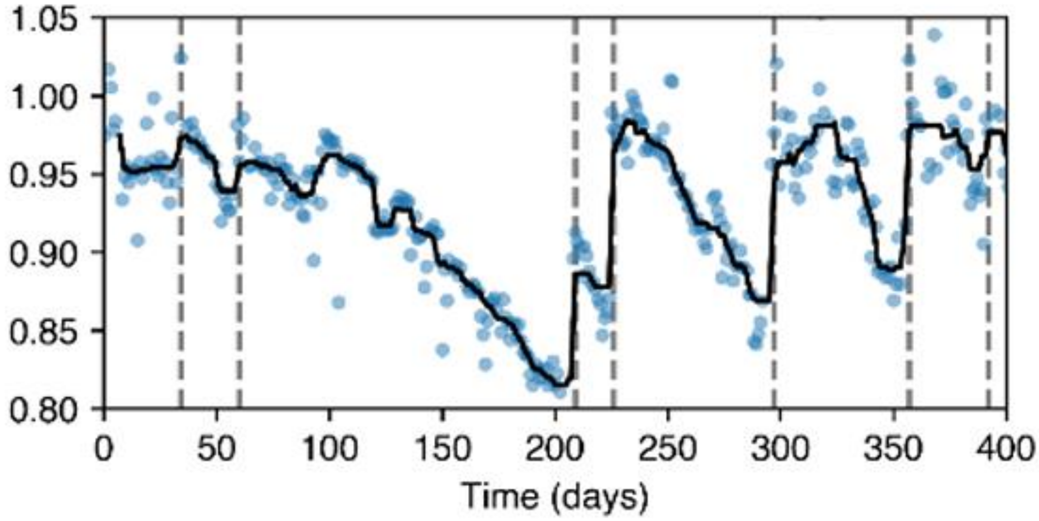

Figure 1-18: Soiling vs rainfall. Figure shows soling at a US test site, the black line is a 13 day rolling average of the normalized module efficiency. Data from M. Deceglie, L. Micheli, M. Muller, "Quantifying soiling loss directly from PV yield," IEEE Journal of Photovoltaics, vol. 8. 2018[51].

The factors that influence soiling include particle size, particle roughness, static charge due to the high voltages of PV arrays[52], the surface chemical properties of the dust, humidity and temperature. Surface adhesion of dust particles can be measured in the lab with the use of atomic force microscopy tests. At higher RH (Relative Humidity) capillary forces can dominate if the water layer is thick enough to overcome the surface asperity (roughness) while at lower RH values, adhesion is dominated by van der Waals forces, However, surface roughness has a major effect on the adhesion process by reducing contact area due to surface topographic features; thus, the value of both forces substantially decreases as roughness increases. At high roughness levels there is little difference in the adhesion of large particles and small particles as the contact area is the same (In theory a rough surface makes contact with a smooth surface at only three points regardless of size).

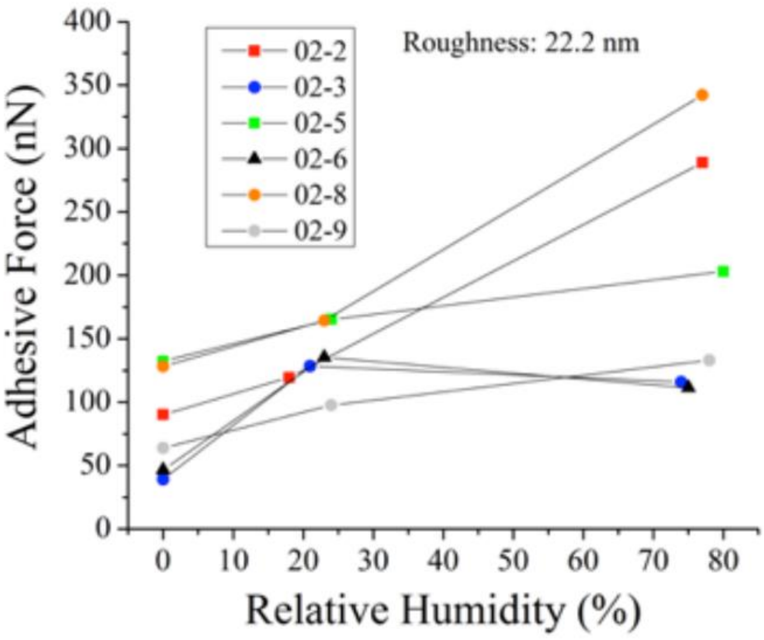

Figure 1-19: Dust adhesion. The legend represents dust particles by size in microns. While humidity clearly increases surface adhesion the impact of particle size is less clear[53].

The term cementation can be used to describe particles that have adhered to surfaces or to each other such that they resist removal by shear forces applied by wind, water, gravity, brushing, or other means. Clays have the highest recorded soiling rate due to their 2D shape providing a large contact area. Some dusts contain water soluble minerals that dissolve in rainwater and then recrystalize on the glass surface causing cementation[53]. These soiling mechanisms will be addressed in more detail in a dedicated chapter later in this thesis.

1.8 State of the Art in AR coatings

Anti-reflection can be achieved by either light trapping with a textured surface or by applying a low refractive index ideally of quarter wavelength thickness between the glass and air[54]. The various low index anti-reflective coatings are described below.

Homogenous AR coatings: consist of a single layer of low refractive index material that ideally has a refractive index of 1.22 and a thickness of $\lambda/4$ to optimally suppress reflection at the glass air interface. These coatings typically reduce reflection from 4% to 3% at the glass air interface at normal angle of incidence.

Inhomogeneous AR coatings: Have multiple layers or a smooth gradient of refractive index. In principle if the refractive index is near that of air at the AR-air interface and near that of glass at the AR-glass interface and the transition is smooth in between then reflection can be totally suppressed. Inhomogeneous AR coatings are not limited to quarter wavelength thickness and can be much thicker provided there is little optical absorption in the AR coating itself.

Single Layer AR coatings: are the most basic of AR coating designs and simply consist of a low index material such as MgF_2 which has a refractive index of 1.38 which is quite far from the ideal 1.22. MgF_2 is unsuitable as a solar module coating as it is an ionic compound which is water soluble. Unfortunately, there is a very limited range of materials that have a lower refractive index than glass (refractive index = 1.5). One advantage of these coatings is that they tend to have good AR properties over a wide range of wavelengths if the material selected has low dispersion across the visible wavelength range[55].

Double and Multilayer AR coatings: The next logical step is to add more layers to produce a stack. For a double-layer AR coating the optimal refractive index for each layer is given by,

$$\frac{n_1}{n_2} = \sqrt{\frac{n_0}{n_s}} \tag{1.16}$$

Where n_1 and n_2 are the AR coating layers while n_0 is the air and n_s is the glass. Each layer of the stack should be of quarter wavelength thickness so light can interact each layer as a separate entity. An example of a double layer AR coating is MgF_2 (n=1.38) on top of fused silica SiO_2 (n=1.85)[56].

Gradient Refractive index: These can be thought of as an infinite number of layers in a multilayer stack[57]. There are however different curves of the gradient such as linear x^1 , cubic x^3 and quintic x^5.

Porous AR coatings: As per effective medium theory[10], when the porosity of a material is on a subwavelength length scale light interacts with the material as though it were mixed with air giving a reduced effective refractive index below that of the materials bulk properties. This effective refractive index is a function of the volume fraction as shown in the equation below[58],

$$n_{pc} = \left[\left(1 - \frac{P}{100}\right)(n_{dc}^2 - 1) + 1\right]^{\frac{1}{2}} \quad 1.17$$

Where P is the volume fraction and n_{pc} is the refractive index of the porous layer and n_{dc} is the refractive index of the bulk material. One major advantage of porous AR coatings is that it allows for the refractive index to be tuned by varying the porosity, thus it is possible to get a refractive index of 1.22 which is ideal for a single layer. Graded porosity can also be used to get near perfect anti-reflection properties. There is a limit to these porous materials and it is not possible to achieve a refractive index very close to unity as the material becomes progressively more fragile as the volume fraction of the pores increases[12].

Moth Eye: Biomimetics is the imitation of biological structures or processes to solve various problems. Moth eyes are covered in sub-wavelength hexagonal nano-cone array (also known as a nipple array) which behaves as a graded effective medium material. As the cones get narrower near the tips the air volume fraction becomes greater thus reducing the refractive index as one approaches the top of the structure. This structure will be further investigated in this thesis in a dedicated chapter.

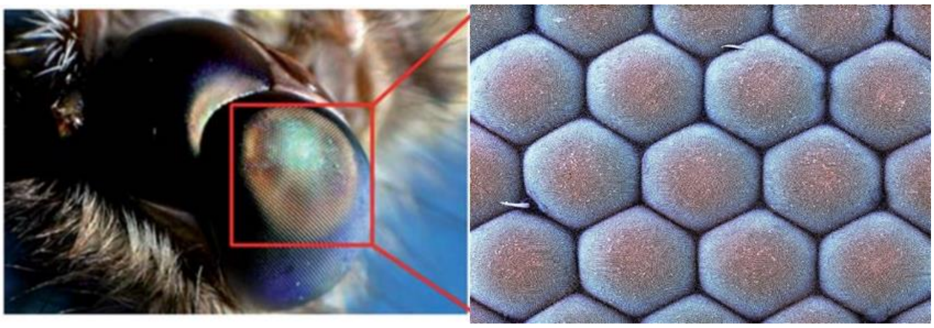

Figure 1-20: The moth eye structure helps nocturnal insects such as moths see in the dark by enhancing the transmission of light into the eye[59]. Image on the right from[60]

Textured Surface AR coatings: These structures are effective at trapping light coming from glancing angles as well as reducing glare by diffusing any light that is reflected. These AR coatings perform best when the features have a high aspect ratio. Light coming in at near 0^o angle of incidence will be well below the critical angle and will thus glance downwards into the structure. Light coming at near 90^o incidence will experience a lower effective angle of incidence as seen in the diagram below on the right. It is as if the entire surface was tilted towards the light[61].

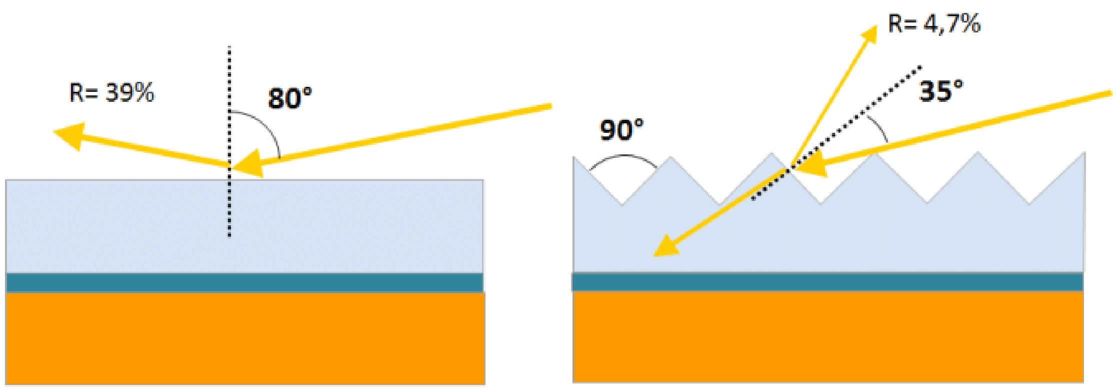

Figure 1-21: Light trapping. Diagrams from PVEducation show the light trapping qualities of textured surfaces.[62]

Solar cells have there own inverted pyramid array textured AR coating, this coating is more important than the AR coating on the module glass as silicon has a high refractive index in the visible range and thus reflection losses would be very high. The inverted pyramid structure gives solar cells their black appearance as light of all visible wavelengths is trapped[63].

1.9 State of the Art Textured AR Coatings

Several textured AR coatings have been designed for solar modules with the goal of reducing glare, improving transmission and providing a self-cleaning effect. As a general rule, higher aspect ratio shapes have better light trapping and hydrophobic properties compared to lower aspect ratio shapes. This is illustrated in a 2020 paper by Hyeongsik Park et al[64] where three different aspect ratios of textured glass are compared with the highest aspect ratio glass yielding the highest current density.

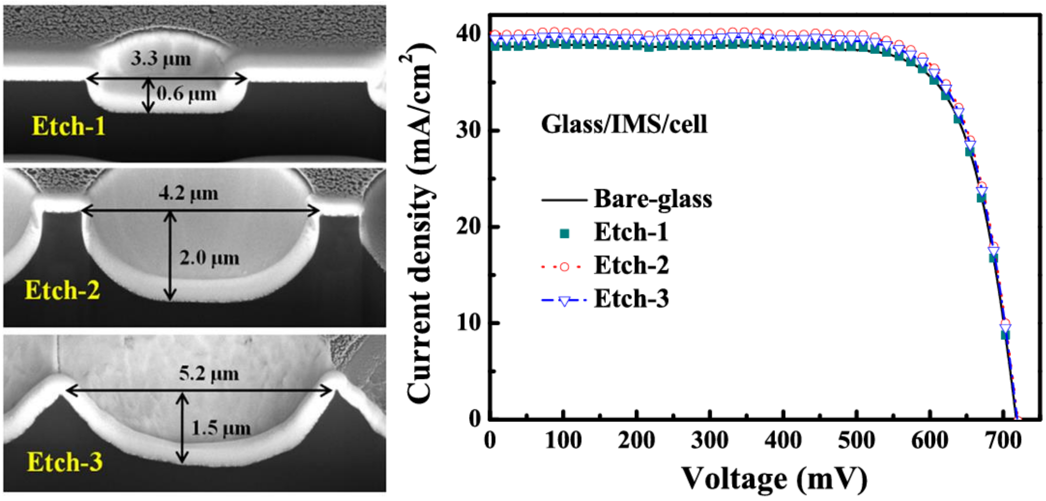

Left: Pitted glass. SEM images of three glass surfaces that have been etched with HF acid, Etch-2 has the highest aspect ratio. Right: J/V sweeps for silicon heterojunction solar cells with the textured glass placed on top. The best performance was for Etch-2 followed by Etch-3, the performance of Etch-1 is the lowest and is barley distinguishable from bare, unetched glass.

Nanoscale moth eye patterns have been shown to improve the self-cleaning and anti-reflective properties of glass in many papers.[65–67] One challenge for these surfaces is that the nanoscale features can be easily scratched off, although this can be somewhat mitigated by chemically strengthening the glass post patterning[68]. These nanoscale textured surfaces have also been done on polymers by hot embossing[69], they still suffer from low durability. One way of mitigating the low durability problem is with a hierarchical structure where larger microscale features protect the smaller nanoscale features from damage.

Texturing of non-glass surfaces such as fluorinated ethylene propylene (FEP) has also been done, with the main objective being to create a superhydrophobic surface but the added benefit of some light trapping. While many polymers degrade when exposed to UV radiation, FEP has high UV stability and thus is more suitable for solar PV applications. The main advantage of working with a polymer instead of glass is the material can be easily shaped with techniques such as hot embossing.[70] Downsides include the potential environmental harm of mass deployment of Teflon like materials which are non-biodegradable or recyclable. This may or may not be a problem as many fluoropolymers are highly chemically inert and non-toxic however this inertness could lead to them accumulating in large quantities in natural systems, the potential problem of microplastics is not fully understood.[71]

1.10 COMMERCIAL ADOPTION OF AR COATING TECHNOLOGY

To date the vast majority of solar module manufacturers use standard porous oxide single layer AR coatings such as SiO_2 applied with the sol gel method. As already discussed, these AR coatings give a 3% improvement to transmission on day 1, but this performance enhancement degrades within the first two years in real world conditions. Porous SiO_2 is also more hydrophilic than regular glass and thus will enhance soiling due to it having a greater surface energy which will increase the adhesion force of dust particles.[72] Despite these problems these AR coatings are still popular as more attention is given to the performance of a solar panel on day one rather than the performance over time.

None of the major solar PV manufactures use hierarchically textured glass, moth eye nanopatterns or the other technologies discussed in this chapter. One problem is that many of the techniques used to make these patterns are not scalable. Magnetron sputtering and compression moulding are more suitable for large scale manufacture than lithography techniques, this is discussed in much greater detail in chapter 4. There are, however, companies that provide retrofittable solutions to reduce reflection, glare and soiling. Phytonics, produces polymer sheets with micro/nano scale rose petal patterns that can be applied to solar panels with a transparent adhesive to increase transmission and reduce glare.[73] Companies such as Hydrosol provide nanoscale superhydrophobic coatings in liquid form that can be applied to solar modules and left to cure at room temperature.[74]

Solar panel glass is a huge market valued at $53.5 billion in 2024.[75] Significantly altering the glass manufacturing process would require huge capital expenditure and a reasonable degree of certainty that the new technology is effective. One potential way of micro texturing glass with minimal disruption to the current method is to use a mould to pattern the glass during the tempering process. When glass is tempered, it is heated to between 650 to 700 degrees C and then rapidly cooled with forced air.[76] This temperature range is also where glass becomes soft and workable, thus it may be possible to pattern the glass at this stage of the production process immediately prior to annealing with the benefit of saving energy by not having to heat the glass a second time.

1.11 Novelty of this Work and Overlap with other Designs

The concept of hierarchically textured glass surfaces for solar PV applications is not unique to this project. Both HF wet etching to form micro pitted glass structures and reactive ion etching to form nanopillars have both been done with solar PV applications in mind. This specific combination of this micro and nanoscale has not been attempted elsewhere. The uniqueness of this project is in the emphasis on antireflection over a broad range of incident angles.

Considerable time was spent evaluating reflection losses at non-optimal angles, the main takeaway from that work was the importance of high aspect ratio features for effective light trapping when the Sun is low in the sky. Another finding of my work was that reflection losses are particularly high for roof mounted solar panels due to their often-suboptimal tilt and orientation. Textured glass surfaces have a better incidence angle modifier (IAM) relative to single layer AR coatings and thus these poorly orientated panels would benefit the most from a textured glass surface. This is discussed in more detail in chapter 2.

Due to their difficulty, angle resolved measurements are relatively rare in the literature and many AR coating designs only show reflection at normal incidence angles. This significantly understates the potential energy yield improvement from adding an AR coating. In chapter 2 I show that for East-West mounted panels, reflection loss is not 4% without an AR coating, it is 15% due to high glancing angle reflection and thus the importance of an AR coating is more important than is often realized.

I also attempt to create a hydrophobic glass surface without altering the surface chemistry of the glass and only altering the geometry of the surface, this is a more difficult undertaking than coating the glass with an intrinsically hydrophobic chemical. The motivation for this was enhanced durability as many hydrophobic chemicals would eventually degrade under outdoor conditions. For more on this see chapter 7 on contact angle measurements and self-cleaning.

1.12 Thesis Scope

In this thesis my initial aim was to address the particularly high reflection losses found in high latitude regions as result of low sun angle. From ray tracing simulations I was able to predict that a sawtooth pattern etched into a polycarbonate sheet would be effective at reducing reflection losses. An advantage lay in knowing that the majority of solar panels are south facing at 25^{o} tilt so an additional 20^{o} sawtooth elevation angle would increase the effective tilt angle of the solar panel. A progression of this design was the fish-scale pattern where the curve of each scale matched the weighted average solar arc through the sky for a given latitude. Thus, the fish-scale pattern would act like a microlens array but optimised for a narrow range of incidence angles.

As the project developed, I decided against the sawtooth/fish-scale design for four main reasons, firstly much of solar irradiance is diffuse and so there is utility in being able to efficiently collect light from all angles, this is particularly true of the high latitude regions I was most concerned about. Secondly a polymer layer on top of the solar cover glass would be vulnerable to UV degradation as well as delamination, in the long run this solution could end up being counterproductive and reducing transmission overall. Thirdly the texturing would increase the surface area of the solar panel which would lead to worse soiling. Fourthly the refractive index of polycarbonate is 1.57 while glass is 1.5 so the material is intrinsically more reflective. Finally, there was no cheap and scalable way to etch these patterns directly into the cover glass. Unlike a polymer sheet that could be patterned by roll-to-roll hot embossing or nano-imprint lithography, the high hardness of glass would require milling which cannot be scaled up to cover the thousands of square kilometres required to make it a viable solution.

My focus then turned to biomimetics where I successfully created a hierarchical structure inspired by the lotus leaf and the rose petal. In this field of study, the microlens array structure was a very popular geometry to use but in my ray tracing simulations I show that the inverse microlens array (pitted surface) has better anti-reflection properties. The pits were formed by hydrofluoric acid wet etching where the goal was to etch the pits all the way out until the edges of each pit came into contact. In practice this was difficult to accomplish due to the lithography mask lifting off when most of the original glass surface was etched away. By modifying the glass surface to improve adhesion of the lithography mask to the glass I was eventually able to create a dense array of pits. Various optical measurements demonstrated showed that these pitted structures improved transmission and were less hydrophilic than non-pitted glass. Thus, my objectives were achieved before the second layer of the hierarchical structure was even applied.

My second layer was a subwavelength nanopillar array fabricated my using a dewetted metal mask and dry etching the glass to form the pillars. The pillar height was tuned to quarter wavelength thickness to maximize its effectiveness as an AR coating. Both the nanoscale pillars and the microscale pits were optically measured separately and in combination to show the contribution of each of the features. Soiling and abrasion tests demonstrated that the microscale structure was robust and able to protect the fragile nanoscale pattern from damage.

1.13 References

(1) Martin, N.; Ruiz, J. M. Calculation of the PV Modules Angular Losses under Field Conditions by Means of an Analytical Model. *Sol. Energy Mater. Sol. Cells* **2001**

(2) Khatib, T.; Deria, R. East-West Oriented Photovoltaic Power Systems: Model, Benefits and Technical Evaluation. *Energy Convers. Manag.* **2022**

(3) Arslan, M.; Çunkaş, M. An Experimental Study on Determination of Optimal Tilt and Orientation Angles in Photovoltaic Systems. *J. Eng. Res.* **2024**.

(4) SPW. *Fixed-tilt vs. tracker: Why a one-size-fits-all approach can limit solar production*. Solar Power World. https://www.solarpowerworldonline.com/2018/02/fixed-tilt-vs-tracker-one-size-fits-approach-can-limit-solar-production/

(5) Sánchez-Carbajal, S.; Rodrigo, P. M. Optimum Array Spacing in Grid-Connected Photovoltaic Systems Considering Technical and Economic Factors. *Int. J. Photoenergy* **2019**

(6) Wittwer, A. R.; Podestá, J. M.; Castro, H. G.; Mroginski, J. L.; Marighetti, J. O.; De Bortoli, M. E.; Paz, R. R.; Mateo, F. Wind Loading and Its Effects on Photovoltaic Modules: An Experimental–Computational Study to Assess the Stress on Structures. *Sol. Energy* **2022**

(7) Sarkın, A. S.; Ekren, N.; Sağlam, Ş. A Review of Anti-Reflection and Self-Cleaning Coatings on Photovoltaic Panels. *Sol. Energy* **2020**

(8) Law, A. M.; Jones, L. O.; Walls, J. M. The Performance and Durability of Anti-Reflection Coatings for Solar Module Cover Glass – a Review. *Sol. Energy* **2023**

(9) Ballif, C.; Dicker, J.; Borchert, D.; Hofmann, T. Solar Glass with Industrial Porous SiO2 Antireflection Coating: Measurements of Photovoltaic Module Properties Improvement and Modelling of Yearly Energy Yield Gain. *Sol. Energy Mater. Sol. Cells* **2004**

(10) Berthier, S.; Lafait, J. Effective Medium Theory: Mathematical Determination of the Physical Solution for the Dielectric Constant. *Opt. Commun.* **1980**

(11) Zheng, Y.; Zhou, Z.; Cao, W.; Li, C.; Wang, Q.; Huang, Y.; Shen, S. Robust, Low Haze and Graded Porous Anti-Reflective Glass by Tailoring the Nanostructures. *Ceram. Int.* **2020**

(12) Murray, C.; Flannery, C.; Streiter, I.; Schulz, S. E.; Baklanov, M. R.; Mogilnikov, K. P.; Himcinschi, C.; Friedrich, M.; Zahn, D. R. T.; Gessner, T. Comparison of Techniques to Characterise the Density, Porosity and Elastic Modulus of Porous Low-k SiO2 Xerogel Films. *Microelectron. Eng.* **2002**

(13) Karin, T.; Jain, A. Visual Characterization of Anti-Reflective Coating on Solar Module Glass. In *2020 47th IEEE Photovoltaic Specialists Conference (PVSC)*; 2020
(14) Fritz, B.; Hünig, R.; Guttmann, M.; Schneider, M.; Reza, K. M. S.; Salomon, O.; Jackson, P.; Powalla, M.; Lemmer, U.; Gomard, G. Upscaling the Fabrication Routine of Bioreplicated Rose Petal Light Harvesting Layers for Photovoltaic Modules. *Sol. Energy* **2020**
(15) Sun, J.; Wang, X.; Wu, J.; Jiang, C.; Shen, J.; Cooper, M. A.; Zheng, X.; Liu, Y.; Yang, Z.; Wu, D. Biomimetic Moth-Eye Nanofabrication: Enhanced Antireflection with Superior Self-Cleaning Characteristic. *Sci. Rep.* **2018**
(16) *EN2024 ISE Study Levelized Cost of Electricity Renewable Energy Technologies*
(17) *Net Zero by 2050, A Roadmap for the Global Energy Sector, IEA, 2021*
(18) *IEA's World Energy Outlook systemically underestimates solar PV development – pv magazine International*
(19) *Dublin Airport Hourly Data - data.gov.ie*. https://data.gov.ie/dataset/dublin-airport-hourly-data
(20) Fernández-Guillamón, A.; Sarasúa, J. I.; Chazarra, M.; Vigueras-Rodríguez, A.; Fernández-Muñoz, D.; Molina-García, A. Frequency Control Analysis Based on Unit Commitment Schemes with High Wind Power Integration: A Spanish Isolated Power System Case Study. *Int. J. Electr. Power Energy Syst.* **2020**
(21) Saha, S. K. Empowering Rural South Asia: Off-Grid Solar PV, Electricity Accessibility, and Sustainable Agriculture. *Appl. Energy* **2025**
(22) Hu, C.; White, R. M. *Solar Cells: From Basics to Advanced Systems*; McGraw-Hill, 1983.
(23) Sbyrnes321. *English: The Shockley-Queisser Limit for the Maximum Possible Efficiency of a Solar Cell*
(24) William Shockley and Hans J. Queisser, Detailed Balance Limit of Efficiency of pn Junction Solar Cells, Journal of Applied Physics, 1961
(25) Green, M.; Guillemoles, J.; Schmidt, T. Project : " Hot Carrier Solar Cell : Implementation of the Ultimate PV Converter " Annual Report April; 2009.
(26) Kavlak, G.; McNerney, J.; Trancik, J. E. Evaluating the Causes of Cost Reduction in Photovoltaic Modules. *Energy Policy* **2018**
(27) *Best Research-Cell Efficiency Chart*. https://www.nrel.gov/pv/cell-efficiency.html
(28) Green, M. A. The Passivated Emitter and Rear Cell (PERC): From Conception to Mass Production. *Sol. Energy Mater. Sol. Cells* **2015**
(29) *A Complete Guide to PERC Solar Panels (vs. Other Techs)*. Solar Magazine. https://solarmagazine.com/solar-panels/perc-solar-panels/
(30) Stutenbaeumer, U.; Mesfin, B. Equivalent Model of Monocrystalline, Polycrystalline and Amorphous Silicon Solar Cells. *Renew. Energy* **1999**
(31) Dullweber, T.; Kranz, C.; Peibst, R.; Baumann, U.; Hannebauer, H.; Fülle, A.; Steckemetz, S.; Weber, T.; Kutzer, M.; Müller, M.; Fischer, G.; Palinginis, P.; Neuhaus, H. PERC+: Industrial PERC Solar Cells with Rear Al Grid Enabling Bifaciality and Reduced Al Paste Consumption. *Prog. Photovolt. Res. Appl.* **2016**
(32) *Optimal Mounting Configuration For Bifacial Solar Modules On Single Axis Trackers-12-10-18*
(33) *China Bifacial 166mm Monocrystalline Solar Cell Suppliers & Manufacturers & Factory - Made in China - Dongshuo*
(34) Thompson, C. *What Does PERC in Solar Mean?*. Unbound Solar. https://unboundsolar.com/blog/about-perc-solar

(35) Bora, B.; Rai, S.; Dhar, A.; Banerjee, C. Effect of UV Irradiation on PV Modules and Their Simulation in Newly Designed Site-Specific Accelerated Ageing Tests. *Sol. Energy* **2023**
(36) Singh, A.; Umakanth, V.; Tyagi, N.; Kumar, S. A Comparative Study of Different Polymer Materials for the Development of Flexible Crystalline Silicon Modules. *Sol. Energy Mater. Sol. Cells* **2023**
(37) *PVsyst*. https://www.pvsyst.com/
(38) Olivier Dupré , Rodolphe Vaillon , Martin A. Green, *Physics of the thermal behavior of photovoltaic devices, Springer, 2017*
(39) Domanski, K.; Correa-Baena, J.-P.; Mine, N.; Nazeeruddin, M. K.; Abate, A.; Saliba, M.; Tress, W.; Hagfeldt, A.; Grätzel, M. Not All That Glitters Is Gold: Metal-Migration-Induced Degradation in Perovskite Solar Cells. *ACS Nano* **2016**
(40) *PV-Manufacturing.org*. PV-Manufacturing.org. https://pv-manufacturing.org/bifacial-solar-cells-and-modules/
(41) Murillo-Soto, L. D.; Meza, C. A Simple Temperature and Irradiance-Dependent Expression for the Efficiency of Photovoltaic Cells and Modules. In *2018 IEEE 38th Central America and Panama Convention (CONCAPAN XXXVIII)*; 2018
(42) N.H. Reich, Charge Yield Potential of Indoor-Operated Solar Cells Incorporated into Product Integrated Photovoltaic (PIPV), Renewable Energy 2011
(43) Mondol, J. D.; Yohanis, Y. G.; Norton, B. Optimising the Economic Viability of Grid-Connected Photovoltaic Systems. *Appl. Energy* **2009**
(44) Wurster, T. S.; Schubert, M. B. Mismatch Loss in Photovoltaic Systems. *Sol. Energy* **2014**
(45) *The Efficiency of Solar Inverters-*. https://www.srnesolar.com/blog/free-guides/the-efficiency-of-solar-inverters
(46) Solar Glare Hazard Analysis Tool (SGHAT) Technical Reference Manual, 2015.
(47) *Yellowhair-2015-Asmt-Pv-Surf, Photovoltaics, 2015*
(48) User, S. *Solar Glint and Glare calculation*. https://www.zehndorfer.at/en/solar-glare/glare-calculation
(49) Michael Gostein; J. Riley Caron; Bodo Littmann, Measuring Soiling Losses at Utility-Scale PV Power Plants, IEEE, 2014
(50) A. Kimber; L. Mitchell; S. Nogradi; H. Wenger, The Effect of Soiling on Large Grid-Connected Photovoltaic Systems in California and the Southwest Region of the United States, IEEE, 2006
(51) Michael G. Deceglie; Leonardo Micheli; Matthew Muller, *Quantifying soiling loss directly from PV yield, IEEE, 2014*
(52) Lin J. Simpson, Increased PV Soiling from High Module Voltages, IEEE, 2019
(53) *Lin Simpson, Addressing Soiling: From Interface Chemistry to Practicality, NREL, 2020*
(54) Raut, H. K.; Ganesh, V. A.; Nair, A. S.; Ramakrishna, S. Anti-Reflective Coatings: A Critical, in-Depth Review. *Energy Environ. Sci.* **2011**
(55) *Anti-Reflection (AR) Coatings*. https://www.edmundoptics.eu/knowledge-center/application-notes/lasers/anti-reflection-coatings/
(56) İpek Girgin Kavakli, Kayhan Kantarli, Single and Double-Layer Antireflection Coatings on Silicon, Turkish Journal of Physics, 2002
(57) Southwell, W. H. Gradient-Index Antireflection Coatings. *Opt. Lett.* **1983**
(58) Yoldas, B. E.; Partlow, D. P. Formation of Broad Band Antireflective Coatings on Fused Silica for High Power Laser Applications. *Thin Solid Films* **1985**
(59) Dacey, J. *Moth eyes inspire more efficient solar cell*. Physics World. https://physicsworld.com/a/moth-eyes-inspire-more-efficient-solar-cell

(60) LIBRARY, D. D. F., KEELE UNIVERSITY/SCIENCE PHOTO. *Moth eye, SEM - Stock Image - C001/7618*. Science Photo Library.
(61) *Optica Publishing Group*. https://opg.optica.org/view_article.cfm?pdfKey=52b24c5f-f0a4-420d-bba654362d4da4fa_7099
(62) *Light Trapping | PVEducation*. https://www.pveducation.org/pvcdrom/design-of-silicon-cells/light-trapping
(63) Smith, A. W.; Rohatgi, A. Ray Tracing Analysis of the Inverted Pyramid Texturing Geometry for High Efficiency Silicon Solar Cells. *Sol. Energy Mater. Sol. Cells* **1993**
(64) Park, H.; Shin, M. hun; Iftiquar, S. M.; Hussain, S. Q.; Ju, M.; Kim, Y.; Cho, E.-C.; Yi, J. The Light-Trapping Effect in Various Textured Cover Glass for Enhancing the Current Density in Silicon Heterojunction Solar Cells. *Opt. Commun.* **2020**
(65) Kwaśnicki, P. Texturized Glass in the Application of Architectural Photovoltaics. *Clean. Eng. Technol.* **2024**
(66) Ji, S.; Park, J.; Lim, H. Improved Antireflection Properties of Moth Eye Mimicking Nanopillars on Transparent Glass: Flat Antireflection and Color Tuning. *Nanoscale* **2012**
(67) Kraus, M.; Diao, Z.; Weishaupt, K.; Spatz, J. P.; Täschner, K.; Bartzsch, H.; Schmittgens, R.; Brunner, R. Combined 'Moth-Eye' Structured and Graded Index-Layer Anti-Reflecting Coating for High Index Glasses. *Opt. Express* **2019**
(68) Luo, X.; Lu, L.; Yin, M.; Fang, X.; Chen, X.; Li, D.; Yang, L.; Li, G.; Ma, J. Antireflective and Self-Cleaning Glass with Robust Moth-Eye Surface Nanostructures for Photovoltaic Utilization. *Mater. Res. Bull.* **2019**
(69) Liu, X.; Li, K.; Shen, J.; Gong, F. Hot Embossing of Moth Eye-like Nanostructure Array on Transparent Glass with Enhanced Antireflection for Solar Cells. *Ceram. Int.* **2021**
(70) Roslizar, A.; Dottermusch, S.; Vüllers, F.; Kavalenka, M. N.; Guttmann, M.; Schneider, M.; Paetzold, U. W.; Hölscher, H.; Richards, B. S.; Klampaftis, E. Self-Cleaning Performance of Superhydrophobic Hot-Embossed Fluoropolymer Films for Photovoltaic Modules. *Sol. Energy Mater. Sol. Cells* **2019**
(71) Lohmann, R.; Letcher, R. J. The Universe of Fluorinated Polymers and Polymeric Substances and Potential Environmental Impacts and Concerns. *Curr. Opin. Green Sustain. Chem.* **2023**
(72) Law, A. M.; Jones, L. O.; Walls, J. M. The Performance and Durability of Anti-Reflection Coatings for Solar Module Cover Glass – a Review. *Sol. Energy* **2023**
(73) Fritz, B.; Hünig, R.; Guttmann, M.; Schneider, M.; Reza, K. M. S.; Salomon, O.; Jackson, P.; Powalla, M.; Lemmer, U.; Gomard, G. Upscaling the Fabrication Routine of Bioreplicated Rose Petal Light Harvesting Layers for Photovoltaic Modules. *Sol. Energy* **2020**
(74) *HYDRASOL | Hydrophobic Nano Coating for Solar Panel | ANT LAB*. https://www.antlab.in/hydrasol-solar-nano-coating.php
(75) *Solar PV Glass Market Size, 2025-2034 Trends Report*. Global Market Insights Inc. https://www.gminsights.com/industry-analysis/solar-pv-glass-market
(76) GmbH, A. I. *What is thermal tempering of glass?*. ACI Industriearmaturen GmbH. https://www.aci24.com/en/

2 ANNUAL REFLECTION LOSSES

2.1 SOLAR IRRADIANCE

Only about 77% of light incident the upper atmosphere reaches the Earth's surface the rest being scattered back into space or absorbed by the atmosphere[1]. Air mass is the normalized distance through the atmosphere the Sun light travels through, AM0 refers to the Solar flux at the top of the atmosphere (1353 W/m^2 also known as the solar constant) while AM1 is the solar Irradiance on the ground when the Sun is 90 degrees in the Sky (this event can only occur between the Tropic of Capricorn and the Tropic of Cancer latitude lines). At AM1.5 the Suns light travels through 1.5 atmospheres and has a flux of 970 W/m^2 this is rounded to 1000 W/m^2 and used as the standard test condition for solar panels. The relationship between air mass and irradiance is as follows,

$$I = 1353 \times 0.7^{AM^{0.678}} \quad 2.1$$

Rayleigh scattering as show in the equation below mean that air mass has a major impact on the spectral content of solar radiation.

$$I \propto \left(\frac{1}{\lambda}\right)^4 \quad 2.2$$

This leads to very low levels of UV irradiation near sunset and a much larger proportion of red and infrared radiation. This can be shown visually in Figure 2-1 by plotting solar spectra at various air masses.

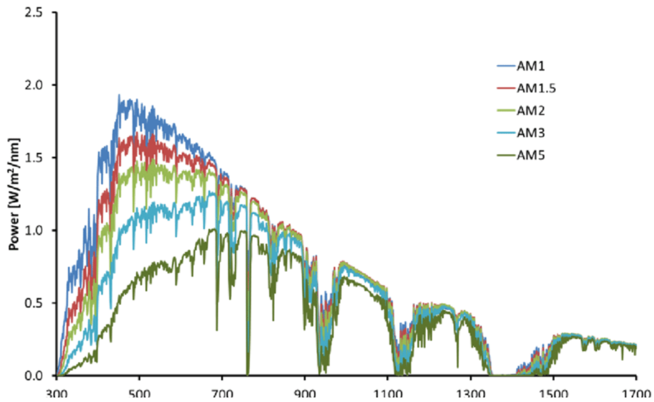

Figure 1-22: Solar spectrum. The spectrum of terrestrial solar radiation at various air masses. It is clear from this figure that the UV content of the solar disk in the sky drops by a huge amount at low angles thus it is safe to view a sunset but not the sun at noon[2]

The spectral composition of sunlight is relevant as solar cells cannot produce photocurrent from infrared radiation as it has energy below the bandgap of silicon and produces very little energy from the higher energy photons as they produce carriers with excess kinetic energy, these hot carriers are often lost to thermalization before the reach the solar cell contacts. The importance of solar cell efficiency in the UV region is often overstated as the front panel glass of a solar module absorbs most of the UV before it reaches the cell.

Solar Irradiance can be broken into several constituent components which include, direct irradiance, isotropic diffuse irradiance, circumsolar diffuse irradiance, ground reflection (direct and diffuse) and horizon brightening. Direct irradiance can be easily modelled as a function of time, date and latitude, knowing the share of direct irradiance is of particular importance for concentrated solar systems as diffused light cannot be concentrated as this would reduce the entropy of the system and thus violate the 2nd law of thermodynamics.[3]

Isotropic diffuse irradiance comes from the scattering of light of air molecules, water vapour as well as atmospheric aerosols such as soot. For this form of irradiance every point in the sky can be treated as a weak light source emitting light in all directions equally. A solar panel oriented horizontally with therefore collect the most isotropic diffuse light as it has the greatest possible view factor of the sky. During the Winter months in Ireland the isotropic diffuse component of sunlight is typically 50%.

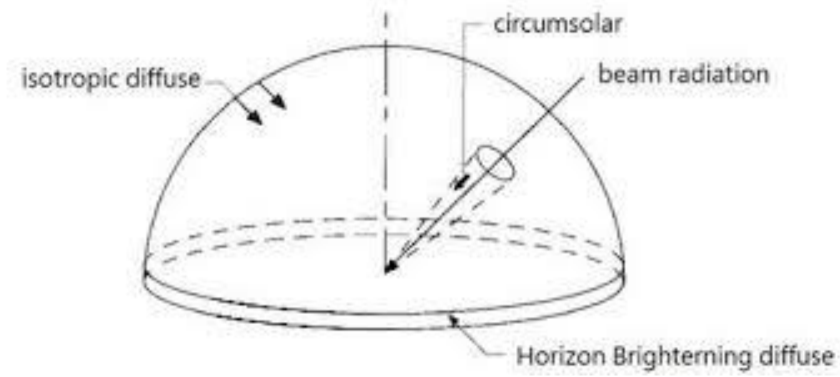

Figure 1-23: Solar radiation components. Solar radiation broken into its' four main components, beam radiation is the largest share on clear days. For maximum collection of diffuse light solar panels should be horizontal as this maximizes the view factor with the sky[4].

Circumsolar diffuse light is a form of anisotropic scattering of light, resulting from light preferentially scattering at small angles. Circumsolar radiation is defined as any light within 3.2 degrees of the real solar disk (circumsolar radiation makes the Sun appear larger than it is). Horizon brightening is caused by the increase in air mass close to the horizon. Diffuse irradiance is more intense where there is more air to scatter from so the horizon acts as a weak light source[4].

2.2 OUTDOOR TESTS

Outdoor Test Site: A remote outdoor solar test site was setup in Louth in 2020, the setup included Mono PERC PV module arrays at various tilt angles and orientations. A weather station was installed to record wind speed, air temperature and solar irradiance using pyranometers at both 90^{o} and 45^{o} from the horizontal. Voltage and current data for each panel were recorded by Victron Energy multiple power point trackers (MPPTs). MPPTs are DC to DC converters that alter the output voltage in order to maximize power, this is necessary as the optimal voltage varies under different conditions of irradiance and temperature. Many MPPTs use a perturb and observe method to find the maximum power point, this involves the MPPT making incremental changes to the voltage to see if it increases or decreases the power output, one problem with this method is that is can be disrupted by a sudden shading event as it can lose the maximum power point and take some time to find it again. The 45^{o} tilt angle was chosen as it is close to the optimal orientation for maximum annual energy yield in Ireland. As a rule of thumb, the optimal tilt angle is equal to the latitude the panel is installed at. Commercial solar farms in the UK and other latitudes similar to Ireland tilt the panels at 25^{o} to reduce the shading of one string of PV modules on the next string allowing the panels to be packed closer together. This is economical when one considers that the cost of land needs to be considered.

Figure 1-24: Solar test site Left: The rear of a solar panel array, Right: A maximum power point tracker

The data was collected at one-minute intervals over the course of three months. The first two months of data were discarded however because of problems with the setup. Initially the power data was collected every second while the weather data was collected every minute. By organizing the power data into the average of 60 second bins the two datasets could synchronized with an error of one minute. Due to the highly overcast conditions in Ireland this proved a significant problem. If a cloud passed over a panel for a few seconds, the pyranometer could read a low value while the cloud was causing shade whereas the power data could be collected 30 seconds later when the cloud had passed showing a high power reading the calculated efficiency would then exceed 100%. Weather data from overcast days was therefore unreliable and from the three months of data only a small number of clear days were used for data analysis. The following plots contrast an overcast day and a relatively clear day.

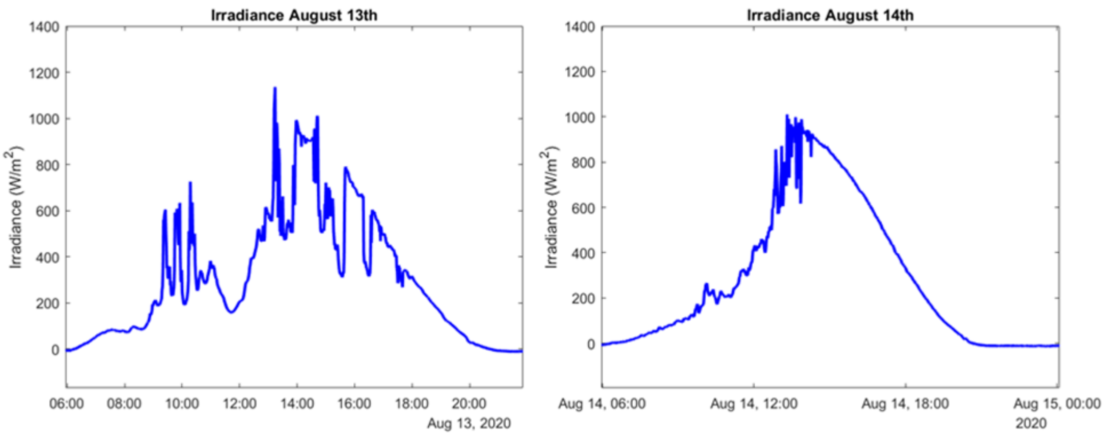

Figure 1-25: Irradiance in Ireland in an overcast and clear day

Several regressions were run controlling for 12 different factors including time of day, panel temperature, wind speed and solar irradiance. The most notable result was the field validation of low irradiance losses as can be seen in the plot below,

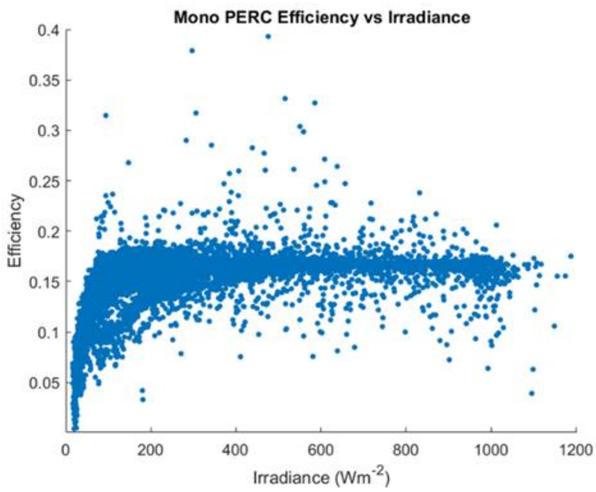

Figure 1-26: Efficiency vs Irradiance. Data from the Louth test site

The high level of noise is a result of having less than one month of reliable data. In order to get less noisy results you have to filter for time of day and temperature but this creates a problem, there are many combinations of temperature, irradiance and time that never arise in the space of a single month.

2.3 MATLAB MODEL

The aim of this chapter is to investigate low irradiance and reflective losses theoretically by creating a Matlab model. The model was created from a first principles basis, in contrast to current popular forms of software such as PVGIS that is created using experimental fitting techniques, thus making it difficult to differentiate individual losses. Key parts of the Matlab script are further discussed in Appendix 1 at the end of the thesis.

Low irradiance losses: Low irradiance losses are the drop in solar panel efficiency due to low light levels. Irradiance levels below 200 Wm^{-2} exasperate defects within solar panels caused by a finite shunt resistance which leads to a small amount of leakage current. The solar cell efficiency dependency (η) on irradiance (G) at low light levels can be expressed as follows:

$$\eta = \eta_0 \left[1 + a \frac{G}{G_{STC}}\right] \qquad 2.3$$

Where a = parameter depending on monocrystaline silicon cell technology.

GSTC = standard irradiance = 1000Wm^{-2}.

η_0 = cell efficiency at standard test conditions.

Shunt Resistance Losses: Evaluating PV panel losses involves comparing the performance of panels to standard test conditions (STC) which are irradiance levels of 1000Wm^{-2} at a temperature of 25^o C . The irradiance loss at low-light levels is caused by internal behaviour of the PV models. There are two parameters that determine the efficiency of PV panels at low-light levels:

- The R-shunt level increases exponentially as irradiance levels drop linearly. This corresponds to diminishing losses. Therefore, lower R-shunt values at STC lead to increased losses being retrieved by the process. This results in a higher low-light level panel efficiency.
- The R-series values are proportional to the square of the current, thus increasing with power. High R-series levels lead to higher PV panel losses at STC

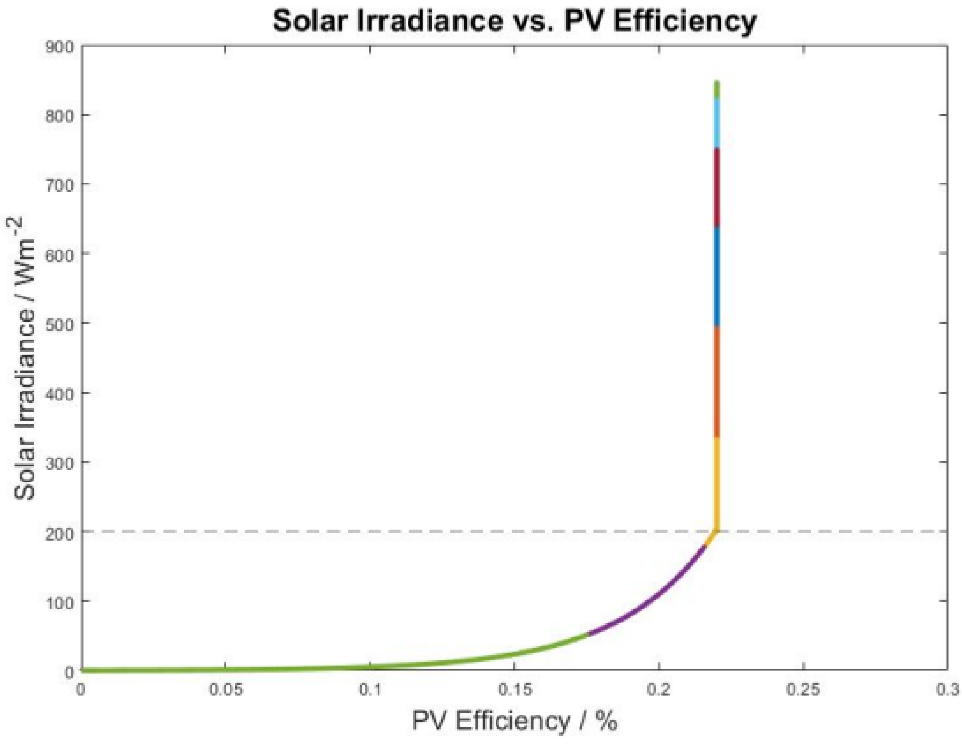

Figure 1-27 Efficiency vs irradiance. This figure shows the low irradiance losses below 200 Wm^{-2}. The low light efficiency effect was treated as a piecewise function in the model where efficiency dropped exponentially below 200 Wm^{-2}.

In order for a solar panel to perform optimally, it should be orientated directly towards the sun. The angle of the sun towards countries with latitudes above and below 40◦ varies significantly between summer and winter months. In Ireland, the sun angles vary from around 60◦ in summer to 13◦ in winter. To compromise for this large variation, solar installations are typically installed at a fixed angle. The falling cost of solar panels has led to a trend towards layouts that maximise power output per unit land area rather than efficiency. Panels that face south are optimally efficient, however strings of panels that lie beside one another must be sufficiently spaced in order to avoid self-shadowing losses.

Positioning panels in an east-west orientation is gaining popularity among solar developers as it mitigates the problem of self-shadowing, More electricity is generated by east-facing panels in the morning and by west-facing panels in the evening.

The land area required for south-facing and east/west-facing panels can be calculated as such:

$$South \rightarrow PL \times \left(\frac{PW \times \sin\beta \cos Acor + PL \times \cos\beta}{tan(\alpha)}\right) \quad 2.4$$

$$East \rightarrow PL \times PW \times \cos\beta \quad 2.5$$

where PL = panel length, PW = panel width, β = tilt angle, α = elevation angle and A_{Cor} = corrected azimuth angle.

The reflective losses of the panels can be quantified using the Fresnel equations:

$$R_S = \left|\frac{n_1 cos\theta_i - n_2 cos\theta_r}{n_1 cos\theta_i + n_2 cos\theta_r}\right|^2 \quad 2.6$$

$$R_P = \left|\frac{n_2 cos\theta_i - n_1 cos\theta_r}{n_2 cos\theta_i + n_1 cos\theta_r}\right|^2 \quad 2.7$$

where R_s = reflectance for s-polarized light, R_p = reflectance for p-polarized light,

θ_i=incident angle, θ_r=reflected angle.

Solar Geometry: The celestial equator is tilted around 23◦ to the plane of the Earth's orbit. The earth passes above and below this plane throughout the year. The sun declination angle (δ) is the angle between the equator and the ray of sun when extended to the centre of the earth. If the sun is passing through the northern hemisphere, ($\delta > 0$)[5]. On the summer solstice (SS), the sun shines directly on the tropic of cancer with an angle ($\delta \approx 23^\circ$) with the equatorial plane[6]. On the winter solstice (WS), the shortest portion of the northern hemisphere is exposed to the sun. The sun shines directly on the tropic of Capricorn located in the southern hemisphere. The sun remains below the Arctic circle for the entire day. The sun declination angle is given by: $\delta \approx -23^o$. Hence, the sun declination angle δ has the following range throughout the year. $-23^o \leq \delta \leq +23^o$ [6]. The solar declination angle can be approximated using the following relation:

$$\sin\delta = 0.39795\cos(N - 173) \qquad 2.8$$

where N = number of days since January 1*st*.

The spring (SE) and autumnal (AE) equinox occurs when the center of the earth lies on the sun's plane. ($\delta = 0^o$). The earth's north-south axis is perpendicular to this plane, hence every location on earth receives 12 hours of sunlight. In the northern hemisphere, $\delta > 0$ for spring and summer whilst $\delta < 0$ for autumn and winter. The latitudinal angle at a certain location is the angle between the line joining the location to the center of the earth and the equatorial plane. All locations at the same latitude experience the same relationship with the sun. The latitude at Dublin (φ_{Dublin}) can be approximated to be ($\varphi_{Dublin} \approx 53.34^o$ and the latitude at Dundalk ($\varphi_{Dundalk} \approx 53.99^o$).

The time of day in which the sun's rays are perpendicular to a given line of longitude is known as the solar noon. It occurs the same time for all locations along a given longitude. For every 15^o east one travels, the solar noon extends by 1 hour. The elevation angles (α) at which the sun's rays reach the surface of the earth can be calculated as follows[7]:

$$\sin\delta = 0.39795\cos(N - 173) \qquad 2.9$$

Figure 2-7 shows the variation in the solar elevation angle (α) on key dates. On the WS, the sun is visible for approximately 7 hours. On the SS, the sun is visible for approximately 17 hours. On both equinoxes, the path of the sun is visible for approximately 11 hours. Approximating the latitude of Dublin φ to be ($\varphi_{Dublin} \approx 53.34^o$). The angle of elevation during the autumnal and vernal equinox is as follows:

$$\alpha_{eqinox} = 90^\circ - (53.35^\circ - 0^\circ) = 36.66^\circ \qquad 2.10$$

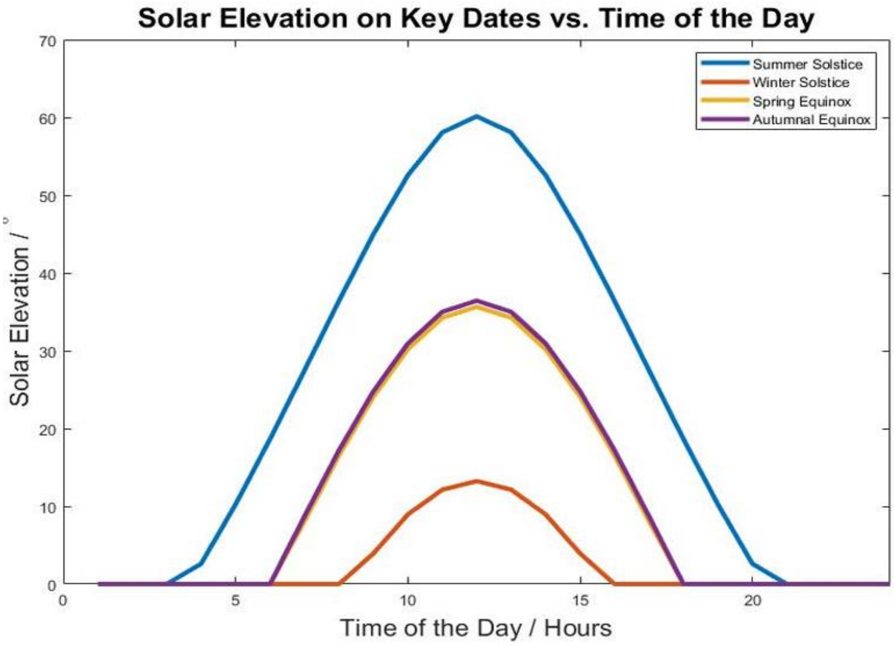

Figure 1-28: Solar elevation angle over to course of the year

Likewise, the angle of elevation for the summer and winter solstices respectively can be calculated at solar noon as:

$$\propto_{summersolstice} = 90^{\circ} - (53.35^{\circ} - 23.5^{\circ}) = 60.16^{\circ} \qquad 2.11$$

$$\alpha_{wintersolstice} = 90^{\circ} - (53.35^{\circ} + 23.5^{\circ}) = 13.16^{\circ} \qquad 2.12$$

Hence, in the northern hemisphere, the angle of elevation on any day is given by:

$$\alpha = 90^{\circ} - (\varphi - \delta) \qquad 2.13$$

where δ = angle of light ray approaching the center of the earth that is parallel to the light ray from the center of the sun approaching Dublin.

The azimuth is the angle (A) between due north and the perpendicular direction of the solar projection down on the horizon measured clockwise. Therefore, 0◦ = due

North, 90◦ = due East, 180◦ = due South, 270◦ = due West. The sunrise equation is given as follows:

$$\cos \omega_0 = -\tan \varphi \tan \delta \qquad 2.14$$

where w_0 = the hour angle, φ = location's latitude, δ = sun declination angle. The hour angle is the angle between the meridian perpendicular to the sun's rays and the meridian of the observer. Using a 24-hour timescale, the hour angle can be found by:

$$\omega = 15(t0 - 12) \circ \qquad 2.15$$

where t_0 the hour of the day. ($0 \leq t_0 \leq 24$). Allowing $\omega = \omega_0$, it follows that before noon[8],

$$t_{sunrise} = \frac{(cos - 1(-\tan\varphi)\tan\delta) \circ}{15 \circ} \qquad 2.16$$

And after noon,

$$t_{sunset} = \frac{(cos - 1(-\tan\varphi)\tan\delta) \circ}{15 \circ} \qquad 2.17$$

Note that at latitudes beyond $\pm$ 65.5◦, $|\tan\delta\tan\varphi| \geq 1$, therefore there is no sunrise/sunset that day. The angle of solar elevation ϕ can be expressed in terms of the sun's declination angle δ on a given date, the current hour angle ω_0 and the observers latitude φ through the following equation.

$$\alpha = sin - 1(sin\,\delta\, sin\,\varphi + cos\,\delta\, cos\,\omega\, cos\,\varphi) \qquad 2.18$$

t $\omega = 15(t_0 - 12)$, therefore

$$\alpha = sin - 1(sin\,\delta\, sin\,\varphi + cos\,\delta\, cos\,[15(t0 - 12) \circ]cos\,\varphi) \qquad 2.19$$

he azimuth (A) can be calculated by the following relation:

$$A = cos - 1(\, sin\,\delta\, cos\,\varphi - cos\,\delta\, cos\,\omega\, sin\,\varphi\,) \qquad 2.20$$

Air Mass: The path length that light travels through the atmosphere when normalized to the shortest possible path length is known as the air mass (AM). As light passes through the atmosphere, it is absorbed by air and dust. The air mass is given by[8]:

$$AM = \frac{1}{cos\theta} \qquad 2.21$$

Where θ = Zenith angle. Note, when θ = 90◦, AM = 1.

Linking Air Mass to Intensity: The intensity of specular sunlight each day can be determined as a function of air mass given the following equation that is experimentally determined.

$$ID = Ks * 0.7^{AM^{0.678}} \qquad 2.22$$

Whereby I_D is the plane intensity perpendicular to the sun's rays. K_s = solar constant = 1.353kW m^{-2}. It is assumed that extraterrestrial solar radiation remains constant.

Model for Isotropic Diffuse Irradiance: The simplest model for diffuse radiation is that which assumes all diffuse radiation is distributed uniformly over the sky dome and that reflection on the ground is diffuse. The total diffuse solar irradiance IT for surfaces tilted at an angle to the horizontal plane is given by:

$$I = DNI \times \frac{1 + cos\beta}{2} \qquad 2.23$$

where DNI = direct normal irradiance. Note* Circumsolar and horizon brightening are assumed to be zero.

2.4 COMPUTATIONAL METHOD

First Principles: The computational PV performance model was created using Matlab. The panel tilt angle is defined and the refractive index of air (n_1=1) and glass (n_2=1.5) are defined as well. The panel elevation (1-tilt) is defined as well as per equation 6. The solar declination angle (δ) is defined as per equation 6, with parameters iterating the function through every hour of the year. The hour angle (ω), the solar elevation angle (α) and the azimuth angle (A) are defined as per equation 13, 16 and 18 respectively, with parameters iterating the functions through every hour of the year. The panel azimuth and elevation angle vectors are converted from spherical co-ordinates to Cartesian co-ordinates, the dot product of these is used to find the incident angle (θ). The reflectance of the panels is defined using the Fresnel equations (equations 4 and 5). The solar irradiance is assumed to be specular and found using equation 20. The absorbed irradiance is found by the product of the specular irradiance and (1 - reflectance). The panel efficiency which incorporates low-light losses is defined using equation 1. The electrical irradiance generated by the panel is found by the product of the absorbed irradiance and the panel efficiency. This basic model is examined in depth, with parameters added to study panels in varying locations and with various different configurations.

Comparison to PVGIS: PVGIS provides a free and open web access to solar radiation and temperature data and to PV performance assessment tools for any location in Europe and Africa, as well as large part of Asia and America. The PV panel theoretical model used in PVGIS was created based on experimental fitting parameters and not from first-principles, hence it is difficult to differentiate low-light losses from thermal losses. For the purpose of this experiment, thermal losses are omitted although the first principles model created in this work allows for the inclusion of thermal losses in future work.

Comparing Spectral Irradiance to Diffuse irradiance Data: The model PV panel system created assumes specular irradiance. This is because the calculation of diffuse irradiance is reliant on the inclusion of real-world DNI data that varies from country to country as well as over different time periods. DNI data gathered by Solcast for Dublin ($\varphi=55^o$) from 01/01/2020 until 31/12/2020 is used in conjunction with equation 21 to calculate diffuse irradiance. This data is compared to the results obtained from the 'first principles' approach to test the validity of it.

In this section, the losses calculated by the theoretical PV panel model are investigated for Dublin ($\varphi_{Dublin} \approx 53.3498^o$) with a fixed panel configuration of 10^o south-facing.

2.5 RESULTS

Energy Collection In Ireland: The plots below show the energy collection in kWh per m^2 at 53^o latitude (Ireland).

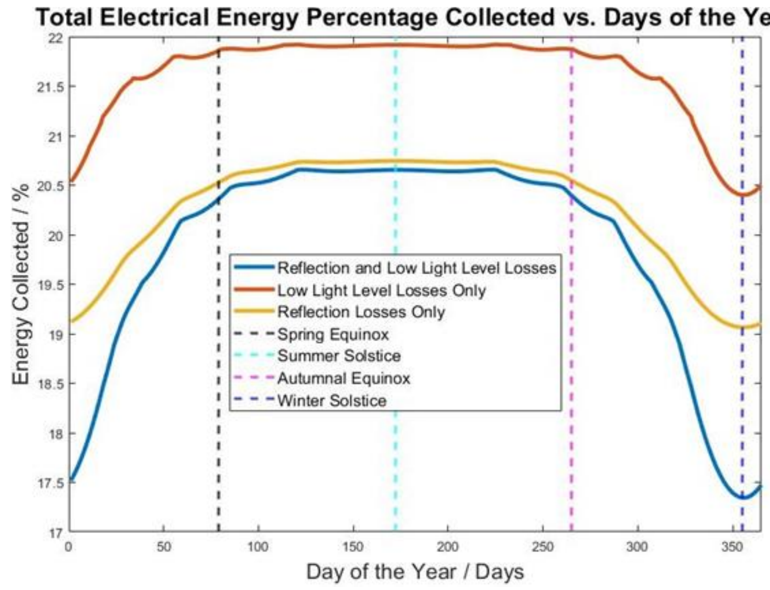

Figure 1-29: Reflection and low light losses over the course of the year in Ireland

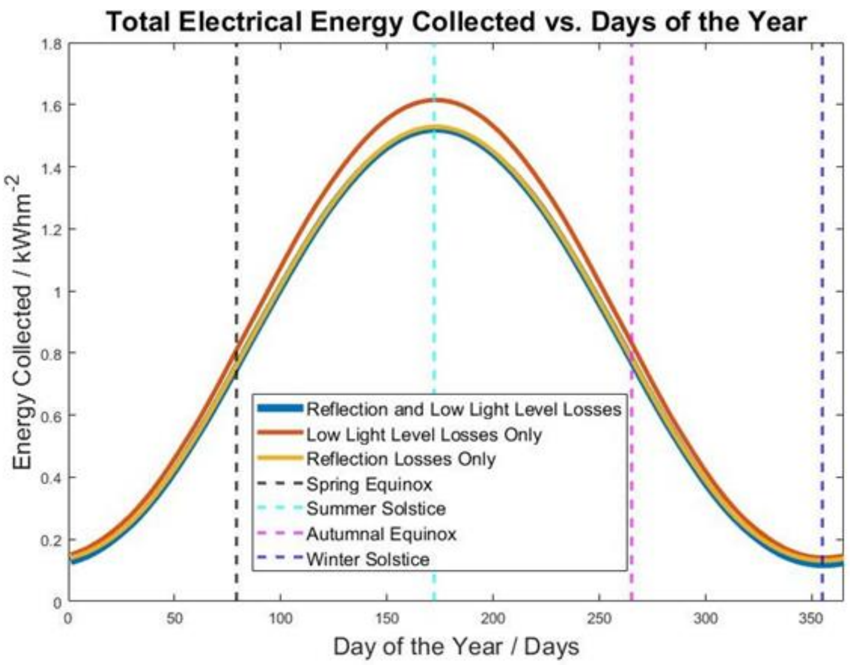

Figure 1-30: Energy collected over the course of the year in Ireland

As expected, the collected energy peaks in the summer period and dips in the winter period. The magnitude of the energy reduction during the winter period is significant as energy is more in demand during this time. The energy collected ranges from 1.52 kWh per m^2 (panel efficiency [pe] = 20.65 %) on the summer solstice (SS, day 172) to 0.12 kWh per m^2 (pe = 17.34 %) on the winter solstice (WS, day 355). Therefore, the PV panel becomes 16.02 % less efficient on the WS when compared to the SS. This reduction is large and significant. The total percentage of collected energy remains at levels similar to the peak value for the majority of the year. On the spring equinox (SE, day 79) and autumnal equinox (AE, day 265), the percentage of collected energies are 20.36% (1.42% efficiency reduction from SS) and 20.39% (1.25% efficiency reduction from the SS) respectively. This means that the panel is operating close to peak efficiency for the majority of the year. The significant winter drop is due to lower irradiance levels in off-peak periods being coupled with lower percentages of energy being collected during these periods. This highlights the importance of minimizing losses during winter periods as well as the importance of improving electrical energy storage methods during summer periods. It should be noted that the low irradiance losses vary from panel to panel as a result of manufacturing defects and design and are a function of shunt resistance losses. These low light losses are negligible in most climatic zones.

Table 1: Total Electrical Energy Collected on Key Dates

	SE	SS	AE	WS
Total Energy Collected ($kWhm^{-2}$)	0.7776	1.5217	0.7524	0.1198
Total Energy Collected (%)	20.3604	20.6543	20.3959	17.3449

Table 2: Energy Collected on Key Dates omitting reflective losses

	SE	SS	AE	WS
Total Energy Collected ($kWhm^{-2}$)	0.8078	1.6146	0.8339	0.1409
Total Energy Collected (%)	21.8582	21.9164	21.8729	20.4015

Table 3: Summer Electrical Energy Collected

Total Energy Collected ($kWhm^{-2}$)	232.1967
Total Irradiance on Panel ($kWhm^{-2}$)	1.1267×10^3
Total Energy Collected (%)	20.6084

Figure 1-31: Energy collected for different solar panel orientation

Table 2 represents the total energy that would be collected if reflective losses were omitted. Removing reflection losses would increase the panel efficiency on the SS from 20.65% to 21.92%. This is a 6% improvement. On the WS, removing reflection losses would increase the panel efficiency from 17.34% to 20.40%. This would make the panel 17.6% more efficient. This further highlights the importance of anti-reflective coatings. The difference for low-light losses (Table 3) are less significant but still important. On the WS, removing low-light losses would increase the panel efficiency from 17.34% to 19.07%. This is 9.9% improvement which indicates the importance of increased research into low-light losses. The ratio of papers published as per Science Direct in 2021 on PV low-irradiance losses to PV thermal losses ≈ 3:1.

Table 4: Summer Electrical Energy Collected

Total Energy Collected ($kWhm^{-2}$)	232.1967
Total Irradiance on Panel ($kWhm^{-2}$)	1.1267×10^3
Total Energy Collected (%)	20.6084

Table 5: Winter Electrical Energy Collected

Total Energy Collected ($kWhm^{-2}$)	60.5702
Total Irradiance on Panel ($kWhm^{-2}$)	309.2402
Total Energy Collected (%)	19.5868

Figure 1-32: Energy collected in the Summer vs Winter

Table 4 and 5 divide the total energy collected into summer and winter periods. The summer period is defined as the period from day 79 (SE) to day 265 (AE). The winter period is from the AE to the SE. Although there is only a 5.22% drop in panel efficiency from the summer period to the winter period, this corresponds to the winter period collecting 20.69% of the total annual energy. This trend does not reflect the needs of Irish electricity generation. According to the Sustainable Energy Authority of Ireland (SEAI), in 2020 Ireland generated ≈ 48 % of its annual electrical energy during the summer period and ≈ 52 % during the winter period.[9] A viable replacement to fossil fuels would need to satisfy this demand distribution.

Energy Losses:

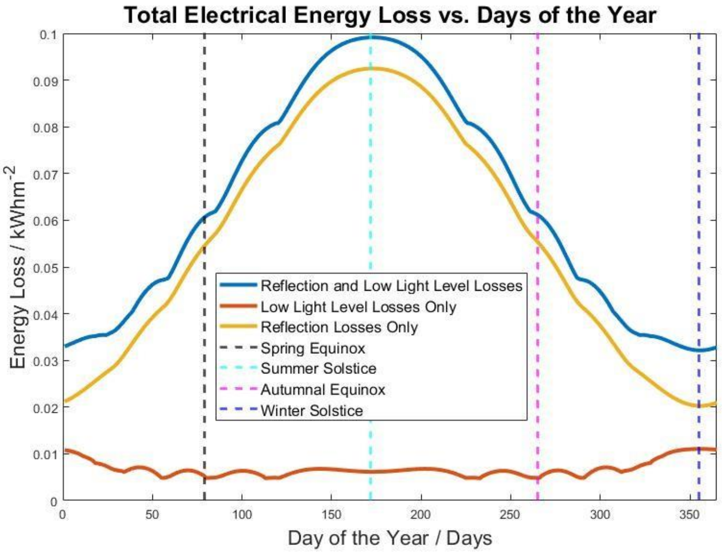

Figure 1-33: Various energy losses, the wobble in the data is from the piecewise efficiency as a function of irradiance.

Table 6: Electrical Losses on Key Dates

	SE	SS	AE	WS
Total Energy Losses ($kWhm^{-2}$)	0.0606	0.00991	0.00612	0.0322
Total Energy Losses (%)	7.4529	6.1166	7.2912	21.1594
Low-Light Level Losses ($kWhm^{-2}$)	0.0052	0.0062	0.0048	0.0110
Low-Light Level Losses (%)	0.6445	0.3798	0.5775	7.2657
Reflective Losses ($kWhm^{-2}$)	0.0545	0.0925	0.0554	0.0203
Reflective Losses (%)	6.7015	5.7057	6.6027	13.3405

Figure 1-34: The energy losses for different panel orientations

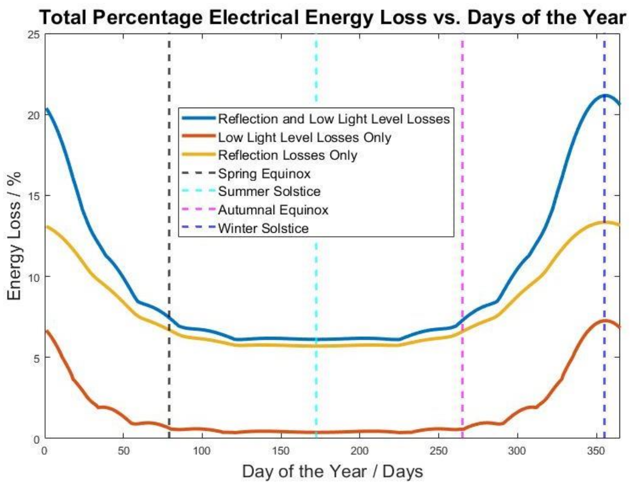

Figure 1-35: The energy losses as a percentage of output at standard conditions

Figure 2-12 shows the variation in total electrical energy losses throughout the year and Figure 2-14 shows the total percentage electrical energy losses throughout the year. These losses correspond to the percentage of solar irradiance that could have been converted to electrical energy, not the total solar irradiance shining on the panel. Total energy losses are higher during the summer period due to increased irradiance levels, however the percentage of total energy lost during the winter period is higher. This is expected. Winter reflective losses are higher as the angle of solar elevation (α) is lower throughout the day. At noon, α_{SS}=60.15° while α_{WS}=13.23°. Hence, the incident angle (θ) to the panel normal is larger (note: $0^{\circ} < \theta < 90^{\circ}$). As per equations 4 and 5, larger incident angles increase the reflectance of a surface. Low-light losses are also higher as a larger percentage of incident irradiance is below the 200 Wm^{-2} threshold.

The total annual losses are 23.14 $kWhm^{-2}$. The majority of the total losses consist of reflective losses (20.56 $kWhm^{-2}$). The annual low-light losses are 2.46 $kWhm^{-2}$. Hence, reflection losses are significant in Ireland.

Compounding Effect:

This section investigates the compounding effect of reflective and low-light losses. It was postulated at the beginning of this project that reflection losses would push irradiance levels below the 200 Wm^{-2} irradiance threshold, thus increasing low-light level losses to a further extent. This section aims to explore whether this is true and whether these compounding losses are significant. If so, anti-reflective coatings play a key role in eliminating both reflective and low-light level losses.

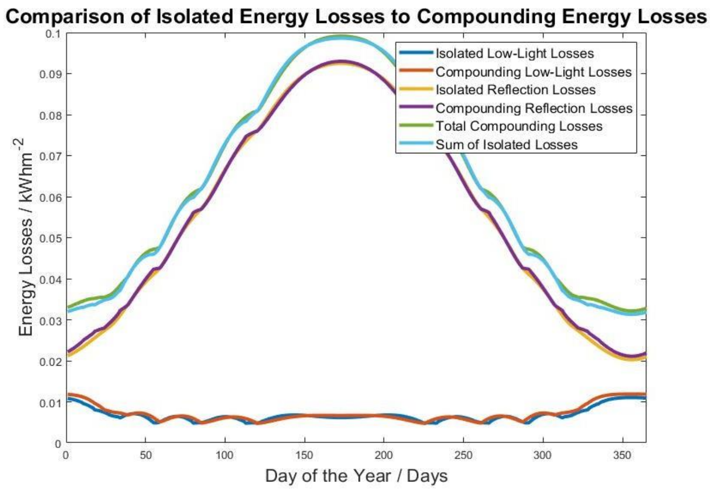

Figure 1-36: Low light losses and reflection losses added and multiplied.

Figure 2-15 shows the difference between the sum of individual losses and the compounding total losses. As shown in the figure, the difference is negligible as isolated losses and compounding losses follow very similar energy loss paths throughout the year. The average compound loss is 0.0634 $kWhm^{-2}$. The ratio of compounding losses to the sum of the individual losses is 1.0096:1. Therefore, for a 10^o south-facing panel in Dublin, the compounding effect is contributing 0.22 kWh energy losses annually.

Comparison with other latitudes:

The theoretical PV model is used to investigate PV performance in Ireland when compared to regions with lower latitudes that typically benefit from solar energy collection to further explore whether solar energy is a viable source in high-latitude regions. The other 3 cities that are involved in this analysis are Madrid (φ = 40.4168◦ N), Dubai (φ = 25.2048^o N), and Singapore (φ = 1.3521^o N).

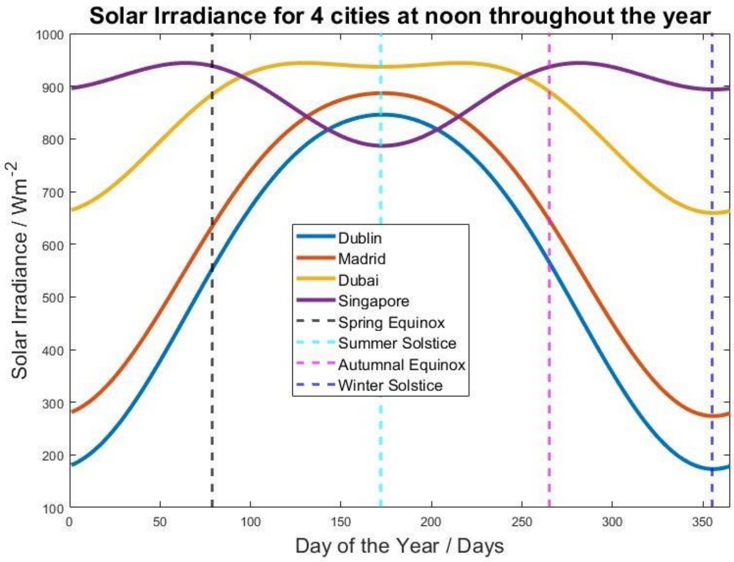

Figure 1-37: Irradiance at different latitudes

Figure 2-16 shows the variation in solar irradiance throughout the year for the 4 cities. Solar irradiance levels are significantly higher in low-latitude regions such as Dubai and Singapore, especially during winter periods. At noon on the SS, α_{Dubai}=88.2584◦, hence it receives the most irradiance.

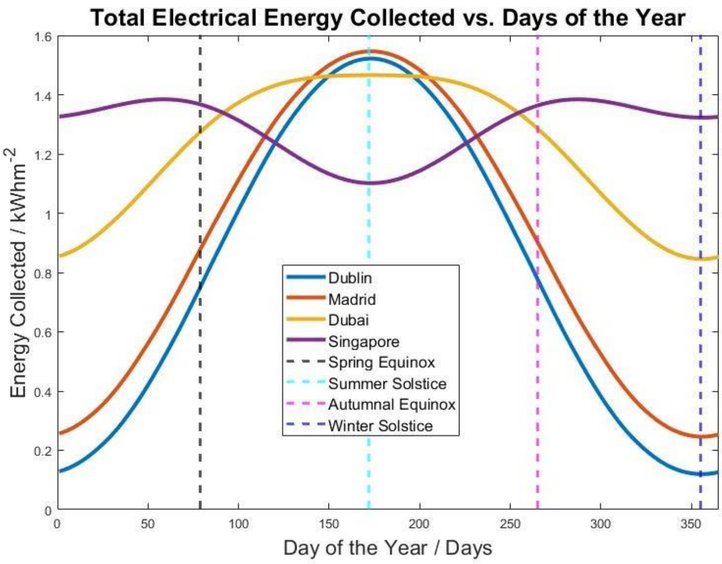

Figure 1-38: Energy produced at different latitudes

Figure 2-17 shows the total electrical energy collected throughout the year for PV panels in the 4 different cities analyzed. High-latitude regions such as Dublin and Madrid experience more energy collected at their peak collection date (SS) however, high-latitude regions also suffer extreme lows during the winter period. The increased energy collection in high-latitude regions on the SS despite lower peak irradiance levels at noon is due to longer solar visibility. On the SS, Dublin receives approximately 15 hours of sunlight whereas Dubai only receives approximately 13 hours of sunlight. Figure 11 shows the total percentage of collected energy throughout the year. During summer periods, panels in high-latitude regions perform at a similar efficiency to low-latitude regions (≈ 20%), however in winter periods, the efficiency of panels in regions such as Dublin and Madrid reduce greatly. A panel in Dublin collects 1.5218 kWh per m^2 on the SS but only 0.1198 kWh on the winter solstice (7.87% of the energy collected on the SS). In Madrid, 1.5463 kWh is collected on the SS and 0.1198 kWh is collected on the WS (15.9% of the energy collected on the SS). In low-latitude regions such as Dubai and Singapore, the annual variation is less significant. In Dubai, 1.4460 kWh is collected on the SS while 0.8453 kWh is collected on the WS (58% of SS energy). In Singapore, peak values are experienced closer to the equinox dates and the energy trough is experienced on the SS, however the total range of energy collection values are notably lower than the other 3 cities. At its peak, a Singapore panel collects 1.3843 kWh while at its trough, it collects 1.1015 kWh (78% of peak value). The consistent performance of panels in low-latitude regions showcases their popularity and utility as viable energy sources. The SS-SE gradient signifies the rate at which panel efficiency decreases as the SS approaches winter periods. The Dublin gradient (8.27×10^{-3}) is approximately 4 times steeper than that of Dubai (2×10^{-3}).

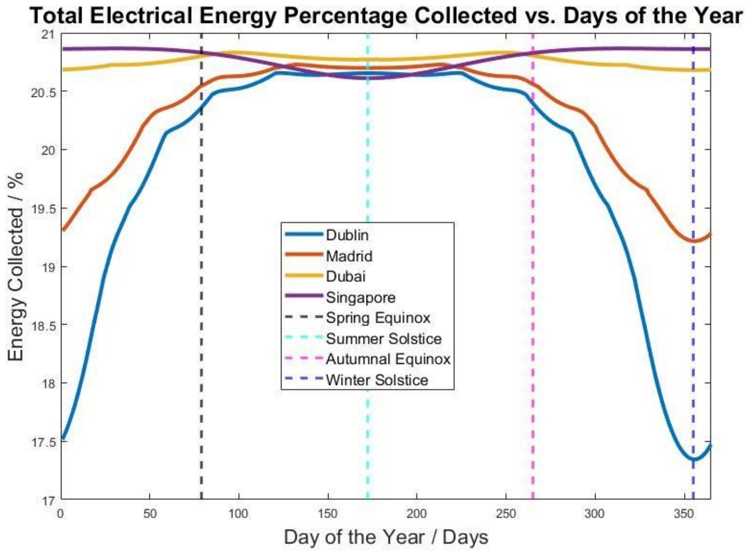

Figure 1-39: Solar panel efficiency over the course of the year

Table 7: Energy Collected for 4 cities on key dates

	SE	SS	WS
Dublin ($kWhm^{-2}$)	0.1198	1.5217	0.7524
Madrid ($kWhm^{-2}$)	1.5463	0.2460	0.8798
Dubai ($kWhm^{-2}$)	1.4660	0.8453	1.2748
Singapore ($kWhm^{-2}$)	1.3843	1.1015	1.3670

Table 8: Energy Collected for 4 cities over long time periods

	Annual Period	Summer Period	Winter Period
Dublin ($kWhm^{-2}$)	292.7669	232.1967	60.5702
Madrid ($kWhm^{-2}$)	329.3648	244.9628	84.4020
Dubai ($kWhm^{-2}$)	446.4486	265.0714	181.3772
Singapore ($kWhm^{-2}$)	470.0285	228.1469	241.8816

Figure 1-40: Energy collected vs panel orientation and season

Table 8 shows the annual collected energy for the 4 cities. Low-latitude regions collect significantly more energy annually. A Dublin panel only collects (~ 60%) of the annual energy that a Singapore panel would collect, this assumes specular irradiance. Dublin collects only (~ 20%) of its annual energy during the winter period whereas Dubai collects (~ 40%)

Commercial Impact: A 2021 study of international electricity prices paid by consumers by Cable found using data dated 15/06/21 that the average price of electricity in Ireland is €0.1886. By comparison, the average price in Spain (as on 8/6/21) is €0.1769, in Dubai (as on 20/05/21) is € 0.0524 and in Singapore (as on 23/08/21) is €0.1767.[10] A standard 10 megawatt (MW) solar farm consisting of 31746×315 W PV panels with a standard surface area of 1.6 m^2 per panel corresponds to 50793 m^2 of panel surface area per farm.

Based on the annual energy collection figures in table 8, a 10 MW solar farm would generate (50793 m^2 × 292.7669 $kWhm^{-2}$) = 1.4817×107 kWh in Dublin. This equates to (1.4817×107 kWh×0.1886 kWh^{-1}) €3,149,620 worth of electrical energy being generated by the farm annually. By comparison, a Madrid 10MW solar farm would generate 1.673×107 kWh (€2,959,537). A 10 MW solar farm in Dubai would generate 2.268×107 kWh (€1,188,432) and a 10 MW solar farm in Singapore would generate 2.387×107 kWh (€4,217,829).

Although a 10 MW solar farm in Dubai would generate 7.88×106 kWh (~ 52%) more than a 10 MW farm in Dublin, the monetary value of the electricity generated in the Dublin farm would be €1,068,209 more due to differences in international energy prices.

Table 10 shows the annual energy losses experienced by PV-panels per m^2 in the four cities analyzed. A 10 MW solar farm in Dublin would lose 1.175×106 kWh annually. This electricity is worth €221,605. Of these losses 1.044×106 kWh (€196,898) are reflective losses and 1.31×105 kWh (€24,706) are due to low light losses. In Madrid, A 10MW solar farm would lose 1.20×106 kWh annually. This electricity is worth €212,280. Of these losses 1.09×106 kWh (€19,821) are reflective losses and 1.05×105 kWh (€18,575) is due to low light losses. In Dubai, A 10MW solar farm would lose 1.34×106 kWh annually. This electricity is only worth €70,216. 1.26×106 kWh (€66,024) of these losses are reflective losses and 8.208×104kWh (€4,301) are due to low light losses. In Singapore, A 10MW solar farm would lose 1.39×106 kWh annually. This electricity is worth €245,613. Of these losses 1.31×106 kWh (€231,477) are reflective losses and 7.982×104 kWh (€14,104) is due to low light losses.

The Effects of Different Mounting Configurations: The theoretical PV model is used to investigate PV performance in Ireland (φ = 53.35° N) at different mounting configurations to investigate optimal performance. Industry standard conditions are typically south-facing with tilt angles varying for different locations. The optimal configuration is that which continually faces the sun, however creating panel mountings that rotate in such a manner is not cost efficient. The solar angle in Ireland varies from 60.15° on the SS to 13.24° on the WS. Solar installations tend to be installed at a fixed angle. Although the most efficient fixed panel configuration is south-facing, panel strings facing in this direction require a gap between them to avoid self-shadowing. East-west facing configurations are becoming more popular within the industry as they negate the problem of self-shadowing. This section aims to explore the energy cost of east-west configurations and also to investigate whether they are more cost efficient per unit land area. East-facing orientations are used to represent both east-facing and west-facing panels for simplicity purposes.

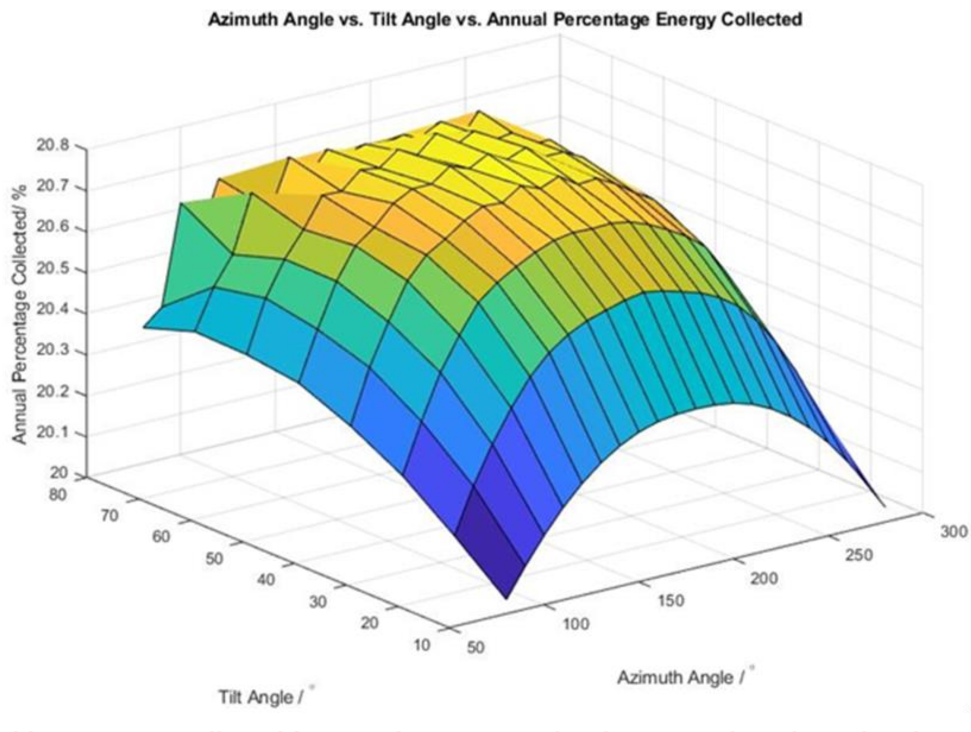

Table 11: Energy Collected for a South-Facing Panel with varying tilt angles on key dates

	SE	SS	WS
10 ° Tilt ($kWhm^{-2}$)	0.7524	1.5218	0.1198
20 ° Tilt ($kWhm^{-2}$)	0.8900	1.5347	0.1992
30 ° Tilt ($kWhm^{-2}$)	0.9957	1.5079	0.2655
45 ° Tilt ($kWhm^{-2}$)	1.0933	1.3856	0.3449

Figure 1-41: Energy collected as a function of tilt and azimuth angle

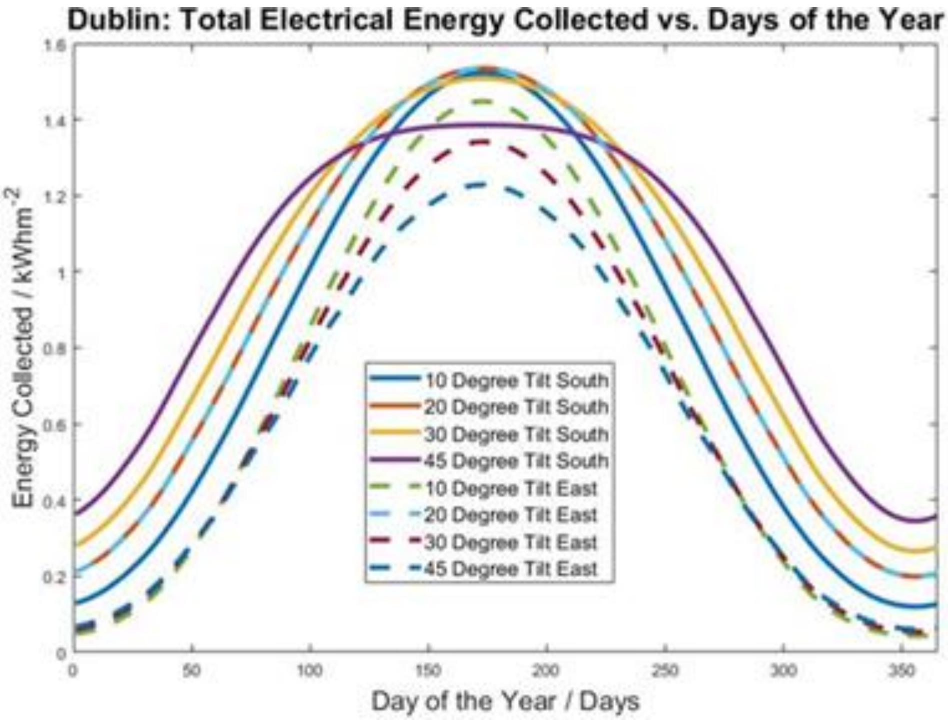

Figure 1-42: Energy collected in Dublin at various angles.

Figure 2-21 shows the total electrical energy collected for various panel orientations. As expected, the graphs resemble a parabolic shape that peaks during the summer period and experiences a trough during the winter period. Panels with a greater tilt angle perform better during the winter period but experience lower peaks during the summer period. A 45^o east-facing panel collects 0.3449kWh per m^2 on the WS and 1.2284 kWh per m^2 on the SS whereas a 10◦ east-facing panel collects 0.1198 kWh per m^2 on the WS and 1.4475 kWh per m^2 on the SS. Larger tilt angles during winter periods maximises the output from the low winter sun, whereas low tilt angles during summer periods allows for overall power output to be maximised. As stated throughout this paper, winter performance is vital when considering panel orientation.

Table 12: Energy Collected for a East-Facing Panel with varying tilt angles on key dates

	SE	SS	WS
10 ° Tilt ($kWhm^{-2}$)	0.5846	1.4475	0.1198
20 ° Tilt ($kWhm^{-2}$)	0.5796	1.4026	0.1992
30 ° Tilt ($kWhm^{-2}$)	0.5732	1.3415	0.2655
45 ° Tilt ($kWhm^{-2}$)	0.5536	1.2284	0.3449

Table 13: The annual energy for various panel orientations

	Annual Period	Summer Period	Winter Period
South Facing: 10 ° Tilt ($kWhm^{-2}$)	292.7669	232.1967	60.5702
South Facing: 20 ° Tilt ($kWhm^{-2}$)	326.0722	245.2884	80.7834
South Facing: 30 ° Tilt ($kWhm^{-2}$)	348.6427	251.0207	97.6220
South Facing: 45 ° Tilt ($kWhm^{-2}$)	361.5427	245.2625	116.2802
East Facing: 10 ° Tilt ($kWhm^{-2}$)	247.6326	209.5310	38.1016
East Facing: 20 ° Tilt ($kWhm^{-2}$)	242.9101	204.0319	38.8783
East Facing: 30 ° Tilt ($kWhm^{-2}$)	236.4082	39.9467	39.6426
East Facing: 45 ° Tilt ($kWhm^{-2}$)	222.9132	182.9664	39.9467

Figure 1-43: Energy collected for various tolts and orientations

Table 13 shows the annual energy collected for various panel orientations. The total land area required for panels (factoring in self-shadowing spacing) is found using equation 2 and 3. These are used to calculate the annual energy per unit land area (Table 14) to determine which panel is most efficient when considering the cost of land. The panels used are assumed to have PL = 1.6m, WD = 1m, α = 5° as this represents 9am to 3pm on the WS and $A_{Corrected}$=80° (corresponds to α = 5°).

Table 14: Annual area per unit land area for different panel orientations

	Area per panel m^{2}	Ann. Energy (kWh) per panel	Ann. Energy per m^{2}
10° South-Facing	2.127	468.4270	220.2229
20° South-Facing	2.589	521.7155	201.5124
30° South-Facing	2.973	557.8283	187.6314
45° South-Facing	3.377	578.4683	171.2965
10° East-Facing	1.576	396.2122	251.4037
20° East-Facing	1.504	388.6562	258.4150
30° East-Facing	1.386	378.2531	272.9099
45° East-Facing	1.131	356.6611	315.3502

Figure 1-44: Energy output per m^2

Integrating Diffuse Data: Figure 2-24 shows the PV model created in this experiment performing against diffuse horizontal irradiance data gathered from Solcast[11]. The red lines represent the total specular irradiance used in the PV model from this experiment. The green lines indicate global horizontal irradiance data for Dublin during 2020 from Solcast. The black lines represent diffuse horizontal irradiance data from Solcast. The ratio of total specular irradiance used in this model to global horizontal data gathered from Solcast is approximately 3:2. This is quite large but expected considering Irish weather. This ratio would be far less significant in the other regions studied: Madrid, Dubai and Singapore. The total annual irradiance shining on a 1 m^2 panel assuming specular data is 1.4359 × 103 kWh. The global horizontal irradiance data returned 968.8760 kWh. The total annual losses dropped from 23.1419 kWh to 20.3306 kWh. Total annual reflective losses dropped from 20.5565 kWh to 16.2270 kWh however the total low-light losses increased from 2.4618 kWh to 4.3711 kWh. This was expected.

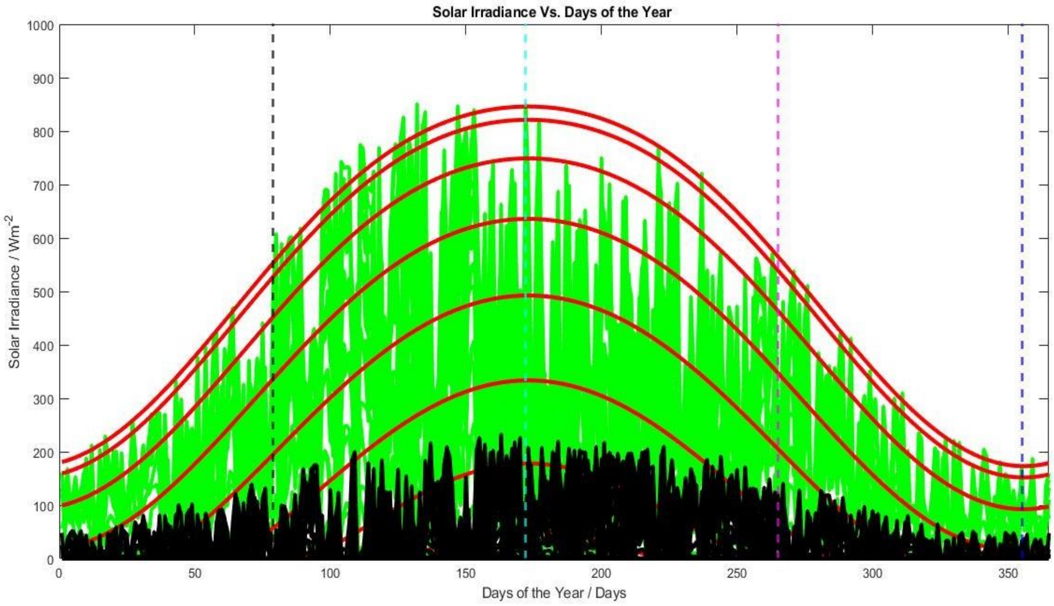

Figure 1-45: Diffuse light. The MATLAB model combined with real weather data from Solcast, the real irradiance can go above the Models prediction when cloud brightening occurs.

2.6 PVGIS DATA

PVGIS Low Light Losses Calculations: Photovoltaic Geographical Information System is a website that uses a large satellite database to calculate the monthly and annual energy yield of a solar farm at any given tilt and orientation. I hypothesised that low light losses would be strongly dependant on latitude and used data the PVGIS-SARAH2[12] satellite data base to generate frequency distributions of 5 years of hourly irradiance values. I then compared countries at different latitudes such as Spain and Ireland. By binning 5 years hourly energy data into the same irradiance intervals, I was able to calculate the percentage of energy produced under low light conditions in the two countries and concluded that low light losses were negligible in Spain but significant in Ireland.

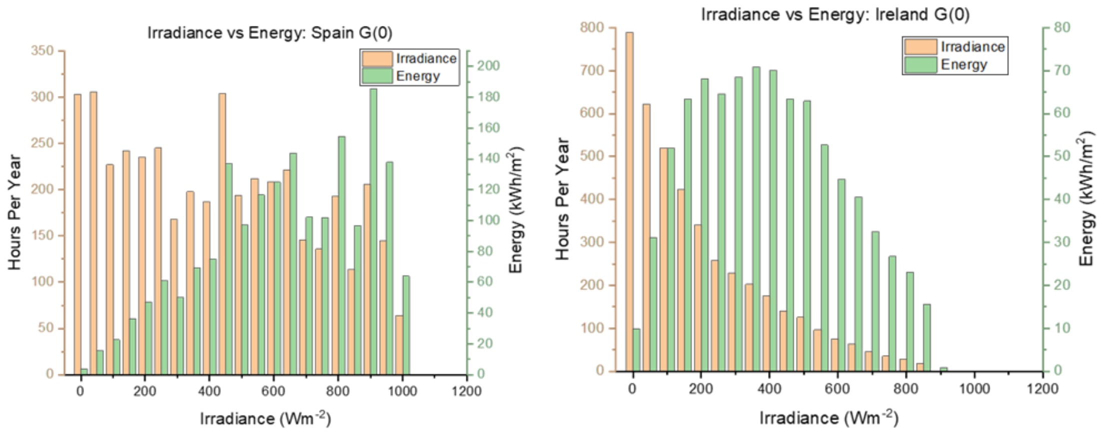

Figure 1-46 Low irradiance regions. This illustrates the significance of low irradiance conditions as a portion of total annual energy output. Irradiance is below 200 Wm^{-2} 60% of the time in Ireland and only 28% of the time in Spain. 22% of the total annual energy in Ireland is produced under low irradiance conditions.

While PVGIS provides good climate data the models of annual energy yield were simplistic and did not give a detailed breakdown of the various energy loss mechanisms. The only losses addressed were angle of incidence losses, temperature and low light (combined) and inverter losses.

PVSyst and Economic Analysis: Similarly to PVGIS, PVSyst[13] uses a combination of satellite data as well as weather station data. The virtual solar farm can be placed at any of the weather stations and almost all parameters relating to the solar panel can be altered. The breakdown of losses was much more detailed. With the option to vary the reflectivity and incidence angle modifier It was possible to do net present value calculations to determine the monetary value of any improvement in the anti-reflective coating.

The net present value is the current value of an investment that will produce income in the future, this future income is discounted by the discount rate in accordance with the principle of the time value of money (money now is preferable to money later, other things equal). The net present value of a PV installation is shown in the equation below,

$$\boldsymbol{Net\ Present\ Value = -Instalation\ Cost - \frac{Cost\ of\ Inverter}{(1 + Discount\ Rate)^{15}} + \sum Discounted\ Income}$$

$$\boldsymbol{Discounted\ Income = Income \times (1 - Discount\ Rate)^{\text{Year Number}}}$$

$$\boldsymbol{Income = Power\ Generation \times Electricity\ Price}$$

$$\boldsymbol{Power\ Generation = Last\ Year\ Generation \times (1 - Degradation\ Rate)}$$

$$\boldsymbol{Electricity\ Price = Last\ Year\ Electricity\ Price \times (1 + Electricity\ Inflation\ Rate)}$$

Using NPV calculations it is possible to determine the monetary value of any improvement to a solar modules' reflective and IAM properties, if this value exceeds the cost of the texturing technique, then the addition of a textured glass surface would be commercially viable. The following table shows the annual energy production for a 10 MWp solar installation in Ireland with various anti-reflective surfaces.

Table 1

Surface	MWh/year	Improvement
Plain Glass	10106	0%
AR Coating	10185	0.78%
No IAM Glass	10467	3.57%

It should be noted that glass has a reflectivity of 4% at normal incidence so these improvements are what can be gained by altering the angular response only, the no IAM glass represents the maximum possible improvement where there is perfect light trapping at all angles. Adding the 4% loss at normal angle of incidence gives a total improvement of 7.57% for the perfect AR coating.

2.7 CONCLUSIONS

A simulation was successfully made that models reflection losses as a function of Sun position. This model compares favourably with PVsyst for measuring reflection as it uses the dot product of the Sun and panel vectors to calculate the angle of incidence rather than the elevation angle. A limitation of this model was that cloud cover was not considered but this was addressed by importing real world hourly weather data from Solcast.

By focusing on reflection losses over a broad range of angles it was found that annual reflection losses could be as high as 10 to 15% for some solar panel configurations e.g. roof mounted East/West panels. The importance of latitude was also emphasised, and it was demonstrated that while absolute reflection losses were higher in regions close to the equator with high solar insolation, reflection losses were proportionally larger in high latitude regions such as Ireland. The result of this work is that those that design anti-reflective coatings should place a greater emphasis on improving the incidence angle modifier, this can be achieved either with textured glass surfaces or with multilayer AR coatings. This chapter also highlights the importance of reflection losses and shows they are greater than the commonly stated figure of 4% for a glass air interface.

2.8 REFERENCES

(1) *The measurement of solar spectral irradiance at different terrestrial elevations*. CoLab. https://colab.ws/articles/10.1016%2F0038-092x%2870%2990006-x

(2) Eeles, A. Performance Characterisation of Photovoltaic Devices: Managing the Effects of High Capacitance and Metastability. thesis, Loughborough University, 2016.

(3) Einhaus, L. M.; Heres, G. C.; Westerhof, J.; Pal, S.; Kumar, A.; Zheng, J.-Y.; Saive, R. Free-Space Diffused Light Collimation and Concentration. *ACS Photonics* **2023**

(4) Wilbert, S. Determination of Circumsolar Radiation and Its Effect on Concentrating Solar Power. thesis, RWTH Aachen, 2014

(5) Cooper, P. I. The Absorption of Radiation in Solar Stills. *Sol. Energy* **1969**

(6) Blanco-Muriel, M.; Alarcón-Padilla, D. C.; López-Moratalla, T.; Lara-Coira, M. Computing the Solar Vector. *Sol. Energy* **2001**

(7) Woolf, H. M. *On the Computation of Solar Elevation Angles and the Determination of Sunrise and Sunset Times*; National Aeronautics and Space Administration, 1968.

(8) Kasten, F.; Young, A. T. Revised Optical Air Mass Tables and Approximation Formula. *Appl. Opt.* **1989**

(9) *SEAI's National Energy Projections Report, News ,SEAI*. https://www.seai.ie/news-and-events/news/energy-projections-report

(10) *Energy Prices - Europe - By Country*. https://tradingeconomics.com/country-list/energy-prices?continent=europe

(11) *Solar API and Weather Forecasting Tool | Solcast™*. https://solcast.com/

(12) *Photovoltaic Geographical Information System (PVGIS) - European Commission*. https://joint-research-centre.ec.europa.eu/photovoltaic-geographical-information-system-pvgis_en

(13) *PVsyst*. https://www.pvsyst.com/

(14) J Jiawei Luo, Stephen Bae, Mengxue Yuan, Erik Schneider, Michael T. Lanagan, Carlo G. Pantano, Seong H. Kim, Chemical structure and mechanical properties of soda lime silica glass surfaces treated by thermal poling in inert and reactive ambient gases, Journal of the American Ceramic Society, 2018

3 NUMERICAL MODELLING

3.1 JUSTIFICATION FOR RAY OPTICS MODELLING

Having established the potential benefits of an idealised anti-reflective coating for various scenarios in the previous chapter it was then necessary to design my own microtextured surface. With COMSOL Multiphysics it was possible to create various geometries (sawtooth, fishscale, square pyramidal, pitted, plate) and then vary the dimensions and tilt angle of the features to get the best light trapping over a broad range of incident angles. Textured surfaces with the best results could then be selected as candidates for real life fabrication. COMSOL modelling allowed me to investigate a much broader range of textured surfaces when compared to real life fabrication with each geometry requiring different techniques (roll to roll nanoimprint lithography, laser ablation, HF wet etching, micromachining).

Ray optics was chosen instead of wave optics as the features investigated where on the lengthscale of 10s of microns and thus complex electromagnetic interactions such as Mie Scattering could be ignored due to the features being significantly larger than the wavelength of visible light. This also helped in reducing compute time which could be reallocated to adding more secondary rays to the ray tracing model and sweeping over more parameters. With ray optics the model was length scale independent and thus if a good pattern was identified then the size of the features could be adjusted to a scale that was practical to make.

3.2 COMSOL RAY OPTICS

The geometric optics module in COMSOL calculates the vector and position of each individual ray and the ray's interaction with boundaries. It is a viable approach when wavelength of the light is on a very different scale to the smallest geometric details of the model. Ray tracing can be used over a very broad range of wavelengths longer than x-rays (at this scale the light interacts and scatters off individual atoms). In most cases the rays simple travel at speed c/n however in graded index media the rays follow a curved path which is determined by integrating coupled first-order ordinary differential equations over time[1].

Geometric optics can be done with either ray tracing and/or time dependent study steps. These studies are quite similar, but the ray tracing study step allows one to set the ray path length steps instead of time steps. Internally, these optical path lengths are converted to corresponding times for convenience. For simple ray tracing models, only the first and last time steps are necessary. The behavior of rays at any intermediate time can be accurately interpolated. If rays interact with boundaries between the stored time steps, the exact time and position of each ray-boundary interaction is also stored and readily available. Time or path length stepping should be made finer if rays will encounter a graded index medium or an attenuating medium where some of the ray energy will be converted to heat. These were not important considerations in my models and thus large path length steps were used.

Whenever a ray intersects with a surface, various ray-boundary interactions may occur, including specular reflection, diffuse reflection, refraction, and different types of absorption. It is also possible to simulate a low index anti-reflective coating by changing the boundary conditions of an interface. The path length, intensity and wavelength of each ray can be evaluated, and this is useful when calculating the intensity of the reflected versus the transmitted light.

Although geometrical optics models vary tremendously in application area and scope, every geometrical optics model requires at least the following basic features:

Ray Release: Every geometric optics model must release some rays into the simulation either by release from a boundary or from a grid. The released rays can be parallel or follow some other directional distribution such as Lambertian. When releasing rays from a boundary the rays distribution depends on the mesh pattern.

Walls or Discontinuity: The rays must interact with at least one geometric boundary with a defined boundary condition such as specular reflection, diffuse reflection or a freeze condition. The freeze condition is useful when measuring transmission as the total intensity of rays on a wall with a freeze condition can be later evaluated.

Ray Properties: Allows the user to set the rays wavelength distribution or to have monochromatic rays of a fixed wavelength. The total power of rays can also be set. The total number of released secondary rays in a model can sometimes grow rapidly and exhaust all of the preallocated secondary degrees of freedom. For example, a single ray reflecting back and forth between two material discontinuity boundaries can create an inordinately large number of rays, each with extremely low intensity. It can be useful to constrain the release of secondary rays at boundaries so that only the most important rays are produced. To do this a threshold intensity is set to avoid insignificant rays.

Meshing: At minimum a surface mesh is required for ray interactions at material boundaries however when graded index materials or light attenuation is being considered then a domain mesh is also required. A high mesh density is required when using curved surfaces such as the pitted structure or the fish scale structure. Meshing does not deal well the geometries with infinitesimals such as the point of contact between two circles. The figure below shows the error in the radial distance over the flat surface of a coarsely meshed sphere with a radius of 1 unit.

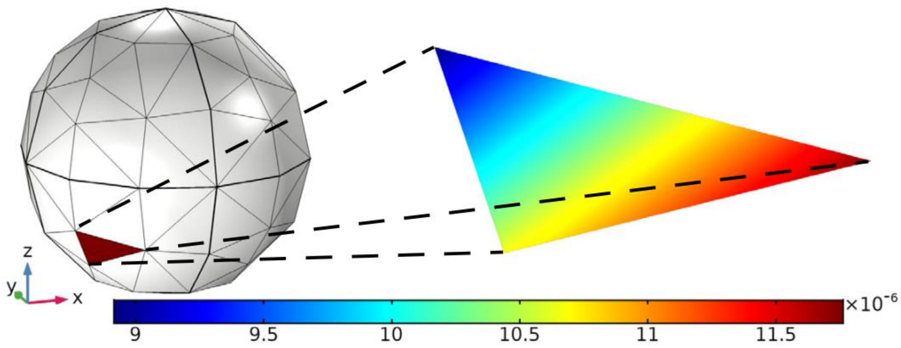

Figure 1-47: Meshing. The blue region deviates most from the actual radius of a unit sphere, the object requires a finer mesh. Image from COMSOL manual.[2]

Study: Time dependant, ray tracing and bidirectionally coupled ray tracing are available however ordinary ray tracing was used for my simulations.

3.3 Design Principles of My Simulations

My simulations consist of four main geometric objects:

Glass Block: A glass block with a square base with 1 cm long sides and a thickness of 2 mm to represent the typical glass thickness of a solar PV module. (Solar modules can have thicker glass such as 3.2 mm thickness). The top interface has the regular boundary conditions for a glass-air interface. The side walls have a spectral reflection boundary condition, this has a similar effect to a periodic boundary condition and reduces the error associated with rays escaping out of the sides of the glass which would be a negligible effect for a 1.5m^2 solar module but these edge effects become more pronounced for smaller glass samples.

The bottom wall has a freeze condition so the rays stop reflecting and can be counted. It is thus assumed in this model that all rays that strike the rear glass interface are transmitted. In reality there will be a small amount of reflection at the interface between the glass and EVA or POE encapsulant as well as a further reflection boundary between the encapsulant and the solar cell which will typically have a square pyramidal anti-reflective pattern. As far as this thesis is concerned what happens beneath the top glass surface is a black box and is outside the scope of this study.

Sun: The Sun in my model is a two-dimensional rectangle with a ray release boundary condition on the side facing the glass block. The number of incident rays was varied depending on the constraints of compute time but was typically 1000 rays with a total power of 1000 Watts. The Sun position was offset from the glass block by 10 cm and could be rotated with a centre of rotation set at the centre of the glass block top surface. The parameter SunAngle was used to set the Sun position where a SunAngle of zero was directly above the glass block. The dimensions of the Sun rectangle were a function of sun angle such that all rays were projected on the top glass block surface and no rays missed the glass block, to do this the sides of the rectangle were defined as 2cm x Cos(SunAngle) so the sun was a 2cm x 2cm square at a SunAngle of 0^o and a 2cm x 1cm rectangle at a SunAngle of 60^o.

Anti-Sun: The anti-Sun was used as a collector for reflected specular light. The dimensions were the same as the Sun but the rotation was set to -SunAngle so the object appeared on the mirror opposite side of the glass block. The boundary facing the glass block was given a freeze condition so the rays could be counted. The distance of the anti-Sun from the glass block was set at double the distance of the Sun to the glass block. This was to ensure that most of the rays that hit the anti-Sun were specular reflection rather than diffuse reflection at small angles, the further away the anti-Sun is from the glass block the lower the contribution of small angle diffusion. It should be noted, however, that small angle diffusion of light also contributes to glare and to fully investigate this angle resolved haze measurement should be taken, this is addressed in Chapter 7 on optical measurements.

Patterned Surface: The method of creating the patterned surface on top of the glass block varied depending on the geometry used but as a general rule the dimensions and angles were parameterized so that they could be varied in a parametric sweep. Patterns with curved surfaces required a finer surface mesh and thus parametric sweeps took longer to run as the surface had to be re-meshed each time the geometry was altered. These surfaces will be discussed individually later. More detail on the model such as boundary conditions are given in Appendix 2 at the end of the thesis.

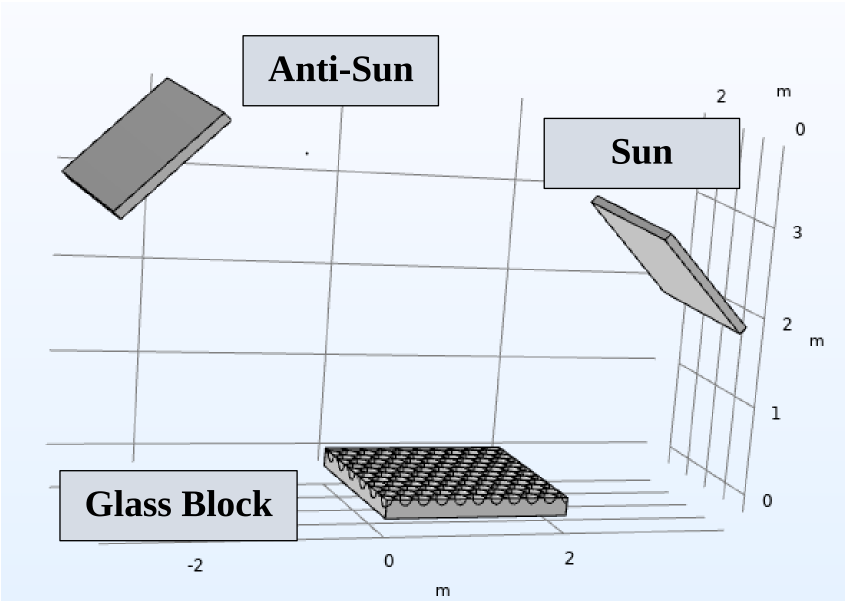

Figure 1-48 Model components. This shows the components of the geometric optics simulation. In this case the SunAngle is set to 45°. The glass block has a 2x2 meter square base rather than 2x2 centimetres, this does not matter geometric optics is scale invariant.

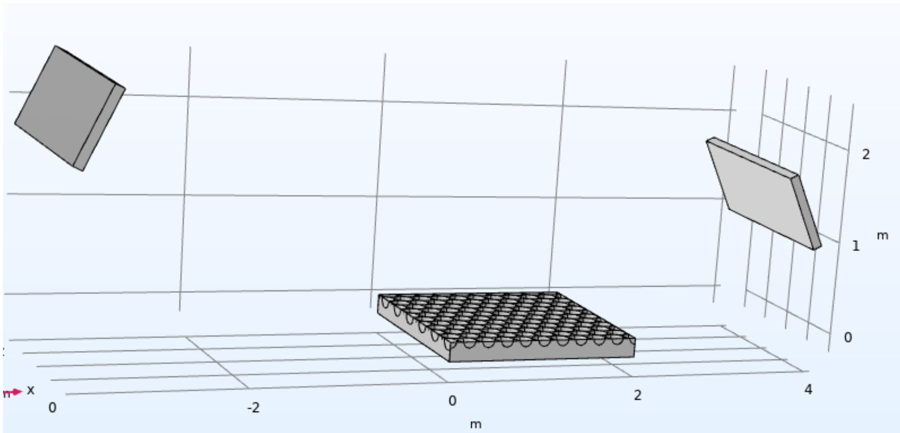

Figure 1-49 Sun and Anti-Sun. This shows the Sun and Anti-Sun at a lower SunAngle. The length of the sides tangential to the circle of rotation get shorter so the rays are always projected on the glass block with no rays missing the target.

By dynamically changing the dimensions of the Sun and Anti-Sun objects the incident ray power on the glass block was always 1000 Watts, light that makes contact with the bottom of the glass block was considered to be transmitted while light that contacts the Anti-Sun was considered to be specular reflection while all remaining light was diffuse reflection. Diffuse reflection therefore could be calculated without being measured directly as can be seen in the equation below,

$$Diffuse\ Reflection = 1000W - Transmission - Direct\ Reflection \quad 3.1$$

The parametric sweep varies the sun angle so reflection and transmission can be measured as a function of incident angle and then normalized to generate incident angle modifier (IAM) curves. These IAMs can then be plugged into GIS models such as PVsyst or PVGIS to estimate the improved electrical yield from the various anti-reflective surfaces.

3.4 Sawtooth Pattern

The sawtooth patten was investigated as it was predicted to achieve good light trapping specifically at glancing sun angles. By orienting the hypotenuse face of the sawtooth towards the sun the effective tilt angle of the solar panel could be increased. For example a solar module that was tilted at 25° at a latitude where the optimal tilt was 45° could be retrofitted with a sawtooth surface with a tilt angle of 20° thus increasing the effective tilt angle to 45°. The Solar irradiance incident on the solar module would still be less than if the panel was tilted at 45° as the Sun's irradiance would still drop by Cosine(Tilt Angle). The figure below shows the initial sawtooth pattern design in two dimensions.

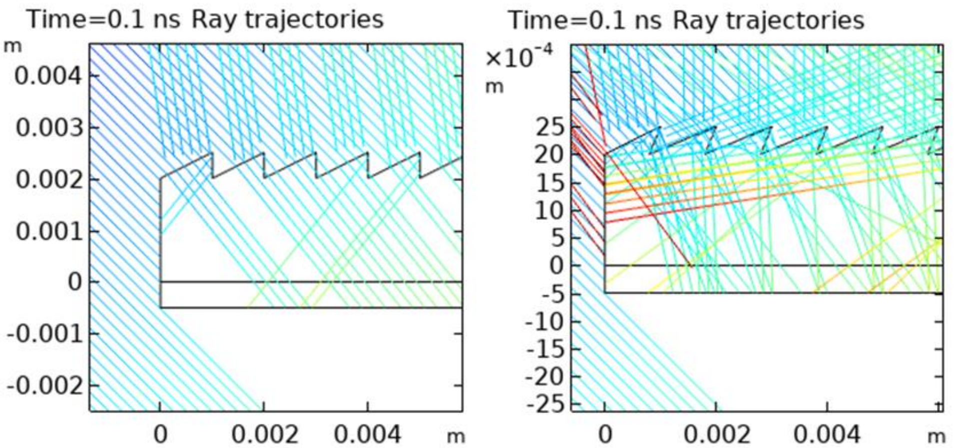

Figure 1-50: Sawtooth. This shows the original sawtooth pattern design in two dimensions. The image on the right has an overhang to enhance the hydrophobic properties. Rays in both images arrive from the top left direction.

Another alternative is to orientate the flat vertical face towards the Sun to achieve light trapping. For this to work the tilt angle must be greater than the maximum sun angle so the sun's rays don't strike the reverse slope of the sawtooth pattern at a glancing angle. The following figure shows the Sun's rays striking the glass from the opposite side. By varying the pitch of the sawtooth the pattern could be optimised for a given solar module tilt angle and latitude. For omnidirectional performance the pitch angle can be set to 45°.

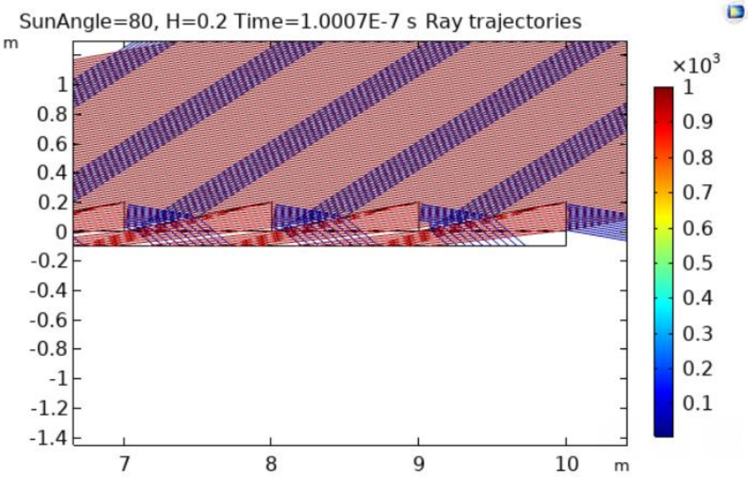

Figure 1-51 Sawtooth rays This shows the Sun's rays striking the vertical faces on the sawtooth, rays that glance of the reverse slope can strike the next vertical face and be internally reflected to the bottom of the glass block. Incident rays come from the top right, red rays are high intensity while blue rays are low intensity.

The three-dimensional sawtooth pattern can be seen below in Figure 3-6. Due to symmetry, there was no difference in performance between the two dimensional and three dimensional models.

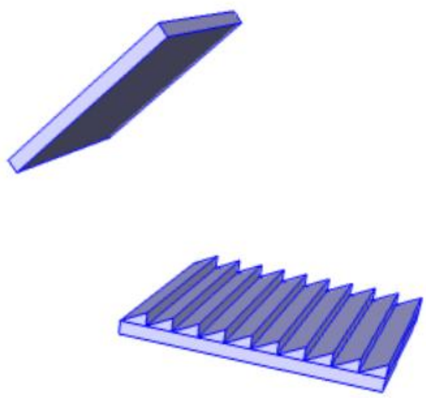

Figure 1-52 3D sawtooth. This shows the 3D sawtooth pattern and the Sun block.

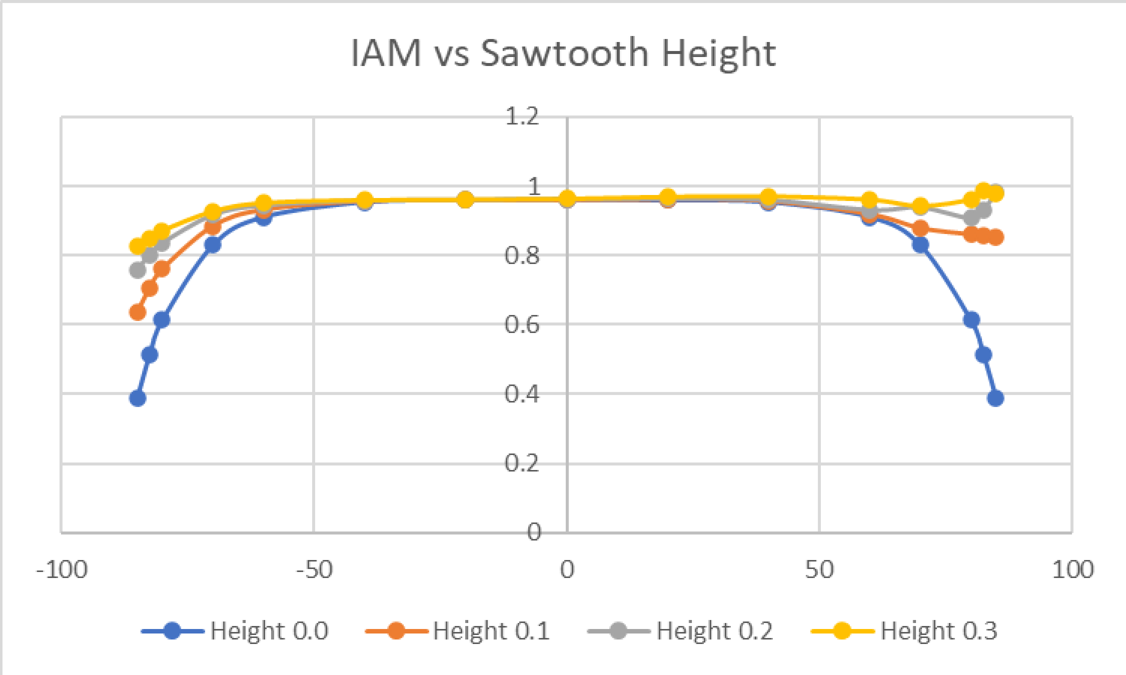

Figure 1-53: *The incidence angle modifier (IAM) for the sawtooth shows near perfect light trapping up to glancing Sun angles. This is largely independent of the sawtooth height where H=0.3 means the ratio of the triangles height to base is 0.3. On the left hand side the Sun faces the hypotenuse and the reflection losses also reduced to a lesser extent.*

These simulations are valid only for a solar module which is oriented horizontally. For a tilted solar panel, the sawtooth features would need to be pitched higher. A limitation of this design is the low degree of light trapping at normal incidence. Ideally the textured surface should have near perfect light trapping at normal incidence and an incidence angle modifier (IAM) that drops more gradually that that of flat glass for higher angles. IAM is calculated by normalizing the angle resolved transmission data. Thus, whatever the transmission is at normal angle of incidence is set to 1. The sawtooth design improves the IAM without significantly improving the transmission at normal incidence.

3.5 Square Pyramidal

The square pyramidal structure is commonly found on the top of silicon solar cells due to the high refractive index of silicon resulting in high reflection losses otherwise.[3] Walls with reflective boundaries were placed at the edges of the square pyramidal pattern to reduce the effect of losses at the edges. This simulation is to see the effect of the square pyramid structure at the air/glass interface rather than the silicon/encapsulant interface for a solar sell within a solar module.

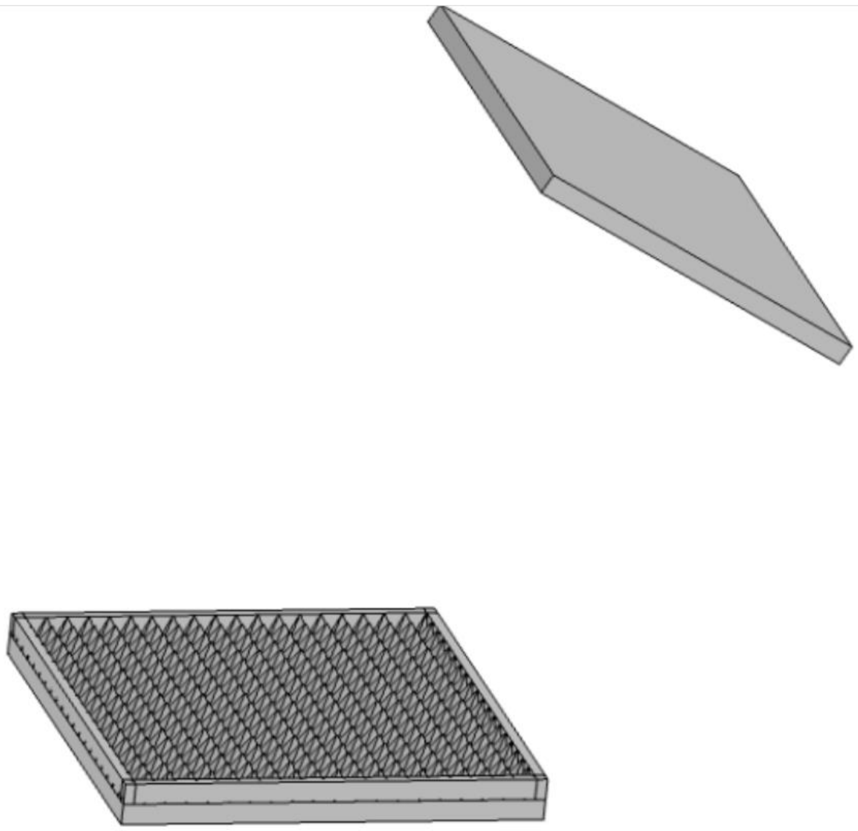

Figure 1-54: The square pyramidal structure with side walls with reflective boundaries to reduce edge related losses, which would be negligible for a full-scale solar module.

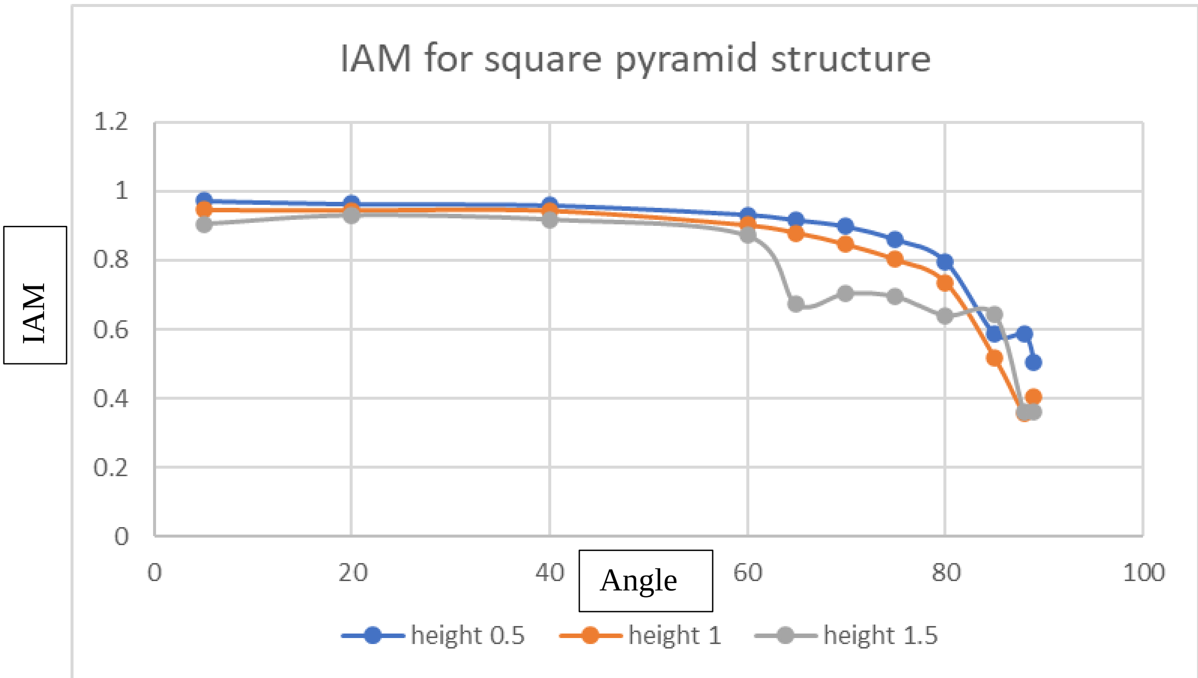

Figure 1-55: Square pyramid IAM. As can be seen in the above plot the square pyramid structure had reduced performance at higher aspect ratios.

An advantage of the square pyramidal structure over the sawtooth structure is its ability to trap light from the front, back and sides rather than just the front and back. This is useful as it can more effectively collect diffuse light which comes from all directions.

3.6 Fish-Scale Pattern

The fish-scale pattern was the next step from the sawtooth pattern. It was found that the vertical face was more effective at anti-reflection than the hypotenuse face for the sawtooth. The fish-scale could act as a specialised microlens array where the lenses are aligned with the Suns path across the sky.

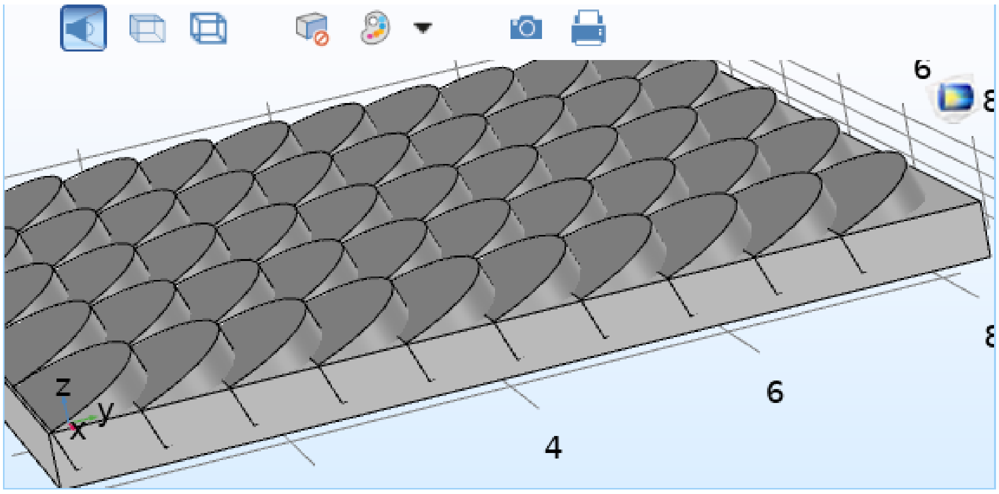

Figure 1-56: Fishscale pattern, is an array of inclined cylinders.

The fish-scale pattern faces the same issues as the sawtooth pattern as it only really works for solar modules that are placed horizontally or at very low tilt angles (such as East/West oriented flat roof mounted panels). One concern with using a lens array is non uniform illumination of the solar cell under the glass. Non-uniform illumination can reduce efficiency if the scale of the non-uniformity is greater than spacing of the metal fingers of the solar cell. Regions of the semiconductor that are less illuminated or not illuminated at all will have a higher electrical resistance as there are no photogenerated charge carriers to conduct electricity, charge carriers far from the fingers of the solar cell must move horizontally through the cell and any reduction in the cell conductivity will increase the recombination rate and lead to a loss of efficiency.[4,5] By making the fish-scales on the 10s of microns length scale this problem can be avoided. Unfortunately, there is no cheap and scalable way to manufacture these fish-scales on that length scale, the low symmetry of the design makes it difficult to do wet etching. Micromachining is an option but that could only produce costly prototypes. As discussed previously roll to roll nanoimprint lithography was not an option as features etched directly into glass were desired and not on a transparent polymer layer as it would be less durable.

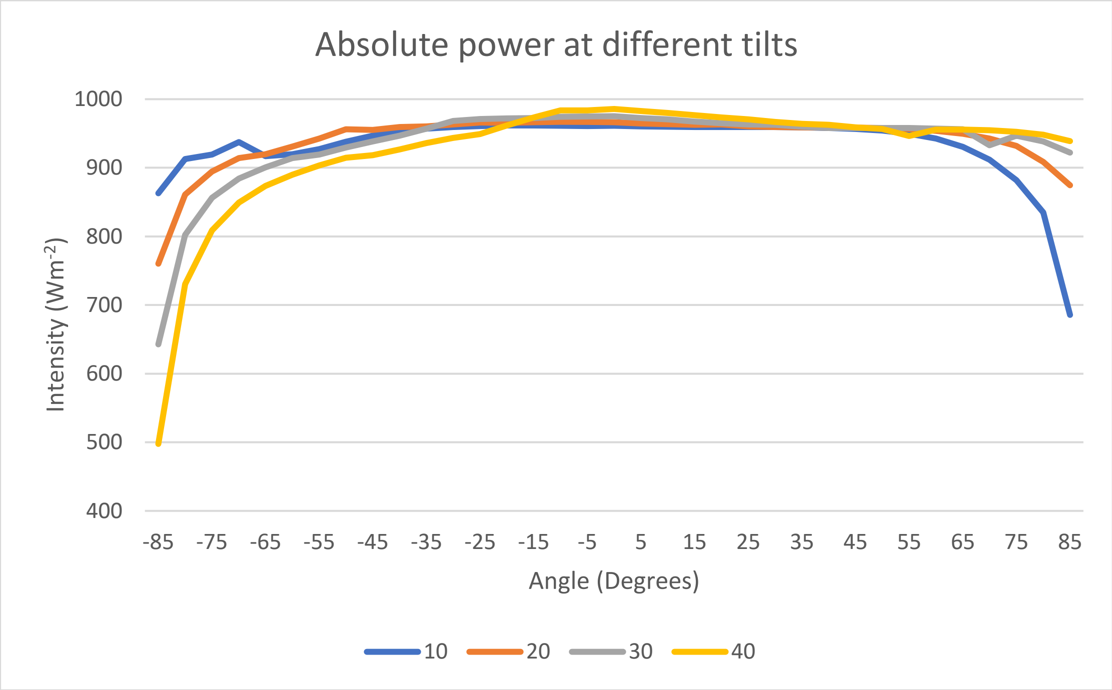

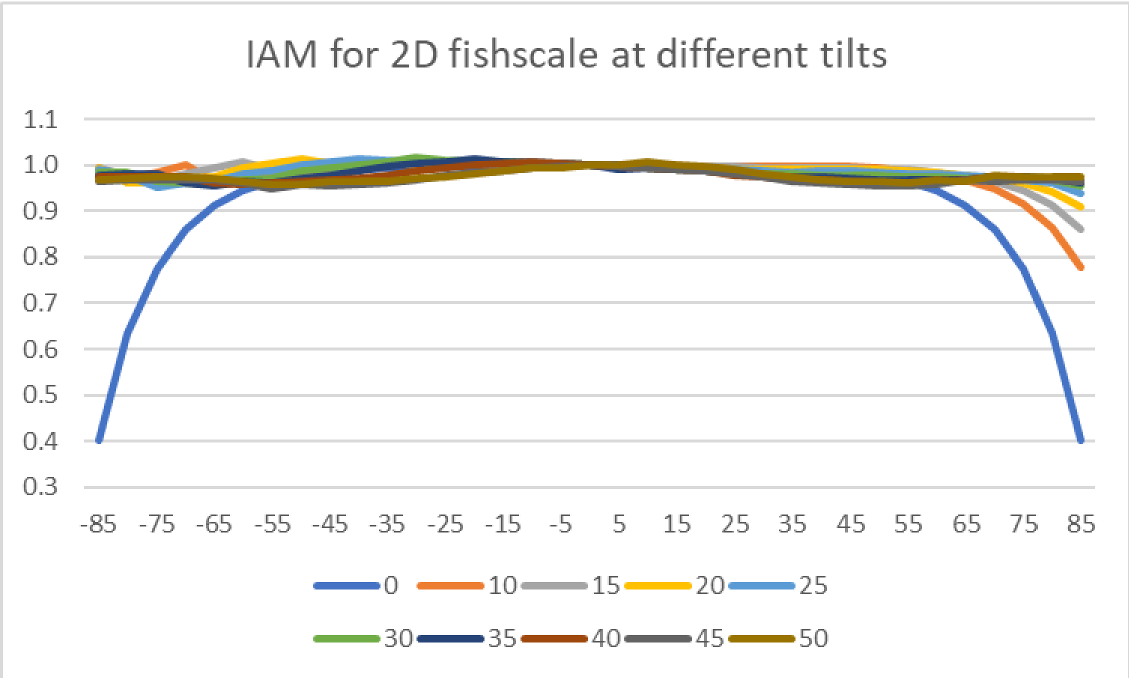

Figure 1-57: The IAMs for the 2D fish-scale patterns outperformed the sawtooth and square pyramidal structures on the left hand side, On the right hand side there was still an improvement as the rays encountered a lower effective tilt angle. The IAM simulations were done for various tilts of the scales ranging from 0 (flat glass), to 50 degrees (a high aspect ratio pattern). Top figure shows absolute values of transmission, 40 degree tilt showed 98.5% transmission at normal incidence while 10 degree tilt showed 96.1%, the same as flat glass.

For the three-dimensional fish-scale simulation a different approach was required. It was not sufficient to rotate the Sun around a single axis, rather the sun arcing across the sky was modelled, thus instead of an IAM for a single dimension a two angle IAM surface plot was generated. This new measurement cannot be directly compared to the ray tracing simulations. As the Sun was free to rotate around two axis it was no longer possible to ensure that all of the Sun's rays would strike the top of the glass block. A hollow hemisphere was created beneath the glass block to collect the incident rays that missed the target, by subtracting those rays from the Sun's rays, the number of rays that impacted the top glass surface could be known.

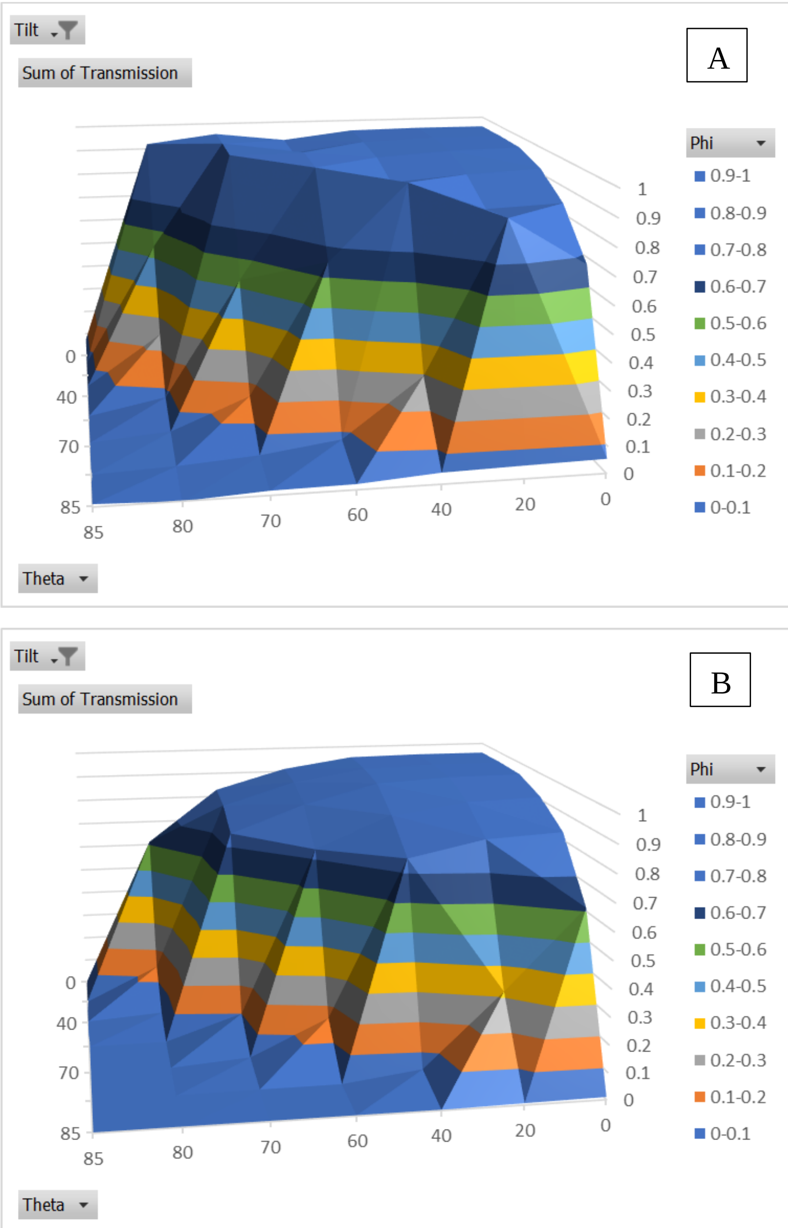

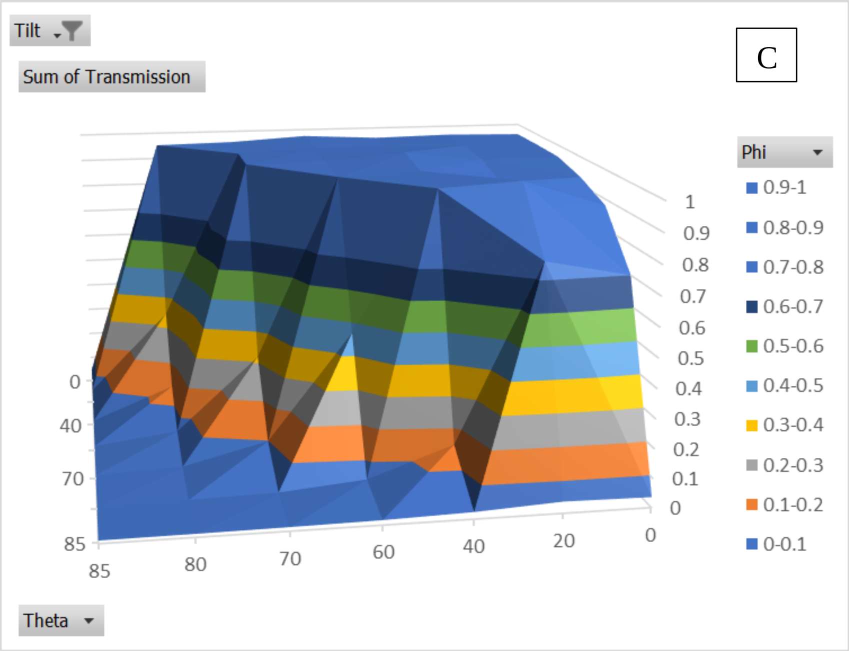

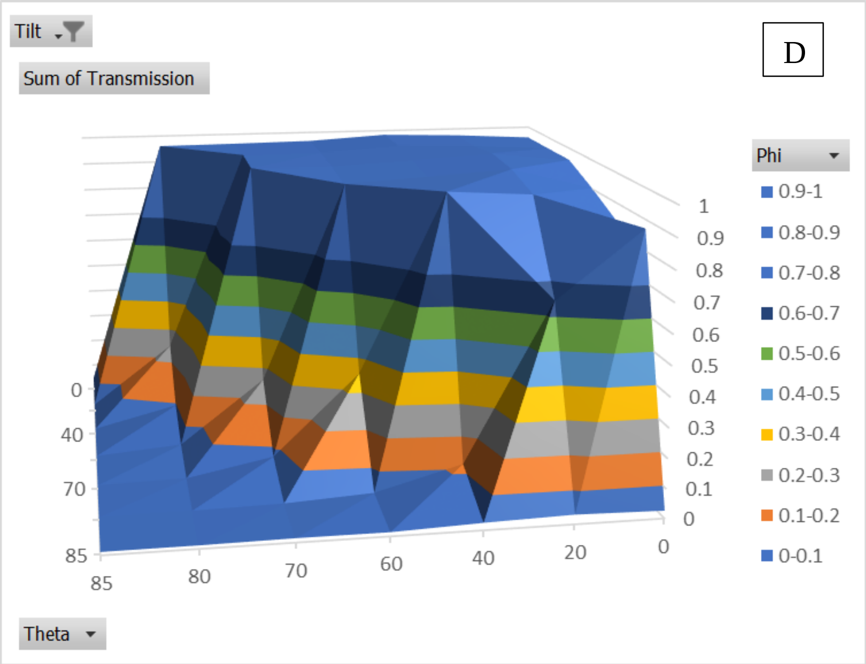

Figure 1-58: Surface plots of the fish scale pattern at different tilt angles. The fishscale tilt is as follows, A=10, B=20, C=30, D=40 degrees. The surface plots show a steep drop in transmission when the sun angle is higher than the tilt angle as the rays strike the reverse slope of the fishscale at a glancing angle resulting in high reflection losses

The surface plots show that more vertically tilted fish scales trapped light over a wider range of incident angles than more horizontally tilted scales. The anti-reflection effect was lost rapidly as the sun angle exceeded the tilt angle much like with the sawtooth patterns. The fishscales where semicircular rather than having a more complex curvature.

3.7 Pitted Glass Pattern

The pitted glass pattern was chosen for its high level of symmetry which allows for a wider range of fabrication techniques. It is also a more suitable design for chemical wet etching when compared to the square pyramid design. As glass is amorphous it does not have different crystal planes that etch at different rates, it is this feature of crystalline silicon that allows the square pyramid structure to be made cheaply by chemical etching. For glass the features will always be more rounded especially on the length scale of 10s of microns. The pitted structure like the square pyramid structure collects light omnidirectionally and has no preferred orientation. As the diffuse component of sunlight is particularly large in high latitude regions it is just as important to collect this diffuse light. The material was always set as glass with refractive index 1.5 in these simulations.

The Pitted glass structure can be considered the inverse of the bio-inspired moth-eye or rose petal pattern. The moth-eye structure can also be referred to as a microlens array or micro-cone array this helps to reduce confusion with the nanoscale moth eye structure which operates as a graded index medium rather than a light trapping structure. By having inset features rather than relief features the pitted glass should be more durable than these organic equivalents.

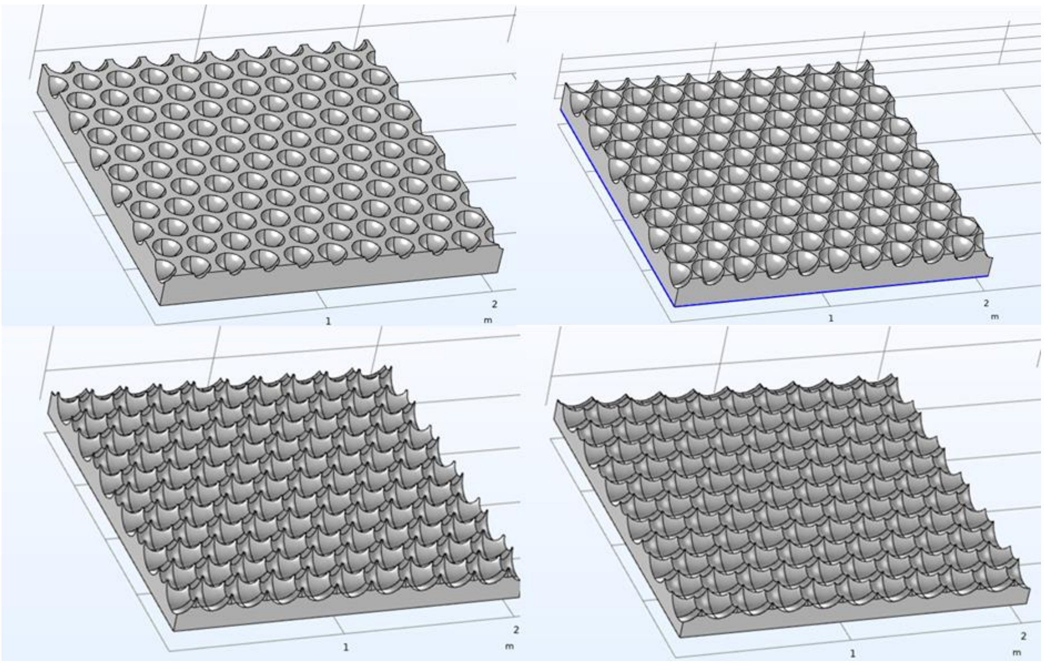

Figure 1-59 Pitted glass model. This shows the pitted glass structures in increasing order of pore size, pore size 0.8 means the pores are 80% of the size where the edges of adjacent pores would touch, due to the limitations of COMSOL I could not generate a pore size of exactly 1 as the meeting of two curved lines creates an infinitesimal that cannot be meshed. Pore sizes are as follows; Top Left:0.8, Top Right: 0.95, Bottom Left: 1.12, Bottom Right: 1.2

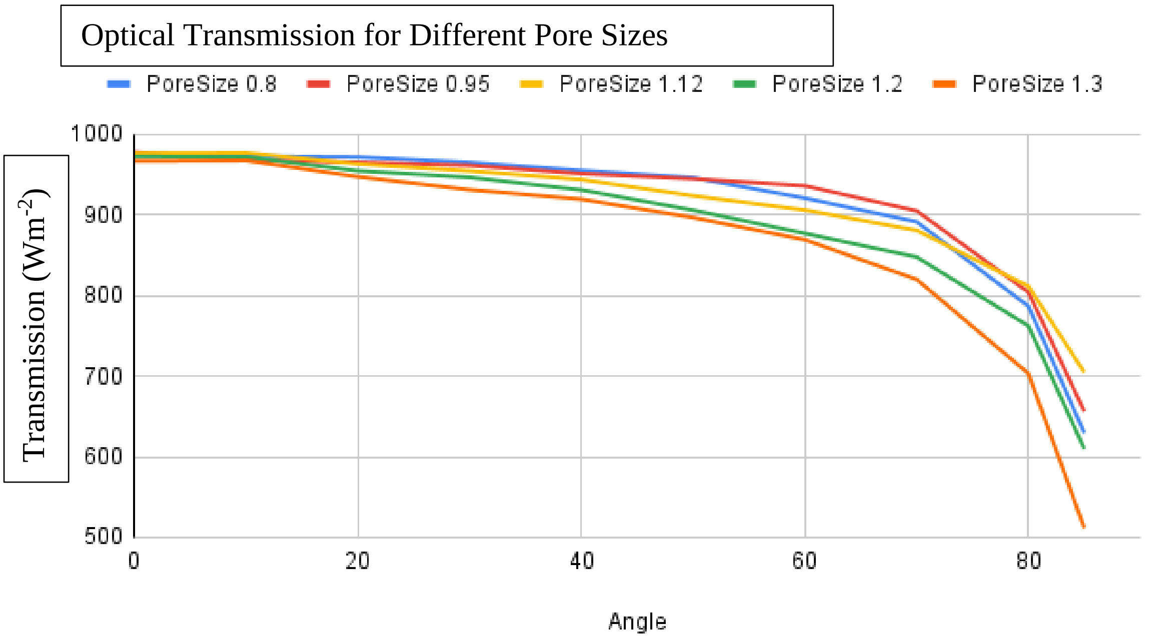

Figure 1-60: Pitted glass transmission. Pore size 1.0 is when the pores (also called Pits) touch. Pore sizes below 1 are underetched and pore sizes.

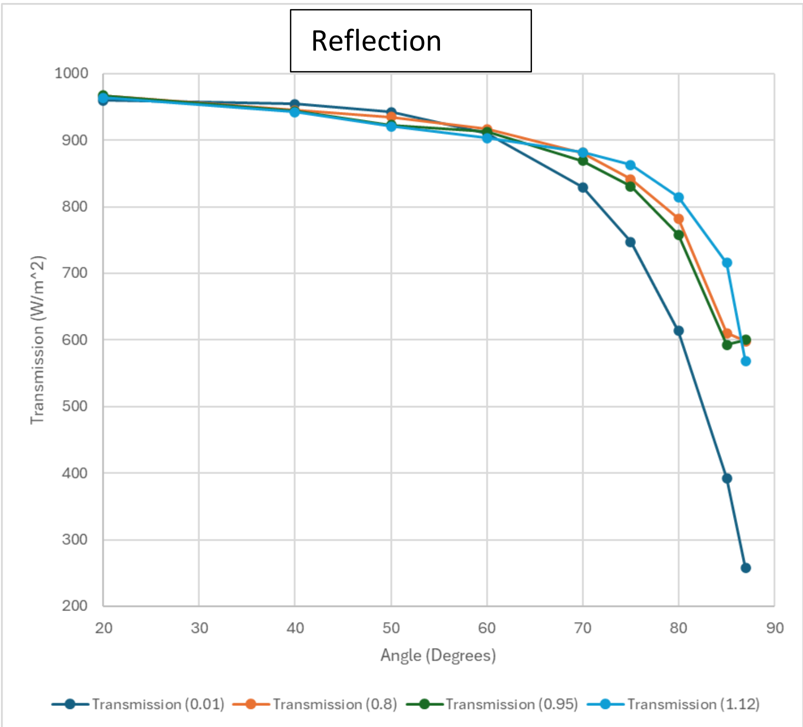

Figure 1-61: Transmission as a function of incident angle for pitted glass with different pore sizes.

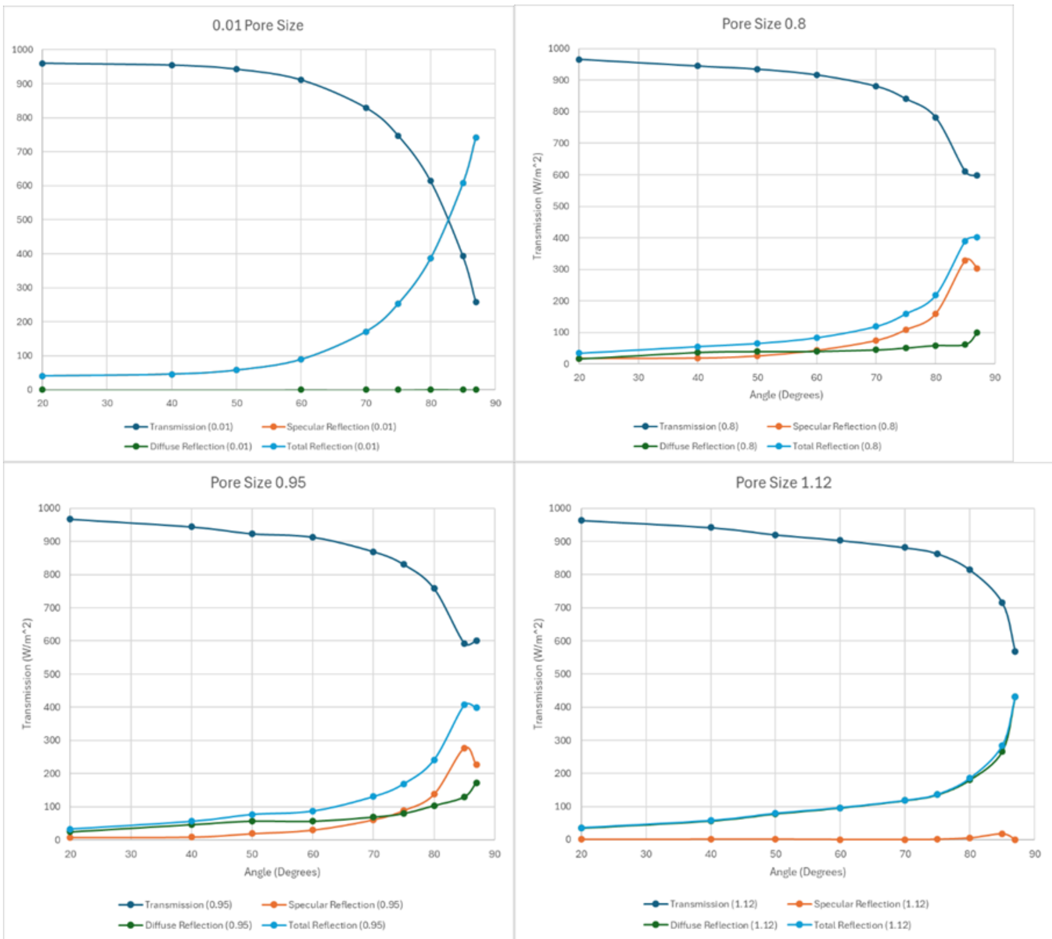

Figure 1-62: IAMs for underetched and overetched pitted glass structures

As can be seen in the figures above the pitted glass extends the IAM curve as well as increases the normal incidence transmission by up to 3%. The transmission is highly diffuse which is not an issue for solar cells as the entropy of the incident light does not affect the efficiency, (diffuse sunlight cannot be concentrated by a lens).

3.8 Moth Eye vs Pitted Glass

The moth-eye structure (microlens array)[6] can be considered the main competitor to the pitted glass design[7] so it is important to directly compare it to the pitted glass pattern in simulation especially since only the pitted glass was fabricated and not the moth-eye structure.

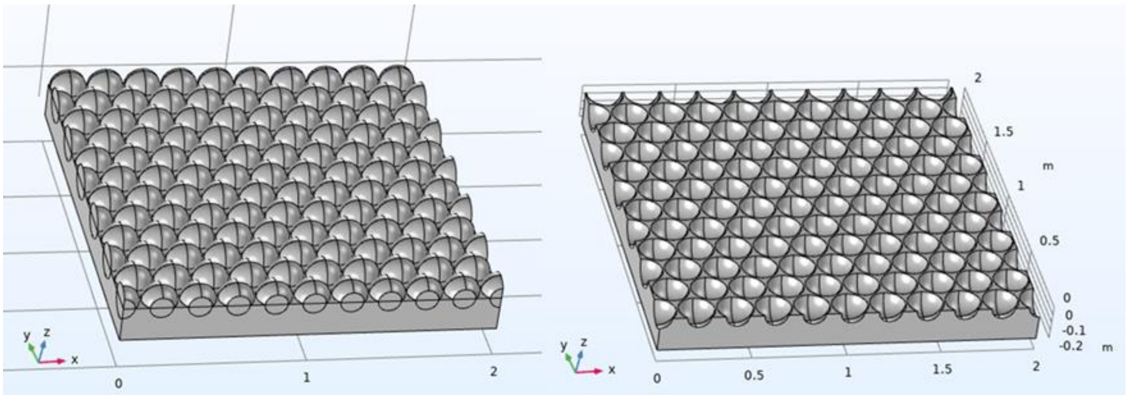

Figure 1-63: Microlens array vs pitted glass

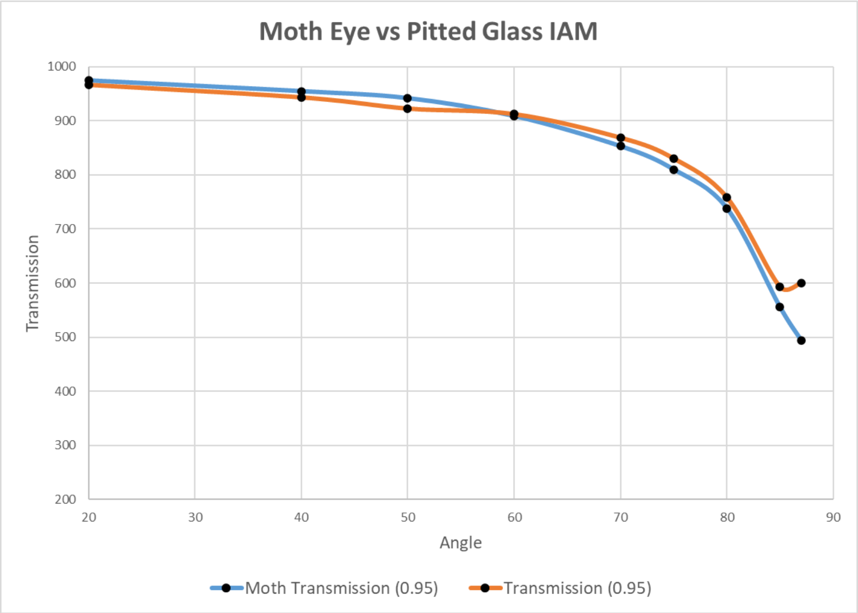

Figure 1-64: Pitted glass vs moth-eye. Performance is similar but the pitted glass structure is slightly better at trapping light at glancing angles.

The pitted glass slightly outperforms the moth eye structure (microlens array) at higher angles but optically both structures can be considered equivalent. This was also observed with rose petal and inverse rose petal structures in literature.

It is important to distinguish the moth eye microlens array structure from the nanoscale biomimetic moth eye structure. The nanoscale structure is subwavelength in scale for visible light and acts as a graded index medium. This is a much larger pattern where light can be accurately represented with ray model rather than an electromagnetic model.

3.9 PITTED GLASS WITH AR COATING

To simulate the combined effect of a micro and nanoscale hierarchical structure a low refractive index AR coating on top of the pitted glass was added to see if the combined effect of both textured and low refractive index would be greater or than either effect on its own. The AR coating was simulated by changing the boundary condition of the top surface to AR Coating and setting the refractive index to 1.22.

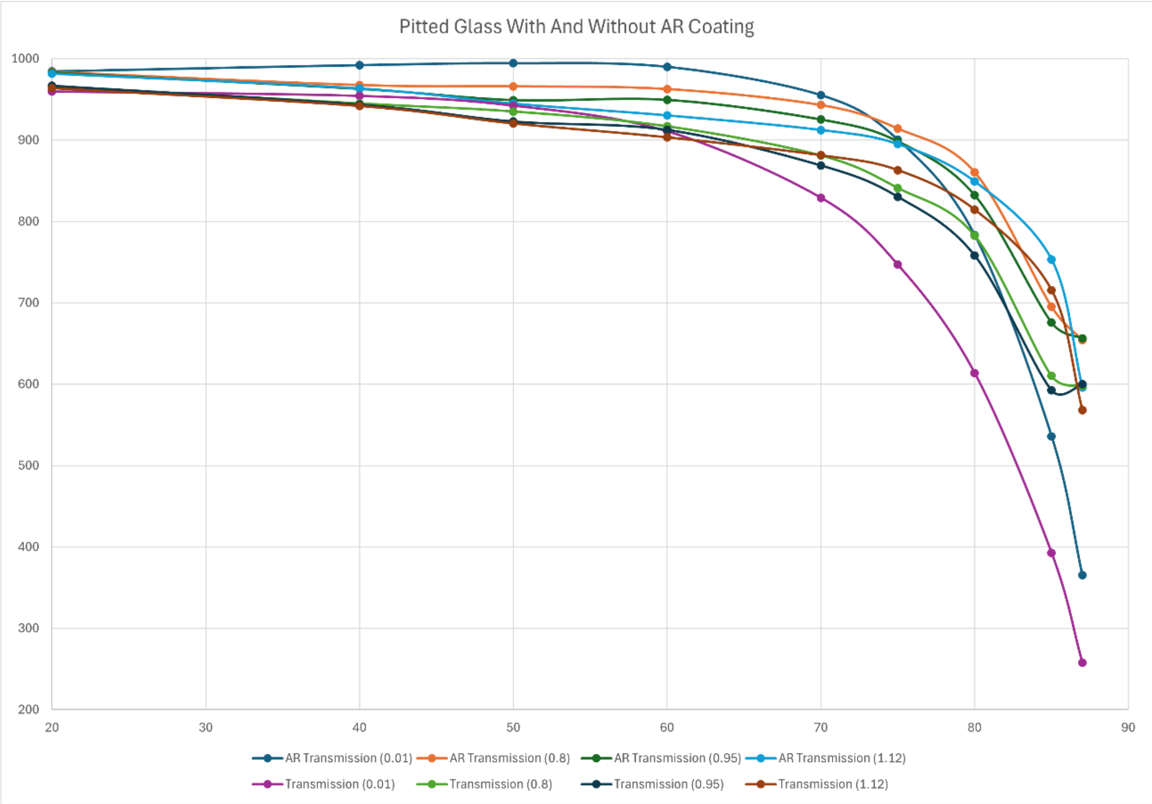

Figure 1-65: Pitted glass with and without a low refractive index coating.

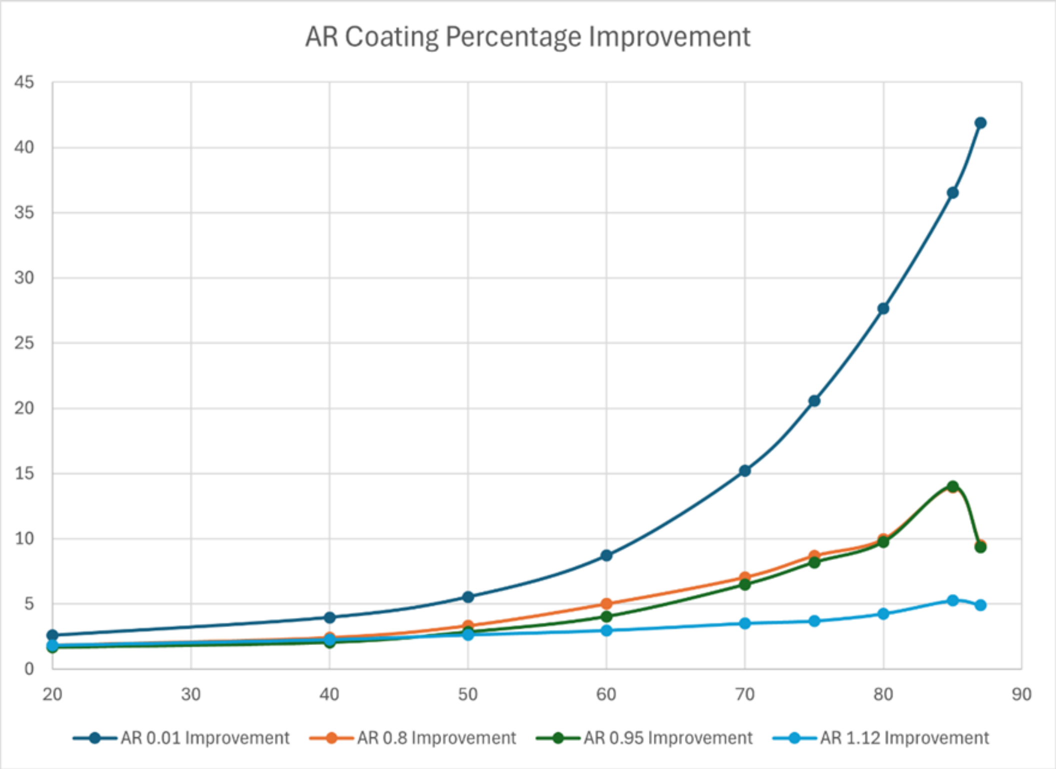

Figure 1-66: The percentage improvement when adding a low index coating to a pitted glass surface.

3.10 ANNUAL ELECTRICAL YIELD COMPARISON

By plugging the IAMs from each structure into the PVsyst model it is possible to evaluate the potential economic benefit of each patterned surface. The following figure shows the system setup in the PVsyst module for a large solar farm in Ireland at 53^{o} latitude. The inverters were oversized on the system to prevent inverter losses due to clipping so that the benefit of the reduced reflection losses could be isolated.

It should be noted that many of the improvements are above 4% meaning that the reflection losses are suppressed over a broad range of angles and the IAM curve is flatter.

General parameters

Grid-Connected System — **No 3D scene defined, no shadings**

PV Field Orientation					
Orientation		**Sheds configuration**		**Models used**	
Fixed plane		No 3D scene defined		Transposition	Perez
Tilt/Azimuth	25 / 0 °			Diffuse	Perez, Meteonorm
				Circumsolar	separate
Horizon		**Near Shadings**		**User's needs**	
Free Horizon		No Shadings		Unlimited load (grid)	

PV Array Characteristics

PV module		**Inverter**	
Manufacturer	Generic	Manufacturer	Generic
Model	Mono 440 Wp Twin 144 half-cells	Model	2000 kWac central inverter
(Original PVsyst database)		(Original PVsyst database)	
Unit Nom. Power	440 Wp	Unit Nom. Power	2000 kWac
Number of PV modules	22728 units	Number of inverters	4 units
Nominal (STC)	10.00 MWp	Total power	8000 kWac
Modules	947 Strings x 24 In series	Operating voltage	800-1500 V
At operating cond. (50°C)		Pnom ratio (DC:AC)	1.25
Pmpp	9083 kWp		
U mpp	899 V		
I mpp	10099 A		
Total PV power		**Total inverter power**	
Nominal (STC)	10000 kWp	Total power	8000 kWac
Total	22728 modules	Number of inverters	4 units
Module area	50569 m²	Pnom ratio	1.25
Cell area	45165 m²		

Figure 1-67: The parameters that were put into the PVsyst model for the net present value calculations

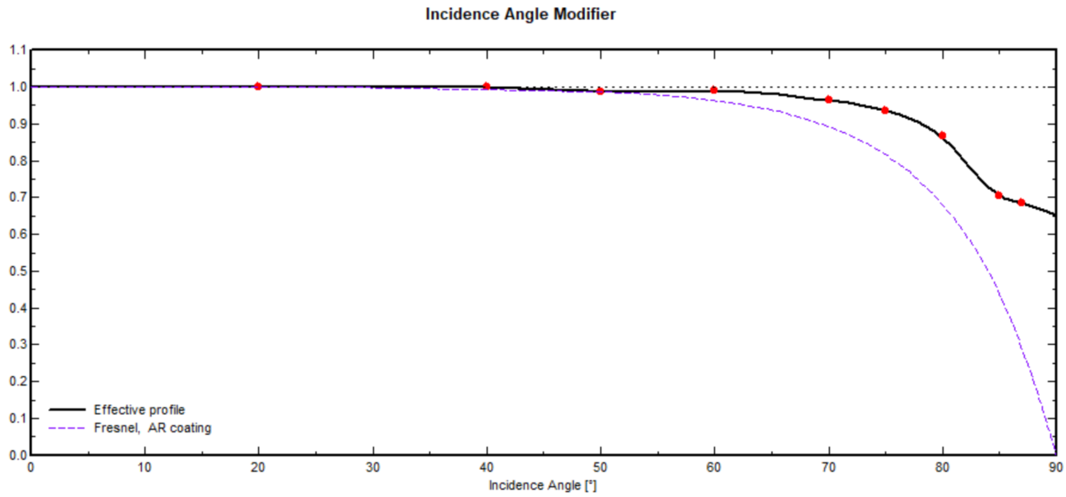

Figure 1-68: IAM or regular AR coating vs simulated IAM for pitted glass

Table 2: Annual transmission improvement over flat glass

Pattern	Annual Energy (MWh Per Year	Annual Energy Modified (MWh Per Year	Modified Percentage Improvement
Flat Glass	10106	10106	0%
Sawtooth H=0.1	10268	10525	4.15%
Sawtooth H=0.2	10355	10604	4.93%
Sawtooth H=0.3	10451	10691	5.79%
Square Pyramid H=0.5	10288	10494	3.84%
Square Pyramid H=1.0	10059	10260	1.52%
Square Pyramid H=1.5	9593	9785	-3.18%
Fish-Scale 10º Tilt	10335	10666	5.54%
Fish-Scale 20º Tilt	10362	10694	5.82%
Fish-Scale 30º Tilt	10295	10624	5.13%
Pitted Glass 0.8	10183	10336	2.28%
Pitted Glass 0.95	10131	10283	1.75%
Pitted Glass 1.12	10138	10290	1.82%
Flat Glass AR	10312	10312	2.84%
Pitted Glass 0.8 AR	10355	10598	4.87%
Pitted Glass 0.95 AR	10415	10660	5.48%
Pitted Glass 1.12 AR	10395	10639	5.27%

For sawtooth height the number refers to the height to base ratio, so H=0.1 means that each sawtooth is 10 times wider than it is tall. The same principle applies to the square pyramid structure.

3.11 Net Present Value Calculations

The Net Present Value is a useful way to envisage the economic benefit of an AR coating of a solar panel as any positive increase in net present value signifies a worthwhile investment while a negative value indicates that money would get a better return in a bank savings account or another no/low risk investment. If the Net Present Value increases by €4 per solar module when a novel AR coating is added, then that is the maximum amount the AR coating may cost for it to be economically viable. Thus, the increase in Net Present Value provides a budget for the AR coatings that should not be exceeded. Assuming an electricity price of 0.3 €/kWh and a discount rate of 2% the following values were calculated.

Table 3: Increase in present value over flat glass

Pattern	Annual Energy Improvement (MWh Per Year	Net Present Value Per Solar Module
Flat Glass	0	€0
Sawtooth H=0.1	419	€5.86
Sawtooth H=0.2	498	€6.96
Sawtooth H=0.3	585	€8.18
Square Pyramid H=0.5	388	€5.43
Square Pyramid H=1.0	154	€2.15
Square Pyramid H=1.5	-321	€-4.49
Fish-Scale 10º Tilt	560	€7.83
Fish-Scale 20º Tilt	588	€8.22
Fish-Scale 30º Tilt	518	€7.24
Pitted Glass 0.8	230	€3.22
Pitted Glass 0.95	177	€2.48
Pitted Glass 1.12	184	€2.57
Flat Glass AR	206	€2.87
Pitted Glass 0.8 AR	492	€6.88
Pitted Glass 0.95 AR	554	€7.75
Pitted Glass 1.12 AR	533	€7.45

3.12 CONCLUSIONS

I investigated several geometries with the goal of finding a practical pattern that had good light trapping characteristics over a broad range of angles. Sawtooth and fishscale patterns were tested first as they were designed to trap light efficiently over a narrow range of angles. The IAM curves showed good performance in this range of angles but then showed poor performance when light glanced off the reverse slope. As diffuse light can contribute as much as 50% to the total irradiance in winter months it was important to move to a design that collected light over a broader span of angles. The inverted pyramid structure was inspired by the textured AR surfaces found on silicon solar cells but adapted for the top surface of glass solar module front covers. The pitted glass structure was also chosen as it is similar to the square pyramid but with rounded features rather than sharp features, this makes it more suitable for glass which is amorphous and thus is there are no crystal planes that can be preferentially etched to form sharp features.

The pitted glass array was then compared to its inverse, the microlens array. The two structures had near identical optical transmission performance meaning the better of these two designs would depend on durability, practicality of manufacture, soiling and wetting characteristics. Finally, the effect of adding an AR coating to the designs in order to simulate the effect of a hierarchical structure. In all cases adding an AR coating was beneficial and by plugging in the IAM data into PVsyst it was shown that pitted glass with an AR coating gave a 5.48% annual transmission improvement over flat glass with no AR coating. Flat glass with an AR coating gave 2.84% improvement which means the hierarchical structure significantly outperforms the AR coatings commercially available on solar modules today. This corresponds to an increase in present value of €7 meaning the new hierarchically patterned glass surface cannot exceed this price if it is to be commercially viable.

3.13 References:

(1) *Modeling Software for Ray Tracing in Optically Large Systems*. COMSOL. https://www.comsol.com/ray-optics-module

(2) *comsol ray optics, https://www.comsol.com/ray-optics-module*

(3) Omar, H. D.; Hashim, Md. R.; Pakhuruddin, M. Z. Ray Tracing of Inverted Pyramids for Light-Trapping in Thin Crystalline Silicon for Solar Cells. *Optik* **2020**

(4) Li, G.; Xuan, Q.; Pei, G.; Su, Y.; Ji, J. Effect of Non-Uniform Illumination and Temperature Distribution on Concentrating Solar Cell - A Review. *Energy* **2018**

(5) Pfeiffer, H.; Bihler, M. The Effects of Non-Uniform Illumination of Solar Cells with Concentrated Light. *Sol. Cells* **1982**

(6) Wang, Z.; Zhu, G.; Huang, Y.; Zhu, X.; Zhu, C. Analytical Model of Microlens Array System Homogenizer. *Opt. Laser Technol.* **2015**

(7) Li, P.; Liu, X.; Cheng, Q.; Liang, Z. Long-Term Photovoltaic Performance of Thin-Film Solar Cells with Diffractive Microlens Arrays on Glass Substrates. *Results Phys.* **2021**

4 FABRICATION METHODS

4.1 CHAPTER INTRODUCTION

Firstly, in this chapter, the choice of directly texturing glass rather than texturing a polymer film that could be laminated on top of the glass is justified. Various state-of-the-art techniques for patterning glass are then reviewed, and their suitability for the project evaluated. Further detail is then given on some fabrication methods that were attempted earlier in the PhD. Finally, the HF etching technique that was used to produce the working pitted glass samples is shown.

4.2 CHOICE OF PATTERNING GLASS INSTEAD OF POLYMER

Crystalline silicon (c-Si) solar cell modules conventionally incorporate a front-side cover composed of glass with a typical thickness of 3.2 mm. Consequently, glass accounts for approximately 70% of the total module mass. This substantial weight imposes constraints on the deployment of c-Si modules, potentially rendering their installation unfeasible in structurally limited environments. The development of lightweight c-Si solar cell modules with a polymer front cover would mitigate these restrictions, thereby enabling a broader range of applications, including integration into building facades, rooftops of industrial facilities, fixed-wing aerial platforms, and vehicular surfaces. Such advancements would significantly enhance the market potential of c-Si photovoltaics by facilitating their implementation in previously inaccessible locations.[1] Another significant advantage of a polymer front cover is the relative ease of forming a patterned surface with techniques such as nanoimprint lithography which is more difficult to do on a high hardness surface such as glass. Several thin-film photovoltaic technologies, including those based on cadmium telluride (CdTe), copper indium gallium selenide (CIGS) or amorphous silicon (a-Si), have already been developed with a polymer front cover.[2]

Despite all the aforementioned advantages of the flexible, lightweight and mouldable polymer front cover for solar modules, glass is vastly more popular as a front cover material. This is because monocrystalline and polycrystalline silicon based solar modules account for 98% of the solar PV market.[3] Crystalline silicon is brittle and cracks under stress and thus glass is needed to provide rigidity to the solar module. Even then vibrations caused by wind loading is known to cause microcracks in crystalline silicon solar cells with glass covers.[4]

Another problem with polymer front covers is UV aging, I have focused on polyethylene terephthalate (PET) but these issues also apply to other transparent polymers. Exposure to sunlight induces various degradation mechanisms in PET, including thermal decomposition via chain reactions between vinyl and carboxyl terminal groups, photodegradation of methylene groups leading to irreversible structural alterations, and overall polymer chain degradation. Additionally, optical clarity degradation, manifested as yellowing, arises from residual compounds introduced during PET synthesis and processing. Photooxidation, or photochemical aging, occurs upon simultaneous exposure to ultraviolet (UV) radiation and atmospheric oxygen. PET exhibits strong UV absorption in the 300–330 nm wavelength range, resulting in the deterioration of a thin surface layer.[5]

As can be seen in the figure below glass has better optical transmission due to lower absorption. PET has a refractive index of 1.57 while glass is 1.51 so PET is also more reflective.[6]

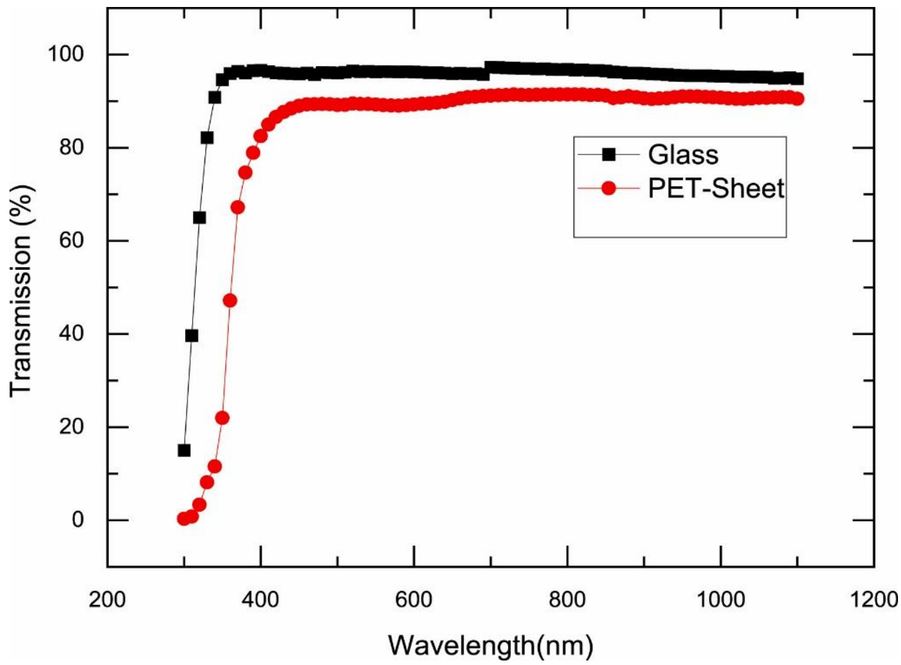

Figure 4-1: Glass vs PET. Data from "A comparative study of different polymer materials for the development of flexible crystalline silicon modules"[7]

In summary, it was decided to pattern glass directly rather than a polymer film on top of glass due to the greater durability of glass, resistance to UV aging and no risk of the polymer film delaminating. Most importantly of all the intrinsic optical properties of tempered low iron soda lime glass are superior to plastics such as PET. By applying a polymer layer on top of the glass I would first be raising the reflection losses before patterning would bring the losses back down again.

4.3 Glass Patterning Techniques Review

The inherent advantages of glass as a material such as good optical transmission, hardness and chemical inertness are also the source of the challenges and limitations of glass fabrication techniques. In particular, many of these techniques suffer from low throughput and thus are impractical for solar PV applications. The review paper "Additive, subtractive and formative manufacturing of glass-based functional micro/nanostructures: A comprehensive review" by Hong Luo et al.[8] gives a good overview of the state of the art in glass texturing techniques, not all of these methods are relevant to solar panels so only some of these will be discussed.

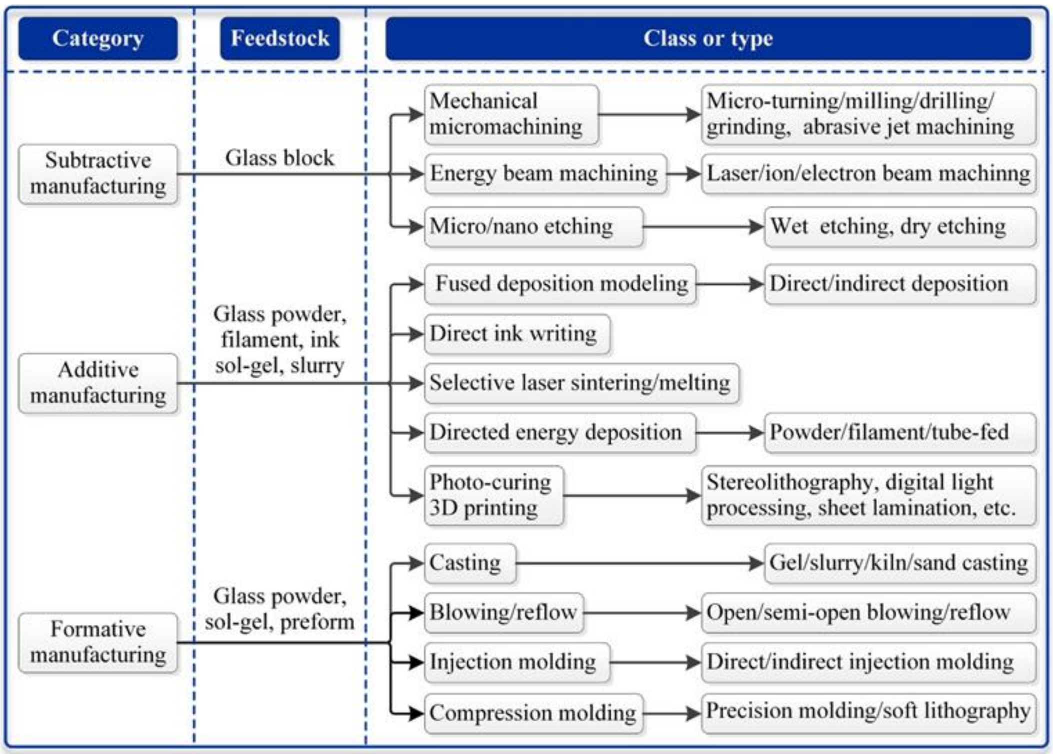

Figure 4-2: Glass fabrication techniques. Diagram of various techniques from "Additive, subtractive and formative manufacturing of glass-based functional micro/nanostructures: A comprehensive review" by Hong Luo et al.[8]

Subtractive manufacturing refers to the removal of material to create the desired shape. This can be done with energy beams such as lasers, cutting tools or chemical etchants like hydrofluoric acid.

Additive manufacturing is 3D printing where feedstocks are bonded and solidified following a digital programme, this method in useful for stacked three dimensional structures and are less relevant to my project.

Formative manufacturing is the reshaping of the original material using moulds and includes techniques like nanoimprint lithography.

4.4 TEMPERED GLASS

The glass used in solar modules is tempered to protect the panels from environmental damage such as hailstones. Thus the top layer of the glass is under high compressive stress and this stress can be rapidly released if there is a crack in the glass. Thermal tempering of glass involves heating then relatively rapid cooling of glass such that the outer layer of glass cools much faster than the inside creating a stress profile. Chemical tempering involves submersing the glass in high temperature molten salt such that large ions in the salt such as potassium replace the smaller sodium ions in the outer layer of glass increasing the stress in that layer. Shown below are the stress profiles of thermally and chemically tempered glass.[9]

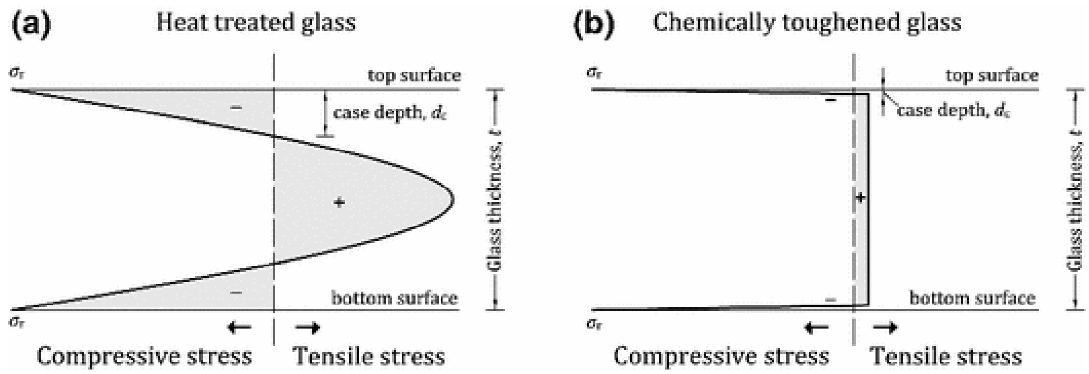

Figure 4-3: *The stress profiles of heat treated and chemically toughed glass. Image from "Kyriaki Corinna Datsiou, Mauro Overend, The strength of aged glass, Glass Structural Engineering, 2017"*[9]

Chemically tempered glass is 15 to 20 times stronger than ordinary float glass while thermally tempered glass is only 3 to 5 times stronger. Surface compression of chemically strengthened glass goes up 600 N/mm^2 (MPa) while thermally tempered glass is only 90 N/mm^2 (MPa).[10] The main advantages and disadvantages of thermally and chemically tempered glass are outlined here.[11]

Thermally Tempered Glass:

- The production cost is low and the process is scalable making it suitable for solar PV applications, the process takes only a few minutes with more rapid cooling increasing the glass strength but also raising the risk of the glass shattering during the tempering process.
- Safety glass will break into small fragments when broken, which can reduce harm to the human body.
- Glass self-explosion can happen randomly or after small perturbations in temperature or applied force.

Chemically Tempered Glass:

- Stronger than thermally tempered glass. There is also greater resistance to bending and thermal shock.
- Chemically tempered glass can be cut without shattering so it is possible to do post temper processing.
- Chemically tempered glass is 2-3 times less vulnerable to thermal shock.
- Suitable for unusual shapes as there is no deformation during the tempering process, this is not an issue for flat glass on solar panels.
- Suitable for ultra-thin products below 3mm such as mobile phone screens "Corning Gorilla Glass"[12].
- Higher production costs makes it more suitable for high value electronic devices rather than solar panels.

Another advantage of chemical tempering is that it can be done after the glass has been microtextured eliminating the risk of the texturing process shattering the glass although this leads to a reduction in compressive stress and thus the added strength is lost[13]. In mthisproject non tempered, low iron, soda lime glass, microscope slides were used as they could be cut without shattering down to a suitable size for my optical measurements. Solar modules use thermally tempered glass.

4.5 DUCTILE VS BRITTLE FRACTURE

Typically machining of glass with the use of conventional tools such as saws and drills is difficult due to the brittle nature of glass, especially tempered glass. However on a microscopic length scale it is possible to use these tools to cut glass as the material experiences ductile flow rather than brittle fracture.[14] The transition from brittle to ductile material removal at reduced cutting depths can be understood through an energy-based analysis of the material removal process known as the Griffith theory of crack propagation.[15,16] This theory is highly applicable to inelastic, brittle materials such as glass while modifications are required for ductile materials like steel.[17]

At lower depths of cut, plastic deformation becomes the energetically preferred mechanism over fracture. This transition is governed by the material's resistance to plastic flow, characterized by its yield stress σ_y. The energy E_p required to plastically deform a given volume V_p of material is given by,

$$E_p = \sigma_y \times V_p \tag{4.1}$$

The energy E_f required for a fracture that creates a new surface of area A_f is given by,

$$E_f = G \times A_f \tag{4.2}$$

Where G is the Griffith crack propagation parameter. When a tool is machining into a material with a cut depth of d then the area A_f is roughly proportional to d^2 and the deformed volume V_p is roughly proportional to d^3. The ratio of E_p to E_f can be described as follows,

$$\frac{E_p}{E_f} = \frac{\sigma_y \times V_p}{G \times A_f} = \frac{\sigma_y \times d^3}{G \times d^2} = \frac{\sigma_y}{G} \times d \tag{4.3}$$

As the yield stress and Griffith crack propagation parameter are material properties the ratio of plastic deformation to fracture energy is proportional to the cut depth.

$$\frac{E_p}{E_f} \propto d \tag{4.4}$$

Thus for deep cuts the plastic flow energy is greater and the material will prefer to shatter which for shallow cuts to opposite is the case.[14] The problem of tempered glass shattering can also be explained with this theory as in equation 4.1 an increase in the yield stress increases the energy required for plastic deformation which makes brittle fracture the more preferable path. As tempering increases the stress on the glass surface E_p is also increased.

4.6 MICRO-MACHINING

Micro-milling uses the principles discussed already to cut glass with ridged micro-cutting tools such as saws to achieve cut depths of up to one micron. Greater cut depths risk damaging the tools as well as going above the critical depth and entering the brittle fracture regime instead of the ductile regime. This poor cut depth can be significantly improved by vibrating the cutting tools at ultrasonic frequencies which reduces the applied cutting force. [18] Cut depth is important as it determines the milling rate and thus the cost and scalability of the process.

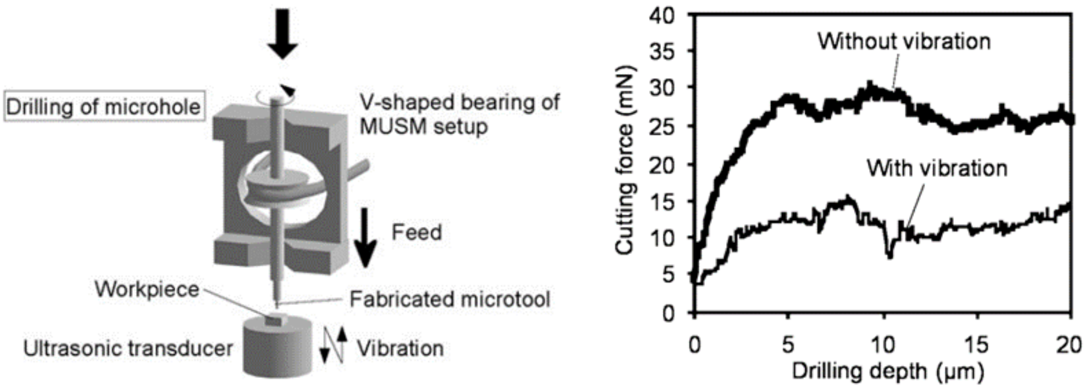

Figure 4-4: Micro-machining. Left: The experimental setup for micro-drilling a vibrating workpiece, Right: The reduction in the required cutting force when vibration is applied (Thrust cutting force (tool diameter = 9.5 μm, penetration = 0.05 μm/s). Both images from "K. Egashira, K. Mizutani, T. Nagao, Ultrasonic Vibration Drilling of Microholes in Glass, CIRP Annals, 2002"[19]

Another variant of micro-milling is laser assisted micro-milling where near infrared laser radiation is directed at the material at the same point that it is being cut. Due to glass having more absorption for infrared radiation than visible light the glass is heated locally near the surface to temperatures in excess of 1000° K at the centre of the laser spot. This is well above the working point of borosilicate glass and above the melting point of soda lime glass. By softening the glass at these high temperatures the required cutting force is greatly reduced which reduces the generation of cracks. With less cracks this technique gives a smoother, less damaged surface than regular mico-milling. One problem with this technique is the minimal resolution of the cut features is limited not only by the tool size but also the laser spot size. Infrared radiation cannot be as focused as visible or UV radiation due to the diffraction limit of light.

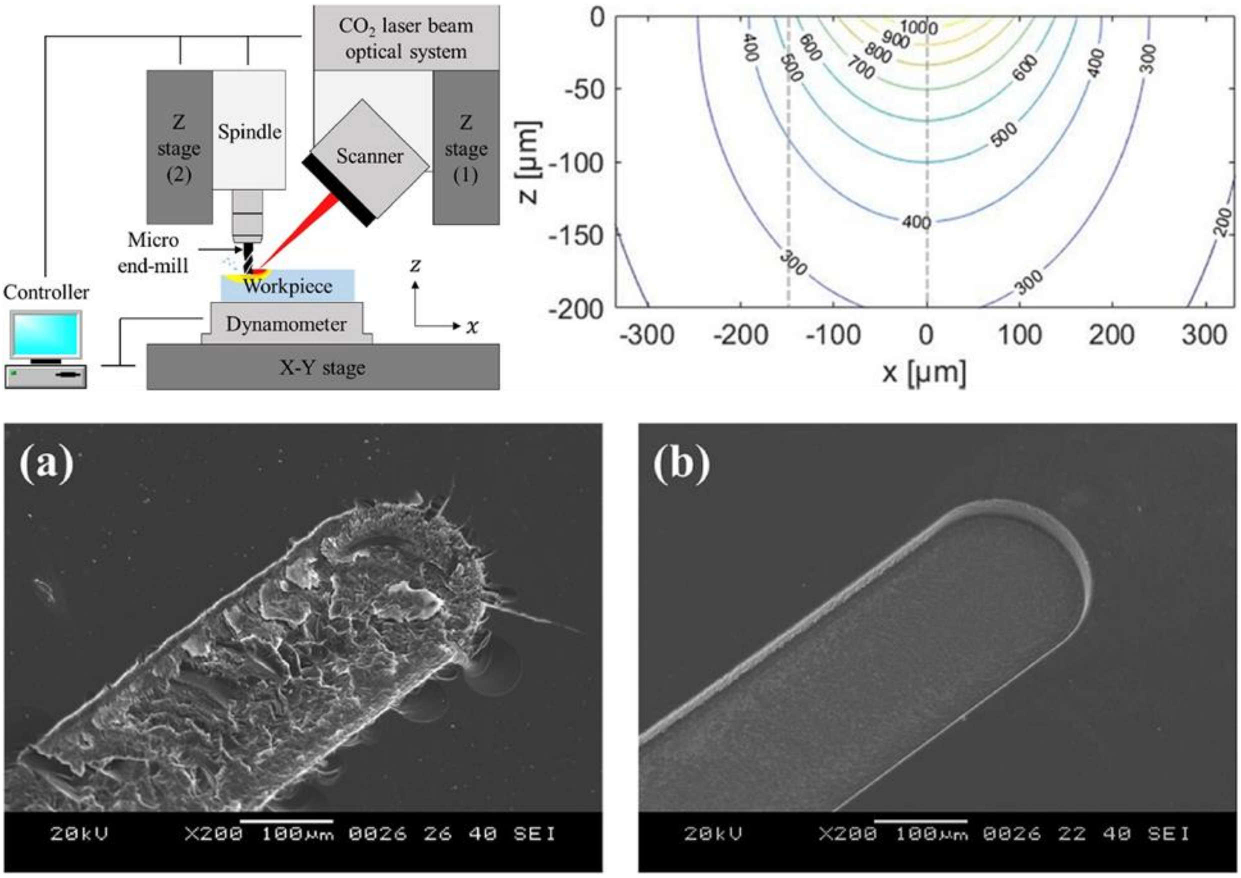

Figure 4-5 Laser assisted milling. Top Left: Diagram of the laser assisted micro-machining setup, Top Right: the cross sectional temperature profile of the glass surface exposed to laser radiation (units in Kelvin), Bottom: the comparison of micro-machining with and without laser assistance. All images from Taekyum Kim, Kui-Kam Kwon, Chong Nam Chu, Ki Young Song, Experimental investigation on CO_2 laser-assisted micro-slot milling characteristics of borosilicate glass, Precision Engineering, 2020[20]

Micro-grinding involves the use of a small grinding wheel with an abrasive surface such as diamond or cubic boron nitride.[21] Micro-grinding has a much higher cutting rate than the previous methods but the trade off is the inability of the grinding wheel to create certain shapes or to create deep high aspect ratio features as one is limited by the diameter of the grinding wheel.

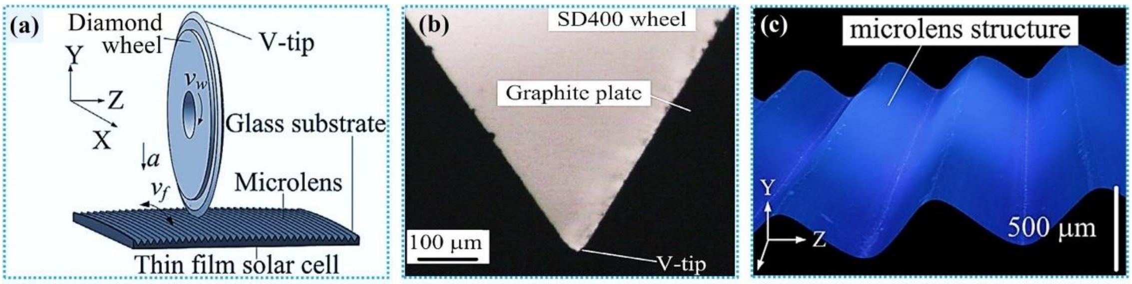

Figure 4-6: Left: A mico-grinding wheel with a diamond V-tip , Centre: the V-tip of the grinding wheel, Right: A microlens structure for solar PV applications. Images taken from "Jin Xie, Keke Wu, Jian Cheng, Ping Li, Jiahua Zheng, The micro-optic photovoltaic behavior of solar cell along with microlens curved glass substrate, Energy Conversion and Management, 2015[22]

The limitations of micro-machining are the low material removal rate, wear on the machining tools, and spatial resolution in the micron length scale. To go to a smaller length scale would require smaller tools and more precise actuators but this would further reduce the cutting rate. As a technique for patterning glass for solar PV applications it would be totally impractical for the aforementioned reasons, however it is a useful technique due to its flexibility for creating small prototype surfaces. It can also be used to create more complex geometries such as the fish-scale pattern discussed in chapter 3 which would be hard to form using some of the other techniques.

4.7 Abrasive jet Machining

Abrasive jet machining (AJM) involves bombarding the glass surface with high-velocity jets of abrasive material. [23] This method is limited by the nozzle diameter which must be relatively wide in order to achieve high velocity jets so the spatial resolution of this techniques is of the order of 10s to 100s of microns. The spatial resolution can be improved however with the use of lithography to create a sacrificial mask so that the downward etch rate is slower in some areas than others.

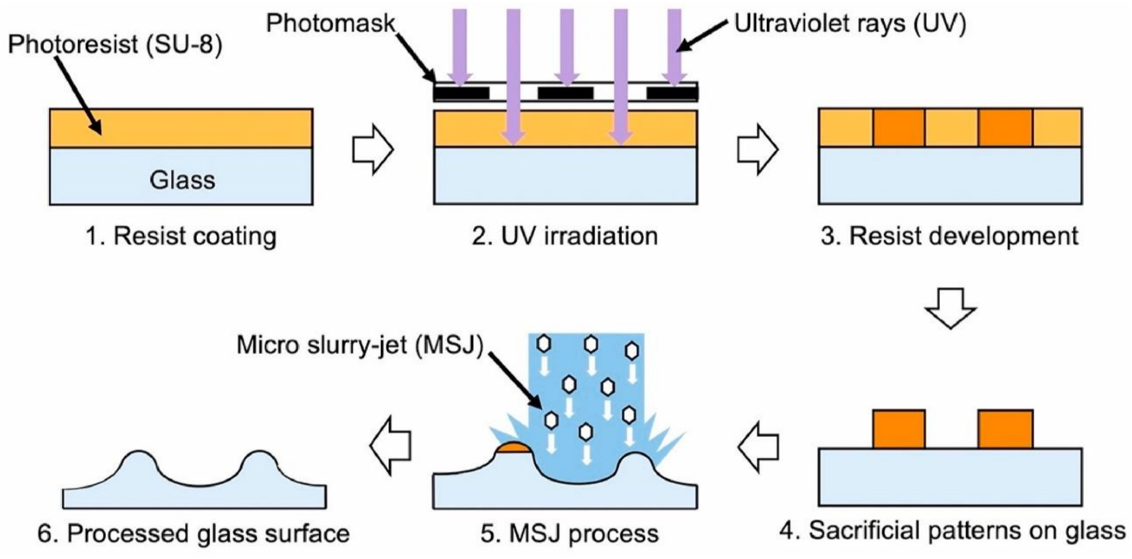

Figure 4-7: Abrasive jet machining. The figure above shows the lithography method to create a photoresist mask (with high resistance to the micro slurry jet).[8]

As can be seen in the above diagram the resist is eventually eroded leading to a loss of spatial resolution. The viability of the technique therefore relies on a resist mask that can survive the micro slurry jet for as long as possible. While not a scalable technique for solar PV applications it could have been used to create the pitted glass structures in this project.

4.8 LASER ABLATION

Laser patterning is a fabrication technique that employs laser ablation to generate permanent patterns by selectively heating and removing material from a substrate. Compared to conventional patterning methods, it offers several key advantages, including high precision, fast processing speed, superior pattern quality, and greater flexibility. Furthermore, unlike electrochemical or mechanical patterning, laser patterning operates as a non-contact process, preventing mechanical stress on the workpiece and minimizing the risk of surface contamination. These attributes make it a highly efficient and versatile method for microfabrication and surface structuring across various material systems.[24]

Due to the high transmission of light through glass in the visible range it is necessary to use an IR or UV laser so that the majority of the energy is transferred to the glass surface in order to achieve ablation. In order to generate sufficient power pulsed lasers are used which have an average power in the 10s or 100s of Watts but peak powers of the order of mega Watts or higher for the duration of nanoseconds, picoseconds or femtoseconds.[25] Femtosecond lasers offer the best precision due to their ability to induce non-linear multiphoton absorption, which confines energy deposition to the focal volume.[26] This unique property allows for both direct and indirect laser-based microfabrication (LBM) of glass, surpassing conventional diffraction limits. In direct LBM processes, such as ultrafast laser direct writing (ULDW), the morphology of the ablated features is highly dependent on pulse energy. By adjusting the pulse energy during ULDW, a wide range of micro- and nanoscale optical structures can be fabricated.

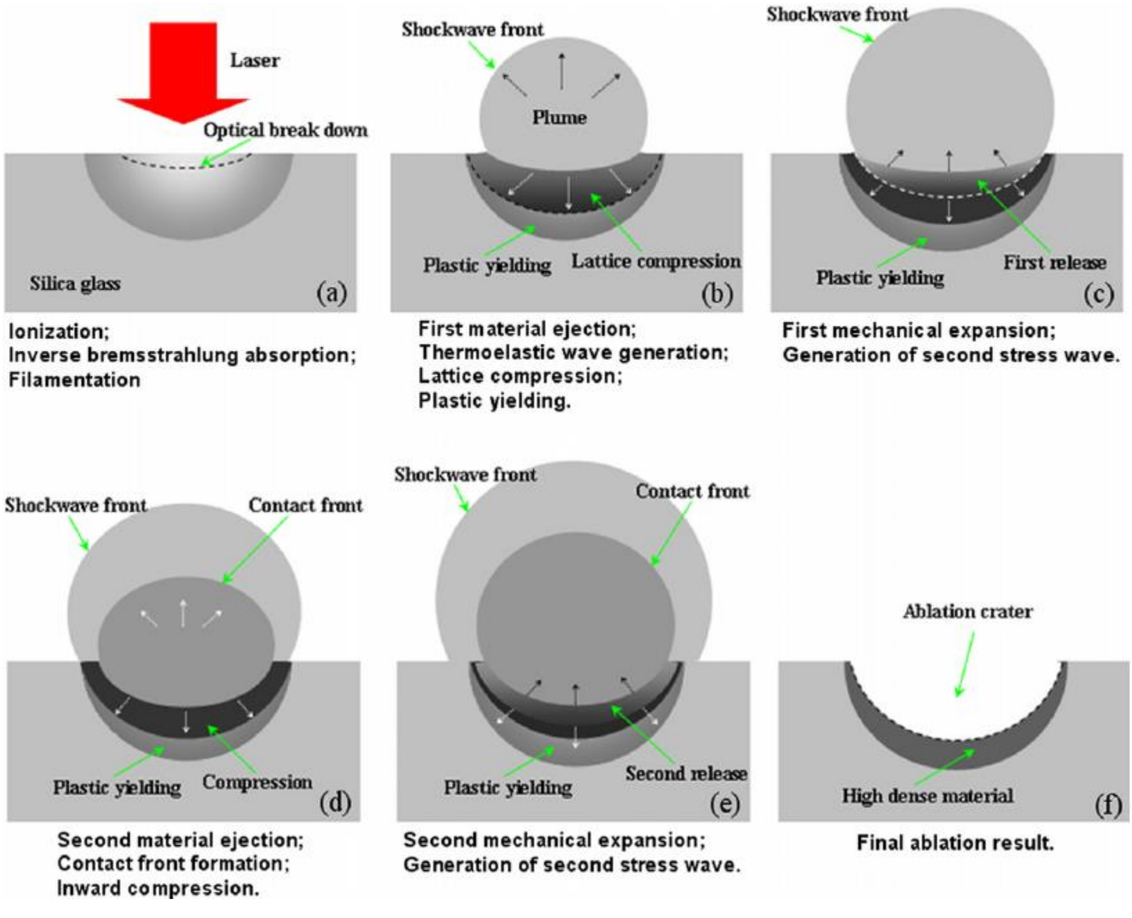

Figure 4-8: Laser ablation. Image taken from Hu, Haofeng & Wang, Xiaolei & Zhai, Hongchen. (2011). High-fluence femtosecond laser ablation of silica glass: Effects of laser-induced pressure. Journal of Physics, Applied Physics, 2011[27]

The ultrafast nature of the pulsed laser minimizes heat diffusion into the surrounding material, thereby reducing thermal damage and preserving the integrity of adjacent regions. The ability to tailor laser parameters—such as pulse duration, wavelength, fluence, and repetition rate—allows for the precise control of ablation depth and feature resolution.[28] This unique property allows for both direct and indirect laser-based microfabrication (LBM) of glass, surpassing conventional diffraction limits. In direct LBM processes, such as ultrafast laser direct writing (ULDW),[29] the morphology of the ablated features is highly dependent on pulse energy. By adjusting the pulse energy during ULDW, a wide range of microscale and nanoscale optical structures can be fabricated.

There are also some disadvantages to patterning with lasers. Firstly, the patterning rate can be quite low (although much faster than physical machining), one way of mitigating this is to use multiple laser write heads in parallel, this would be expensive to setup but would benefit from economies of scale. Secondly the glass can crack due to thermal shock particularly when the repetition rate is too high, this can also be mitigated by heating the glass substrate, so it doesn’t experience such massive temperature fluctuations.

The power requirements can also be high and there is an inherent inefficiency of some of the laser power penetrating deeper into the glass which heats the glass without causing ablation, one way to concentrate the laser power on the glass surface is to coat it in a highly absorbent dye or coating such that the dye absorbs all of the laser energy and this energy is transferred to the glass beneath. Subaquatic ablation of glass involves having water in contact with glass and passing laser light through the glass side. The laser wavelength is chosen to have high transmission through glass and high absorption in water, thus the water at the glass water interface is ablated causing cavitation bubbles which etch into the glass as thy implode.[28]

The first attempt to pattern glass in the first year of the project was with a KrF Coherent COMPexPro201F eximer laser with a wavelength of 248 nm, repetition rate of 10 Hz and a maximum pulse energy of 700 mJ. There were several problems which led to this method being abandoned. Firstly the KrF gas and thus the pulse power degraded at a rapid rate as can seen in the figure below, Secondly the quartz optics used did not focus the light sufficiently to generate enough fluence for ablation, this could have been mitigated with the use of a high absorption dye but without good focusing, the feature sizes that were desired could not be made with the equipment that was available. In conclusion laser ablation is a powerful technique which was more viable than the techniques mentioned previously.

Refill 1	Time	Pulse Energy (mJ)
Date: 03/09/2021	14:39	642
Settings: 10 Hz 27kV	14:41	601
Gas 3413 mbar	14:42	585
	14:46	567
	14:47	561
	14:50	552
	14:52 14:59	546 525
	15:35	500
	15:40	495
	15:54	480

Figure 4-9: Excimer laser. Left: The degradation rate of the eximer laser power over time, this made the setup impractical for consistent and reliable material removal, Right: An image of the eximer laser setup.

4.9 PRECISION GLASS MOULDING

Compression moulding is a formative process where a glass preform is heated before compressing it between two moulds. During this process, the softened glass undergoes thermo-viscoelastic deformation, conforming to the mould shape. The formed component is then subjected to controlled annealing and cooling, ensuring structural integrity and minimizing residual stresses.[30]

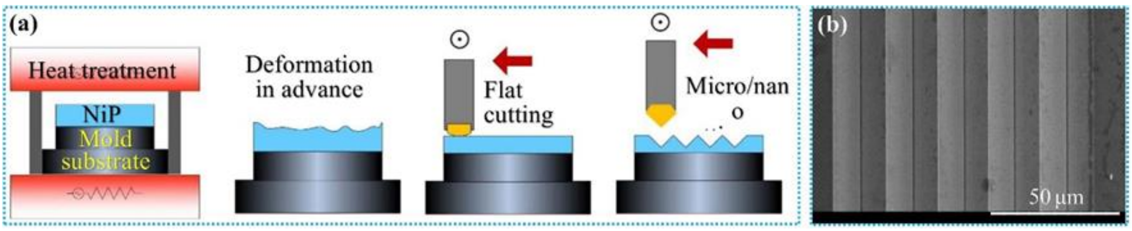

Figure 4-10: Moulding Left: The formation of a NiP mould, this can also be done by magnetron sputtering on a hard substrate patterned by lithography.8 Right: SEM image of microgrooved crystalline NiP plating after 500 moulding cycles.[31]

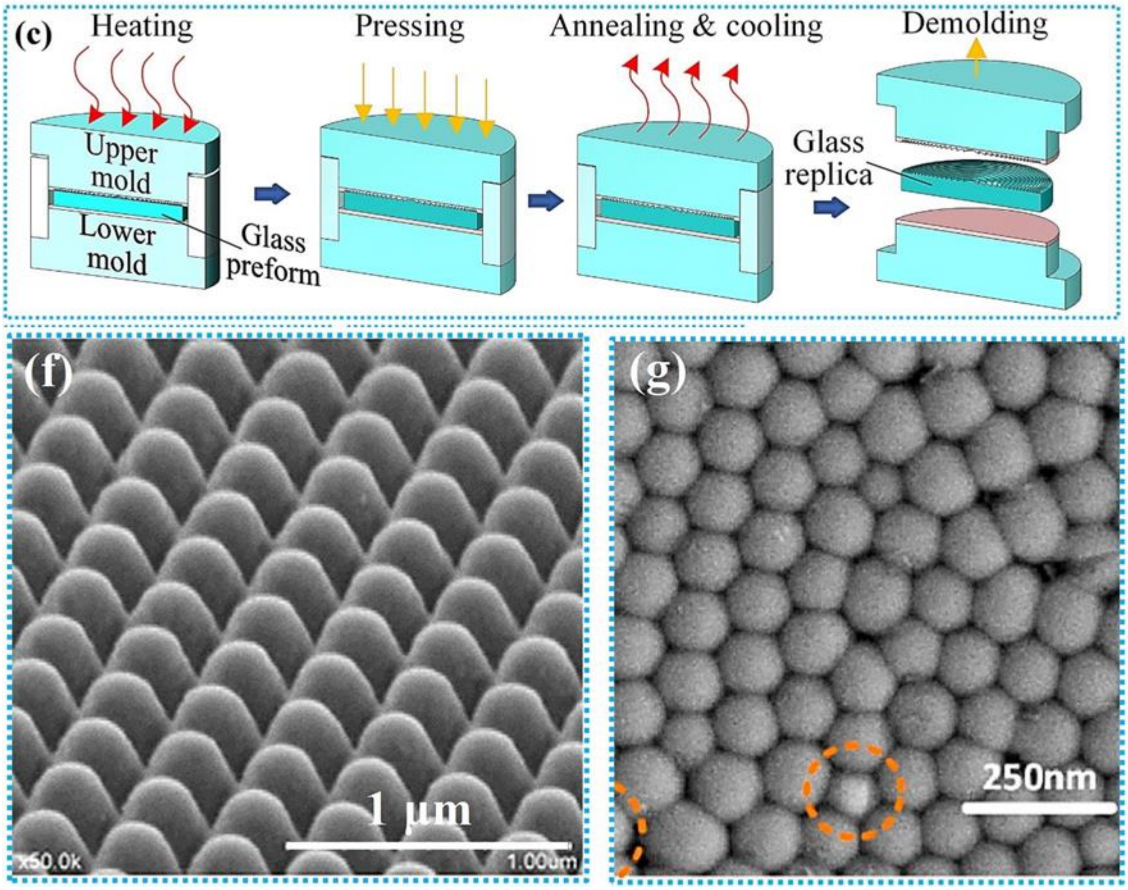

Figure 4-11: Moulding sub-micron features. Top: The precision glass moulding process.[8] *Bottom Left: SEM image of a molded glass surface featuring antireflective (AR) convex nanocones.*[32] *Bottom Centre: Molded moth eye-like glass AR nanostructures with diameters of ~100 nm.*[33]

Perhaps the most complex aspect of this technique in the manufacture of the mould itself. There is a huge range of techniques available as one is not working with glass but a hard, often metallic material that does not suffer the same issues of brittleness or optical transparency that limit glass patterning. Nonmechanical processing methods, such as reactive ion etching (RIE) and focused ion beam (FIB) milling, have gained significant attention for mould micro-fabrication and nano-fabrication due to their non-contact nature. These techniques enable precise structuring of mould surfaces, facilitating the direct imprinting of high-resolution glass nanostructures. For instance, electron beam lithography combined with reactive ion etching has been used to fabricate silicon carbide (SiC) moulds with nanoscale periodic features[32], which allow for the direct formation of antireflective glass nano-cone arrays. Focused ion beam lithography has been used to create moulds with features between 100nm and 500nm, through partial-filling hot embossing (PFHE), glass nanostructures with ultrasmooth surfaces can be formed within these mould cavities[34]. Additionally, nanoporous anodic aluminium oxide (AAO) moulds have been employed in partial filling hot embossing processes to transfer AR nano-protrusions onto glass surfaces[35], this is promising as it allows for randomised patterns.

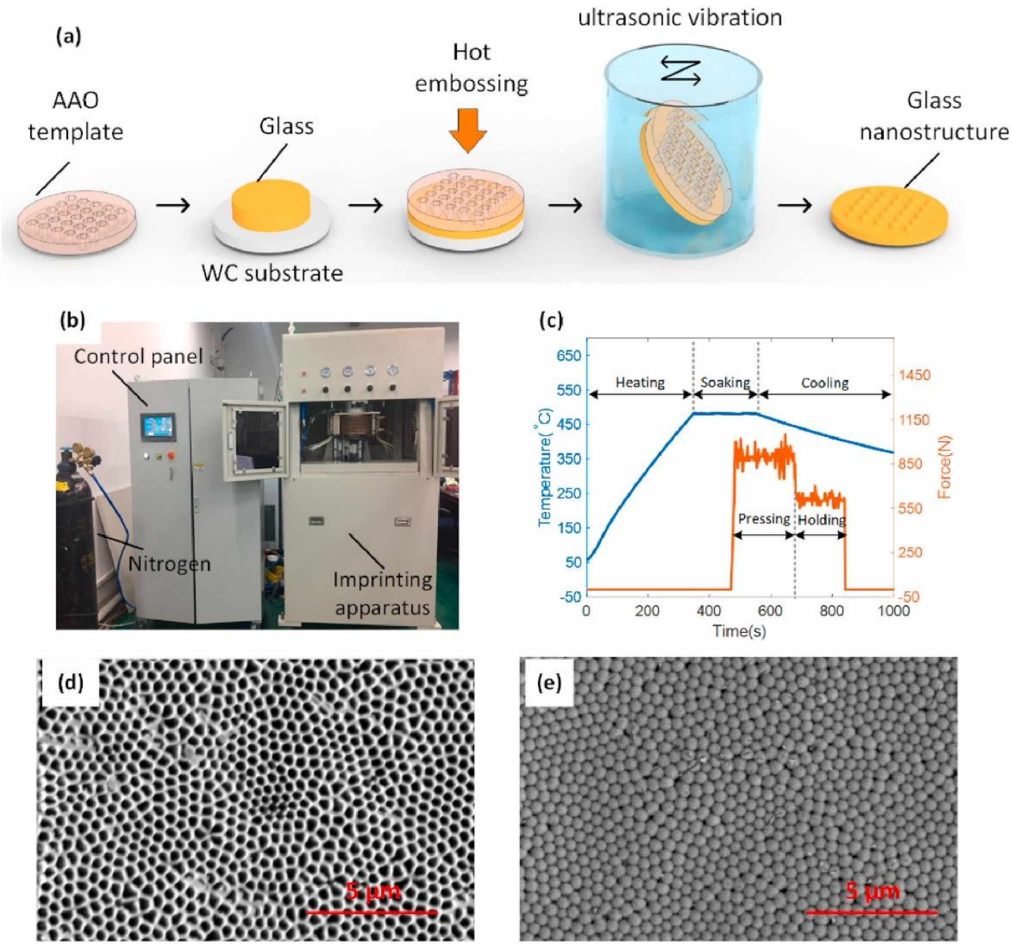

Figure 4-12: Nano-moulding. Image taken from "Xiaohua Liu, Kangsen Li, Jun Shen, Feng Gong, Hot embossing of moth eye-like nanostructure array on transparent glass with enhanced antireflection for solar cells, Ceramics International, 2021[36]

For microscale optical components, the design of the mould cavity, particularly in structures with sharp angles, imposes limitations on the rheological behaviour of glass, often leading to incomplete filling. This incomplete material flow results in shape deviations and optical defects within the final glass component.[37] Additionally, conventional heating methods, including thermocouples, infrared radiation, and thermal currents, rely on heat conduction, convection, and radiation to heat both the mould and the glass preform. However, these traditional approaches suffer from several drawbacks, such as low heating efficiency, non-uniform temperature distribution, significant thermal gradients, and reduced optical quality in the moulded glass.[38]

To address these challenges, researchers have explored alternative techniques, such as ultrasonic vibration and high-frequency microwave heating, for glass moulding processes. Ultrasonic-assisted molding has been shown to enhance the microscale flowability of glass, significantly improving mold-filling efficiency while also contributing to superior surface quality in the demolded glass structures. The observed improvements can be attributed to ultrasonic-induced effects, including localized heating, interfacial modifications, and enhanced thermo-mechanical interactions, which collectively facilitate the release of complex nanostructured glass components. By optimizing heat distribution and reducing thermal gradients, these approaches contribute to more uniform glass flow, minimizing defects and enabling the fabrication of high-precision optical structures.[39]

In conclusion glass moulding is by far the most effective and scalable process investigated so far for creating textured hierarchical anti-reflection coatings. There are, as usual, some challenges that have prevented widescale adoption in the PV industry. The high temperatures required to soften the glass increases the energy cost of producing solar modules. The process also only works on non-tempered glass as reheating tempered glass relaxes the surface and bulk stresses, it may be possible to do post tempering after the glass has be patterned rather than before. Creating large mould dyes for solar module sized plates of glass would have a high initial cost but provided the mould has a high durability this wouldn’t be a problem.

This manufacturing process was considered, and there was access to a roll-to-roll nano-imprint lithography tool but this is only suitable for patterning soft materials and cannot heat glass to the required temperatures for it to be easily workable. A roll-to-roll precision glass moulding system would be ideal although throughput would be greatly slowed by the need for the glass to anneal and cool before the mould is removed.

4.10 WEAK ACID LEACHING

Standard soda-lime glass contains about 74% silica and the remaining being glass modifiers and formers as well as impurites such as iron oxide. Iron ions act as light scattering sites and thus glass with a high iron content has poor transmission. Network modifiers such as soda and lime are not bonded strongly to the silicon oxygen network and instead exist in ionic form. It is thus possible to leach out the calcium and sodium ions from the glass. Hydronium ions that exist in large concentrations in an acid solution can replace the glass modifers. Hydronium ion much smaller than alkali metals so the molar volume of the leached glass is reduced. Tensile stress builds to a critical point until the glass surface starts to crack. The etching rate is much faster at the cracks and thus a random surface roughness in formed with 1 micron feature sizes.

Silica	SiO_2	73.6%
Soda	Na_2O	16.0
Lime	CaO	5.2
Potash	K_2O	0.6
Magnesia	MgO	3.6
Alumina	Al_2O_3	1.0
Iron Oxide	Fe_2O_3	--
Boric Oxide	B_2O_3	--
Lead Oxide	PbO	--

Figure 4-13 Glass composition. This shows the typical chemical composition of soda lime glass. This form of glass is the most common in the world and is used as architectural for buildings as well as solar PV panels.[40]

This leaching process takes 6 hours under at 95^{o} C with a citric acid concentration of 30% Wt/Vol. By altering the temperature and citric acid concentration the surface properties can be modified. As can be seen in the diagram below the surface pattern depends on the leaching depth which is a function of time, temperature acid concentration and the concentration of sodium and calcium ions in the glass.[40]

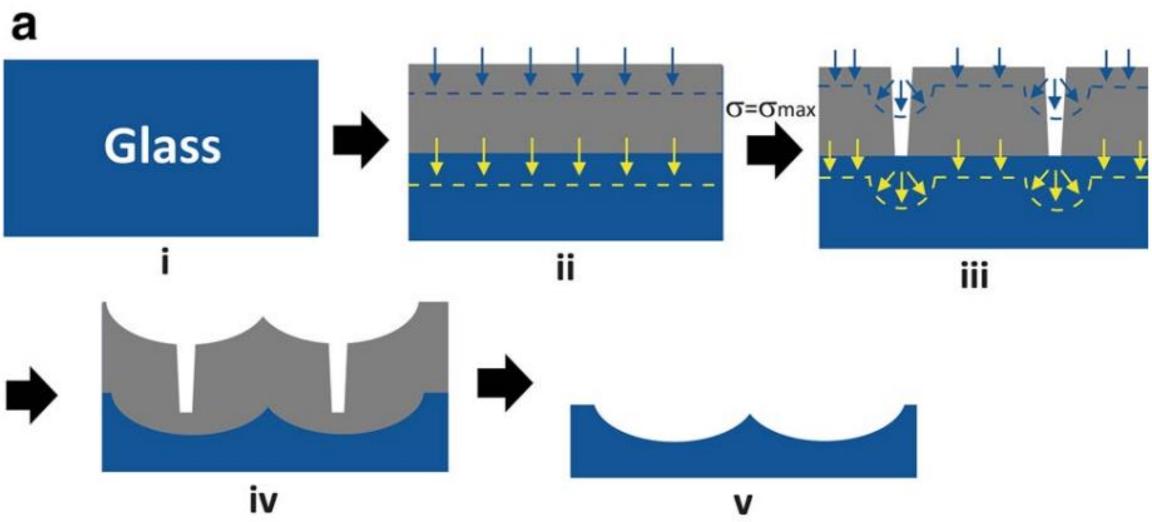

Figure 4-14: Glass leeching. The grey area represents the glass that has been leached of sodium ions. The final pattern at stage v is on the scale of microns.

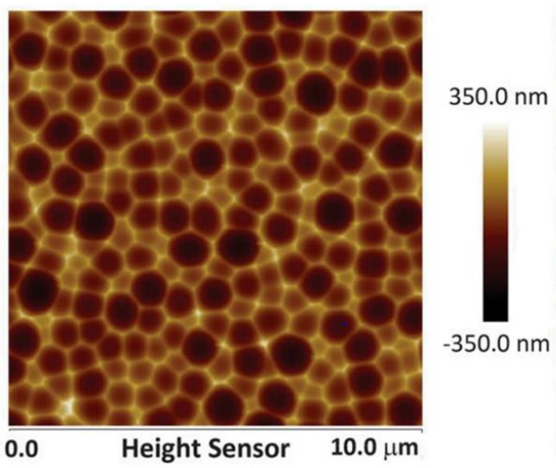

Figure 4-15: Leeched glass feature sizes. An atomic force microscopy image of the micro-textured surface demonstrating that the feature size is of the order of 1 micron.

This technique was attempted prior to doing HF wet etching primarily due to citric acid being much safer to work with and less environmentally toxic than hydrofluoric acid. In the end it was decided to move onto HF wet etching as it gave greater control of feature sizes and allowed one to replicate the ray tracing models unlike the weak acid etching method which was more random (average feature size depends on acid concentration, the amount of sodium and calcium in the glass and the temperature of the acid solution). Another issue with this method is that it requires tempered glass so that the reduction on density on the surface will cause the microcracks. This prevented the use of microscope glass slides as the substrate.

4.11 Acid Wet Etching

Wet etching of glass can be categorized into three main approaches: conventional wet etching, laser-assisted wet etching, and electrochemical wet etching. While conventional wet etching typically requires a contact mask to define the etched regions, both laser-assisted and electrochemical methods can operate without masks. Each technique offers unique advantages and is suited for specific applications in glass microfabrication.

Conventional wet etching relies on chemical reactions between the etchant and the glass substrate to achieve material removal. This method has long been recognized as an effective technique for microstructuring glass surfaces. A common example of wet etching is the use of hydrofluoric acid (HF)-based solutions, which selectively break the bridging oxygen bonds in the glass network, facilitating controlled dissolution. To further enhance etch rate and improve surface quality, buffering acids such as hydrochloric acid (HCl), nitric acid (HNO_3), and sulfuric acid (H_2SO_4) are often introduced into the HF solution. These additives help regulate the chemical environment, reducing surface roughness and improving the uniformity of the etched features.

1st etching reaction system	**2nd etching reaction system**
• $SiO_2 + 4HF \rightarrow SiF_4 + 2H_2O$	$H_2SiF_6 + SiF_4 + H_2SO_4 \rightarrow 2SiF_4 + \mathbf{2HF} + H_2SO_4$
• $SiO_2 + 6HF \rightarrow \mathbf{H_2SiF_6} + 2H_2O$	$\mathbf{2KF} + H_2SO_4 \rightarrow 2K_2SO_4 + \mathbf{2HF}$
• $Na_2O + 2HF \rightarrow \mathbf{2NaF} + H_2O$	$\mathbf{2NaF} + H_2SO_4 \rightarrow Na_2SO_4 + \mathbf{2HF}$
• $K_2O + 2HF \rightarrow \mathbf{2KF} + H_2O$	$\mathbf{CaF_2} + H_2SO_4 \rightarrow CaSO_4 + \mathbf{2HF}$
• $Ba_2O_3 + 6HF \rightarrow \mathbf{2BaF_3} + 3H_2O$	$\mathbf{2BaF_3} + 3H_2SO_4 \rightarrow Ba_2(SO_4)_3 + \mathbf{6HF}$
• $ZnO + 2HF \rightarrow \mathbf{ZnF_2} + H_2O$	$\mathbf{2ZnF_2} + 2H_2SO_4 \rightarrow 2ZnSO_4 + \mathbf{4HF}$
• $CaO + 2HF \rightarrow \mathbf{CaF_2} + H_2O$	

Figure 4-16: Wet etch chemistry. The reactions involved in HF wet etching of glass. Image from Park et al, A Review of Wet Chemical Etching of Glasses in Hydrofluoric Acid based Solution for Thin Film Silicon Solar Cell Application, Current Photovoltaic Research, 2017[41]

In hydrofluoric acid (HF) solutions, certain oxides, including CaO, MgO, and Al_2O_3, react to form insoluble compounds that can accumulate on the etched surface. These deposited byproducts act as masking layers, leading to increased surface roughness and a gradual reduction in the etching rate over time. As a result, extensive wet etching is more effective for glass compositions with low concentrations of these oxides, minimizing the formation of insoluble residues that could hinder the process.

Among the various transparent glass substrates, fused silica stands out as a particularly advantageous material for wet etching applications. While borosilicate glass already offers desirable properties such as optical transparency and chemical resistance, fused silica further enhances these characteristics with superior thermal stability and exceptional chemical purity. Composed entirely of silicon dioxide (SiO_2), it exhibits minimal contamination from secondary oxides, making it highly suitable for precision microfabrication and applications requiring high-purity glass structures.[42]

Due to its combination of chemical inertness, resistance to thermal fluctuations, and compatibility with wet etching processes, fused silica has become a preferred material for advanced optical, microfluidic, and semiconductor applications. Its ability to maintain structural integrity while allowing for precise etching makes it an ideal choice for fabricating intricate microstructures with high fidelity and minimal surface defects.

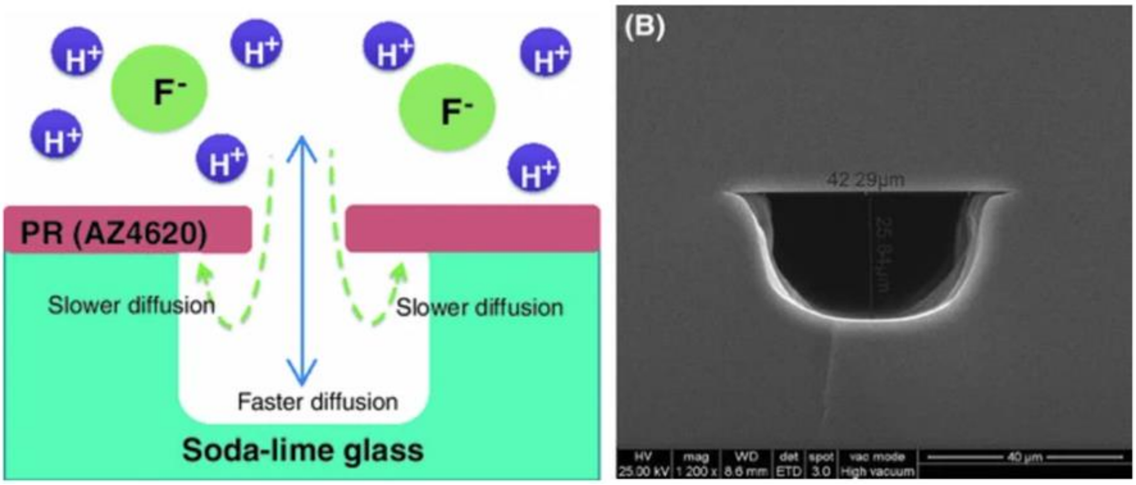

Figure 4-17: Wet etched pits Left: A schematic of HF wet etching with a slightly preferential downward etch rate. Right: A SEM image of a microfluidics channel made with HF wet etching. From "Che-Hsin Lin · Kuan-Wei Chen · Tang-Yu Li, Rapid soda-lime glass etching process for producing microfluidic channels with higher aspect ratio, Microsystems Technologies, 2014"[43]

By carefully optimizing the composition of the etching solution and process parameters, conventional wet etching can produce well-defined microstructures with smooth surfaces. However, challenges such as etch selectivity, isotropic material removal, and the need for precise mask alignment remain key considerations. To address these limitations, alternative wet etching techniques, including laser-assisted and electrochemical methods, have been developed to enhance patterning precision and broaden the range of achievable glass microstructures.[44]

Laser-assisted wet etching (LAWE) is an advanced mask-free etching technique that leverages laser irradiation to induce localized material modifications, enabling selective removal in a subsequent wet etching step. This approach allows for precise patterning of glass without the need for traditional masking techniques, making it a highly flexible and efficient fabrication method. By altering the material properties in targeted regions, LAWE facilitates the creation of complex microstructures that would otherwise be challenging to achieve through conventional etching processes.[45]

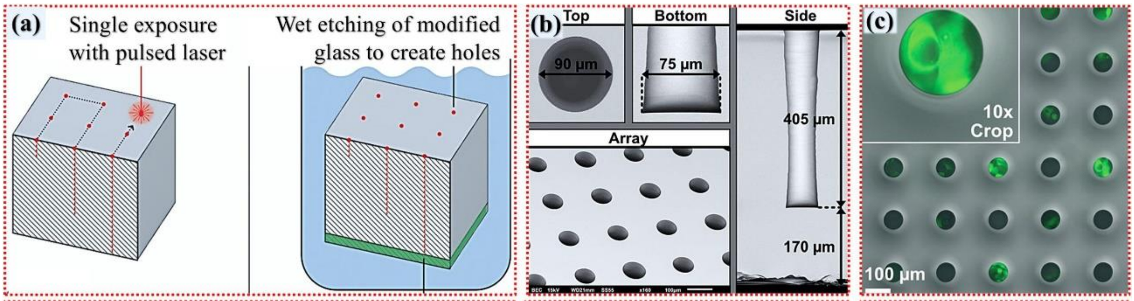

Figure 4-18: Laser assisted wet etch. Schematic illustration of high-throughput fabrication of glass microwell arrays using laser-assisted deep wet etching, (b) the fabricated hourglass F-well array in a double layer chip, and (c) fluorescence imaging of live cells in the F-well array. Wilfred Blanc et al, "The past, present and future of photonic glasses: A review in homage to the United Nations International Year of glass 2022, Progress in Material Science, 2023"[46]

In general, wet chemical etching has the advantage over many of the other techniques as the entire glass plate for a solar module can be patterned simultaneously by immersing the masked plate in buffered hydrofluoric acid. Etching time is about one hour which reduces the potential throughput for mass production. The masking process can be upscaled from laser write lithography on photoresist to soft lithography which uses a die to quickly imprint the pattern on a resist mask. The largest drawback is that of environmental impact and safety due to the acute toxicity of hydrofluoric acid. [47]

4.12 DRY CHEMICAL ETCHING

Dry etching is a material removal process conducted in a plasma or gaseous environment, utilizing energetic species such as plasma ions or photons to achieve selective etching of a substrate. For glass micromachining, common dry etching methods include plasma-based and laser-induced techniques.

Plasma-based dry etching encompasses several distinct methods, including plasma etching (PE), ion beam etching (IBE), and reactive ion etching (RIE).[48] PE relies on chemical reactions between reactive species and the glass surface, offering high etch selectivity. However, its practical application in deep etching is constrained by poor anisotropy and a relatively low etch rate. In contrast, IBE is a purely physical process that achieves excellent anisotropy through ion bombardment, though it can lead to undesirable redeposition and radiation-induced damage. RIE, which integrates both chemical etching and physical sputtering, provides a balance between anisotropy, selectivity, and processing speed, making it a widely used technique for fabricating glass micro- and nanostructures.[49]

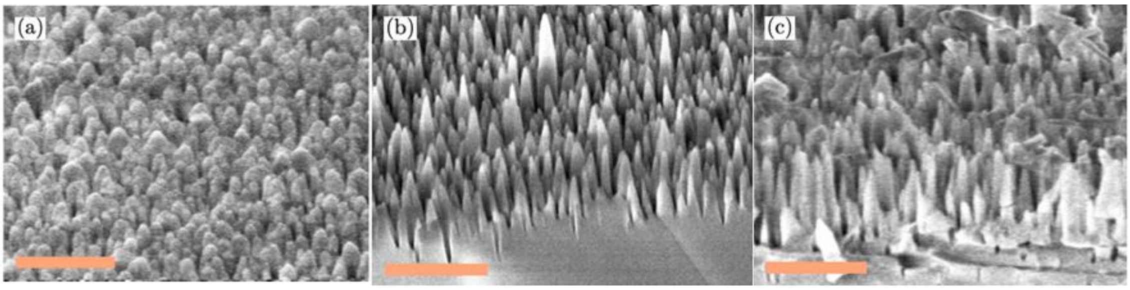

Figure 4-19: Nanopillars. Angled SEM images of substrates etched on a single side with nominal pillar heights of (a) 170nm, (b) 270nm and (c) 400nm. Scale bars are 500nm. Images from "Brian D Jennings et al, Large-area patterning for broadband, quasi-omnidirectional low-reflectance glass, Journal of Micromechanics and Microengineering, 2022"[50]

The relative advantages and disadvantages of dry etching versus wet chemical etching can be seen in the table below from the whitepaper "Plasma Etching: Comparing PE, RIE and ICP-RIE, Plasma Therm"[44]

Table 4

CHARCTERISTC	PERFORMANCE	
	Wet Etching	Plasma Etching
Profile Control	Poor (limited to crystallographic cases)	Good
CD Control	Difficult (especially sub-micron)	Excellent
Aspect Ratio	Poor	Superior (may be >100:1 for some materials)
Mask Film adhesion	Very critical	Not typically issue
Damage (radiation/ physical)	None	Presents challenges
Cleanlieness	Good to very good	Very good
Selectivity	Very good	Challenges
Uniformity	Fair	Good
Flexibility (range of materials)	Excellent	Good
Cost of chemicals	High	Moderate
Equipment cost	Relatively inexpensive	Relatively expensive
Environmental Impact	High (disposal costs)	Low
Production automation	Challenging	Easy
Throughput	High with batch	Good
Process understanding	Good	Challenges
Operating parameters	Few (concentration, temperature)	Many
Control of etching rate	Difficult	Good

Reactive ion etching was used to create the nanoscale glass patterns on top of the microscale pitted structure that was generated by wet HF etching. One difficulty was the lack of etch rate control. The etch rate drops as the plasma mills more deeply into the glass substrate as the kinetic energy of the incident ions is counteracted by the backflow of reaction products, once the backflow pressure reaches a threshold level the etching terminates. [51]

4.13 Conclusions

Several glass texturing techniques were investigated and evaluated for their suitability for solar PV applications. While useful of producing complex patterns as prototypes, methods such as grinding, cutting and milling have a very low throughput and cannot be done in parallel and thus the technique cannot be scaled up for the solar PV industry.

Abrasive jet machining is more scalable but the geometries that are produced are dependant on the survival of the mask, it is therefore difficult to produce features with curved edges reliably unless mask thickness can be varied across the surface.

Laser ablation was attempted for this project but it laser beam focus and consistency in the pulse power where problems which made this technique infeasible. The method could be scaled up by having an array of laser beams raster scan the solar module glass surface. Challenges would include the high cost of the lasers as well as high energy costs. Ablation can be achieved on glass with the help of highly absorbing dyes on the glass surface such that the laser pulse energy is concentrated on the glass surface rather than dissipated over a larger volume of glass.

Heat assisted compression moulding can achieve submicron resolution when the mould is vibrated such that the viscous heated glass can fill all the voids left by the mould. The throughput of this method is limited by the need for the glass to cool before removal of the mould. One potential efficiency would be to mould the glass during the tempering process as the glass is already heated to the working temperature of glass (600 to 700 C) so the glass could be moulded just before it is annealed. For this project compression moulding was not used as it did not provide flexibility in the size and shape of the microscale features.

Weak acid leaching is a promising technique which does not require a mask or the use of dangerous and environmentally harmful chemicals such as hydrofluoric acid. There were two main downsides, however. Firstly the etched pits cannot be precisely controlled as the centre of these pit nucleate from semi randomly occurring cracks in the leeched glass. This problem leads to unavoidable overetching of the pits and a loss of aspect ratio and thus light trapping qualities. The second issue is the technique only works on tempered glass meaning the samples could not be cut after being patterned. Hydrofluoric acid wet etching was useful for producing the pitted glass structures produced in the COMSOL ray tracing models however the use of a laser write head that took one hour to pattern a few square cm of the resist mask as well as etch times of one hour makes this technique non scalable.

4.14 REFERENCES

(1) Tachibana, T.; Shirasawa, K.; Tanahashi, K. Development of Lightweight and Flexible Crystalline Silicon Solar Cell Modules with PET Film Cover for High Reliability in High Temperature and Humidity Conditions. *Sol. Energy Mater. Sol. Cells* **2023**

(2) *Polymers VS Glass. A five-year comparison.* https://www.solbian.eu/en/blog/polymers-vs-glass-a-five-years-comparison-n255

(3) *Solar*. IEA. https://www.iea.org/energy-system/renewables/solar-pv

(4) Bhore, C. V.; Andhare, A. B.; Padole, P. M.; Loyte, A.; Sofia Vincent, J.; Devarajan, Y.; Vellaiyan, S. Experimental Investigation on Minimizing Degradation of Solar Energy Generation for Photovoltaic Module by Modified Damping Systems. *Sol. Energy* **2023**

(5) Vasylius, M.; Tadžijevas, A.; Šapalas, D.; Kartašovas, V.; Janutėnienė, J.; Mažeika, P. Degradation of Mechanical Properties of A-PET Films after UV Aging. *Polymers* **2023**

(6) *Refractive Index of Polymers by Index – scipoly.com*. https://scipoly.com/technical-library/refractive-index-of-polymers-by-index/

(7) Singh, A.; Umakanth, V.; Tyagi, N.; Kumar, S. A Comparative Study of Different Polymer Materials for the Development of Flexible Crystalline Silicon Modules. *Sol. Energy Mater. Sol. Cells* **2023**

(8) Luo, H.; Zhang, Y.; Yu, J.; Dong, X.; Zhou, T. Additive, Subtractive and Formative Manufacturing of Glass-Based Functional Micro/Nanostructures: A Comprehensive Review. *Mater. Des.* **2023**

(9) Datsiou, K. C.; Overend, M. The Strength of Aged Glass. *Glass Struct. Eng.* **2017**

(10) *Chemically Strengthen Glass - Overview - Vs Thermal Temper Glass*. http://www.xinology.com/Glass-Mirrors-Products/chemical-strengthen/overview/vs-thermal-temper-glass.html

(11) Kim, S. W.; Im, H.-T.; Lee, J. E.; Kim, H. S.; Kim, J. H.; Hwang, J. Physical Properties of Chemically Strengthened Thin Glass Prepared by the Spray Method Using an Original KNO3–Al2O3 Slurry. *Mater. Chem. Phys.* **2021**

(12) *What is Corning Gorilla Glass and How is It Made? | Corning Gorilla Glass*. https://www.corning.com/gorillaglass/worldwide/en/a-look-behind-corning-gorilla-glass.html

(13) Abramov, A. A.; Black, M. L.; Scott Glaesemann, G. Laser Separation of Chemically Strengthened Glass. *Phys. Procedia* **2010**

(14) Bifano, T. G.; Dow, T. A.; Scattergood, R. O. Ductile-Regime Grinding: A New Technology for Machining Brittle Materials. *J. Eng. Ind.* **1991**

(15) Erdogan, F. Fracture Mechanics. *Int. J. Solids Struct.* **2000**

(16) Griffith, A. A. The Phenomena of Rupture and Flow in Solids. *Philos. Trans. R. Soc. Lond. Ser. A* **1921**

(17) Irwin, G. R. Analysis of Stresses and Strains Near the End of a Crack Traversing a Plate. *J. Appl. Mech.* **2021**

(18) Egashira, K.; Mizutani, K.; Nagao, T. Ultrasonic Vibration Drilling of Microholes in Glass. *CIRP Ann.* **2002**

(19) Egashira, K.; Mizutani, K.; Nagao, T. Ultrasonic Vibration Drilling of Microholes in Glass. *CIRP Ann.* **2002**

(20) Kim, T.; Kwon, K.-K.; Chu, C. N.; Song, K. Y. Experimental Investigation on CO2 Laser-Assisted Micro-Slot Milling Characteristics of Borosilicate Glass. *Precis. Eng.* **2020**

(21) Ashwani Pratap, Karali Patra & Aleksandr A. Dyakonov, A Comprehensive Review of Micro-Grinding: Emphasis on Toolings, Performance Analysis, Modeling Techniques, and Future Research Directions, The International Journal of Advanced Manufacturing Technology, 2019
(22) Xie, J.; Wu, K.; Cheng, J.; Li, P.; Zheng, J. The Micro-Optic Photovoltaic Behavior of Solar Cell along with Microlens Curved Glass Substrate. *Energy Convers. Manag.* **2015**
(23) Nakanishi, Y.; Nakashima, Y.; van der Heide, E. Microstructuring Glass Surfaces Using a Combined Masking and Microslurry-Jet Machining Process. *Precis. Eng.* **2021**
(24) Jiang, W.; Xie, X. Z.; Wei, X.; Hu, W.; Ren, Q. L.; Zou, Z. S. High Contrast Patterning on Glass Substrates by 1064 Nm Pulsed Laser Irradiation. *Opt. Mater. Express* **2017**
(25) Ting HE, Zhen CAO, ChaoYang WEI, JianDa SHAO, *High precision laser ablation of fused silica using pulsed CO2 laser, SCIENTIA SINICA Physica, Mechanica & Astronomica, 2019*
(26) Grehn, M.; Seuthe, T.; Höfner, M.; Griga, N.; Theiss, C.; Mermillod-Blondin, A.; Eberstein, M.; Eichler, H.; Bonse, J. Femtosecond-Laser Induced Ablation of Silicate Glasses and the Intrinsic Dissociation Energy. *Opt. Mater. Express* **2014**
(27) Glumac, N.; Elliott, G. The Effect of Ambient Pressure on Laser-Induced Plasmas in Air. *Opt. Lasers Eng.* **2007**
(28) Gómez-Varela, A. I.; Sanchez, R.; Carnero, B.; Diaz-Gomez, L.; Flores-Arias, M. T.; Bao-Varela, C. Subaquatic Indirect Laser Ablation Technique for Glass Processing. *Opt. Express* **2022**
(29) Tan, D.; Zhang, B.; Qiu, J. Ultrafast Laser Direct Writing in Glass: Thermal Accumulation Engineering and Applications. *Laser Photonics Rev.* **2021**
(30) Ming, W.; Chen, Z.; Du, J.; Zhang, Z.; Zhang, G.; He, W.; Ma, J.; Shen, F. A Comprehensive Review of Theory and Technology of Glass Molding Process. *Int. J. Adv. Manuf. Technol.* **2020**
Q.; Zhao, B.; Zhao, W.; Liu, P.; Wang, X. A Review of the Techniques for the Mold Manufacturing of Micro/Nanostructures for Precision Glass Molding. *Int. J. Extreme Manuf.* **2021**
(32) Yamada, K.; Umetani, M.; Tamura, T.; Tanaka, Y.; Kasa, H.; Nishii, J. Antireflective Structure Imprinted on the Surface of Optical Glass by SiC Mold. *Appl. Surf. Sci.* **2009**
(33) Liu, X.; Li, K.; Shen, J.; Gong, F. Hot Embossing of Moth Eye-like Nanostructure Array on Transparent Glass with Enhanced Antireflection for Solar Cells. *Ceram. Int.* **2021**
(34) *Deformation Behavior of Glass Nanostructures in Hot Embossing | ACS Applied Materials & Interfaces*
(35) Feng, Y.; Liu, X.; Li, K.; Gong, F.; Shen, J.; Lou, Y. Glass Flow Evolution and the Mechanism of Antireflective Nanoprotrusion Arrays in Nanoholes by Direct Thermal Imprinting. *ACS Appl. Mater. Interfaces* **2021**
(36) Liu, X.; Li, K.; Shen, J.; Gong, F. Hot Embossing of Moth Eye-like Nanostructure Array on Transparent Glass with Enhanced Antireflection for Solar Cells. *Ceram. Int.* **2021**
(37) Jianwu Yu, Hong Luo, Thai Vinh Nguyen, Yuetuo Lu, Liang Huang, Yingying Zhang, Mechanism Study on Microformability of Optical Glass in Ultrasonic-assisted Molding Process, Journal of Applied Glass Science, 2018

(38) McGRAW, D. A. Transfer of Heat in Glass During Forming. *J. Am. Ceram. Soc.* **1961**
(39) Yan Chen, Xu Feng, Gongming Xin, Experimental Study on Ultrasonic Vibration-Assisted WECDM of Glass Microstructures with a High Aspect Ratio, Micromachines, 2021
(40) Jin, Y.; Li, A.; Stewart, R. J.; Hancock, R. R.; Baker, D. E.; Yongsunthon, R.; Hughes, K. K.; Weidman, D. L. A Template-Free, More Environmentally Friendly Approach for Glass Micro-Texturing. *Sci. Rep.* **2022**
(41) Park, H.; Cho, J. H.; Jung, J. H.; Duy, P. P.; Le, A. H. T.; Yi, J. A Review of Wet Chemical Etching of Glasses in Hydrofluoric Acid Based Solution for Thin Film Silicon Solar Cell Application. *Curr. Photovolt. Res.* **2017**
(42) Iliescu, C.; Jing, J.; Tay, F. E. H.; Miao, J.; Sun, T. Characterization of Masking Layers for Deep Wet Etching of Glass in an Improved HF/HCl Solution. *Surf. Coat. Technol.* **2005**
(43) Lin, C.-H.; Chen, K.-W.; Li, T.-Y. Rapid Soda-Lime Glass Etching Process for Producing Microfluidic Channels with Higher Aspect Ratio. *Microsyst. Technol.* **2014**
(44) Shubhava; Jayarama, A.; Kannarpady, G. K.; Kale, S.; Prabhu, S.; Pinto, R. Chemical Etching of Glasses in Hydrofluoric Acid: A Brief Review. *Mater. Today Proc.* **2022**
(45) Bellouard, Y.; Said, A.; Dugan, M.; Bado, P. Fabrication of High-Aspect Ratio, Micro-Fluidic Channels and Tunnels Using Femtosecond Laser Pulses and Chemical Etching. *Opt. Express* **2004**
(46) Blanc, W.; Gyu Choi, Y.; Zhang, X.; Nalin, M.; Richardson, K. A.; Righini, G. C.; Ferrari, M.; Jha, A.; Massera, J.; Jiang, S.; Ballato, J.; Petit, L. The Past, Present and Future of Photonic Glasses: A Review in Homage to the United Nations International Year of Glass 2022. *Prog. Mater. Sci.* **2023**
(47) Schwerin, D. L.; Hatcher, J. D. Hydrofluoric Acid Burns. In *StatPearls*; StatPearls Publishing: Treasure Island (FL), 2025.
(48) Huff, M. Recent Advances in Reactive Ion Etching and Applications of High-Aspect-Ratio Microfabrication. *Micromachines* **2021**
(49) Weigel, C.; Brokmann, U.; Hofmann, M.; Behrens, A.; Rädlein, E.; Hoffmann, M.; Strehle, S.; Sinzinger, S. Perspectives of Reactive Ion Etching of Silicate Glasses for Optical Microsystems. *J. Opt. Microsyst.* **2021**
(50) Jennings, B. D.; Gatensby, R.; Giraud, E. C.; Selkirk, A.; Husain Mir, S.; Mokarian-Tabari, P. Large-Area Patterning for Broadband, Quasi-Omnidirectional Low-Reflectance Glass. *J. Micromechanics Microengineering* **2022**
(51) Tang, Y.-H.; Lin, Y.-H.; Chen, P.-L.; Shiao, M.-H.; Hsiao, C.-N. Comparison of Optimised Conditions for Inductively Coupled Plasma-Reactive Ion Etching of Quartz Substrates and Its Optical Applications. *Micro Nano Lett.* **2014**

5 MAKING HIERARCHICAL STRUCTURES

5.1 LITERATURE REVIEW CONCLUSIONS

All of the aforementioned manufacturing processes that were discussed in the previous chapter were considered before the hierarchical glass structures were patterned. Hydrofluoric acid wet etching for the microscale pits and ICP reactive ion etching for the nanoscale pillars was ultimately chosen. While precision glass moulding had been the prime candidate due to its relative simplicity and scalability, the necessary equipment was not available. Another issue had been the inflexibility of the process— a die would first have to be created, and creating a new die to vary the dimensions of the textured glass later would have required additional time and expense. Instead, an attempt was made to replicate the structures generated in the COMSOL models, with a focus on achieving the correct geometry; transferring that geometry to a more practical manufacturing process was left for future work.

A paper titled "Large-area patterning for broadband, quasi-omnidirectional low-reflectance glass" was published by Brian D. Jennings, Riley Gatensby, Elsa C. Giraud, Andrew Selkirk, Sajjad Husain Mir, and Parvaneh Mokarian-Tabari, all from Trinity College Dublin, on ICP etching of glass as an AR coating. This technique was availed of, with some modifications, for the nano-pillars. Assistance and advice were received from Riley Gatensby, who had experience in reactive ion etching. Chris Murray, who had extensive expertise in lithography techniques, was also extremely helpful in the fabrication of the pitted glass structures. Therefore, the decision was influenced by the equipment, knowledge, and experience that had been available within the research group.

5.2 EQUIPMENT

- **ICP Reactive Ion Etch:** Oxford Instruments PlasmaLab 180 ICP etch tool. The etchant supply was a mixture of CHF_3 and O_2. The pressure, gas composition, and source powers were varied in order to create an optimised etch recipe.
- **Glass Sample Dicer:** The Disco DAD 3220 wafer dicer is an automatic wafer dicing tool capable of processing up to 150mm wafers. It features automatic alignment for device extraction and has four definable cutting axes. It can process

Silicon, MgO and Sapphire wafers and is capable of defining chips below 1 mm2. The tool is mostly used for dicing large wafers to small chips for deposition, but also for final device extraction from a full wafer.

- **Laser Mask Writer:** This Heidelberg DWL66 maskless lithography system is a direct write tool used for both mask manufacture and direct substrate patterning.
- **Barrel Asher:** This Diener PICO Barrel Asher is a semi-automatic plasma barrel asher which is mainly used for surface pre-treatment and resist (organic) removal. O2 and CF4 are both connected to the tool to offer greater cleaning and surface preparation flexibility. There is a 40 KHz 200W power supply integrated in the system.
- **Acid Wet Bench:** There are three tanks in this bench. These are used for HF, BOE and hot phosphoric acid processing. These can process samples up to 100 mm in diameter. There are two cascade rinse tanks for HF processing, and a QDR tank for use with the hot phos process.

Figure 5-1: The acid wet bench used for HF etching of glass

- **Scanning Electron Microscope:** The Zeiss ULTRA Plus is a high resolution and analytical field emission Scanning Electron Microscope. Equipped with both InLens and SE2 detectors, users can obtain high resolution and topographical details of their samples, respectively. It also has an energy selective backscatter detector (EsB) for low kV compositional details of the samples.

5.3 Outline of Fabrication process

Below is a basic outline of the finalised fabrication process which will be discussed in more detail later, each of these steps was calibrated and optimised and after making over 50 batches (including calibration samples) before the hierarchical structures were successfully made.

- Low iron, un-tempered, soda lime glass, microscope slides where cleaned in sodium hydroxide solution and then rinsed in hot (80^{o} C) deionised water in an ultrasonic bath for 5 minutes. The slides were then ashed in an ozone asher for another 5 minutes.
- When a photoresist mask was used, the glass slides were coated in Hexamethyldisilane (HMDS), the details of this are discussed later. Otherwise, the glass slides were placed in a magnetron sputtering tool and coated with 40 nm of chromium.
- Photoresist was spun on to the glass slide (Micro Chem S1813 at 5 krpm) and then patterned with the Heidelberg laser write tool. The exposed photoresist was then removed with a resist developer, Propylene Glycol Monomethyl Ether Acetate (PGMEA).
- The resist was then baked for 75 seconds at 115^{o} C to increase its hardness and ashed again to remove resist scum at the bottom of the holes made by the laser write tool.
- If a chromium layer was added, then the chromium exposed by the holes in the resist mask was removed with chrome etchant (nitric acid or perchloric acid and ceric ammonium nitrate mixture)
- The glass slides where then wet etched in buffered HF solution (1:7 concentration with water, higher concentrations lead to dangerous fumes). The etch times were varied.
- The photoresist and chromium layers where then removed leaving the micro-pitted surface.
- The glass slide was diced down to a size that would be suitable for my optical measurements (14x14 mm squares around a 12x12 mm patterned surface giving a 1 mm wide flat glass margin around the pattern)

- The samples were once again cleaned and then brought back to the magnetron sputtering tool to be coated with a thin layer of silver (5-7 nm depending on the desired nanopillar size).
- The silver coated glass sample was then heated to 250^{o} C on a hot plate to dewet the silver to create a self-assembled metal mask. The dewetting can be visually confirmed by a colour change of silver/blue to brown/red.
- The glass was then placed in the ICP reactive ion etch tool to create the nanoscale pillars with CH_3F gas. The glass was then ashed to remove the Teflon like residue that coated the glass after the ICP etch.
- Finally the remaining silver mask was removed with chrome etchant leaving a hierarchically textured glass sample.

5.4 SAMPLE PREPARATION

Glass slides were initially cleaned in Helmanex (a high concentration NaOH solution) and then rinsed in hot deionised water in an ultrasonic bath. While this was effective at removing contamination from the glass surface it modified the surface chemistry as the strongly alkaline Helmanex introduced hydroxyl groups to the glass surface making the glass strongly hydrophilic (glass is already somewhat hydrophilic to begin with). This was an issue as it lowered the adhesion of the photoresist mask causing it to delaminate prematurely during wet etching. The reduced adhesion was the result of water molecules being trapped between the glass and the photoresist, for laminated glass the presence of water reduces the adhesion strength by 50 to 70%.[1,2] While a hydrophobic surface has less surface energy and thus poorer adhesion properties this is compensated by the absence of condensed water vapour on the glass surface. Figure 5-2 below show the effect of poor mask adhesion as the mask has prematurely lifted off in some areas leading to an uneven etch rate across the surface.

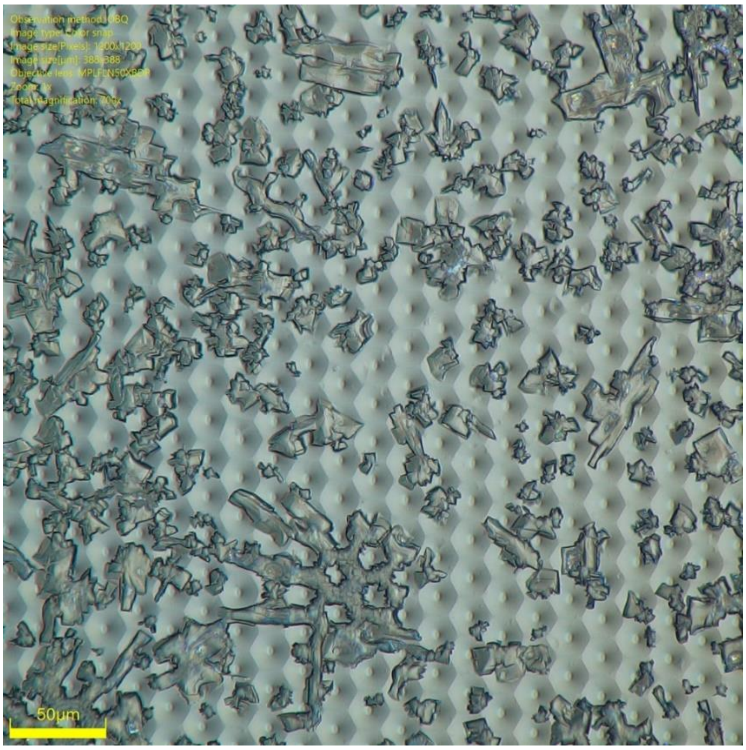

Figure 5-2: Optical microscope image of a pitted glass structure that has been over-etched, as can be seen the photoresist mask failed in different places at different times, it is important that the mask adhesion is strong enough so that it doesn't delaminate as the HF acid etches beneath it.

This issue was resolved by coating the glass surface with hexamethyldisilazane (HMDS) after the cleaning process. The silicon atom of HMDS binds to the oxygen atoms of the hydroxyl groups on the glass surface causing the elimination and release of ammonia gas. The polar hydroxyl outer layer of the surface is thus replaced with a non-polar layer of methyl groups as can be seen in the figure 5-3 below.

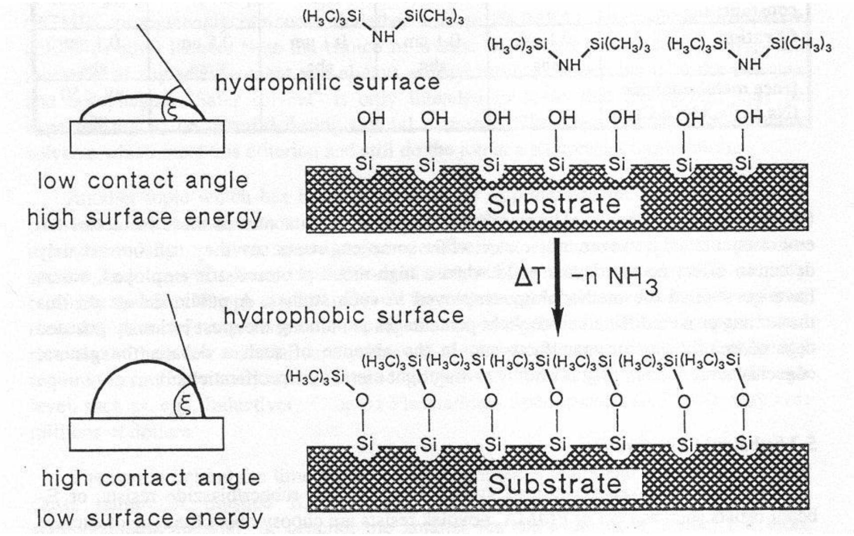

Figure 5-3: HMDS on glass. Image from Dammel et al[3]

The HMDS was applied by leaving the cleaned glass slides in a desiccator for at least 200 minutes with liquid HMDS present in the chamber. It is unnecessary to coat the surface with liquid HMDS as it only coats the surface with a single molecular layer. The degree of HMDS coating could be indirectly measured by the change in the water droplet contact angle.

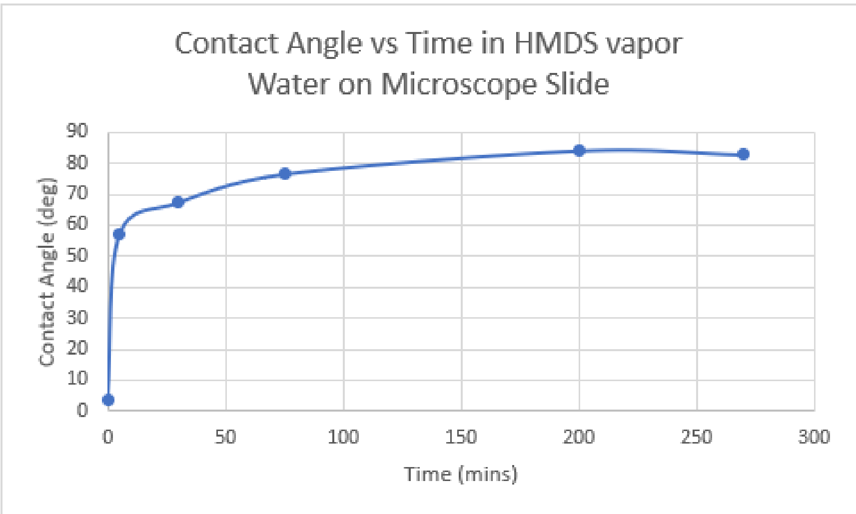

Figure 5-4: HMDS vapour completes coating the surface after 3 hours

Figure 5-5 below shows how the addition of HMDS increases the water contact angle while cleaning with Hellmanex (Hx, high concentration sodium hydroxide) reduced contact angle.

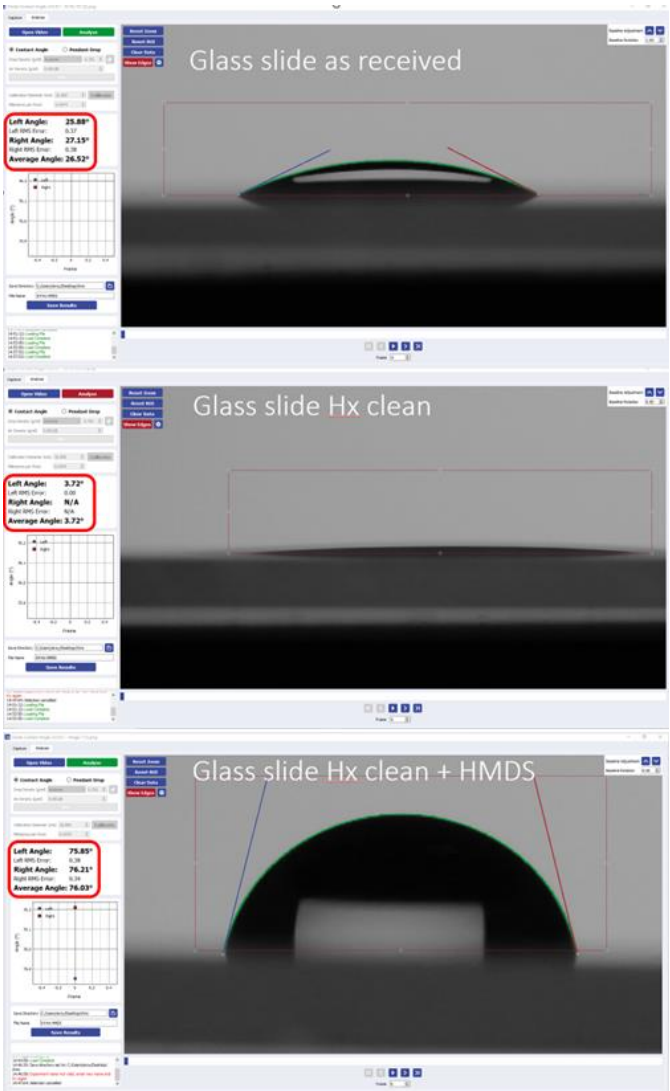

Top: Contact angle vs surface treatment. The ordinary hydrophilic nature of a glass slide before cleaning with hellmanex solution, Middle: Super-hydrophilic glass after hellmanex cleaning, Bottom: Glass is more hydrophobic

1. As received glass slides are generally hydrophilic (C.A. = 26°)
2. Hellmanex cleaning of glass increases hydrophilicity (C.A. = 4°). Bake out didn't improve adhesion.
3. Ozone treatment further increases hydrophilicity. (C.A. ≈ 4°)
4. HMDS vapour priming makes the glass hydrophobic. (C.A. = 76°)

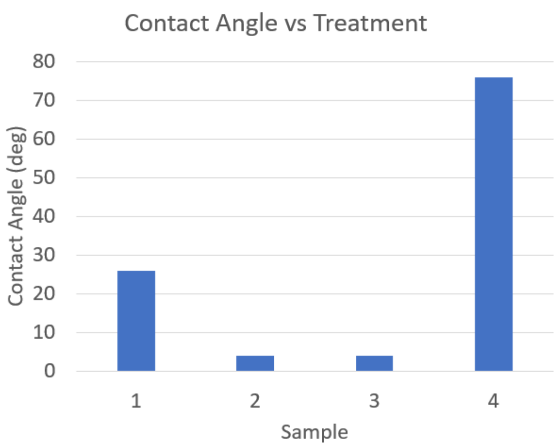

Figure 5-5: Contact angle data which corresponds to HMDS coverage

5.5 HEIDELBERG LASER POWER DOSE TEST

After cleaning the glass samples the next significant step was to spin on the photoresist (MicroChem S1813 at 5krpm). As the photoresist showed excellent resistance to the HF wet etching process it was spun on at a the highest spin rate to make a thin layer which could more easily be exposed by the Heidelberg laser write tool. Here another problem arose, the laser spot intensity follows a Gausian distribution so the centre of the patterned holes were fully exposed but the edges were only partially exposed. This was a major issue as small variations in the laser power or the thickness of the resist across the glass slide would lead to a large change in the hole size. The issue is more clearly demonstrated by the diagram below.

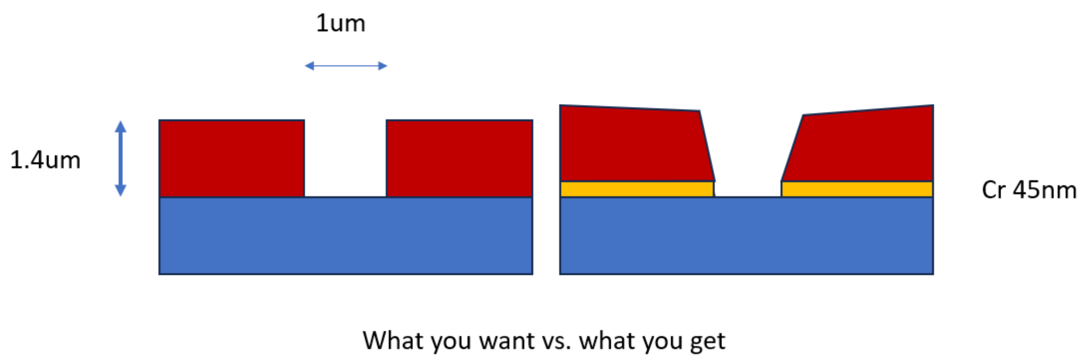

Figure 5-6: Mask dot size. Initially the holes in the resist mask were set to 1μm diameter but they became 2μm as a result of partial photoresist exposure at the edges of the laser spot. The yellow chrome layer is not relevant at this point.

The solution was to maximise the laser power as well as double expose each dot, this ensured that the entirety of the dot and its surroundings were fully exposed but this came at the cost of producing larger holes than were initially desired. The figure below shows the removal of the shadow at the hole edges which is a photoresist thickness gradient when the laser power is increased. To produce these images a thin chromium layer was first deposited on the glass such that the holes would expose the chromium which would provide high contrast allowing one to determine how much of the glass surface was exposed.

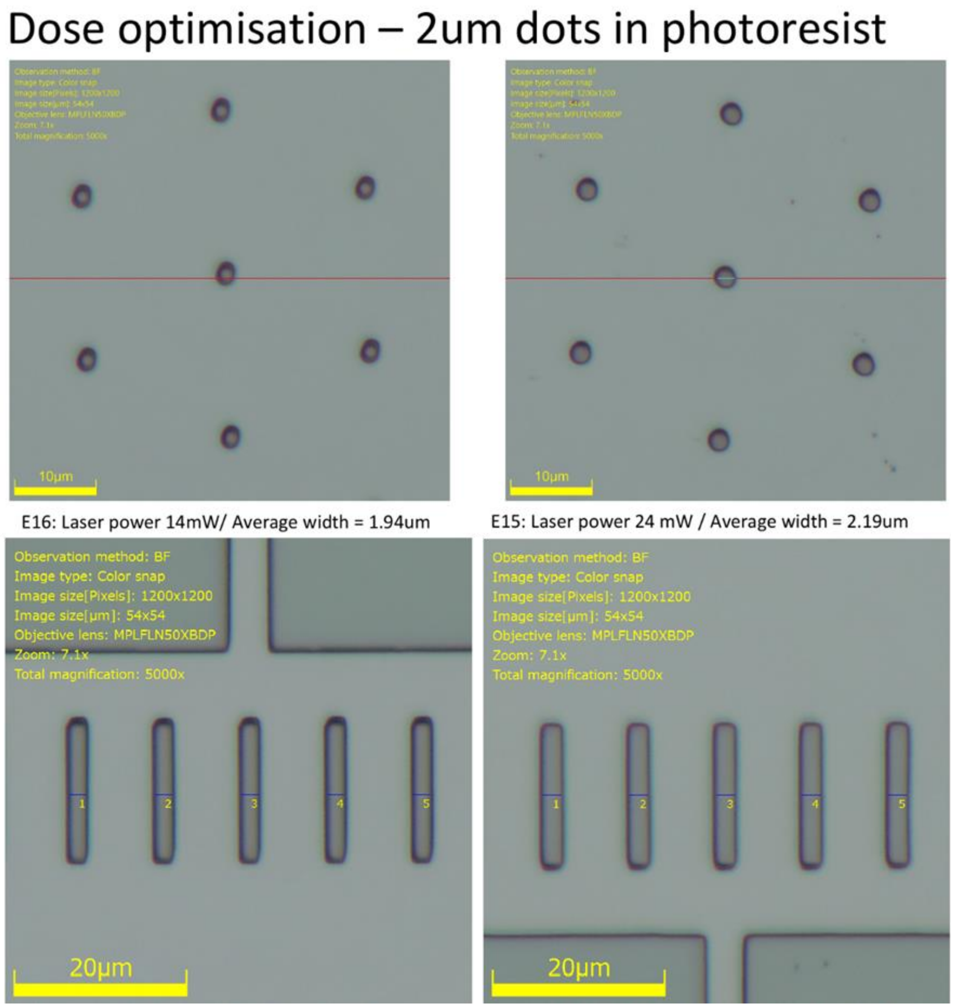

Figure 5-7: Mask dots microscope image. The hole size continued to increase with laser power but with a smaller variance in hole size as the average hole size increased.

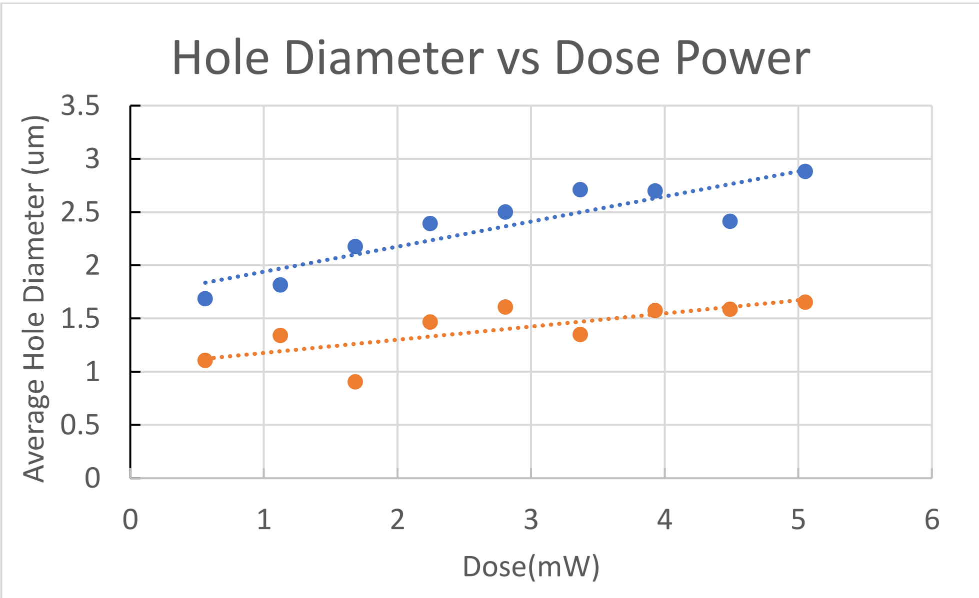

Figure 5-8: Hole diameter vs dose power. Blue data is for a target diameter of 2 um and orange for a target diameter of 1 um.

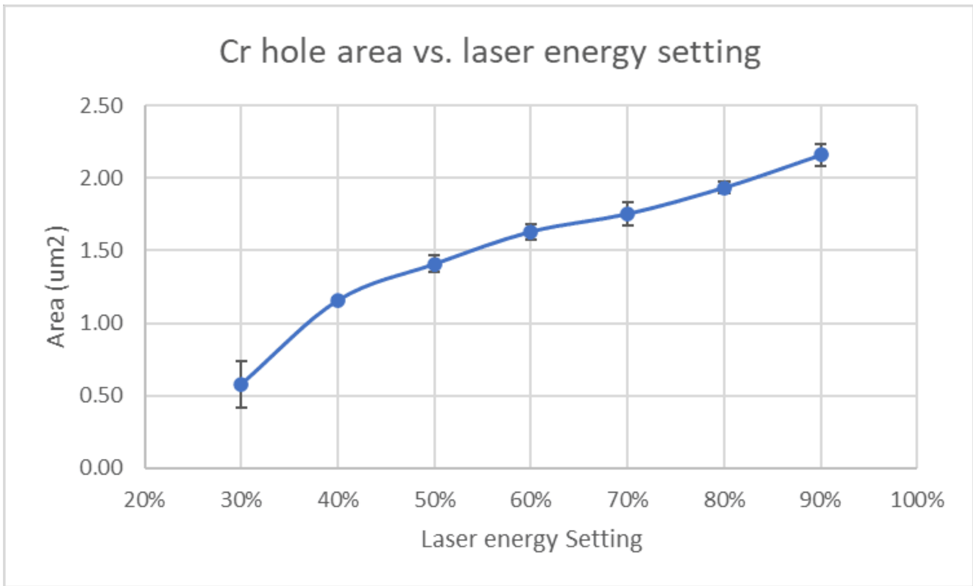

Figure 5-9 Chromium area test. The area of the chromium relates to the areas od exposed glass surface. Chromium is not removed for this test as it provides high contrast in microscope and SEM images. Laser is 5 mW at 100% power.

5.6 Mask Baking

Before wet etching the photoresist, the mask was baked for 75 seconds at 115^{o} C, these baking conditions were determined by trial and error, less intense baking resulted in a resist mask that sagged when it was under-etched while more intense baking caused the resist to become too brittle and it would shatter during wet etching. Baking could also be done prior to exposure to the Heidelberg laser writer.

5.7 Wet Etching

The wet etching process to create pitted glass is well known in literature. It was largely rejected as a technique to produce antireflective coatings as the glass pits had to be spaced widely apart reducing the packing density of micro features. The pits were spaced apart as the mask would delaminate as more and more of the original surface was etched away. Perfect packing density of an array of circles was also achieved by increasing mask adhesion and tuning the resist hardness by baking so it would stay in place with only 1% of the original surface remaining. Below is a diagram of the masking and wet etching process with a chromium mask.[4]

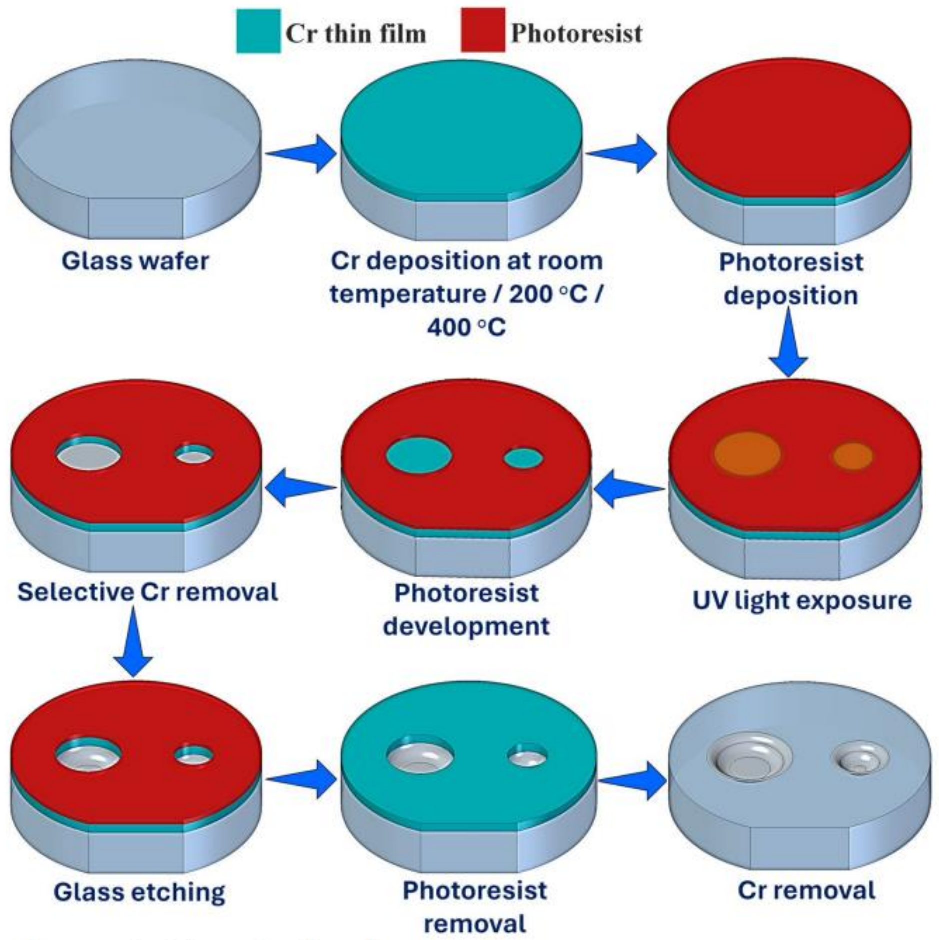

Figure 5-10:Lithography steps. Image from Vishal Sahu et al, A study on chromium thin film with positive photoresist as a masking layer towards the wet bulk micromachining of Borofloat glass, Micro and Nano Systems Letters, 2024[4]

The etch rate of soda lime glass in buffered HF solution was known from literature[5], but it was important to calculate the etch rate as the etch rate could be limited by mass transfer being throttled by the small hole diameter of the mask. There is also some variance when using soda lime glass as the sodium and calcium ions act as etch masks causing an overall slower etch rate as well as some roughness. It was found that there was significant increase in the etch rate when the hole diameter was increased from 2 microns to 5 microns. The etched pattern left a flat circle directly below the hole in the mask making the resulting etched pits imperfect hemispheres. For this reason, the hole size was changed to 5 microns and the spacing between the holes was doubled from 20 microns to 40 microns. This led to larger pits in the glass that were more consistent in size. Below are optical microscope images of the mask and an etched glass sample

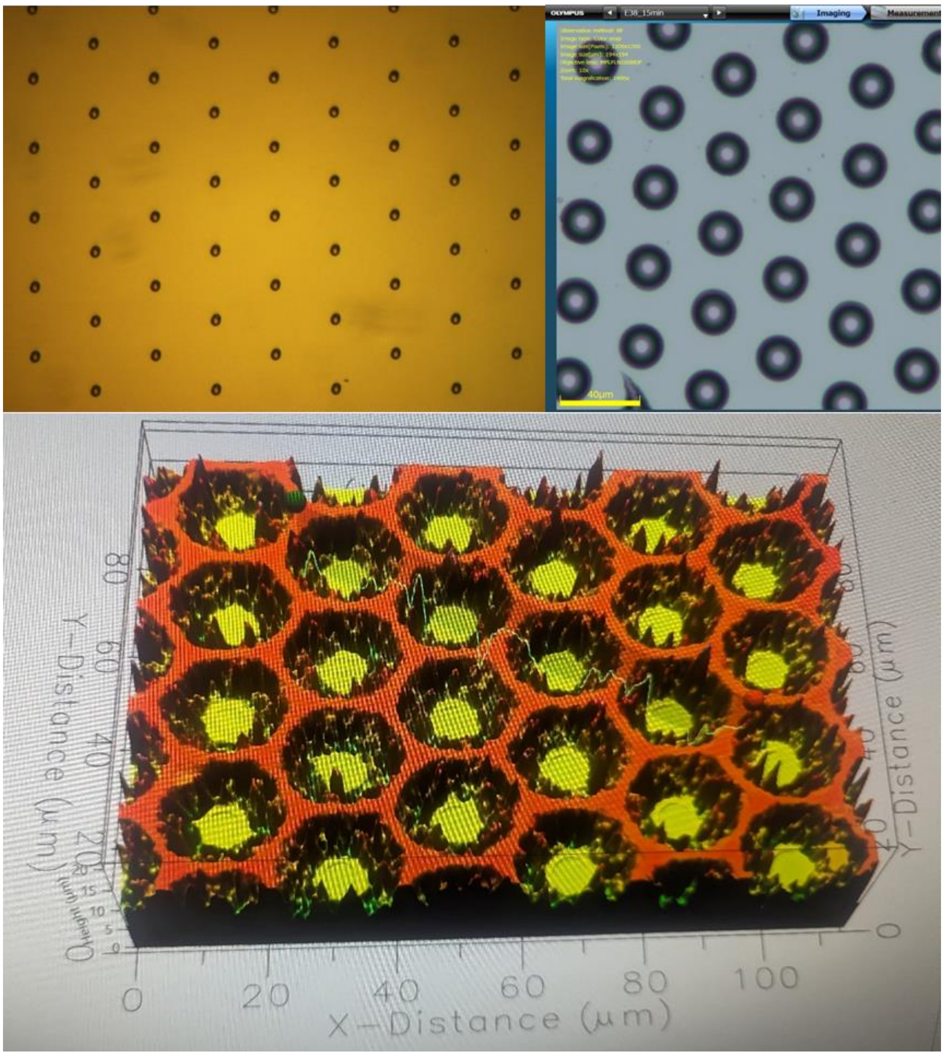

Figure 5-11: White light interferometry. Top Left: Microscope image of the photoresist mask with holes developed. Top Right: Microscope image of the pitted glass surface after wet etching (this sample is under-etched). Bottom: White light interferometry image which clearly shows the flat circles in the centre of each pit which corresponds to the hole in the mask.

5.8 Wet Etching Without Chromium Mask

Wet etching was first attempted without a chromium layer between the photoresist and the glass surface. With the addition of HMDS the photoresist did not lift off entirely until 99% of the original surface was etched away. As can be seen in the image below all that remains of the original glass surface is an array of small triangles, this corresponds to my COMSOL models of pitted glass with PoreSize = 1.12 (12% over-etched). This is near perfect packing of the microscale features, any further etching would simply flatten out the features which would reduce their aspect ratio and thus light trapping abilities.

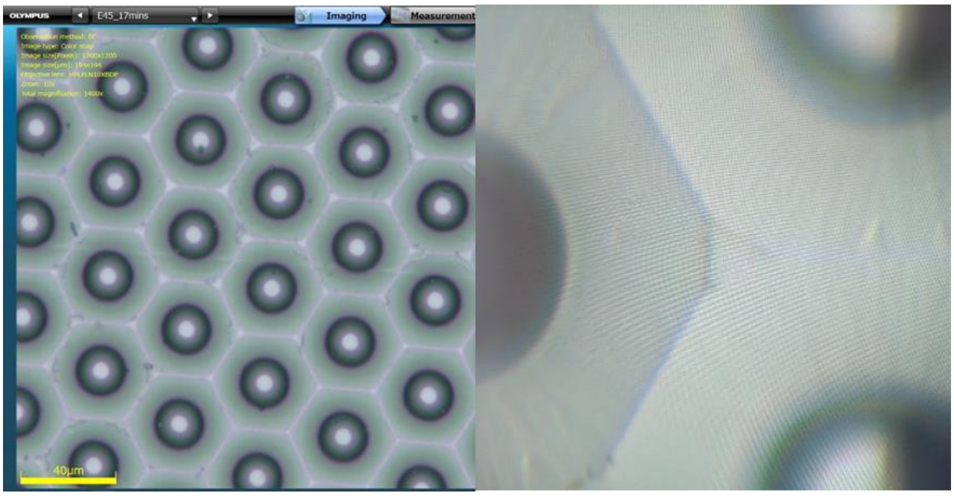

Figure 5-12: Mask delamination, caused by mask delamination. The small triangle is the original glass surface

There is still a problem, a deep circular bowl can be seen in the centre surrounded by another bowl with a shallower gradient, this can be called the pasta bowl shape. It is the result of two separate etch rates, The central bowl is formed by the ordinary etching of glass by HF while the shallow part is caused by the delamination of the resist as HF unzips it from the glass, I call this the delamination rate. This delamination rate was about 2 microns per minute but varied from batch to batch depending on small variations in the cleaning process and sample preparation, this was 4 times larger than the etch rate of buffered HF solution on soda lime glass. Thus, the features are not as deep as they could be as horizontal etching was faster than the vertical. Below is a pasta bowl for reference.

Figure 5-13: Bowl shaped pits. Left: A pasta bowl which has a remarkably similar geometry to the pitted glass structures. Right: Pitted glass with PoreSize=0.95 (slightly underetched)

How the pasta bowl shape can be described mathematically has been illustrated. The shape can be broken into the components of a cylinder (for the central flat disk), a torus (for the deep bowl in the centre) and a triangular torus (for the shallow bowl around the edge). While this shape showed good light trapping properties (discussed in the optical measurement chapter) it was decided to improve the mask adhesion further with the addition of a chromium mask.

t = etch time (s)

r_0 = radius of holes in mask (μm)

r_1 = acid etch rate (μ m/s)

r_2 = mask delamination rate (μm/s)

$d = r_1 t$ = etch depth (μm)

$V_c = \pi r_0^2 d$ = cylinder volume (μm³)

$V_d = \frac{1}{2}\pi(r_1 t)^2(2\pi r_0)$ = torus volume (μm³)

$V_t = \left(\frac{r_2 \times t \times d}{2}\right)\left(2\pi\left(r_0 + \frac{r_2 \times t \times d}{2}\right)\right)$ = trianglular cross section toroid volume (μm³)

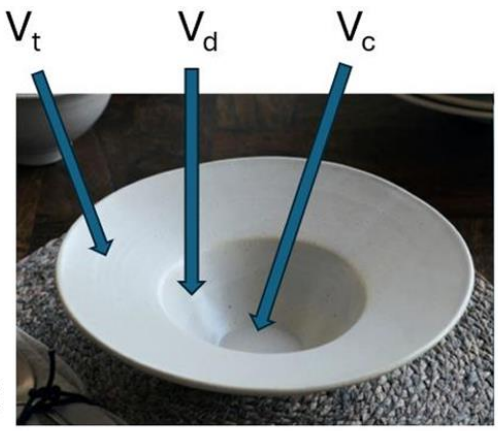

Figure 5-14: The Volume of a Bowl can be calculated by breaking it down into components.

5.9 WET ETCHING WITH A CHROMIUM MASK

The chromium mask/adhesion layer was added after the problem of photoresist delamination was identified. The ordinary fabrication procedure was followed except the addition of HMDS was replaced by the deposition of 40 nm of chromium in the magnetron sputtering tool. 5-micron diameter dots spaced 40 microns apart in a hexagonal were double exposed at maximum laser power with the Heidelberg laser writing tool. The photoresist was not stripped off prior to the wet etching process so that the polymer photoresist would lend additional structural strength to the chromium mask and prevent it from sagging as it was undercut. As can be seen in the figure below where there is no outer shallow gradient as mask delamination was eliminated.

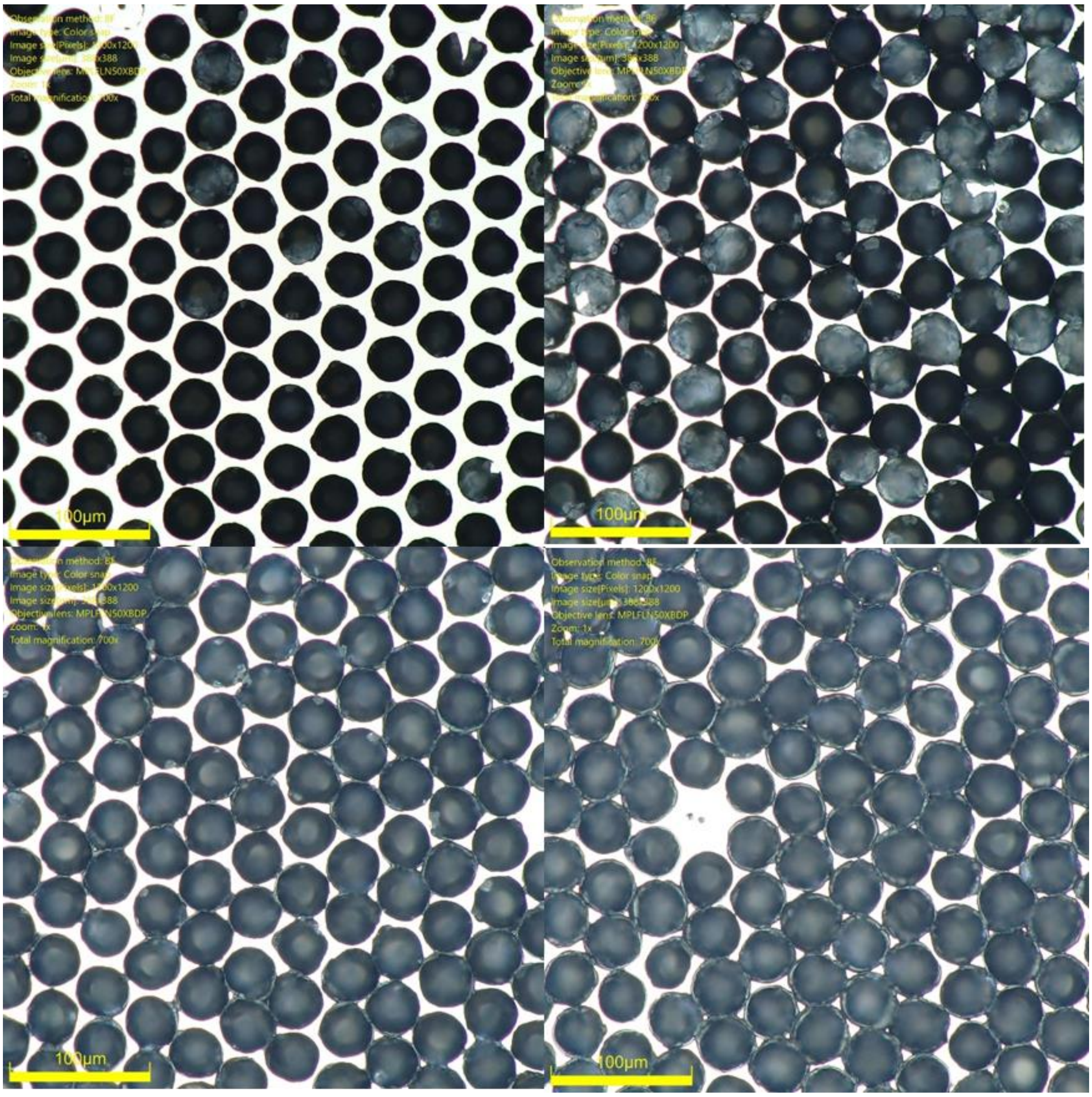

Figure 5-15: Etched pits with chromium. Top Left: 50 min etch, Top Right: 55 min etch. Bottom Left: 60 min etch. Bottom Right: 65 min etch. The chromium mask was not removed to improve contrast for these images.

Etching time was 4 times longer than the case without the chromium mask/adhesion layer. There is some variance in hole size in the above images that are a result of photoresist scum partially blocking some of the holes, this issue was later eliminated by ashing the samples prior to wet etching. Below are the 14x14mm wet etched samples in order of etch time in minutes. While almost opaque in appearance the transmission is just highly diffuse, thus the glass can be considered translucent, allowing light through while destroying the image. It is shown in the optical measurement chapter that transmission of these samples increased despite their similar appearance to low transmission sandblasted glass.

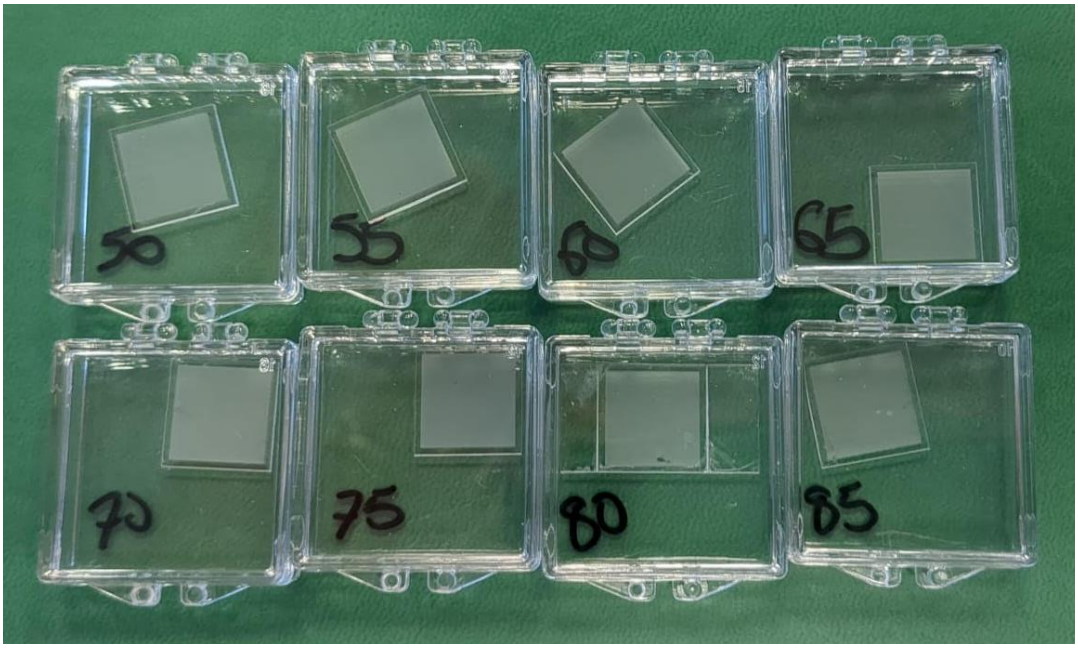

Figure 5-16: Different etch times for pitted glass.

The patterned surfaces are squares of 12x12 mm surrounded by a 1 mm thick un-patterned margin. This was the largest possible size when using glass microscope slides due to the spun-on photoresist thinning at the edges of the slide as can be seen here the samples were cut from the region of uniform thickness in the centre.

Figure 5-17: Spun on photoresist, the photoresist gets thinner near the edges.

5.10 UNDER-ETCHING AND OVER-ETCHING

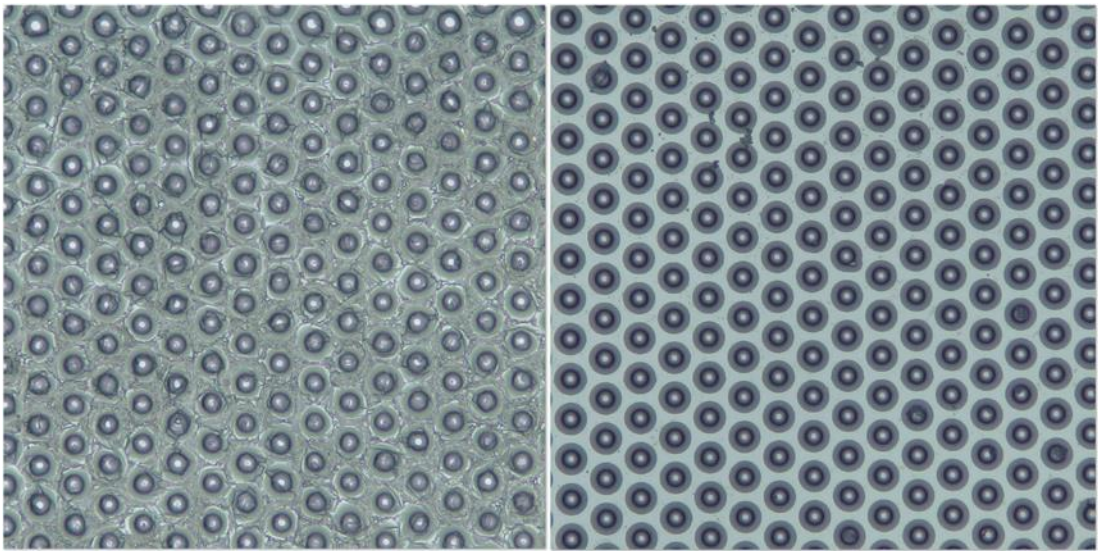

Figure 5-18: Under/Over etching Left: An over-etched sample. Right: An under-etched sample

The ideal PoreSize=1 according to my COMSOL simulations, with slightly under-etched sample outperforming slightly over-etched samples. In practice there was an advantage to deliberately under-etching the samples as the over-etched samples led to an increase of roughness causing them to behave more like sandblasted glass rather than a textured AR coating. Interestingly optical transmission continued to improve as the etched pits got larger until over-etching first occurs which leads to a rapid decline in optical performance, this performance then recovers as the over-etching continues as the roughened features are smoothed out, this will be further discussed in the optical results chapter.

5.11 DEWET METAL MASK

Solid films, particularly in their as-deposited state, are often metastable or unstable, making them susceptible to dewetting or agglomeration when subjected to elevated temperatures. This phenomenon is primarily driven by the minimization of surface energy and can occur well below the film's melting temperature due to surface diffusion, especially in ultra-thin films. While unintentional dewetting during micro- and nanosystem processing is generally undesirable, the effect can be used to produce self-assembled metal masks for nanoscale etching.[6,7] The effect is only observed in thin films as surface properties begin to dominate over the bulk properties of the material.

Silver was used as a dewet silver mask although both chromium and nickel were viable alternatives. This was because the wetting properties of silver were well known in my research group as this paper "Amy L. Lynch, Christopher P. Murray, Evan Roy, Clive Downing, David McCloskey, Extreme Dewetting Resistance and Improved Visible Transmission of Ag Layers Using Sub-Nanometer Ti Capping Layers, ACS Omega, 2024"[8] had recently been published. This was useful as the relationship between silver thickness and wettability had already been measured. 10 nm of silver was deposited on the micro-pitted glass surface with the magnetron sputtering tool before being transferred to a hot plate set at 250° C for 20 mins. The dewetting of silver and the formation of nanoparticles could be confirmed visually by the colour change from blue to red (the absorption peak of silver blueshifts as the silver nanoparticles decrease in size).

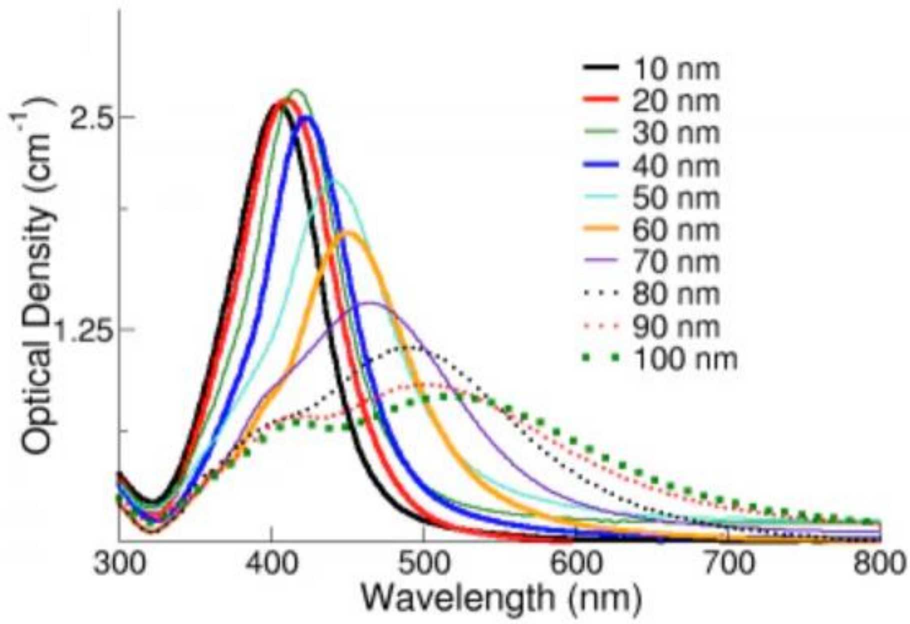

Figure 5-19: Silver nanoparticle spectra. The absorption peak shifts to the left as nanoparticle size increases, visually the silver goes from metallic/blue in colour to brown or red as it dewets. Image from "D. Paramelle et al, "A rapid method to estimate the concentration of citrate capped silver nanoparticles from UV-visible light spectra", Analyst, 2014"[9]

Figure 5-20 Silver dewetting visual confirmation Top: 10 nm thick silver on a glass slide, Bottom: Silver on a glass slide after being heated to 250^o C

The dewetted silver was also observed under SEM. The images below show the silver nanoparticles on an under-etched pitted glass sample. On the side walls on the pits the nanoparticles are smaller in size, this is due to magnetron sputtering tool depositing metal more thinly on the side walls.

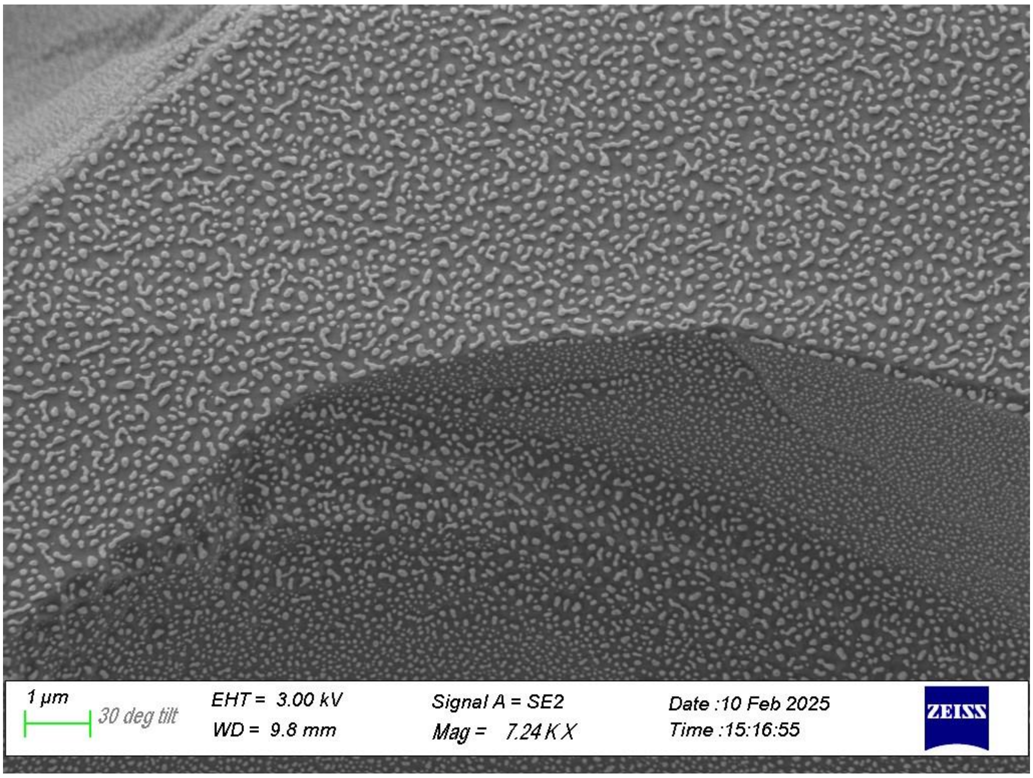

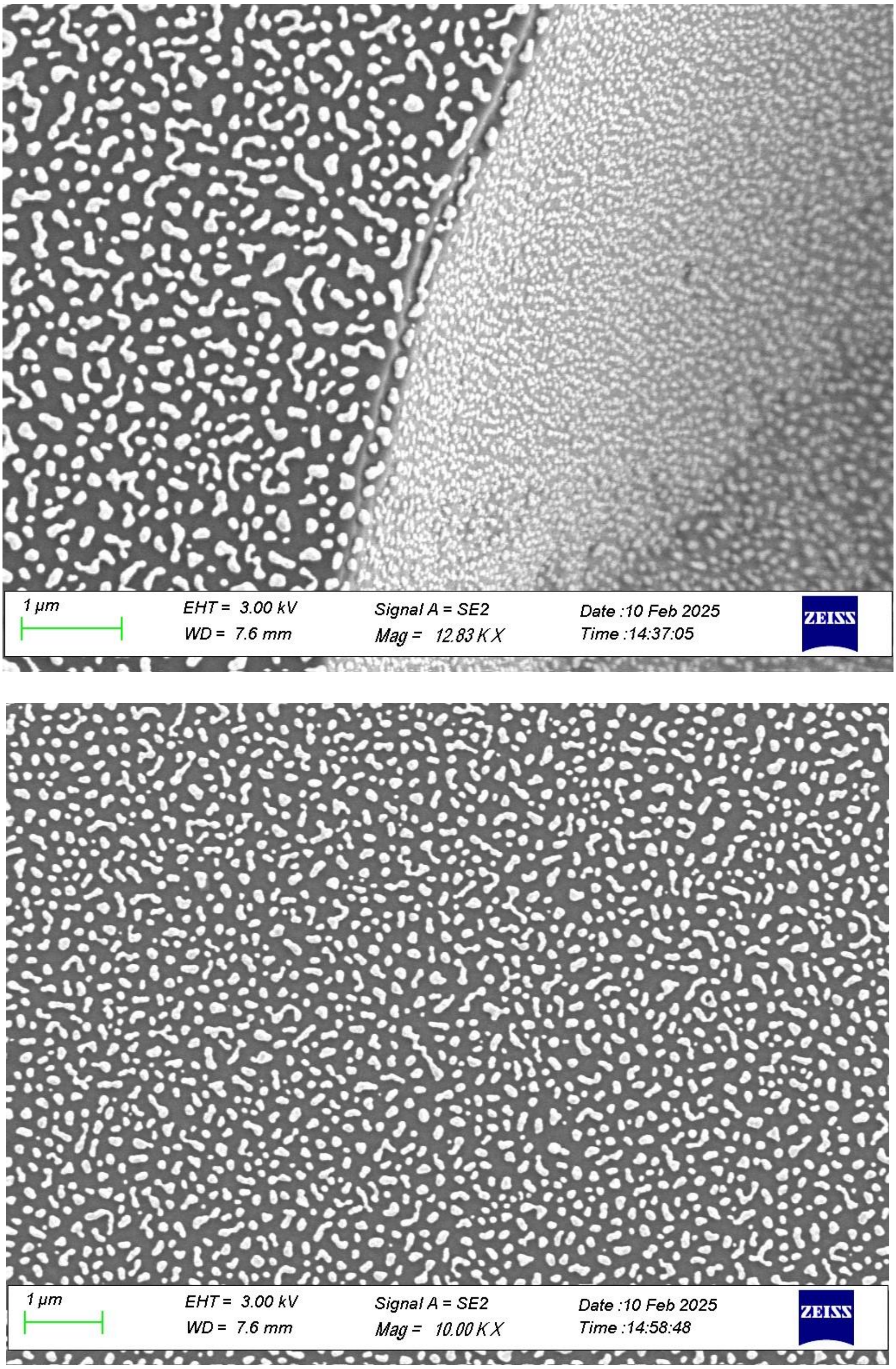

Figure 5-21: SEM images of dewetted silver on the pitted glass surface

5.12 ICP REACTIVE ION ETCHING

After applying the dewetted metal mask the pitted glass samples were etched with CH_3F gas in the Oxford Instruments inductively coupled plasma etcher. The diagram below shows the reactive ion etching process, it should be noted that this is fused silica glass rather than soda lime glass, for soda lime glass, calcium and sodium ions will act as etch masks reducing the maximum etch depth as well as lowering the etch rate and roughening the surface.

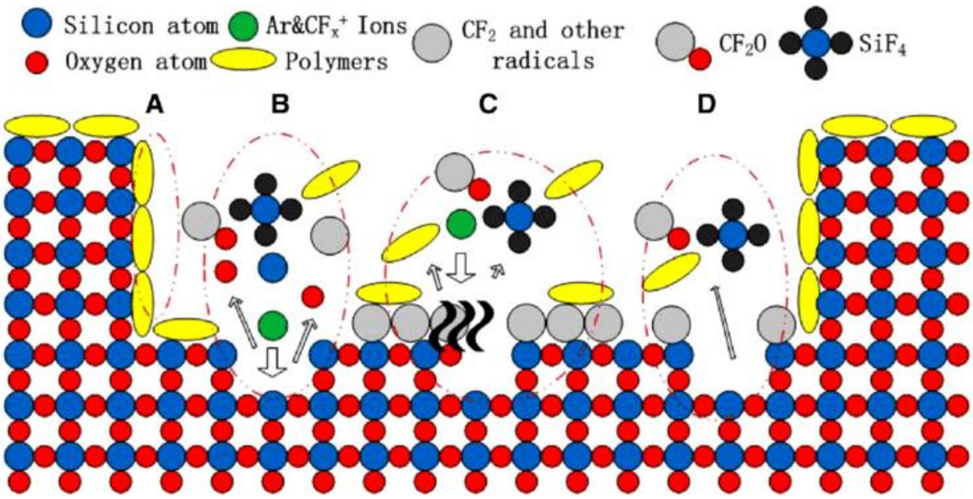

Figure 5-22: Dry etching diagram. Image from Laicun Lin et al "Dry etching of fused silica glass in C4F8/Ar inductively coupled plasmas for through glass via (TGV) applications", Microsystem Technologies 2015[10]

In order to create a low density, low refractive index AR coating the resulting pillars would need to be less than quarter wavelength in length scale. As the short end of the visible spectrum is 380 nm the nanoscale pillars should have feature sizes of 100 nm or less. The maximum depth of the nanoscale pillars was limited by the size of the silver nanoparticles as well as the power of the etching plasma. The silver nanoparticles gradually shrink in size as they are etched away by the plasma causing a sharpening effect on the pillars underneath, when the silver is completely removed however the pillars will lose their aspect ratio. The formation of a Teflon like fluoropolymer on the sides of the pillars in beneficial as it acts as a self-limiting barrier that makes the etch more anisotropic. The etching will eventually terminate as the pressure of the reaction products in the etched cavities will counter the pressure of the incident reactive gas.

5.13 SEM Images of Hierarchically Textured AR Coatings

The following 4 SEM images show an under-etched pitted glass structure with glass nanopillars at increasing magnification.

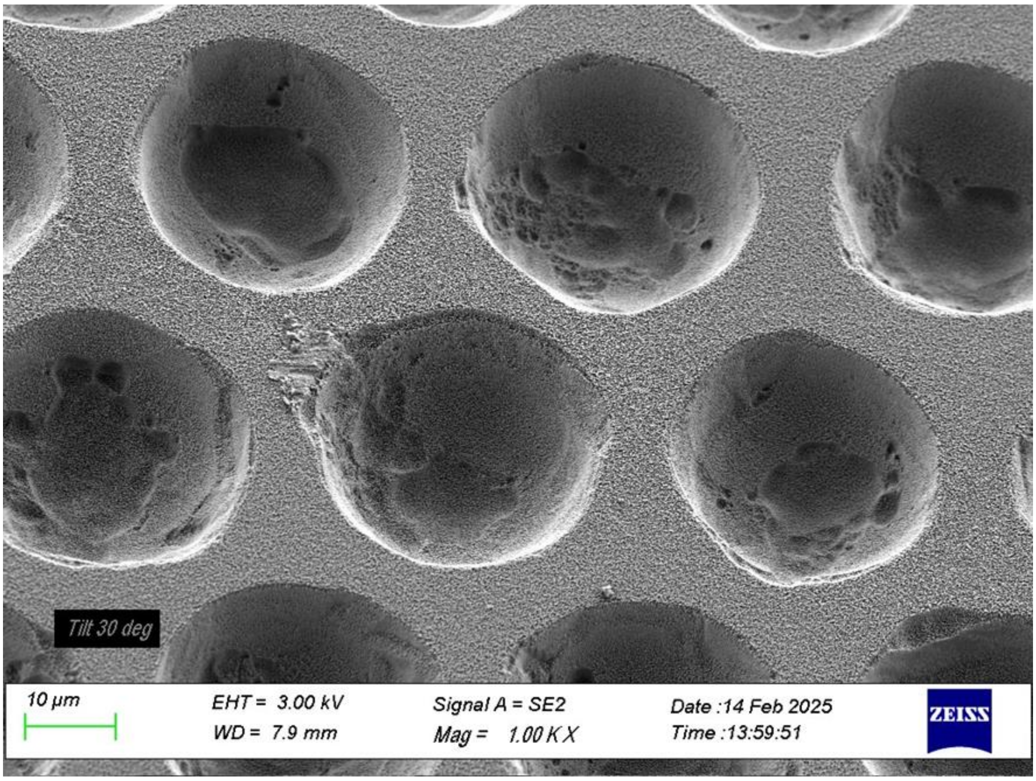

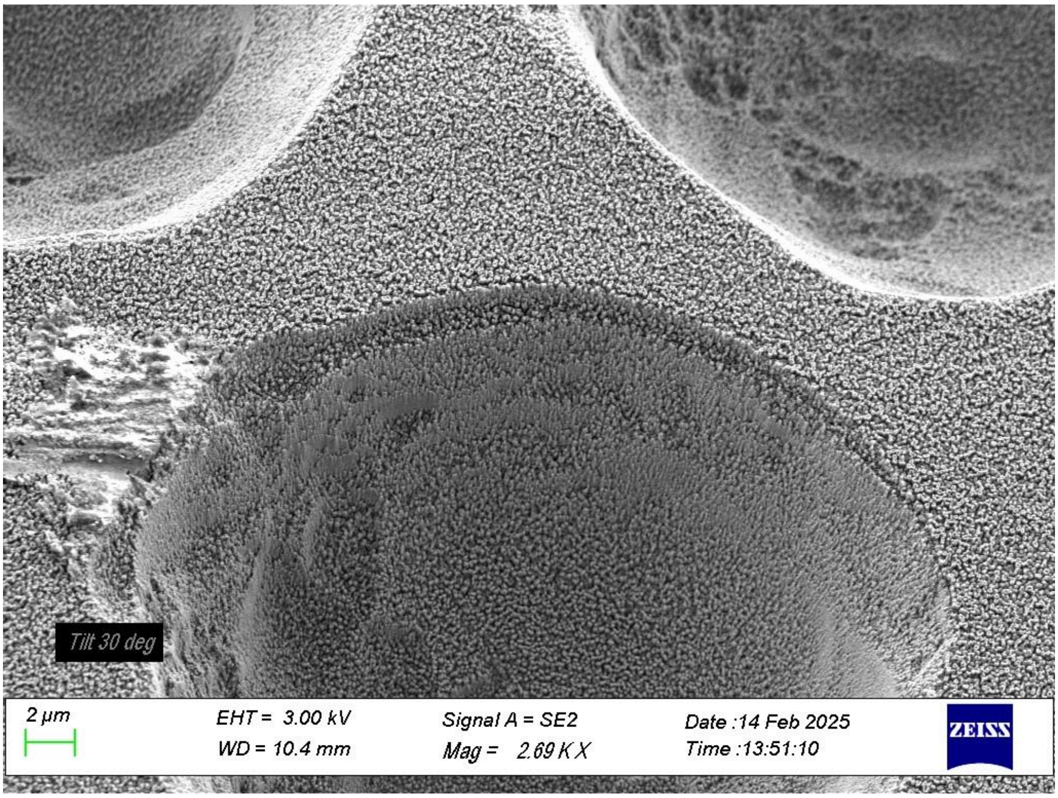

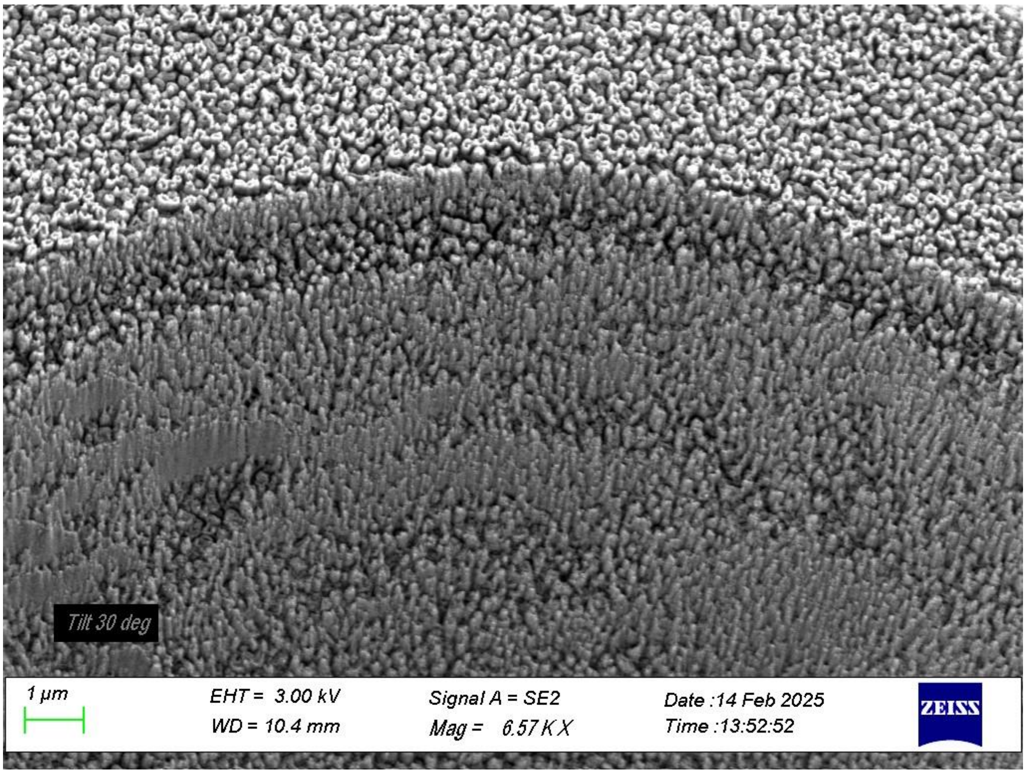

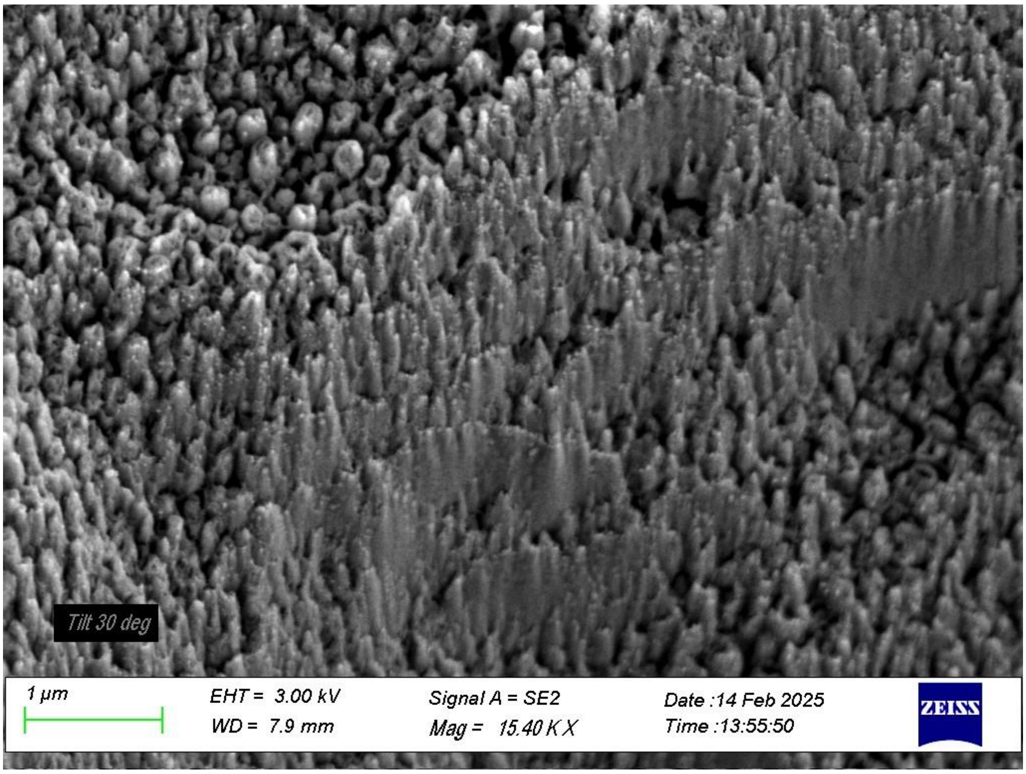

The next 2 images are of an over-etched pitted glass structure with nanopillars. It can be seen that the nanopillars successfully form even on rough surfaces.

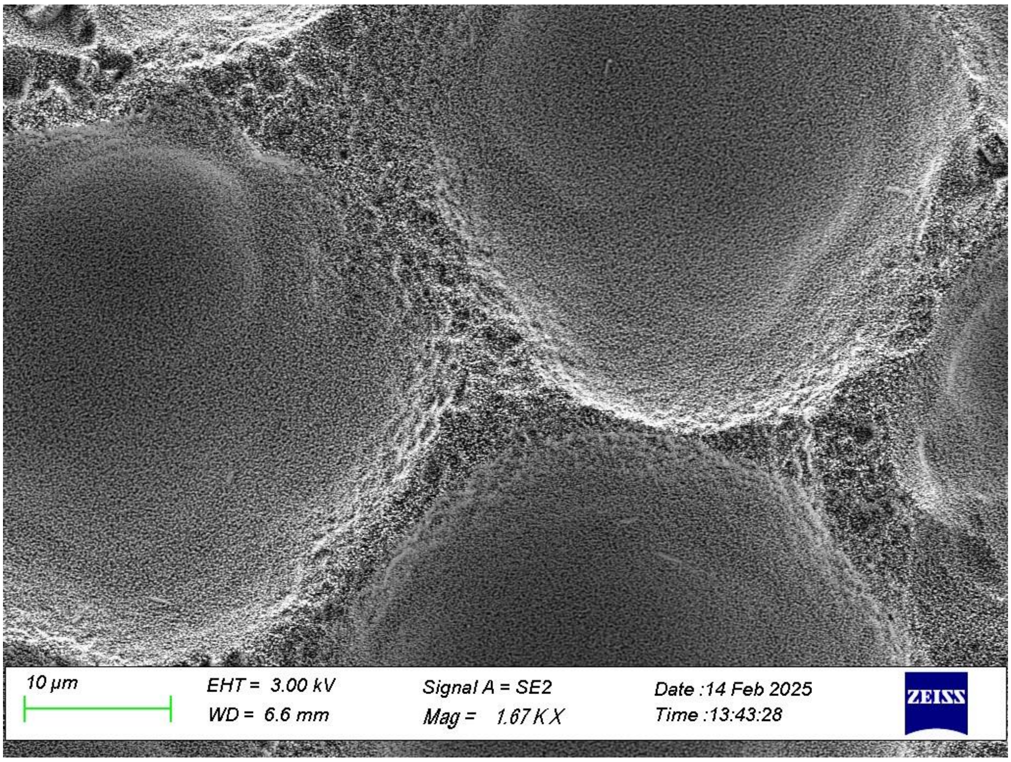

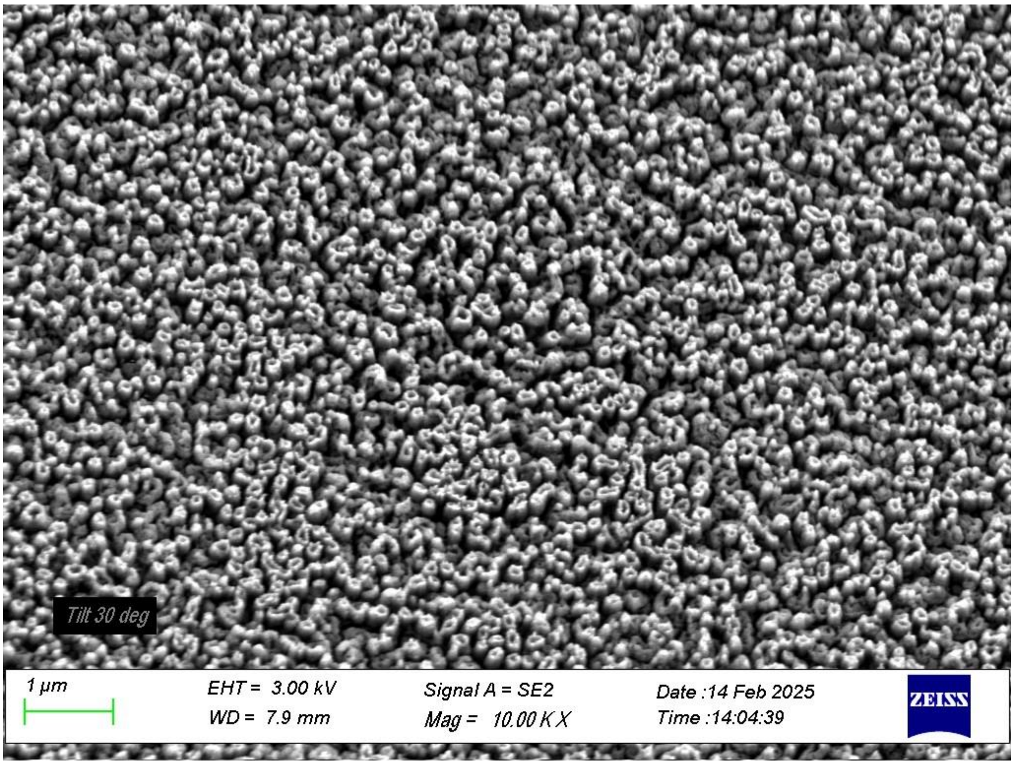

The samples were ashed in oxygen plasma to remove any fluoropolymer residue and then dipped in chrome etchant to remove what remained of the silver mask. As will be explained in the optical measurements chapter there was reason to believe there could be some remaining silver or fluoropolymer on the glass so Energy Dispersive Spectroscopy

(EDS), an X-ray technique was used to do some elemental analysis. Trace amounts of silver was found which was unexpected due to the effectiveness of chrome etchant solution in removing silver. Insufficient ashing of the fluoropolymer could have left some silver trapped beneath the Teflon like residue so it couldn't later be removed by chrome etchant.

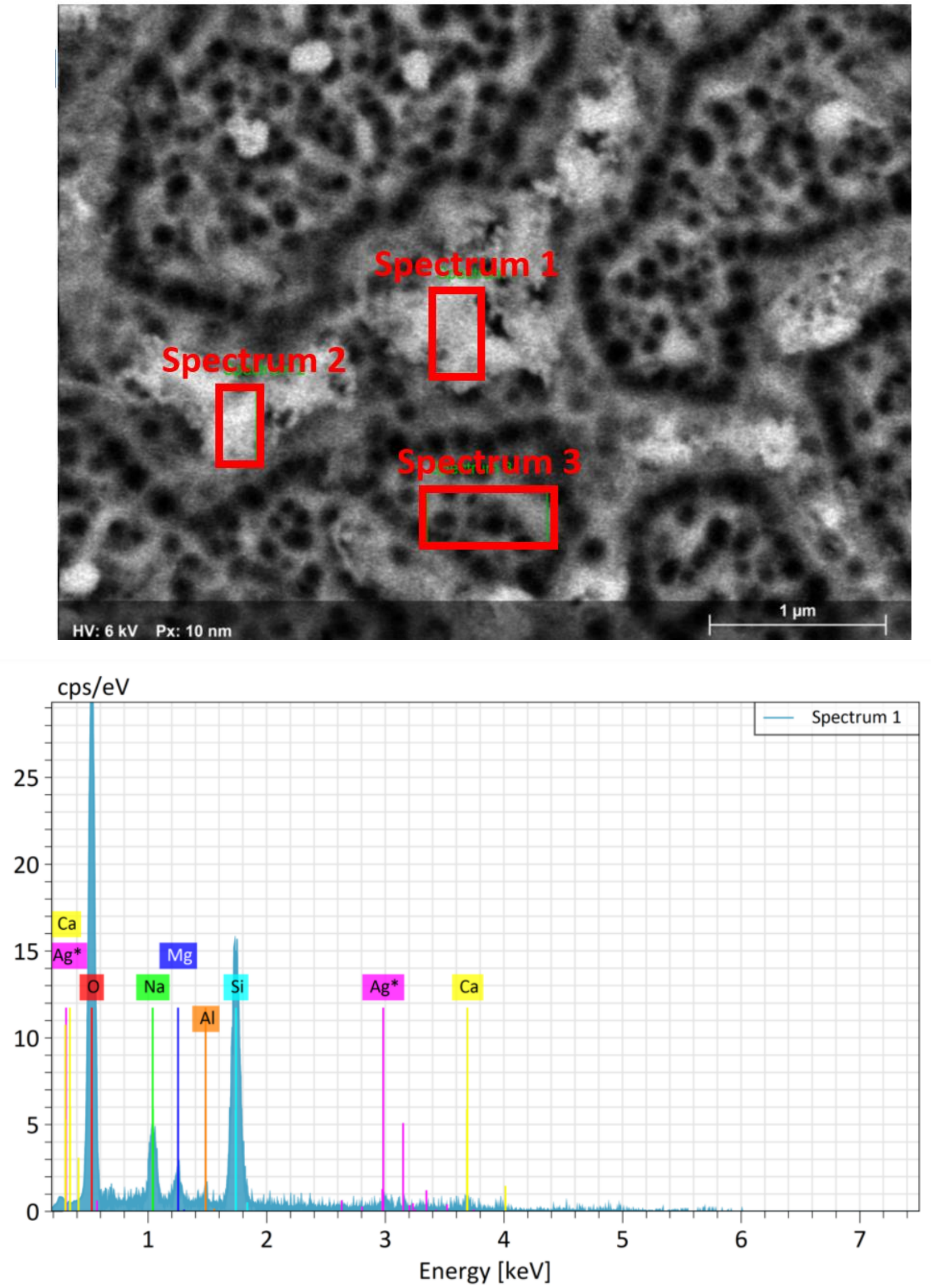

Figure 5-14: EDS data. Top: SEM of residue on glass, Bottom: EDS data showing trace amounts of silver but no evidence of fluoropolymer (no carbon or fluorine), Spectra 2 and 3 are not shown here but they had no silver peaks.

The sample was characterized with EDS as the electron microscope has this function, so it was possible to target the bright spots on the SEM image to see if they contained silver. One downside of EDS is that it less surface sensitive than X-ray photoelectron spectroscopy XPS, as the deposited silver was only 7 nm in thickness surface EDS was the less suitable technique.

5.14 Conclusions

A large range of pitted glass samples were successfully made. The earlier designs had a bowl-like shape due to the mask delaminating at a steady rate. For the later samples a chromium layer was added which greatly improved mask adhesion and resulted in much deeper pits being formed. After it became possible to make the pitted glass in a consistent manner the etch rate was varied so that a range of pitted glass samples was made ranging from under etched to over etched. COMSOL ray tracing experiments indicated that perfectly etched samples where the pits touched each other at the edges (pore size =1) was ideal. One issue was the small variance in the size of the holes in the photoresist mask which was a result of the spun-on photoresist having a greater thickness in the centre of the glass slide than the edges. The small variance in hole size meant that when a pore size of 1 was targeted some holes would be slightly overetched while others where underetched. Overetched holes had a higher roughness as the mask would delaminate in an irregular and uncontrolled manner causing uneven etching. Therefore slightly underetched pits were found to be the ideal.

The glass nanopillars where fabricated by dewetting silver on the pitted glass surface and then dry etching. This technique gave less control than wet etching as the only parameters that could be altered were the silver thickness and the dry etch time. SEM images confirmed that the nanopillars were made however EDS measurements suggest that some silver and or fluoropolymer residue remains.

5.15 References

(1) Chen, X.; Lin, B.; Schuster, M.; Chen, S.; Xu, B.-X.; Schneider, J. Effect of Moisture on the Delamination Properties of Fractured PVB-Laminated Glass: A Joint Experimental and Numerical Study. *Compos. Struct.* **2023**

(2) Chen, X.; Lin, B.; Schuster, M.; Chen, S.; Xu, B.-X.; Schneider, J. Effect of Moisture on the Delamination Properties of Fractured PVB-Laminated Glass: A Joint Experimental and Numerical Study. *Compos. Struct.* **2023**

(3) AllAdmin. *Resist-Wiki: Haftvermittler HMDS und Diphenylsilandiol - Allresist DE*. Allresist EN. https://www.allresist.com/resist-wiki-adhesion-promoter-hmds-and-diphenylsilanediol-ar-300-80
(4) Vishal Sahu, Priyanka Dewangan, Robbi Vivek Vardhan, Vanlal Rinfela, P. Krishna Menon & Prem Pal, A Study on Chromium Thin Film with Positive Photoresist as a Masking Layer towards the Wet Bulk Micromachining of Borofloat Glass. Micro and Nano Systems Letters, 2024
(5) Shubhava; Jayarama, A.; Kannarpady, G. K.; Kale, S.; Prabhu, S.; Pinto, R. Chemical Etching of Glasses in Hydrofluoric Acid: A Brief Review. *Mater. Today Proc.* **2022**
(6) Thompson, C. V. Solid-State Dewetting of Thin Films. *Annu. Rev. Mater. Res.* **2012**
(7) Lee, Y.; Koh, K.; Na, H.; Kim, K.; Kang, J.-J.; Kim, J. Lithography-Free Fabrication of Large Area Subwavelength Antireflection Structures Using Thermally Dewetted Pt/Pd Alloy Etch Mask. *Nanoscale Res. Lett.* **2009**
(8) Lynch, A. L.; Murray, C. P.; Roy, E.; Downing, C.; McCloskey, D. Extreme Dewetting Resistance and Improved Visible Transmission of Ag Layers Using Sub-Nanometer Ti Capping Layers. *ACS Omega* **2024**
(9) Paramelle, D.; Sadovoy, A.; Gorelik, S.; Free, P.; Hobley, J.; Fernig, D. G. A Rapid Method to Estimate the Concentration of Citrate Capped Silver Nanoparticles from UV-Visible Light Spectra. *Analyst* **2014**
(10) Lin, L.; Zhang, M.; Qiu, D.; Jing, X.; Jiang, F.; Yu, D. Dry Etching of Fused Silica Glass in C4F8/Ar Inductively Coupled Plasmas for through Glass via (TGV) Applications. In *2014 15th International Conference on Electronic Packaging Technology*; 2014

6 Optical Measurements

6.1 Introduction

After making the hierarchically textured surfaces it was then necessary to measure the optical characteristics and compare them to the simulated results from COMSOL. There were three main types of optical measurements, transmission at normal incidence (direct and diffuse), angle resolved transmission and glare. The transmission measurements were taken with a Perkin Emler, Lambda UV/Vis Spectrophotometer, while both the angle-resolved and glare measurements required a custom setup to be built. The samples measured were 14x14 mm glass squares with a 12x12 mm pattered surface in the centre. The table below lists all of the samples which were investigated, the nanoscale features were only deposited on the latest samples. Sandblasted glass samples were also measured as they appeared almost identical to the micropatterned surfaces but had much lower transmission. It was important to demonstrate that my hierarchically textured surfaces outperformed ordinary frosted glass as found in bathrooms despite its near identical appearance on the macro scale.

Table 5

Microstructure	**Nanostructure**
Flat Glass	No
Flat Glass	Yes
Flat Glass	Yes (smaller features)
Under Etched	No
Under Etched	Yes
Over Etched	No
Over Etched	Yes
Perfect Etch	No (roughened surface)
Sandblasted Glass	No
Pasta Bowl Geometry	No

It should be noted that only one side of the glass has a textured AR coating so the maximum possible transmission in each case is 96% due to the 4% reflectance loss at the rear glass air interface. In a real solar module this will be a glass EVA interface.

6.2 TRANSMISSION MEASUREMENTS,

The UV/Vis spectrophotometer covered a spectrum from 250 to 800 nm and allowed for both direct and diffuse transmission measurements. The photodetector was located in an integrating sphere with diffusely reflective walls such that light coming in at any angle would be collected with the same efficiency. In practice there is a small angular dependence due to the mica walls of the integrating sphere not being perfectly clean, as well as the finite size of the inlet allowing some light to escape.

Direct transmission measurements were taken by placing the glass samples far from the integrating sphere such that only light transmitted though a narrow solid angle would reach the integrating sphere. The total transmission was measured by placing the glass samples at the integrating sphere inlet as can be seen in the image below. Diffuse transmission was calculated as the difference between the total transmission and direct transmission.

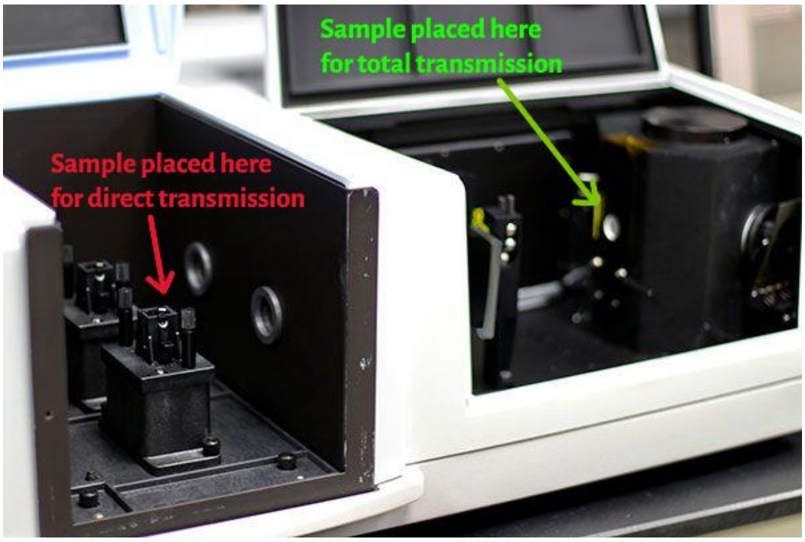

Figure 6-1: The Perkin Emler UV/Vis photospectrometer, the integrating sphere inlet is at the tip of the green arrow.

The first set of samples measured were the micro pitted surfaces with the pasta bowl geometry. The performance was generally excellent improving the transmission at normal incidence from 92% to 95% (out of a maximum of 96% as there is a 4% reflection loss at the rear of the glass). Some of the graphs have peaks around 365 nm, this is a calibration issue related to using a combination of borosilicate and soda lime glass slides.

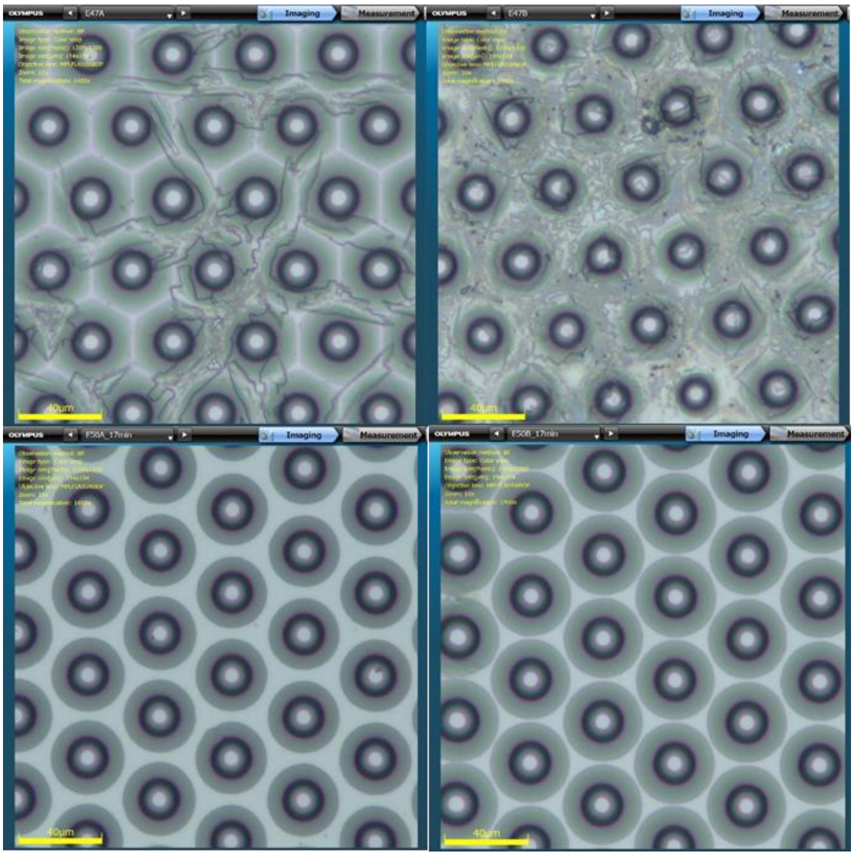

Figure 6-2: Pitted glass samples Top Left: E47A, slightly over-etched. Top Right: E47B, more over-etched. Bottom Left: E50A, under-etched. Bottom Right: E50B, slightly under-etched

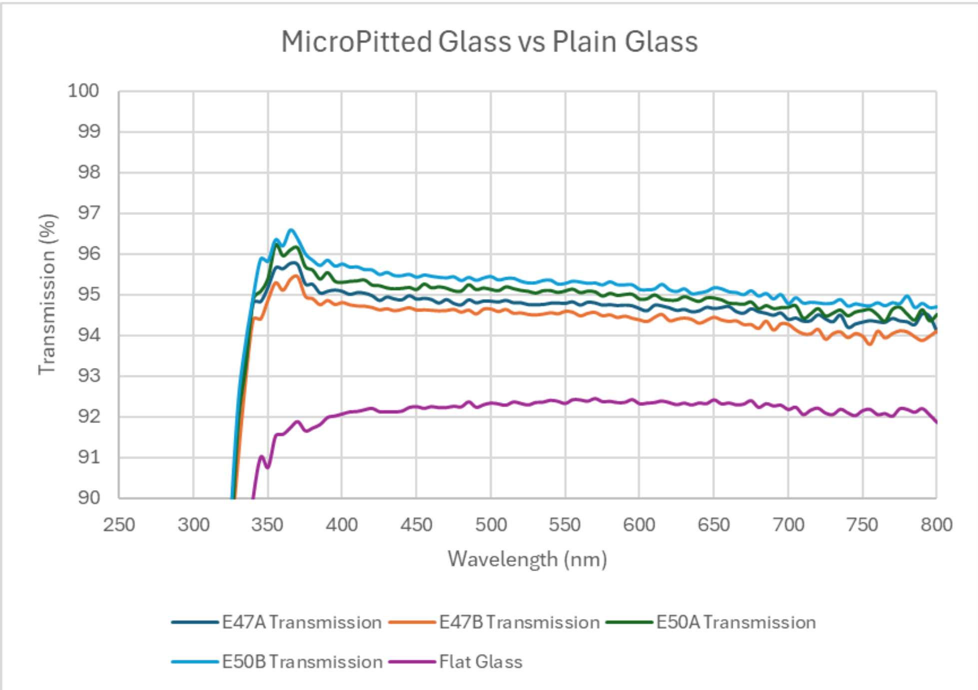

Figure 6-3: Pitted glass transmission. All of the pitted glass surfaces showed improved performance over plain glass. The apparent higher values for shorter wavelengths is due to borosilicate glass being used for the plain glass measurement instead of soda lime glass.

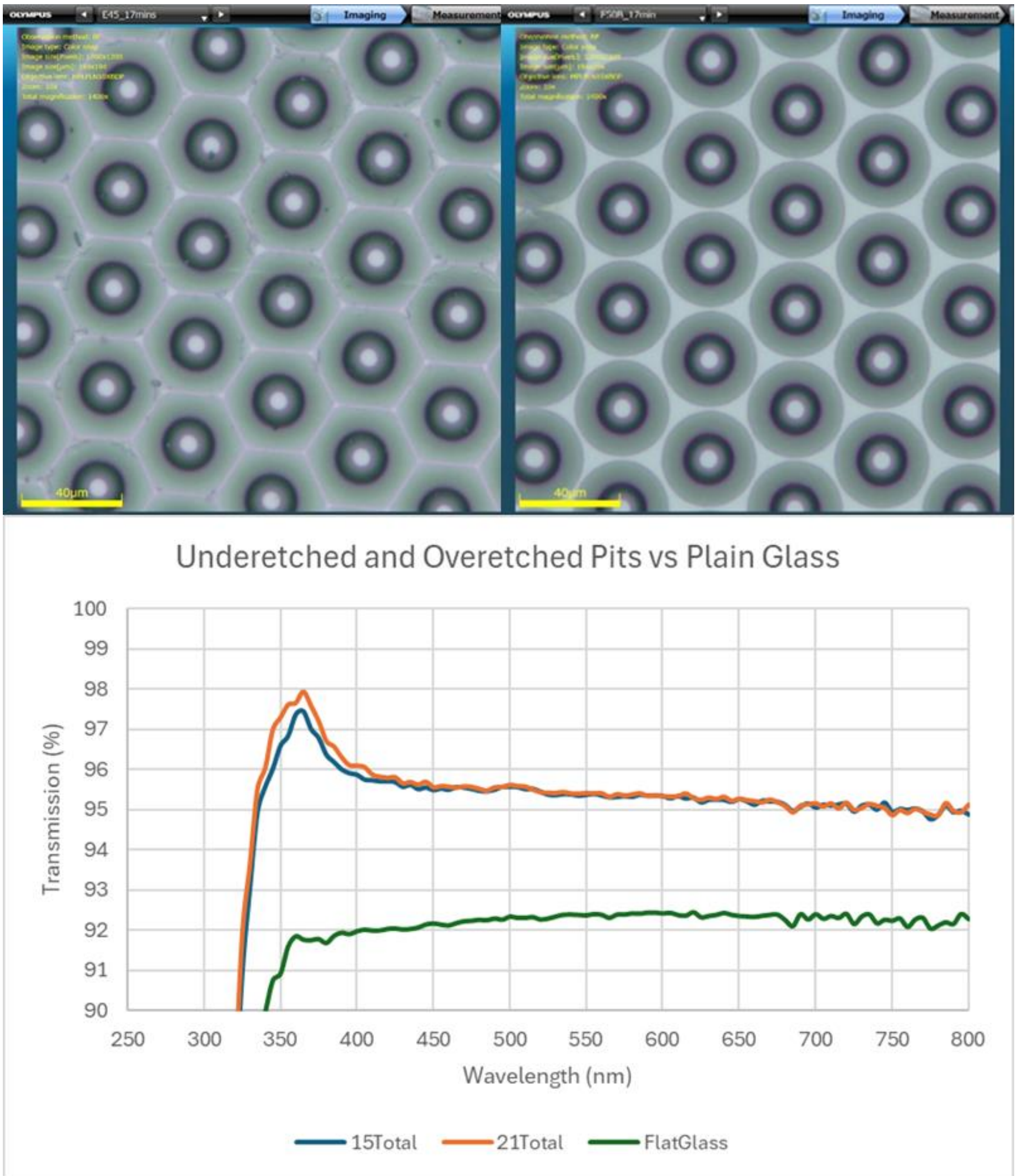

Figure 6-4: Flat Glass vs near perfectly etched pasta bowl shaped pits, again there is a calibration issue resulting in the peaks around 365 nm. 15 and 21 refers to the etch times in minutes.

It was important to demonstrate that the pitted glass outperformed sandblasted glass that simply has a roughened surface. The figure (Figure 6-5) below shows the sandblasted glass under a microscope.

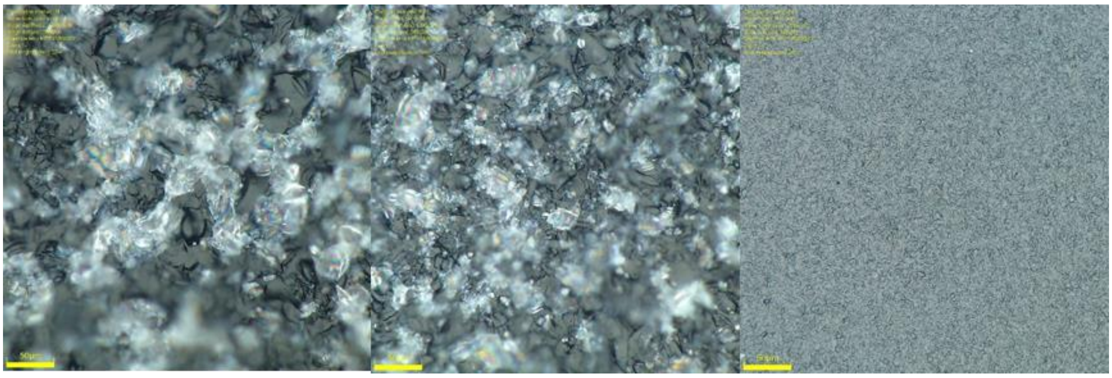

Figure 6-5:Sandblasted glass microscope images. Left to Right: sandblasted glass with 120, 500 and 600 micron grit size

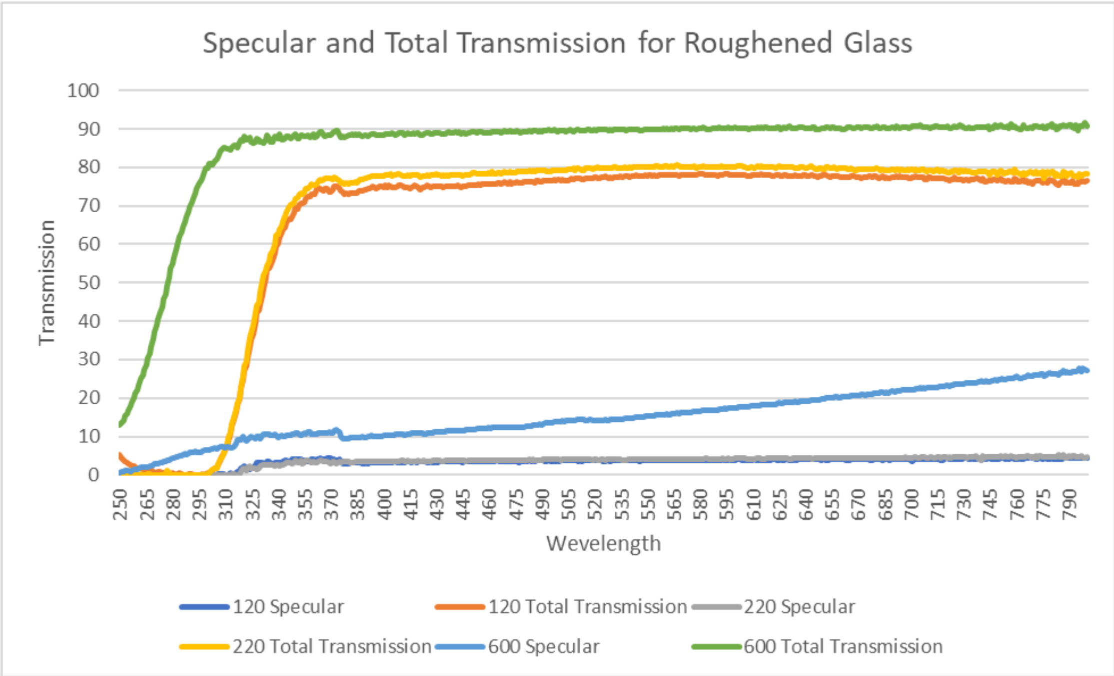

Figure 6-6: Sandblasted glass spectra. All sandblasted glass samples performed worse than plain flat glass for optical transmission due to a large amount of light being scattered backwards.

6.3 Nanoscale Pillars Reducing Short Wavelength Transmission

The samples with the nanoscale pits show reduced transmission for shorter wavelengths when compared to ordinary flat glass. This is a significant issue as the nanopillars reduce performance over almost all the visible range. The micro texturing behaved as expected as the under etched glass outperformed the over etched glass which outperformed the flat glass as expected from the COMSOL simulations.

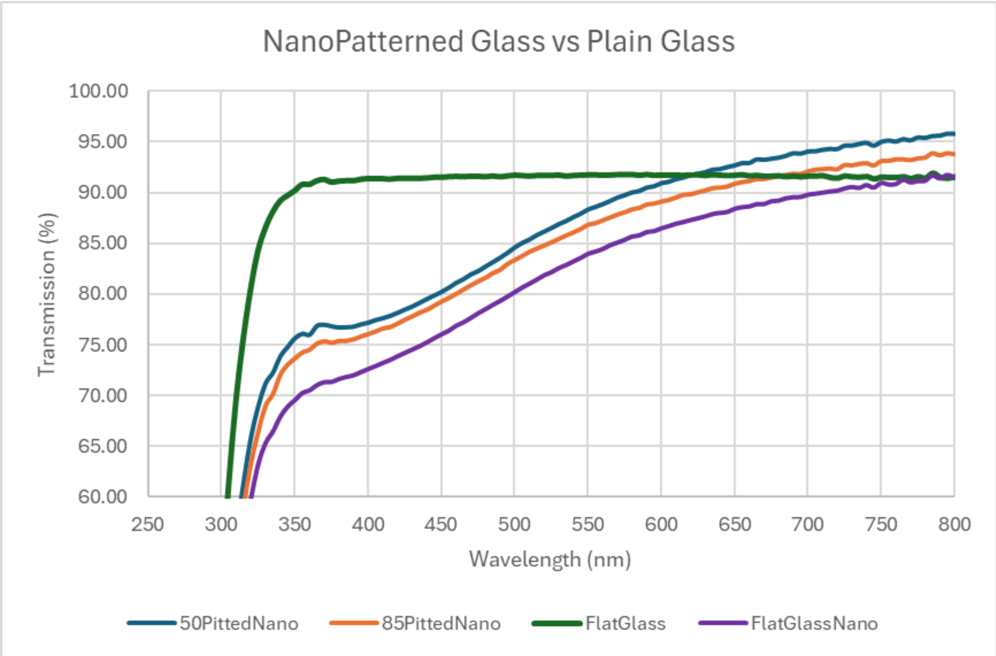

Figure 6-7: Plain flat glass vs glass with nanopillars

Two possible causes of this were considered. Firstly, there could be some dewetted silver remaining on the glass surface that was not successfully removed with chrome etchant. The Teflon like residue that results from reactive ion etching could also remain if the oxygen plasma ashing step was not sufficient to remove it. Below are the transmission spectra for silver nanoparticles and Teflon.

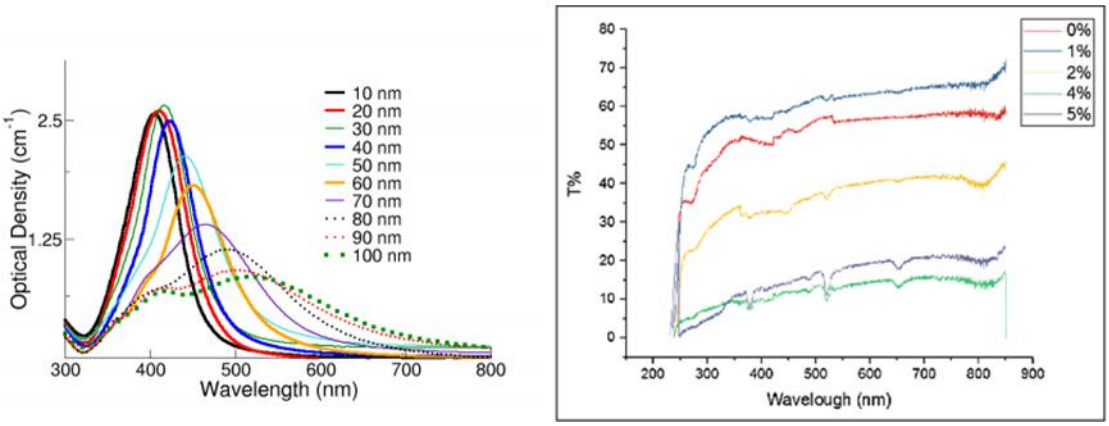

Figure 6-8: Spectra of residue. Left: The transmission spectra for different silver nanoparticle sizes. Right: Transmission spectra for Teflon of increasing concentration

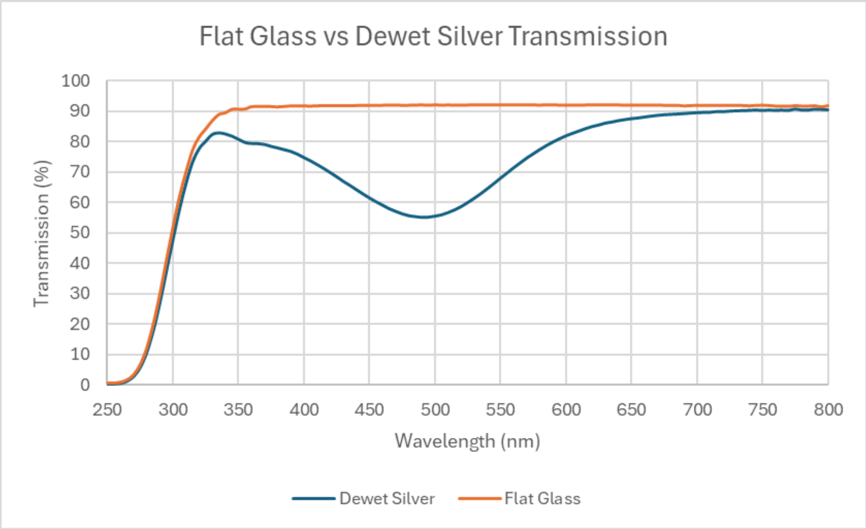

Figure 6-9: Transmission spectrum for the dewetted silver mask on a plain glass slide prior to dry etching.

The presence of silver reducing transmission in unlikely as there is no peak around 500 nm. Another explanation for the reduced transmission at short wavelengths is that the nanoscale pillars were too large. Thus, longer wavelength light saw the nanopillars as an effective medium with a low refractive index while the shorter wavelengths saw the nanopillars as a highly rough surface which scattered the light. To confirm this hypothesis reflection measurements were taken, if the shorter wavelengths were being scattered backwards then the reflected spectrum should be bluer than the transmission spectrum.

Figure 6-10: Reflection Spectra for the nanopillars, ignore the absolute values of transmission, that is a calibration issue related to using glass samples of different sizes

The reflection spectra show increased reflection for short wavelengths making the second hypothesis that the nanopillars are too large and are scattering blue light more likely. The solution to this was to decrease the size of the silver nanoparticles by depositing a thinner layer of silver, by reducing the silver layer from 10 nm to 5 nm in thickness the silver nanoparticles reduced from 100 nm to 20 nm in diameter on average. These smaller silver nanoparticles are a problem when dry etching as they are more quickly etched away by the reactive ion etch so the features cannot be as deep. Unless a gas is used with better selectivity between metal and glass a trade-off exists between the etch depth and the diameter of the pillars using this method.

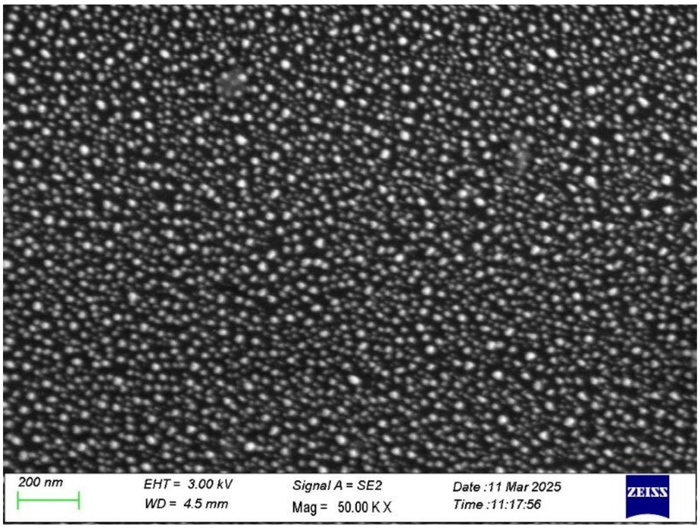

Figure 6-11: A SEM image of a 5nm silver layer that dewet, the resulting nanoparticles are significantly smaller and should produce smaller nanopillars when dry etched.

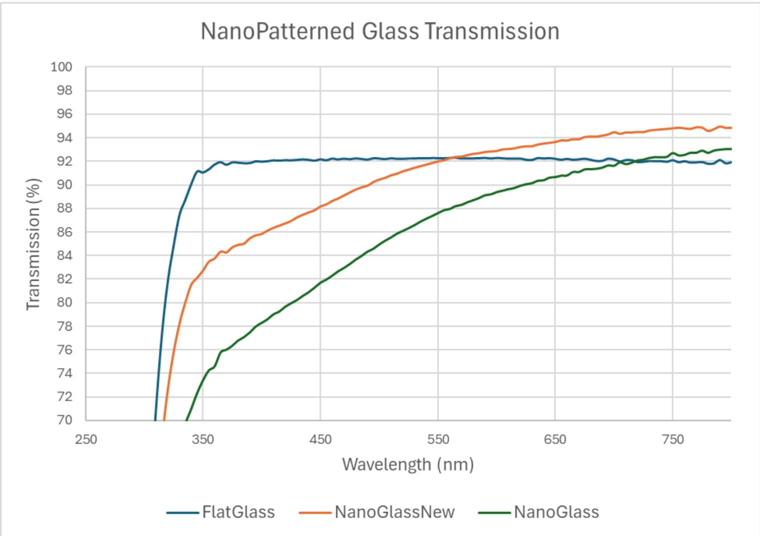

Figure 6-12: The new nanopatterned glass (smaller pillars 5nm of silver instead of 10nm) compared to the larger pillars.

As can be seen in Figure 6-12, the new nano glass with smaller nanopillars (produced with the thinner silver mask) shows improved transmission across all measured wavelengths. This makes the hypothesis that the shorter wavelengths were being scattered less likely. Another explanation is that the ashing step was ineffective at removing the fluoropolymer residue. The smaller nanopillars were etched for only one fifth the time as the larger pillars so there is most likely a thinner layer of fluoropolymer. This could be why the transmission was improved.

Henniker Plasma[1] claims that oxygen plasma is ineffective at removing fluoropolymer and hydrogen plasma should be used to convert the fluoropolymer to a hydrocarbon with the release of fluorine gas. The hydrocarbon-based polymer could then be removed by oxygen plasma etching. Unfortunately, there was no time remaining to do this step for the thesis.

6.4 ANGLE RESOLVED TRANSMISSION

The main difficulty in angle resolved reflectometry is the projection of a light spot on a surface will become longer as the angle of incidence increases, with an inverse cosine relation. This means it is difficult to go to high angles as the projected light spot will become larger than the glass sample which is a problem as the incidence power will not be accurately known. One way around this problem is to have a wide light source and to consider the sources irradiance (Wm^{-2}) rather than power (W). This way the glass sample can be rotated to glancing angle and a cosine correction can be applied to the incident light in order to calculate the transmission.

A solar simulator with an irradiance of 1000 Wm^{-2} and 1.5 AM spectrum was used as a uniform light source. A silicon photodiode was placed on a custom-built sample holder which could also hold the 14x14 mm glass samples in place. Index matching fluid was placed between the photodiode and the glass sample to avoid a lossy glass-air, air-silicon set of interfaces at the rear of the glass sample.

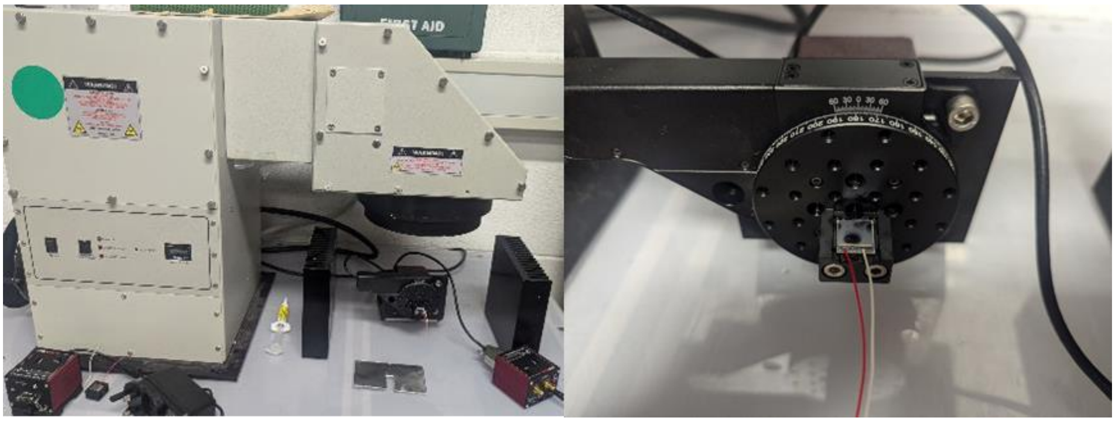

Figure 6-13: Solar simulator Left: The solar simulator. Right: Silicon photodiode on a rotating stage, glass samples fit securely in the 3D printed sample holder. The sample can be rotated to 90 degrees without falling out, this is aided by the adhesive effect of the index matching fluid.

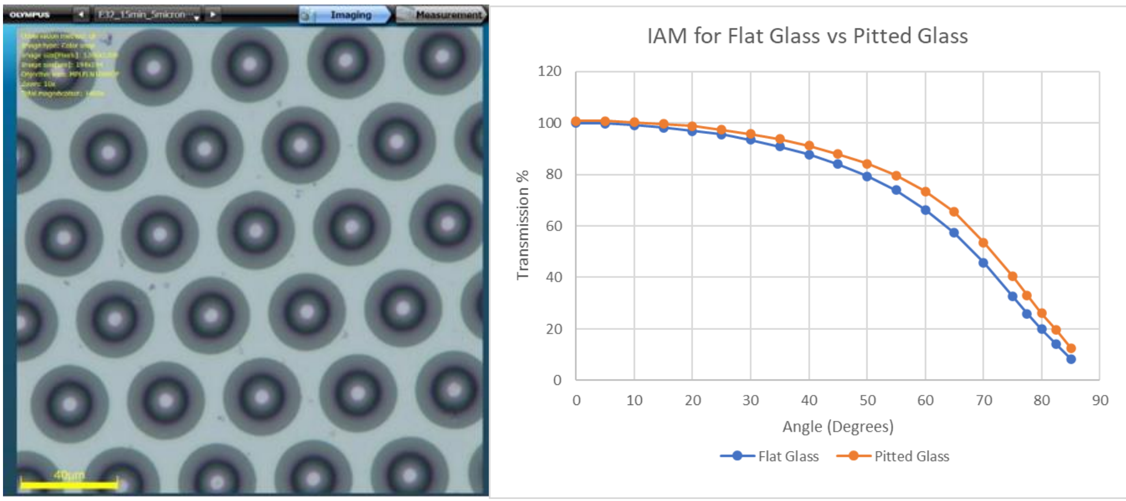

Figure 6-14: Measured angular transmission Left: Sample E32 underetched pitted glass. Right: Incidence angle modifier for flat glass vs pitted glass (Sample E32).

In Figure 6-14 above it should be noted that the measurement accuracy is greatly reduced as the tilt approaches a glancing angle. Reasons for this include the light from the solar simulator being somewhat diffuse and thus being incident on the glass sample over a broad range of angles and reflection from nearby objects causing the sample to receive more light at high angles than expected. These problems can be mitigated somewhat by enclosing the apparatus and having a small 14x14 mm aperture on top. The use of a collimated light source such as a laser could be used however this would make it difficult to measure glancing angles as the projection of the laser spot would overshoot the detector making it difficult to determine the power of the incident light.

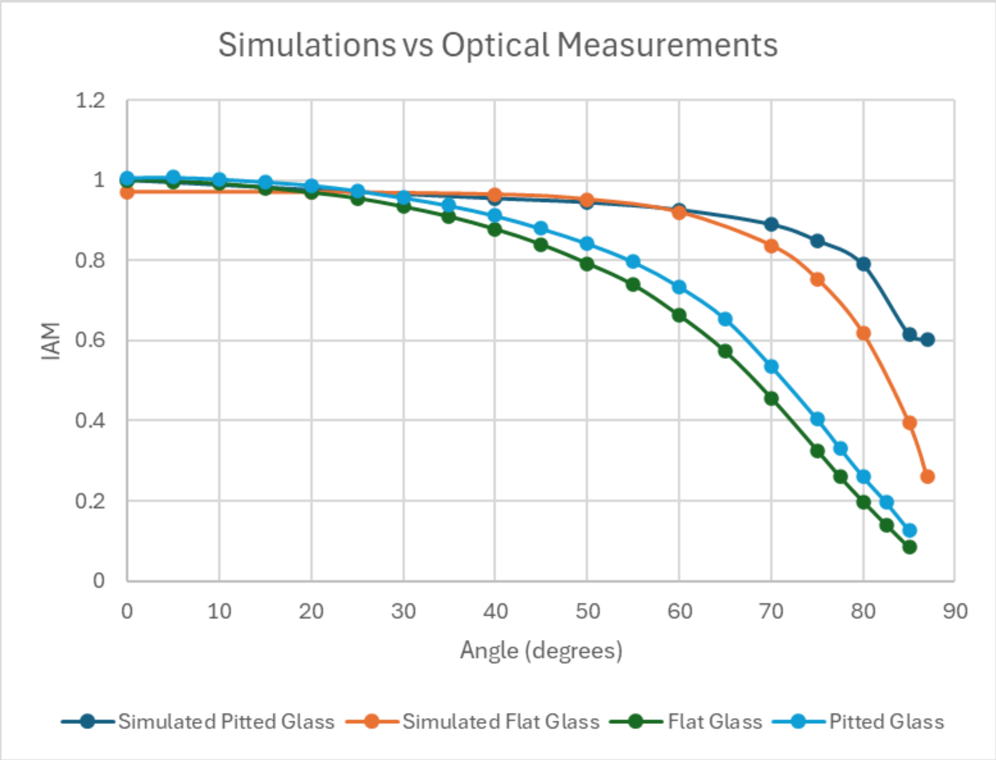

Figure 6-15: IAM curves for flat glass and pitted glass with pits 32 microns in diameter (Pore size of 0.8).

While these measurements suffer from low accuracy at glancing angles, they demonstrate the principle that pitted glass have improved broad angle reflection properties over flat glass which was also seen in the COMSOL simulations, thus the optical measurement can still be used to rank the textured surfaces from best to worst but the absolute values of transmission and reflection cannot be relied upon until the systemic errors mention earlier are addressed.

6.5 Haze and Glare Measurements

As discussed in the introduction chapter haze is light scattering within a material or medium, reducing contrast and clarity while glare is excessive or uncontrolled brightness that reduces visibility or causes discomfort. Glare is the result of unwanted specular reflection, for outdoor settings glare is often the unpleasant and sometimes harmful effect of seeing the image of the sun on a reflective surface. A high haze surface reduces glare by reducing the degree of specular reflection by broadening the range of angles that the light is reflected at. [2]

An angle resolved reflectometer was built to measure haze (diffuse reflection) and glare (specular reflection). The reflectometer had independently moving emitter and detector arms with 270° freedom of movement. A green laser was used as a light source rather than a white light source due to its higher power and lower dispersion. The high power of 5mW was necessary because the non-specular reflectance was often very faint, with readings approaching the photodetector's lower sensitivity threshold. Of the 5mW only 1.8 mW was received by the photodiode detector when the collector and emitter arms were aligned at 180° due to losses.

The laser was passed through a multimode fibre as this had reduced losses compared to a single mode fibre due to its larger aperture. This was a trade-off however as the multimode fibre allows a large range of propagation paths, leading to beam distortion and divergence. As a result, the output beam was less collimated. Small movements by the fibres themselves due to vibration or the reflectometer arms rotating led to mode mixing and thus a change in the power output. Dampening the vibrations of the fibres by clamping them helped reduce the power fluctuation due to mode mixing.

Parabolic mirrors were used on each arm to reflect the light to or from the fibres by 90° and to collimate the beam. As collimation was not perfect due to the use of multimode fibres apertures were put in the arms to narrow the beams, this came at the cost of power. A beam splitter was used on the detector arm to redirect the collected light towards the second parabolic mirror at the base of the collector arm. The second fibre connected the parabolic mirror to a photodiode which read the output. The stage adjusted so that the surface of the glass samples was on the axis of rotation of the two arms.

A beam splitter was used instead of a mirror on the collector arm as this allowed reflection measurements at normal angle of incidence. In that case the half of the incident beam would go through the beam splitter on the first pass and half of the reflected light would be directed towards the photodetector, thus the measured power would be half of that as measured for other angles. The use of the beam splitter instead of a mirror halved the power transmission for non-normal angle of incidence and quartered it for normal angle of incidence. The setup can be seen in the figure below.

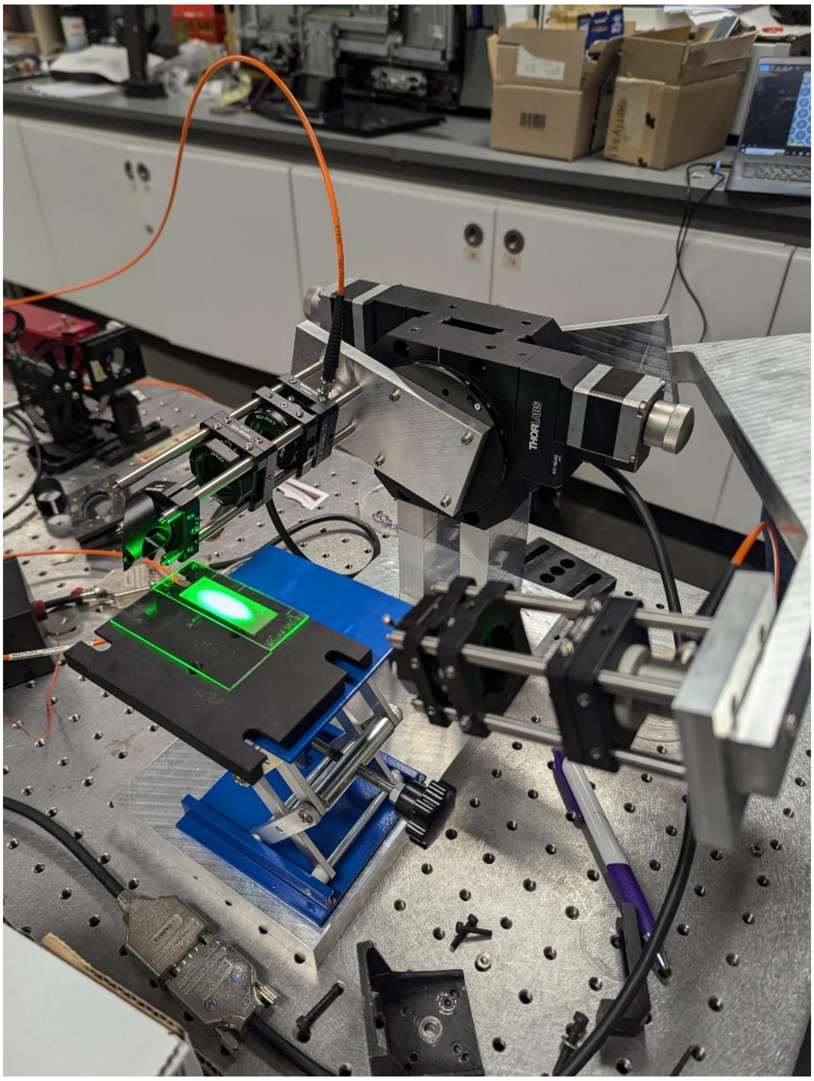

Figure 6-16: The angle resolved reflectometer, on the left is the detector arm and on the right the emitter arm. Special elongated patterned surfaces were made for this experiment which allowed glancing angles to be measured.

Glare measurements were taken for angles of incidence between 20 and 70 degrees. It was not possible to take measurements below 20 degrees as the projected light spot became longer than the patterned glass surface. To address this better collimation (with the use of additional lenses or apertures) would result in a smaller light spot. The range of 0^{o} to 30^{o} degrees is relevant to solar farms located near airports as when solar panels are oriented at a shallow tilt they can interfere with the pilots vision within this range.[3] The specular reflection (glare) measurements were taken by varying the emitter arm angle and then adjusting the collector arm angle until the signal was maximized. This was done with the plain flat glass microscope slide, once the appropriate collector arm angle was found the flat glass was replaced with textured glass and the output on the photodetector recorded.

Special elongated patterned surfaces were made for this experiment which allowed glancing angles to be measured. Microscope images of them can be seen below.

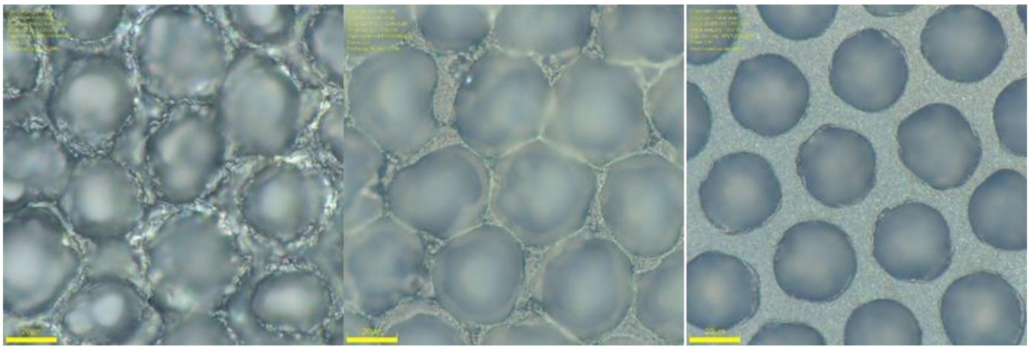

Figure 6-17: Left to Right: Overetched, overetched with nanopillars, underetched with nanopillars

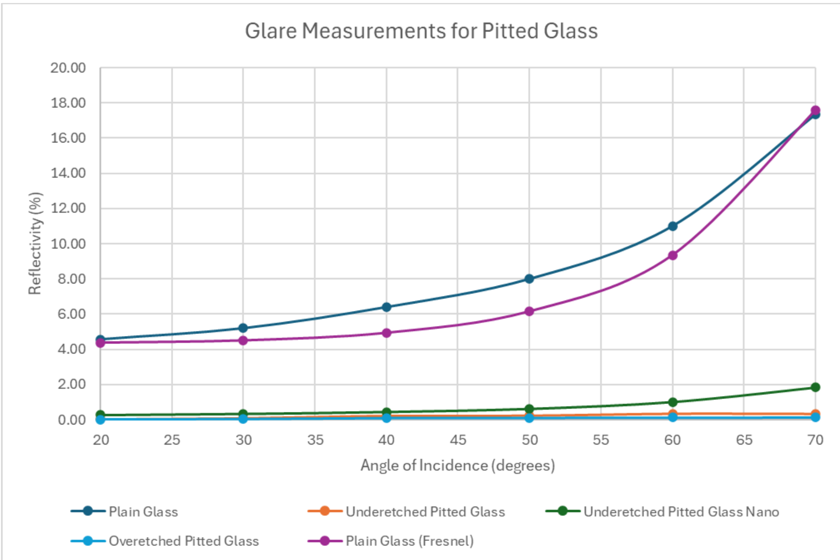

Figure 6-18: The specular reflection of flat glass and some textured surfaces. The flat glass measurement is compared to the Fresnel reflection of a material with a refractive index of 1.5, this helps show the quality of this measurement system as the flat glass and Fresnel curves should be as close as possible.

As can be seen the over etched pitted glass surfaces were able to reduce specular reflection by a factor of 100 while the under etched pitted glass reduced specular reflection by a factor of 10. The under etching means there is some original flat glass surface remaining, so the surface as a whole has properties between that fully pitted glass and flat glass. This introduces an interesting trade-off. In previous optical measurements and COMSOL simulations slightly under etched outperformed the over etched ones but there is an increase in specular reflection. Thus, longer etch times than otherwise suggested are desirable if glare is a concern.

The reduced glare can also be observed visually by reflecting the image of a light source such as a ceiling light towards one’s eye. Below in an image of textured glass supressing glare.

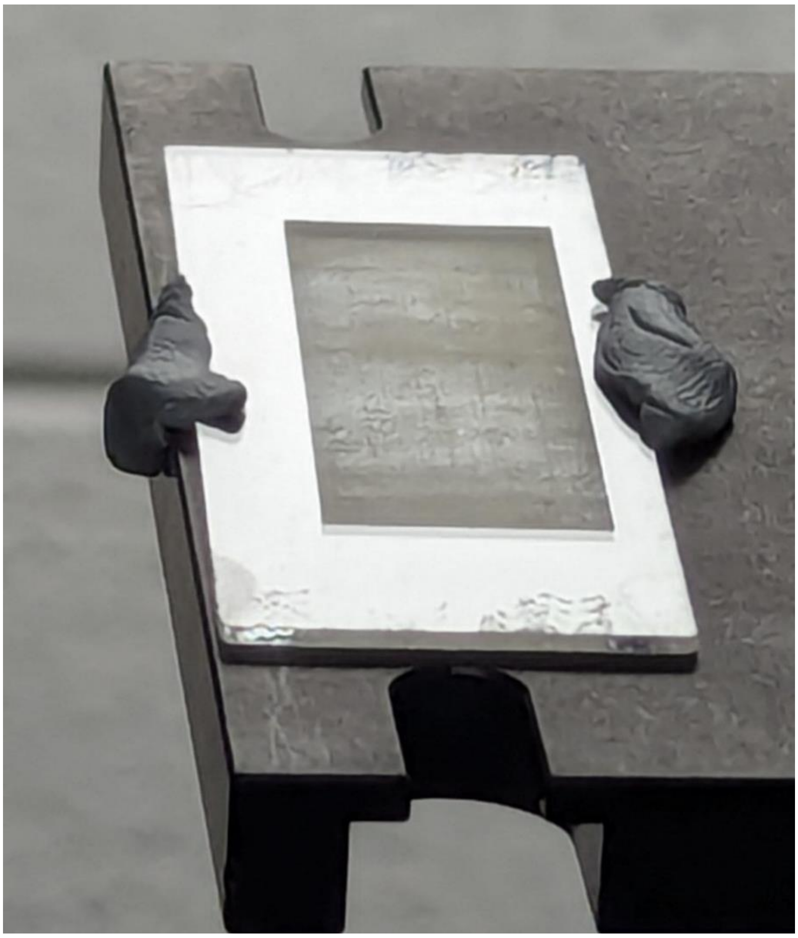

Figure 6-19: Textured glass slide that is catching the specular reflection of a ceiling light, the pattered surface in the centre is less bright.

Haze measurements were taken by setting the emitter arm at 30^{o} and then incrementally increasing the collector arm angle and recording the output. All measurements showed a peak at the specular position but the broadness of the peak indicated the amount of haze. The haze measurements were normalized relative to the peak as the shape of the curve is more important than the absolute values in this case. The absolute values of the specular peaks is known from the glare measurements anyway. A perfectly Lambertian surface would show no peak by definition.

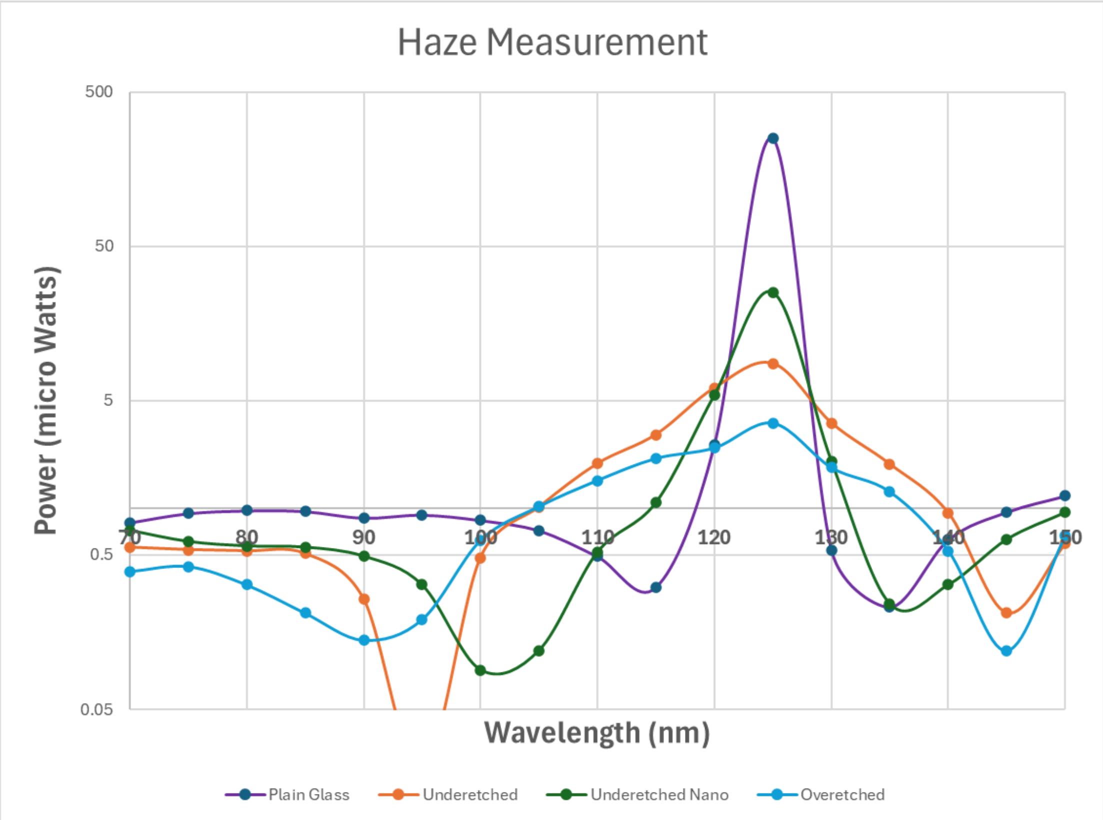

Figure 6-20: Haze for the three samples as well as plain glass. The roughest surface showed the most haze as expected.

Haze in glass can also be measured by placing the glass on a page with letters and the raising the height of the glass until the letters can no longer be read. The shorter the required distance the higher the haze.

6.6 CONCLUSIONS

The photo spectrometry measurements demonstrated that the pitted glass surfaces improved transmission by 3 to 3.5% out of a maximum of 4%. It was also shown that the shallower pasta bowl shaped pits improved transmission by 3%. The nanoscale pillars did not achieve broadband anti-reflection as there was a significant reduction in transmission on the blue end of the spectrum. Possible reasons for this are the presence of fluoropolymer residue or silver nanoparticles which were not successfully removed. Another possibility is the nanopillars were too large and thus scattered the shorter wavelengths while the longer wavelengths saw the pillars as a low refractive index layer. While the source of the reduced short wavelength transmission was not confirmed some likely causes were investigated and a body of evidence was compiled.

The angle resolved transmission experiments showed that the pitted glass structures had better incidence angle modifier curves, meaning transmission did not fall of as sharply as the angle of incidence was increased. The measurement requires significant refinement in order to get reliable quantitative data. There was a significant divergence between the COMSOL ray tracing simulations and the optical measurements particularly at high angles. Reasons for this include the light source being diffuse and thus more light was incident on the detector than expected if collimated light was assumed. Another potential cause of error was light entering the edges of the glass sample and being internally reflected towards the photodetector. The photodetector was made of silicon and thus had a refractive index of 3.5 to 4 in the visible range, the index matching fluid had a refractive index the same as glass (1.5) thus there is high reflection at the fluid/silicon interface which would become even greater as the angle of incidence increases as per the Fresnel equations.

The haze measurements showed that the specular reflection peaks were effectively suppressed by the textured glass samples. This shown that both increased transmission and effective anti-glare can be achieved at the same time. The reduction in glare was also visually apparent as can be seen in Figure 6-19.

6.7 References

(1) Henniker Plasma, Plasma Treatment of Fluoropolymers, https://plasmatreatment.co.uk/knowledge-base/press-releases/201-press-release-plasma-treatment-of-fluoropolymers

(2) Danbi Yoo, Peter Tillmann, Tobias Kraus, Johannes Sutter, Angelika Harter, Sergei Trofimov, Boris Naydenov, Klaus Jäger, Hubert Hauser, Christiane Becker, Comparative Optical Analysis of Imprinted Nano-, Micro- and Biotextures on Solar Glasses for Increased Energy Yield, RRL Solar, 2023

(3) Evan Riley, Scott Olson, A Study of the Hazardous Glare Potential to Aviators from Utility-Scale Flat-Plate Photovoltaic Systems, International Scholarly Research Notices, 2011

7 CONTACT ANGLE MEASUREMENTS

7.1 THE PROBLEM OF SOILING

As discussed in the introduction chapter, soiling is the build-up of dirt, dust, sand, bird droppings, pollen and pollutants on the surface of a solar module. Losses vary greatly by region as each type of soling has its own mechanism and effect[1,2]. In regions with high rainfall water droplets can be relied upon to periodically wash the solar panels while in arid climates this effect is less significant. Power losses associated with soiling are between 3-5% on a global scale[1] however there is massive regional variation with the highest losses occurring in arid sandy regions. The map below shows soiling losses in Europe.

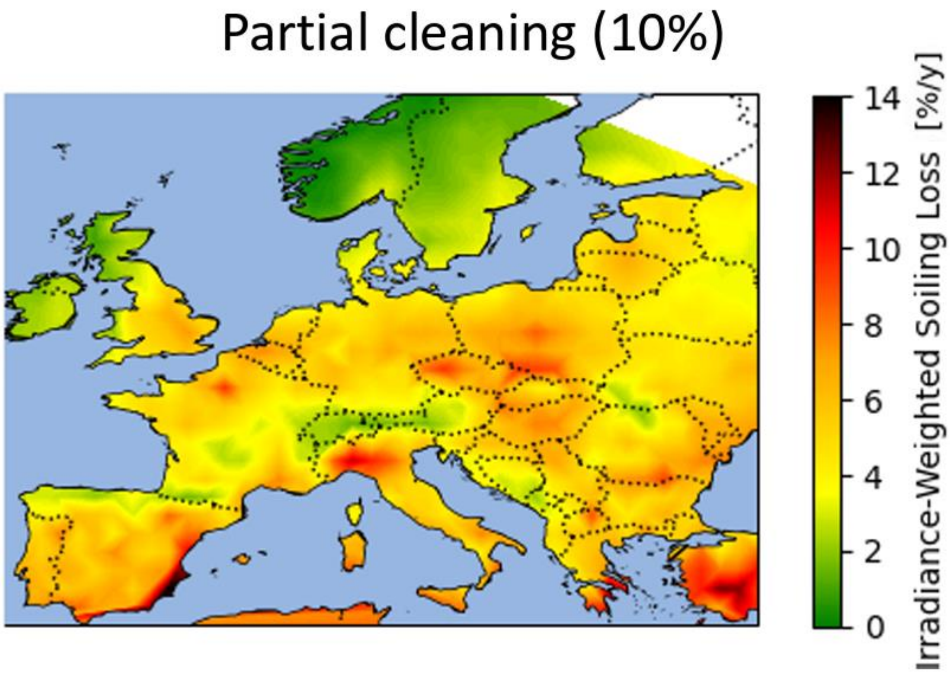

Figure 6-21: Annual soiling losses in a simulated scenario where rainfall removes 90% of dirt. Data is interpolated from 11 real life test sites around Europe using a similar technique to other GIS maps. Image from Álvaro Fernández Solas et al, Photovoltaic soiling loss in Europe: Geographical distribution and cleaning recommendations, Renewable Energy, 2025.[3]

As can be inferred from the map soiling losses are highest in sandy, arid regions as well as urban and industrial regions with higher levels of industrial pollution such as soot e.g. from road traffic and coal power plants. The main factors that influence the severity of soiling are discussed below.

Concentration of soiling particles: Perhaps the most obvious predictor of soiling is the amount of dust or other soiling particles in the air. In “Muller, An Investigation of the Key Parameters for Predicting PV Soiling Losses, NREL, 2017” a 90% R^2 correlation between the concentration of particles below 10 and 2.5 microns in diameter and the rate of soiling.[4] Apart from mineral dust originating from desert regions, airborne dust can stem from various sources such as industrial processes (including exhaust emissions and process dust), traffic (soot and carbon particles), agriculture (soil displacement, dust from animal feed, and emissions from livestock), and organic materials (such as pollen, seeds, bird droppings, leaves, lice, lichen, algae, and moss). The contribution of these sources to airborne dust and subsequent soiling differs greatly across locations.

Dust Adhesion: Dust particles can be physically adhered to the surface of a solar module by either van der Waals forces or electrostatic forces. In desert regions sand often accumulates a large electrostatic charge due to friction with the air, thus charged sand and dust particles can easily stick to the glass. This effect is enhanced by the high voltage conditions of a solar PV array where many panels are connected in series.[5]

Cementation as another more permanent adhesion mechanism whereby minerals in the dust which are soluble in water such as gypsum or salt are dissolved when there is condensation on the panels or high levels of humidity, when the panel dries out these minerals are redeposited and form a hardened layer which is difficult to remove.[6] Cementation is further enhanced by the presence of high levels of SO_2 or NO_2 which make the water acidic and dissolve more minerals.

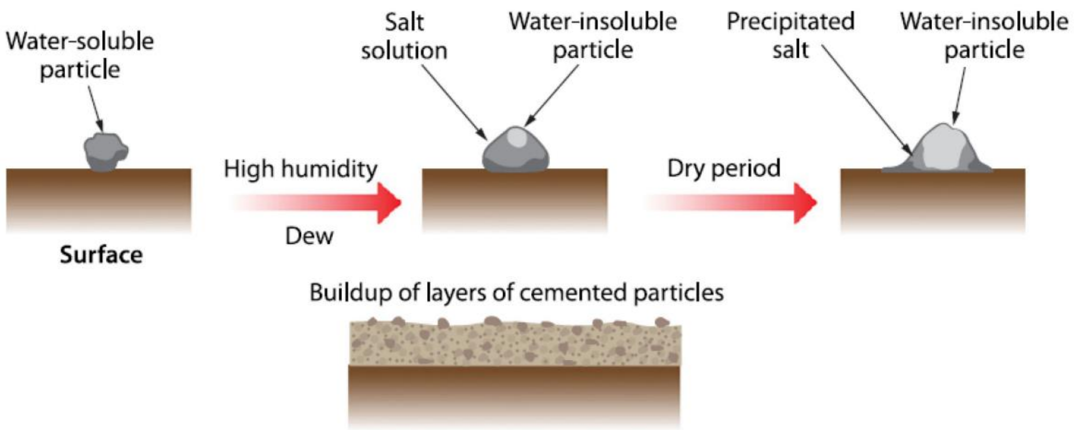

Figure 6-22:Cementation. Image from Mohammad Istiaque Hossain, Anti-Soiling Coatings for Enhancement of PV Panel Performance in Desert Environment: A Critical Review and Market Overview, Materials, 2022

Heat induced sintering happens in very hot conditions and involves dust particles melting or softening on the solar panel glass which can then fuse more permanently to the surface when they cool.

Particle Size: The size of the dust particles affects both the adhesion as well as the degree of absorption and scattering of the dust. The smallest particles include clays and soot and typically have a size below 10 microns. Due to their small size, they can pack more densely than larger particles. There is also the issue of Rayleigh scattering with its λ^{-4} dependence. Rayleigh scattering is relatively isotropic so some of the light is scattered backwards which contributes to diffuse reflection.

For larger particles such as pollen, Mie scattering becomes dominant. There is less wavelength dependence in this case so no apparent change in colour. The absorption of the larger particles can also be greater than for smaller particles.

Large particles such as fine sand reduce solar module output primarily by shadowing the solar panel rather than scattering. Adhesion of smaller particles is generally greater as the adhesion forces are proportional to the surface area while the mass is proportional to volume. Thus, as the particles get larger their weight begins to win out against their adhesion to the surface as it scales more slowly.

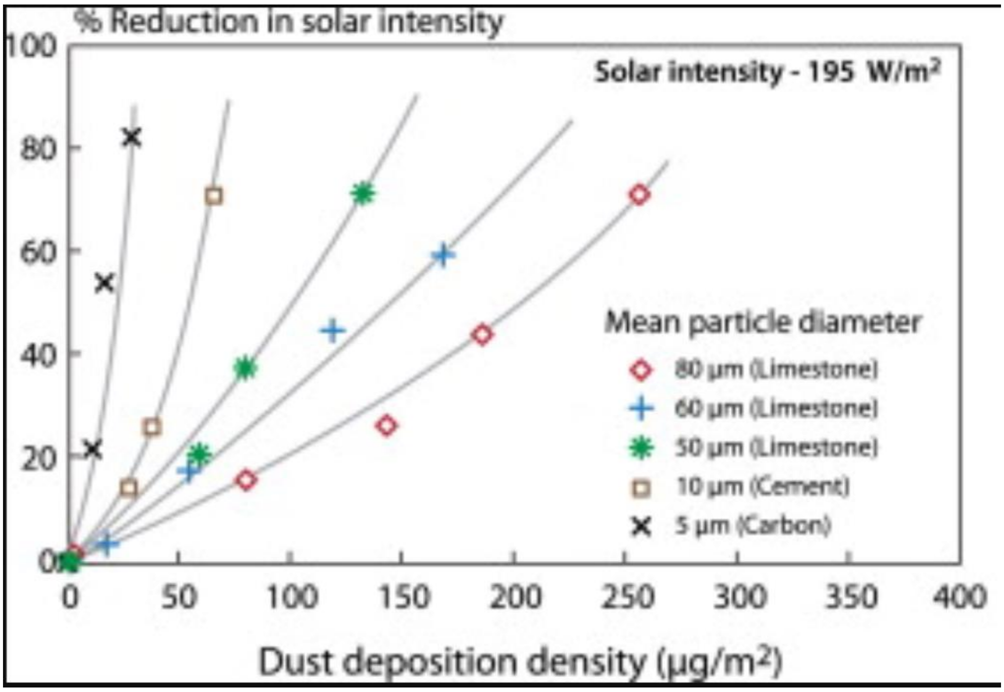

Figure 6-23: Soiling and particle size. Image from Mohammad S. El-Shobokshy, Fahmy M. Hussein, Degradation of photovoltaic cell performance due to dust deposition on to its surface, Renewable Energy, 1993

Biological Films: For these films to develop mineral dust particles as well as pollution and organic material such as pollen must first be deposited to give microbes a surface to latch onto as well as a source of nutrients. Microbes such as bacteria and fungi can then form colonies along the surface of the glass. Many microbes that form biofilms produce extracellular polymeric substances (EPS) which are high molecular weight biopolymers that anchor the organisms to the solar modules surface.[7] The biofilms also trap other types of soiling beneath their surface thus creating a surface that cannot be removed by rainfall. Biological films are a problem in warm humid regions such as Brazil.[8]

Wind Speed: Wind speed strongly effects the mass flow rate of dust and other soiling particles as well as the size of the average particles deposited. In order for fine sand (100 microns diameter) to be deposited the wind speed must be above 3 ms^{-1}. At lower wind speeds only fine silts and clays are deposited.[9,10]

Rainfall: The frequency of rainfall events influences the annual soiling losses for solar modules. As can be seen in the graph below from NREL, each rainfall event partially resets the soiling losses but there is a gradual accumulation without other cleaning methods.

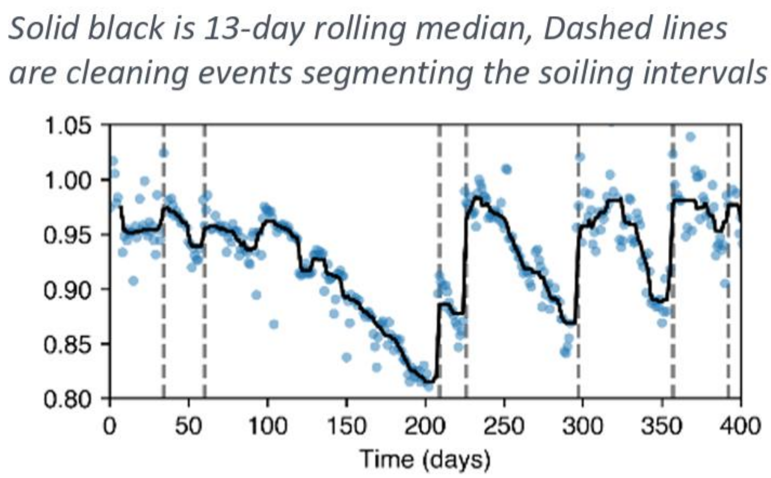

Figure 6-24:Rain cleaning. Graph from M. Deceglie, L. Micheli, M. Muller, "Quantifying soiling loss directly from PV yield," IEEE Journal of Photovoltaics, vol. 8. 2018.[11]

Bird droppings: Bird droppings can be particularly harmful to solar PV modules as they leave some solar cells partially shaded while others are fully unshaded. This causes non uniform illumination of the solar module leading to hotspots as the non-illuminated cells have a higher resistance and thus suffer from Joule heating from the current generated by the other cells connected in series. Solar cells that experience hotspots degrade at a much faster rate than their neighbours as thermal degradation rate of solar cells is governed by the Arrhenius equation, so is exponential with respect to temperature.

Figure 6-25: Various soiling types. The image is from Klemens Ilse et al, Techno-Economic Assessment of Soiling Losses and Mitigation Strategies for Solar Power Generation, Joule, 2019[12]

7.2 Surface Energy and Contact Angle

Surface energy quantifies the extra energy present at a material's surface due to disrupted intermolecular bonds. Since surface atoms have more energy than those in the bulk, surfaces are less energetically stable. Surface energy can be defined as the work required to create a new surface or cut a solid, generating two new surfaces with excess energy from incomplete bonding. In an ideal vacuum, surface energy equals half the material's cohesion energy. However, real surfaces often undergo changes like passivation or adsorption to reduce their energy.

Wetting describes how a liquid remains in contact with a solid surface due to intermolecular interactions occurring when they come into proximity. The extent of wetting, known as wettability, depends on the interplay between adhesive forces (which attract the liquid to the solid) and cohesive forces (which keep the liquid molecules bound together). Wettability is commonly assessed through the contact angle, which is the angle formed where the liquid-vapor interface meets the solid-liquid interface.[13] Young's equation provides a fundamental relationship for calculating this contact angle on an ideal, smooth, and homogeneous surface. It is expressed as:

$$\gamma_{SG} = \gamma_{SL} + \gamma_{LG}\cos(\theta) \tag{7.1}$$

Where γ_{SG} is the energy of the solid-gas interface, γ_{SL} is the energy of the solid-liquid interface and γ_{LG} is the energy of the liquid-gas interface. Theta is the contact angle.[14] The diagram below illustrates the physical situation described by the Young equation.

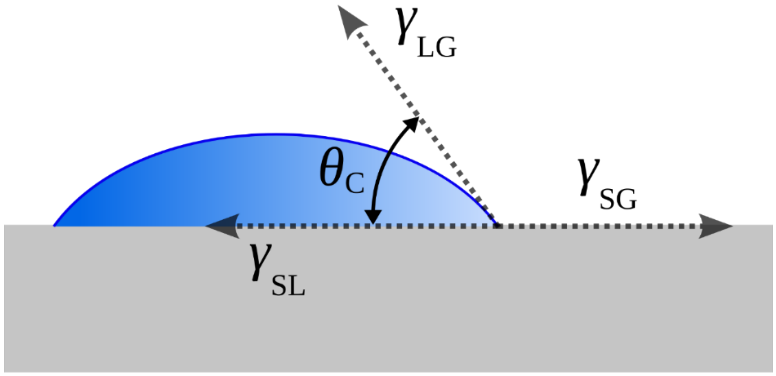

Figure 6-26: Contact angle diagram with 3 interface energies shown

A smaller contact angle (below 90°) signifies high wettability, indicating that the liquid spreads broadly across the surface. In contrast, a larger contact angle (above 90°) reflects low wettability, meaning the liquid beads up, limiting its interaction with the surface.

On an ideal solid surface—one that is smooth, rigid, flat, and chemically uniform—the contact angle remains stable and does not exhibit hysteresis, meaning there is no difference between the advancing and receding contact angles. However, in practical conditions, surface irregularities or chemical variations introduce contact angle hysteresis. This results in multiple stable contact angles, influencing how the liquid spreads. Contact angle hysteresis is given by the equation,

$$H = \theta_a - \theta_r \tag{7.2}$$

Where θ_a is the advancing (larger) contact angle and θ_r is the receding (smaller) contact angle. Surface roughness causes contact angle hysteresis as microscopic irregularities trap liquid, requiring additional force to advance or recede, leading to a range of stable contact angles. Contact angle hysteresis can also be caused by a non-uniform surface energy due to the material being inhomogeneous or contamination on the surface causing both roughness or surface energy non-uniformity. Highly viscous liquids will also display contact angle hysteresis due to their resistance to flow and deformation. Typically surfaces with a high contact angle hysteresis are hydrophilic while low contact angle hysteresis surfaces are hydrophobic.

The Young model is adequate for describing droplets on flat surfaces but for rough surfaces there are two other models to describe the system. The Wenzel model proposes that the liquid infiltrates surface roughness, enhancing wettability on hydrophilic surfaces while diminishing it on hydrophobic ones. The Cassie–Baxter model suggests that the liquid remains atop surface features, trapping air underneath. This mechanism often reduces wettability and will be discussed in more detail later.

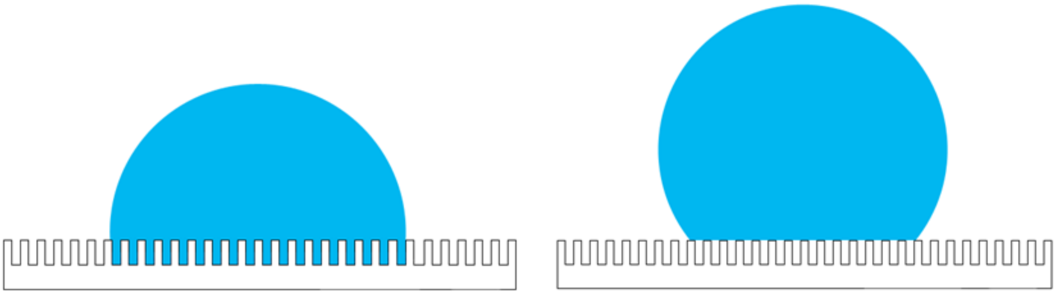

Figure 6-27: Wenzel vs Cassie-Baxter. The Wenzel model (left) and Cassie-Baxter model (right) images taken from the Wikipedia article on wetting[15]

The Wenzel wetting mechanism can be described by the following equation,

$$cos(\theta^*) = r\ cos(\theta) \quad 7.3$$

Where θ^* is the measured contact angle and θ is the contact angle for the system had the surface been flat. The variable r is the roughness ratio and is the ratio of the total surface area to the equivalent surface area had the system been flat. In the Wenzel model the surface roughness simply amplifies the inherent hydrophobicity or hydrophilicity of the surface. The Cassie-Baxter model is more complex and is given by the equation below,

$$cos(\theta^*) = r_f\ f\ cos(\theta) + f - 1 \quad 7.4$$

Where r_f is the roughness ratio of the parts of the surface that are wet, while f is the ratio of wet surface to non-wet surface. When r_f and f are equal to 1 then the Cassie-Baxter model simplifies down to the Wenzel model. Typically, the Cassie-Baxter state will abruptly transition to the Wenzel state as the spacing between the features of a roughened or patterned surface grows beyond a critical size. The Cassie–Baxter to Wenzel transition condition is given by the following equation,

$$cos(\theta_C) = \frac{f - 1}{r - f} \quad 7.5$$

Where θ_C is the critical contact angle and the other variables are the same as before. The critical angle represents the lowest contact angle a droplet can maintain while still being supported by the trapped air pockets beneath it. If the contact angle decreases beyond this point, the capillary forces and surface tension overcome the ability of the roughness to trap air, resulting in liquid infiltration. This transition is typically irreversible and leads to increased adhesion between the liquid and the surface. Normally the liquid fills the gaps from the centre and then propagates outwards beyond the boundaries of the droplet. This wicking effect is illustrated in the below diagram.

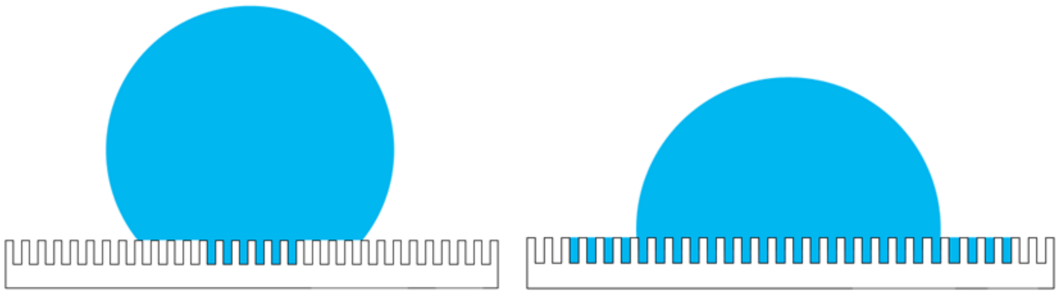

Figure 6-28: The Cassie-Baxter to Wenzel transition. The transition nucleates in the centre of the droplet and propagates outwards to form a film around the droplet. Image from Wikipedia[15]

The formation and spread of a water film typically begins when water starts to invade the roughness due to condensation, external pressure, or electrostatic and capillary forces. Condensation within the surface microcavities displaces air, allowing the liquid to penetrate deeper. If pressure is applied to the droplet, either mechanically or through environmental forces like wind or vibration, water is forced into the texture, accelerating the transition. Additionally, surface energy variations, such as electrostatic attraction or capillary action, can further drive water infiltration. For super-hydrophobic surfaces (contact angle above 150^{o}) droplets will quickly roll of a surface, particularly if it is at an angle. This reduces the chance of the droplet penetrating the features.

The Cassie-Baxter to Wenzel transition is highly important when designing a textured hydrophobic or hydrophilic surface. By understanding this process, it is possible to determine the optimal feature sizes to achieve either Cassie-Baxter (hydrophobic) or Wenzel (usually hydrophilic unless the surface chemistry is already hydrophobic) wetting.[16] When designing patterned micro/nano surfaces having a superhydrophilic surface may mean one is close to having a superhydrophobic surface if the features are made just a bit smaller. The following figure shows the required roughness for super hydrophilic (contact angle near zero) behaviour.

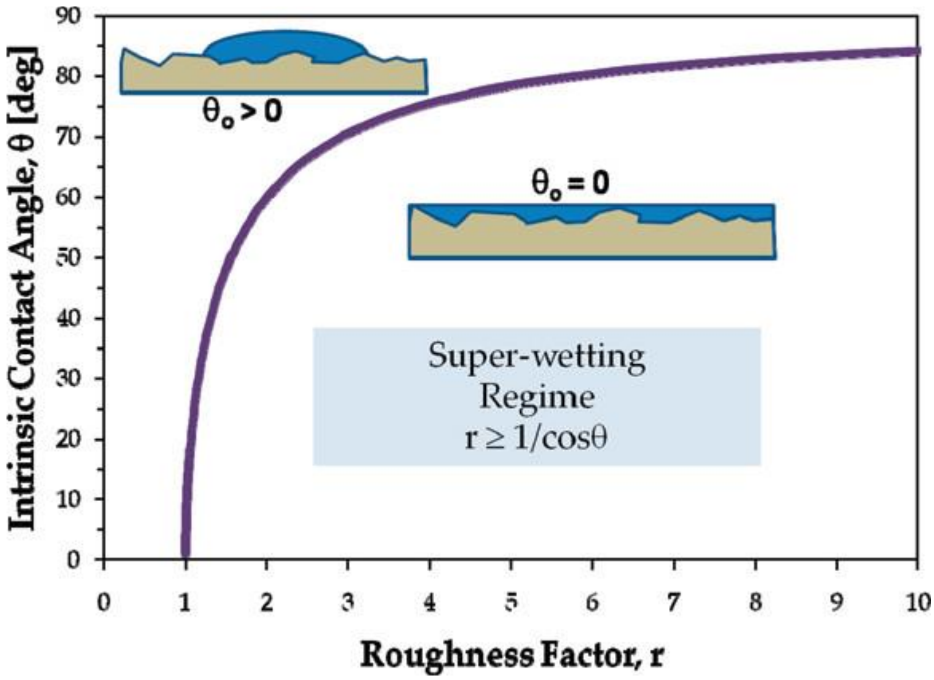

Figure 6-29: The roughness factor required to make a surface superhydrophilic for a given intrinsic contact angle (contact angle if the surface were flat). Image from Jaroslaw Drelich, Emil Chibowski, Superhydrophilic and Superwetting Surfaces: Definition and Mechanisms of Control, Langmuir, 2010[17]

7.3 SURFACE WETTING IN NATURE

Surface wetting plays a crucial role in nature, with plants evolving specialized surface structures to control water behaviour. Two of the most well-known examples are the lotus leaf and the rose petal, both of which exhibit super hydrophobicity but with distinct wetting properties.

The lotus leaf demonstrates extreme water repellence and self-cleaning behaviour, known as the lotus effect. This effect arises from the combination of a hydrophobic wax coating and a hierarchical surface structure. The surface consists of microscopic protrusions covered with nanoscale wax crystals, creating a rough texture that traps air pockets beneath water droplets. As a result, droplets remain in the Cassie-Baxter state and roll off effortlessly, removing dirt and contaminants in the process. This self-cleaning mechanism has inspired various biomimetic applications, including self-cleaning coatings, waterproof textiles, and anti-fouling surfaces.

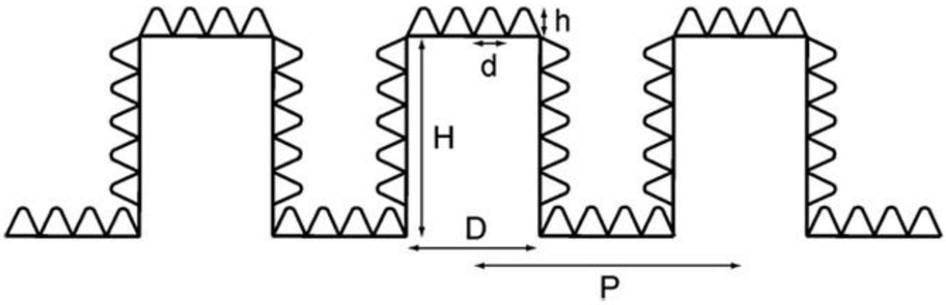

Figure 6-30: An idealized hydrophobic structure inspired by the lotus leaf. Image from Bharat Bhushan, Yong Chae Jung, Natural and biomimetic artificial surfaces for superhydrophobicity, self-cleaning, low adhesion, and drag reduction, Progress in Materials Science, 2011.[18]

In contrast, the rose petal also exhibits super hydrophobicity but with high water adhesion. Unlike the lotus leaf, where water droplets roll off easily, droplets on a rose petal remain pinned to the surface even when the petal is inverted. This adhesion is due to the presence of micro papillae on the petal's surface, which, although similar in size to those on the lotus leaf, feature additional nanoscale folds that partially trap water within their structure. This results in a Cassie-impregnated state rather than a purely Cassie-Baxter state. The droplet retains its spherical shape but adheres strongly to the petal due to capillary forces and localized contact with the nanostructures. Unlike the lotus leaf, the rose petal does not exhibit self-cleaning properties, but its ability to retain water droplets may contribute to hydration and the attraction of pollinators.

Figure 6-31: The rose petal effect can be seen on this rose. The droplets have a high contact angle but remain adhered to the petals even when the droplets are upside down.

Both surfaces demonstrate super hydrophobicity but lead to different functional outcomes. The lotus leaf promotes water repellence and self-cleaning, whereas the rose petal retains water through strong adhesion. These distinct natural wetting behaviours have inspired numerous engineered materials. The lotus effect has led to the development of hydrophobic coatings, stain-resistant fabrics, and self-cleaning glass, while the rose petal effect has provided insights for designing high-adhesion surfaces, bio-inspired adhesives, and microfluidic systems for controlling liquid movement.

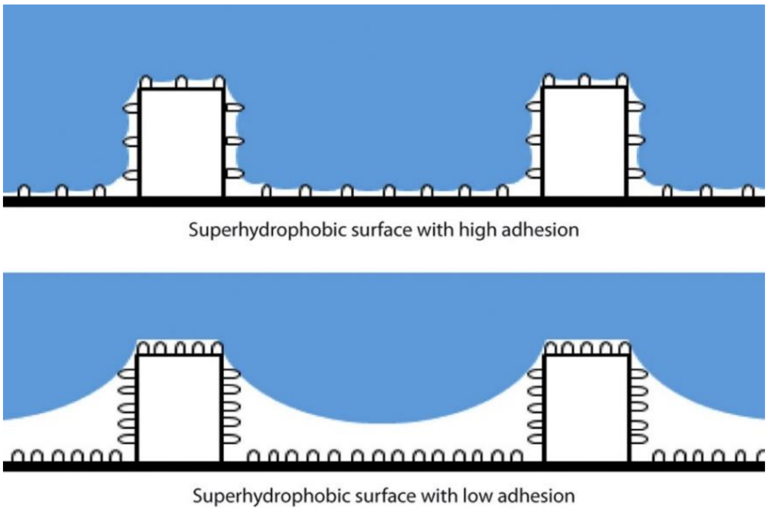

Figure 6-32: This diagram illustrates the difference between the rose petal effect (Top) and the lotus leaf effect (Bottom) . Image from Daniel Ebert, Bharat Bhushan, Wear-resistant rose petal-effect surfaces with super hydrophobicity and high droplet adhesion using hydrophobic and hydrophilic nanoparticles, Journal of Colloid and Interface Science, 2012.[19]

7.4 SELF-CLEANING TEXTURED SURFACES

Hydrophobic Self-Cleaning: The self-cleaning ability of superhydrophobic surfaces is primarily due to low adhesion and rolling water droplets that remove contaminants. The mechanism can be broken down into several key interactions. The first of these is rolling water droplets picking up dirt. When water droplets land on a superhydrophobic surface, they form a near-spherical shape due to the low surface adhesion. Due to the trapped air and minimal contact area between the droplet and the surface, the droplet has very low friction and can roll off easily. As the droplet rolls, it picks up dust, dirt, and other contaminants from the surface, carrying them away. This is due to the dirt's greater adhesion to the droplet than the surface.

Dirt particles typically adhere to surfaces through van der Waals forces, electrostatic interactions, or capillary bridges (in humid conditions). On superhydrophobic surfaces, the trapped air layer reduces these adhesive forces, making it difficult for particles to stick. If a dust particle lands on the surface, it rests on the micro/nanostructures with a minimal contact area, significantly lowering adhesion. The air cushion in the Cassie-Baxter state also prevents the formation of liquid bridges (propagated liquid film caused by wicking) that would otherwise cause contamination to adhere during humid conditions. In dry conditions such as in deserts, rainfall cannot be relied upon to remove soiling. Thus, anti-soiling coatings in these regions should reduce dust adhesion without the need for rolling droplets to carry the dirt away. In real-world conditions, wind and vibration can also help remove loosely attached contaminants from superhydrophobic surfaces. Since adhesion is low, even mild mechanical disturbances (such as rain impact or airflow) can remove dirt effectively.

Hydrophilic Self-Cleaning: Super-hydrophilic surfaces are those that exhibit extremely low contact angles, usually less than 5°, meaning that water spreads almost completely across the surface rather than forming droplets. This spreading occurs because the high surface energy of the surface pulls the water molecules toward it, causing the droplet to flatten and form a very thin water film. The spreading of water creates a dynamic flow across the surface, which can carry away dirt and contaminants that might be present. As the water spreads, it can trap dirt particles or contaminants, effectively loosening them from the surface. The flow of water is typically unimpeded due to the high wettability of the surface, making it easier for the water to carry away even small debris or particles. The movement of this water film can also be a very effective method for removing biological contaminants, such as bacteria or algae, from the surface. The continuous motion of water prevents such organisms from adhering firmly, thus keeping the surface clean without requiring frequent interventions.

Super-hydrophilic surfaces can also exhibit antifouling properties, which means that they resist the accumulation of unwanted materials such as microorganisms or algae. Because water spreads uniformly across the surface, it prevents these contaminants from attaching strongly, reducing the risk of biofilm formation. The uniform layer of water effectively discourages the attachment of contaminants, ensuring the surface remains cleaner for longer periods.

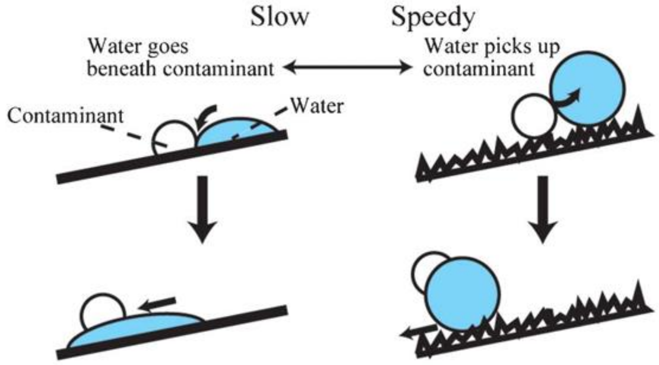

Figure 6-33: Comparison of the superhydrophilic self-cleaning mechanism and the superhydrophobic self-cleaning mechanism. Image from Shunsuke Nishimoto and Bharat Bhushan, Bioinspired self-cleaning surfaces with superhydrophobicity, superoleophobicity, and superhydrophilicity, RCS Advances, 2013.[16]

Hydrophobic vs hydrophilic: In conclusion, regarding the suitability of superhydrophobic and hydrophilic surfaces for use as anti-soiling coatings for solar panels both designs have their merits. Hydrophobic surfaces have the advantage of low effective surface energy, this is useful as it reduces the adhesion not only of water but also dust, pollen and other small particles. As a result they are more suited to arid, dusty environments where water assisted cleaning cannot be relied upon. One difficulty with this technology is its relative fragility, glass is naturally hydrophilic and only a micro/nano patterned surface of the correct dimensions will make it hydrophobic, thus if the pattern wears away or is scratched in places then the surface will revert to being hydrophilic. The surface chemistry can be altered by adding Teflon like fluorocarbons or chemicals that form a non-polar surface such as HMDS (Hexamethyl di-siloxane). These chemicals will eventually degrade when exposed to the UV radiation in sunlight which can break organic bonds but not the strong bonds in the glass silica networks.

Super hydrophilic surfaces on the other hand are only useful for self-cleaning in environments with high levels of rainfall or humidity.[20] Otherwise the high surface energy just increases the adhesion forces of dust to the solar module surface. Their main advantage lies in their relative simplicity, as glass is already somewhat hydrophilic this effect is enhanced by patterning the surface to increase the overall surface area, this will increase the hydrophilicity as per the Wenzel model. [21] Hydrophilic surfaces are also less affected by small defects than hydrophobic surfaces, a small scratch in a hydrophobic surface can stop the droplets from rolling by pinning them in place.

7.5 DROPLET SIZE AND SELF CLEANING

Another solution is to use a combination of both hydrophobic and hydrophilic surfaces to enhance self-cleaning by increasing droplet size and water collection.[22] Hydrophilic surfaces are good hygroscopic surfaces meaning they promote the condensation of water vapour. This is useful as it leads to dew forming on solar panels in humid conditions even when it is not raining. By having dots or strips of the solar modules surface that are hydrophilic while the rest of the surface is hydrophobic droplets will form more regularly and will roll off the panel when they reach a critical size where their weight overcomes their adhesion to the glass.

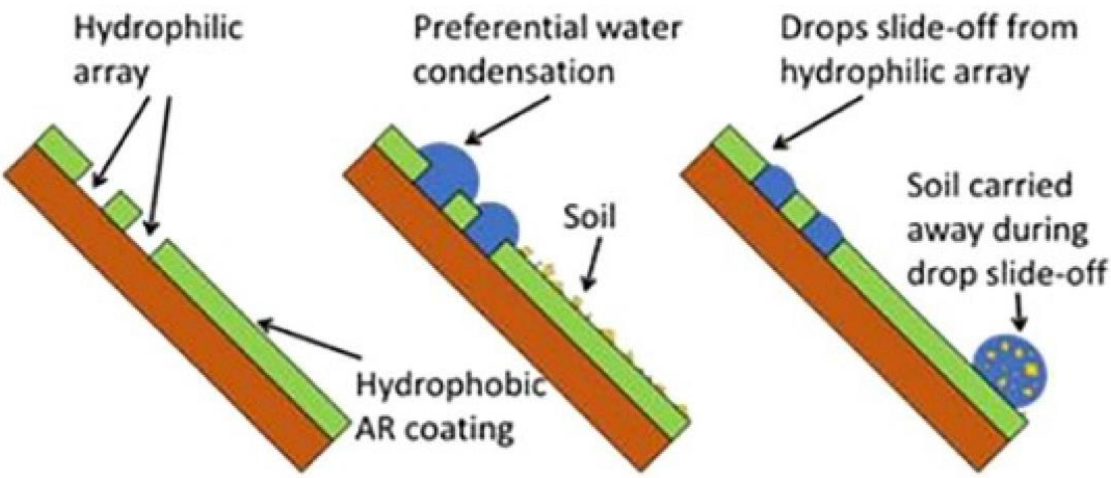

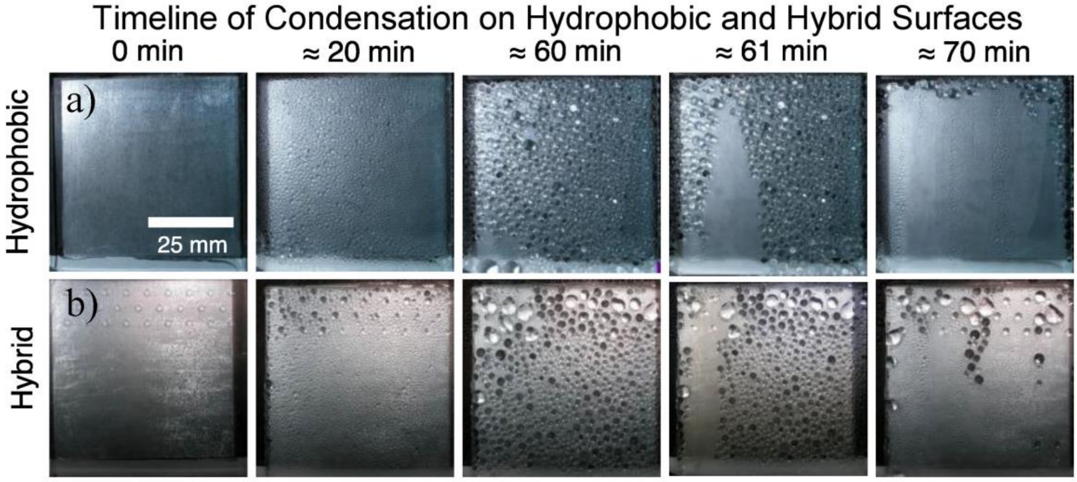

Figure 6-34: Hybrid surface. Top: A hydrophobic coating with holes exposing a hydrophilic layer, this causes droplets to nucleate at this point until they reach a critical size and roll off. Bottom: Condensation of water on two surfaces, note the larger average droplet size on the hybrid surface. Top image from https://www.duramat.org/projects/hybrid-coating[23]. Bottom image from Illya Nayshevsky, QianFeng Xu, Alan M. Lyons, Hydrophobic-Hydrophilic Surfaces Exhibiting Dropwise Condensation for Anti-Soiling Applications, IEEE JOURNAL OF PHOTOVOLTAICS, 2019[24]

Hybrid hydrophobic-hydrophilic surfaces can create a coalescence effect, where water droplets merge due to the controlled hydrophilic regions. As smaller droplets combine into larger ones, they sweep up dust that might have otherwise been left behind, resulting in a more thorough cleaning process. Larger droplets possess greater mass and inertia, allowing them to overcome pinning forces more easily and roll across the surface with minimal resistance. As they move, they exert a stronger drag force on contaminants, effectively picking up and removing dust and dirt particles.

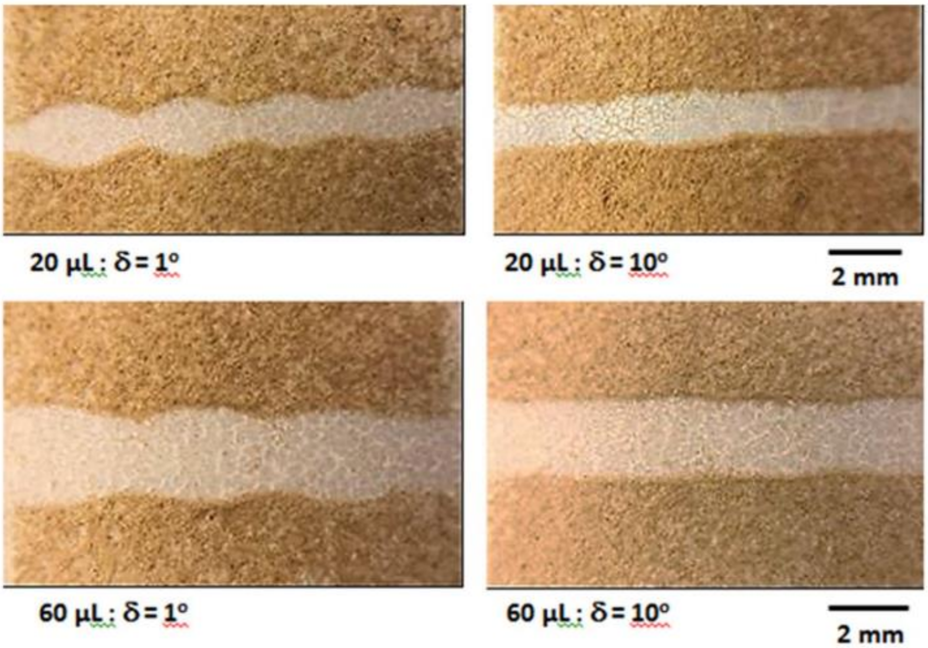

Figure 6-35: Droplet size. Figure shows the improved cleaning ability of larger water droplets (20µL vs 60µL). As can be seen the droplets wobble when angles at 1 degree while they roll in a straight line when angled at 10 degrees. Image from Ghassan Hassan, Bekir Sami Yilbas, Abdullah Al-Sharafi & Hussain Al-Qahtani, Self-cleaning of a hydrophobic surface by a rolling water droplet, Nature Scientific Reports, 2019[25]

Larger droplets will roll at higher velocity due to their greater weight without a proportional increase in drag forces. Higher droplet velocities amplify the shear forces acting on dust particles, leading to more effective cleaning of surfaces such as solar panels.[26] Another key advantage of larger droplets is their ability to minimize residue and streaking. Smaller droplets tend to evaporate quickly, often leaving behind mineral deposits and dust that can cement onto the surface, reducing transparency and light transmission. In contrast, larger droplets are more likely to completely remove contaminants before they evaporate, keeping the panel clear for longer periods.

7.6 CONTACT ANGLE RESULTS

Contact angle measurements were taken with an Ossila contact angle goniometer. The working principle of the goniometer is based on capturing high-resolution images of a droplet deposited on a substrate and analysing the droplet's shape to determine the contact angle. The measurement process begins with precise liquid deposition. A syringe or micropipette is used to dispense a small, controlled volume of liquid onto the solid surface. The instrument ensures consistent droplet formation, minimizing variations caused by external factors such as evaporation or surface contamination.

Once the droplet is placed on the substrate, the goniometer captures a side-view image using an integrated camera and a high-contrast backlight. The quality of this image is critical, as accurate edge detection of the droplet is necessary for precise contact angle measurements. Thus, care should be taken to ensure the image is in focus. The software then processes the image, identifying the liquid-solid and liquid-gas interfaces. Image analysis algorithms fit a mathematical curve, typically a Young-Laplace or polynomial approximation, to the droplet profile to determine the contact angle at the three-phase boundary.[27]

Figure 6-36: The Ossila contact angle goniometer. Image from the Ossila website[27]

Each of the pitted glass samples had their water contact angles measured. Before taking the measurement, every sample was ashed in an ozone plasma asher for 3 minutes to ensure that there were no organic contaminants that would alter the surface chemistry. This was an important step as it was important to demonstrate that changing the geometry of the surface would alter its wettability rather than the surface chemistry which is a more trivial observation. Samples that were coated in HMDS were not ashed as the purpose of the HMDS was to alter the surface chemistry. The table below shows all of the contact angle measurements that were taken. When a number of minutes is mentioned, it refers to how long the sample was wet etched in hydrofluoric acid. The samples below 70 minutes were under etched while anything above was over etched. Nano refers to the glass having nanoscale pillars produced by dry etching.

Table 6

Glass Sample Description	**Contact Angle (Degrees)**
50 min Pitted Glass	47.03
55 min Pitted Glass	56.87
60 min Pitted Glass	82.88
65 min Pitted Glass	82.92
70 min Pitted Glass	80.17
75 min Pitted Glass	28.24
80 min Pitted Glass	20.72
85 min Pitted Glass	55.52
85 min Pitted Glass (Large)	85.21
50 min Pitted Nano	35.24
50 min Pitted Nano (Large)	9.79
50 min Pitted Nano Ashed*2 (Large)	0 (angle too low to measure)
85 min Pitted Nano	4.21
Flat Glass Unmodified	49.85
Flat Glass Nano	5.39
Flat Glass HMDS	96.48
17 min Bowl	30.38
17 min Bowl HMDS	54.17
120 grit sandblasted glass	22.17
500 grit sandblasted glass	72.22
600 grit sandblasted glass	22.67
Flat Glass Nano (extra small pillars)	0 (angle too low to measure)

As can be seen in the table, the nanopillars made any given surface more hydrophilic, with (50 min and 85 min) pitted and flat glass having super hydrophilic properties (contact angle below 5 degrees). As for the microtextured but not nano textured surfaces the relationship between etch time and contact angle was not straightforward. As was seen in Chapter 6 the over etched samples were very rough. This high roughness increases the roughness factor r so according to the Wenzel model if the glass is hydrophilic to begin with then the roughened glass with a greater effective surface area will be even more so. When the etching time was increased to 85 mins the contact angle increased again, this is because the roughness peaks around the time that the mask fails during the wet etching process as this failure is not perfectly uniform causing uneven etching. As the etching process progresses further beyond this point the roughed features are smoothed out somewhat. The sensitivity to roughness can be clearly seen for the sandblasted samples where 500-micron sized grit, sandblasted glass had a very different contact angle to 120 and 600 grit.

Some of the most interesting contact angle measurements are shown here. The microtexturing increases the surface area of the glass in contact with the water. This increased surface area makes hydrophobic surfaces more hydrophobic and hydrophilic surfaces more hydrophilic.

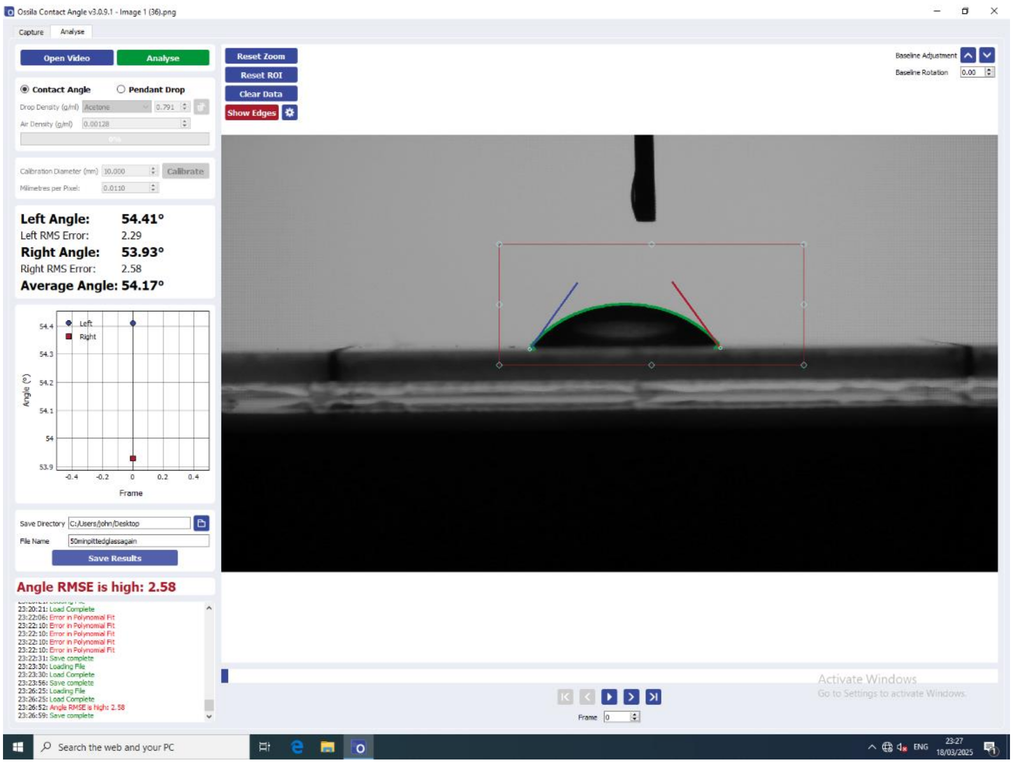

Figure 6-37: 50 min Pitted: This underetched sample did not alter the normal water contact angle significantly (contact angle went from 49.85 to 54.17 degrees)

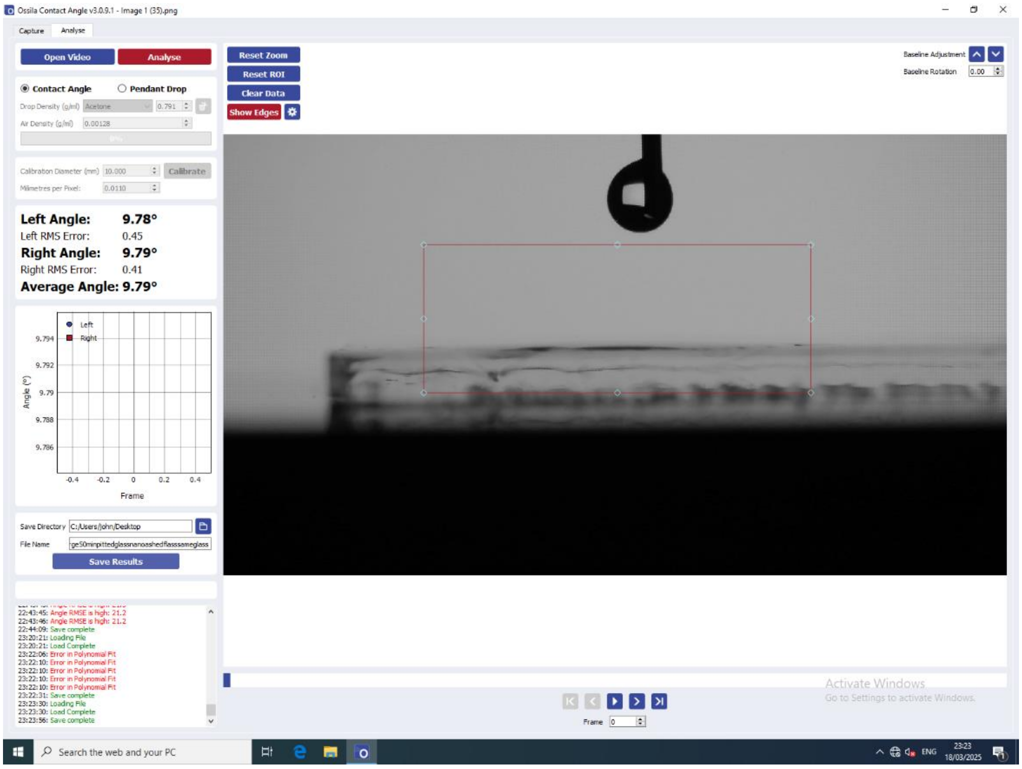

Figure 6-38: 85min Pitted Nano: This overetched surface with nanopillars showed super-hydrophilic behaviour. The contact angle was too small to measure so was set to zero.

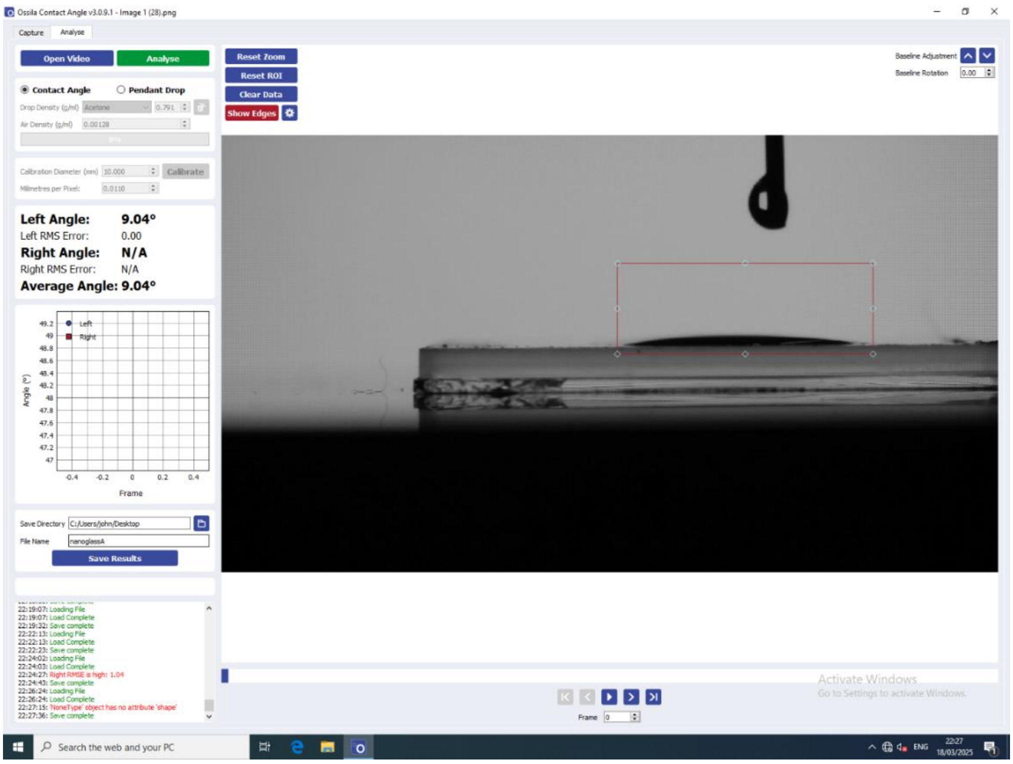

Figure 6-39: Flat Glass Nano: Nanopillars on flat glass, contact angle is larger than the hierarchical structure but is still highly hydrophilic.

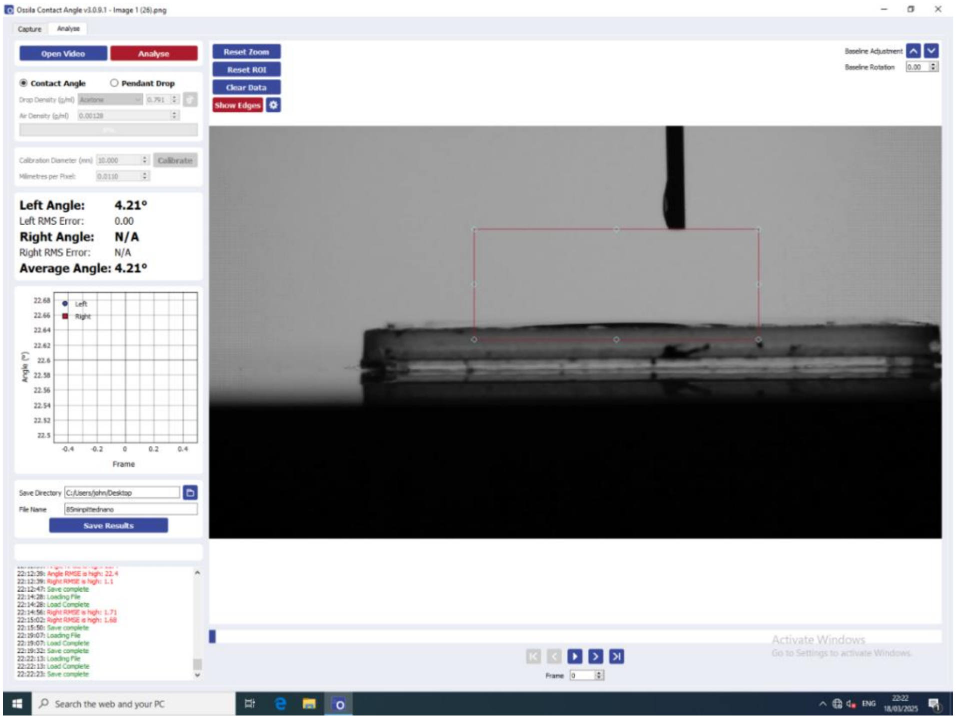

Figure 6-40: 50 min Pitted Nano: Hierarchical structure this time with underetched pits. It is super-hydrophilic like the previous hierarchical structure with a slightly higher contact angle due to the reduced surface area of the underetched pits which are less rough and have a higher surface area.

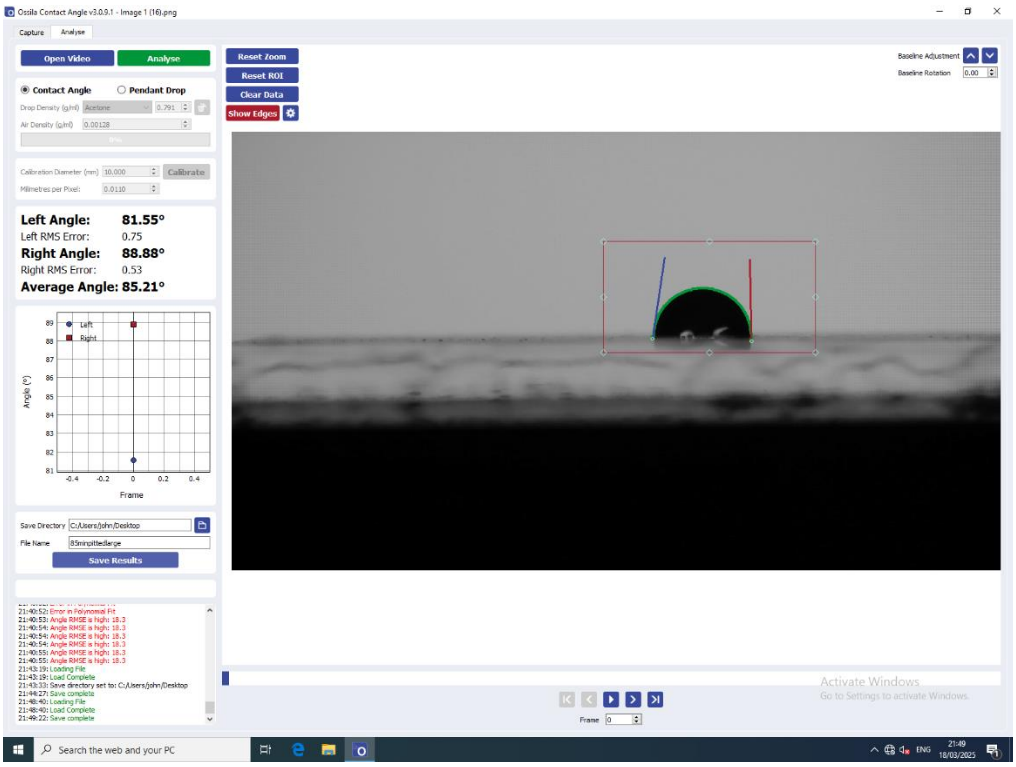

Figure 6-41: 85 min Pitted (Large). Overetched pitted glass with no nanostructure. Large refers to special glass samples with a greater textured area that were used in haze measurements.

7.7 Sand and Dust Adhesion Test

For dry adhesion tests two materials were used, coarse sand and fine sand. The materials were viewed under an optical microscope to grade their typical particle size. Coarse sand was quickly discarded as a candidate as it displayed no adhesion under any circumstances due to its large particle size. Fine sand can be seen in the following figure.

Table 7

Name				Size range (mm)
Very coarse soil		Large boulder	lBo	>630
		Boulder	Bo	200–630
		Cobble	Co	63–200
Coarse soil	Gravel	Coarse gravel	cGr	20–63
		Medium gravel	mGr	6.3–20
		Fine gravel	fGr	2.0–6.3
	Sand	Coarse sand	cSa	0.63–2.0
		Medium sand	mSa	0.2–0.63
		Fine sand	fSa	0.063–0.2
Fine soil	Silt	Coarse silt	cSi	0.02–0.063
		Medium silt	mSi	0.0063–0.02
		Fine silt	fSi	0.002–0.0063
	Clay		Cl	≤0.002

Chart that grades grains by particle size, data from Charles W. Finkl, Chris Makowski, Encyclopedia of Earth Sciences Series, 1978[28].

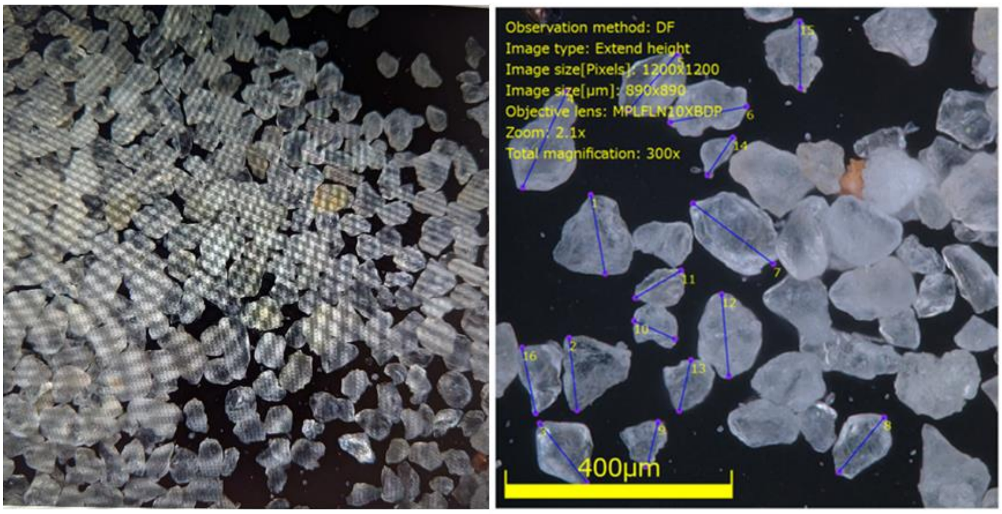

Figure 6-42: Microscope image of fine sand with an average particle size of 100μm. Some particles were below 10μm and can be classed as silt.

The sand was applied to the glass samples by pouring the sand onto the glass until it was completely buried then lifting the glass up with a tweezers and tilting it 90 degrees. Due to the relatively low adhesion of fine sand this gentle method was employed so that at least some sand would adhere to the surface. The results can be seen below.

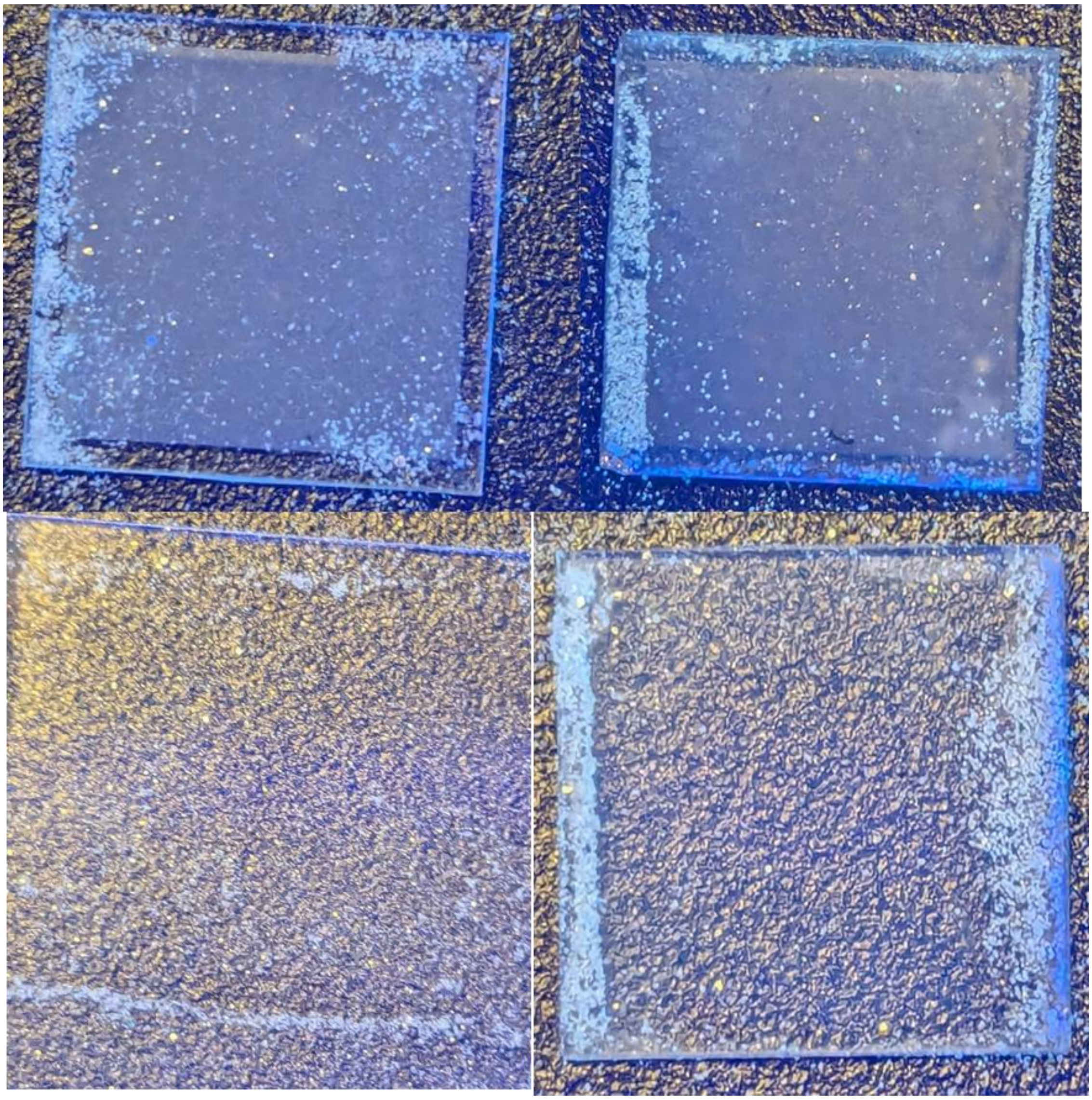

Figure 6-43: Sand adhesion Top Left: 50 min Pitted Glass Nano, Top Right, 85 min Pitted Glass Nano, Bottom Left: Glass Slide, Bottom Right: Flat Glass Nano

As can be seen the fine sand adhered well to the flat glass margin around the textured samples but was unable to adhere to the textured glass surface. The explanation for this is that the sand particles are larger than the micro pits which are 40 microns in diameter, this means the sand particles cannot lodge themselves within the pits and only have a limited contact area with the glass which lowers the total adhesion force. The flat glass with nanopillars also displayed reduced sand adhesion for the same reason. The samples were taken under a microscope where the difference in the concentration in sand particles on and off the patterned surface is more visible.

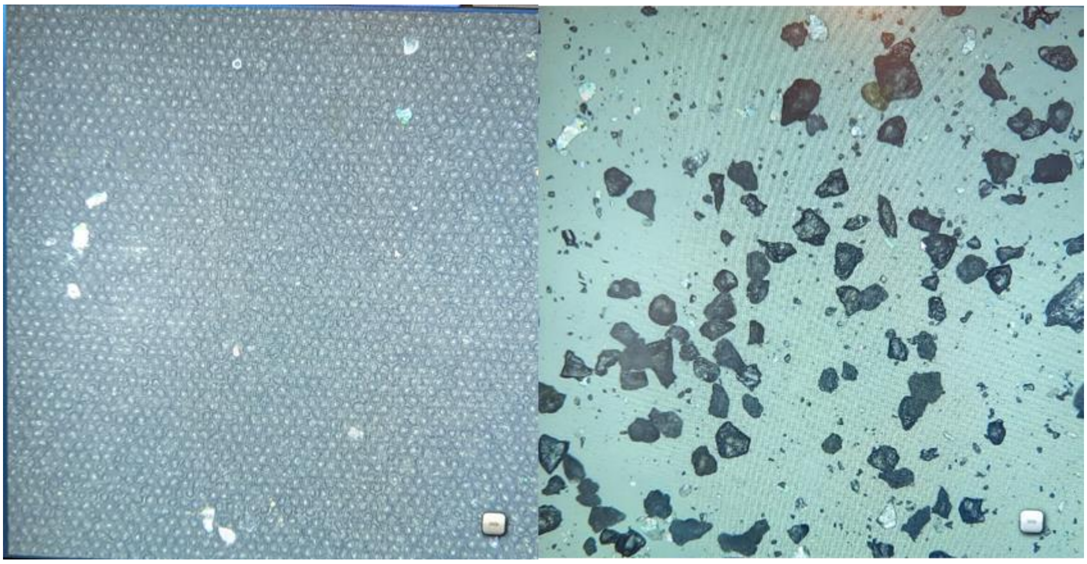

Figure 6-44: Sand adhesion (microscope image). Left: density of sand particles on the 85 min etched surface with nanopillars. Right: The density of sand particles on the flat glass margin around the 85 min etched surface with nanopillars.

The super-hydrophilic cleaning mechanism was demonstrated by coating the 85min etched surface with nanopillars in sand and then dropping a single droplet in the centre of the glass sample. Microscopic and macroscopic images were taken before and after.

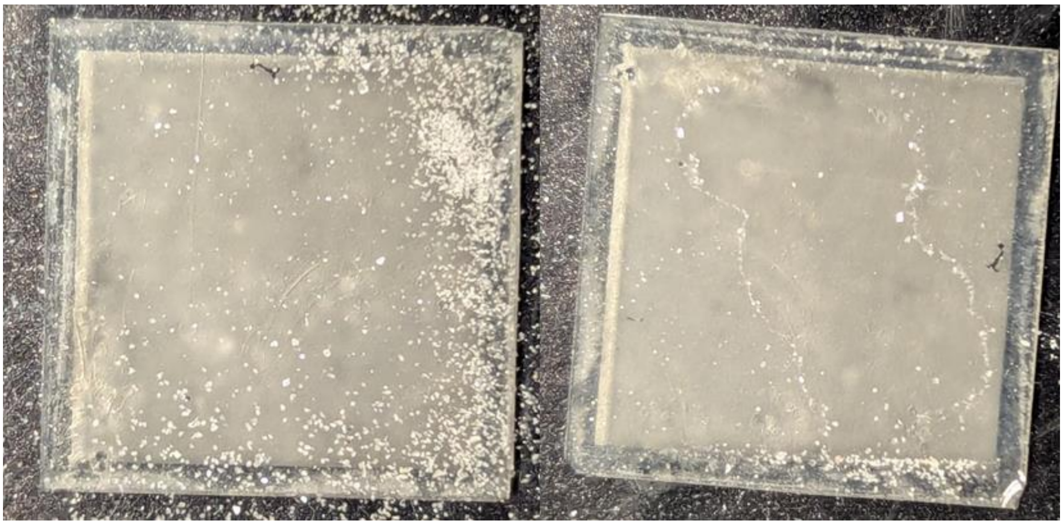

Figure 6-45:Sand cleaning. Left: Micro/nano textured glass before water droplet. Right: the same glass sample after water droplet.

As can be seen in the macroscopic images the sand has been displaced from the centre and has deposited at the edge of the wetted area. This boundary between the wetted and non-wetted area can be more easily seen in the microscope images.

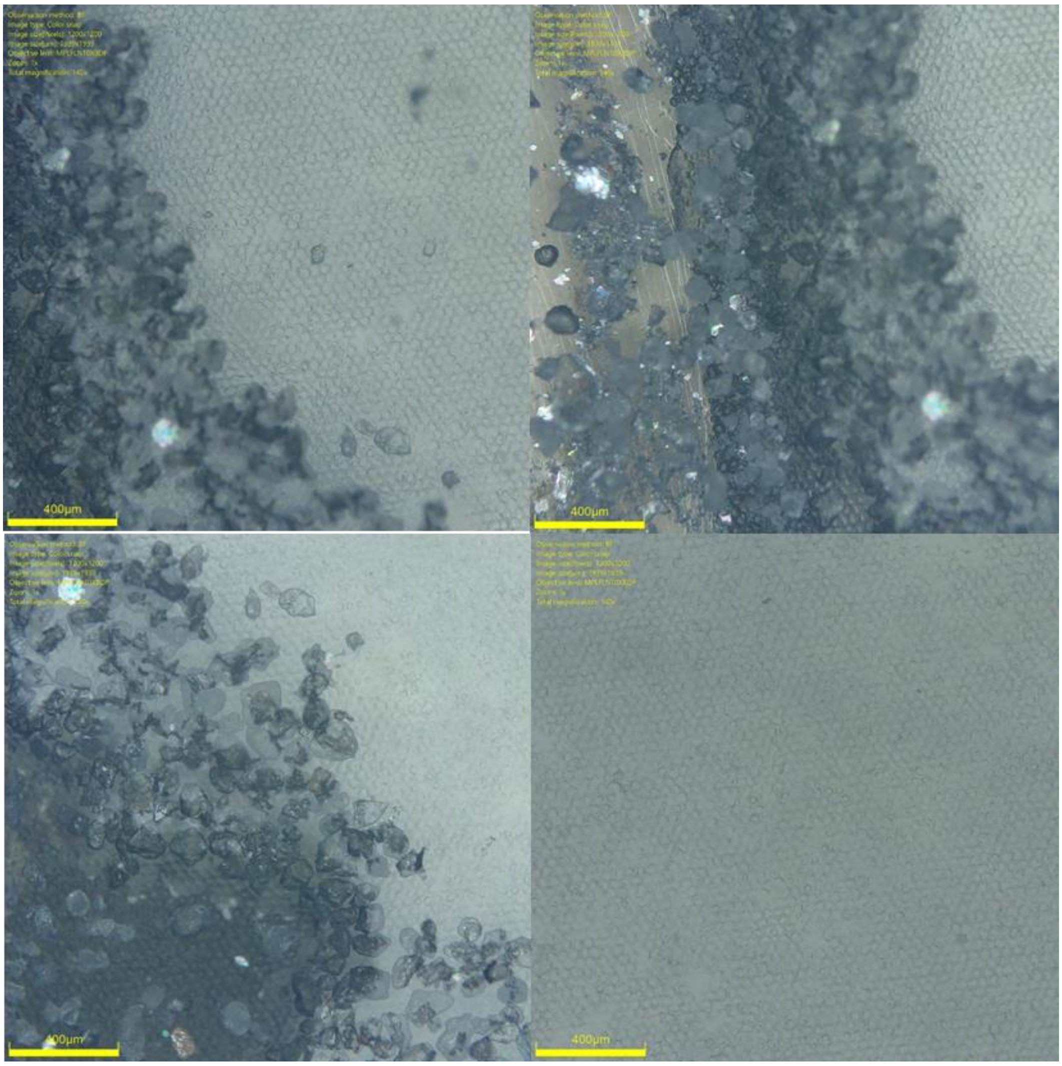

Figure 6-46: Sand cleaning (microscope image). The concentration of sand particles at the edge of the wetted area, light coloured areas are covered in water while the dark areas are dry. The bottom right image is in the centre of the wetted area where all of the sand particles have been removed.

7.8 Effect of Ordinary Droplet on Fine Sand

As can be seen in Figure 7-26, the fine sand particles were effectively displaced by the droplet on a superhydrophilic surface. It was important to show that this displacement of fine sand and dust is less effective for high contact angle droplets. The following Figure 7-27 shows a high contact angle droplet (48^{o} degrees on pitted glass with no nanopillars).

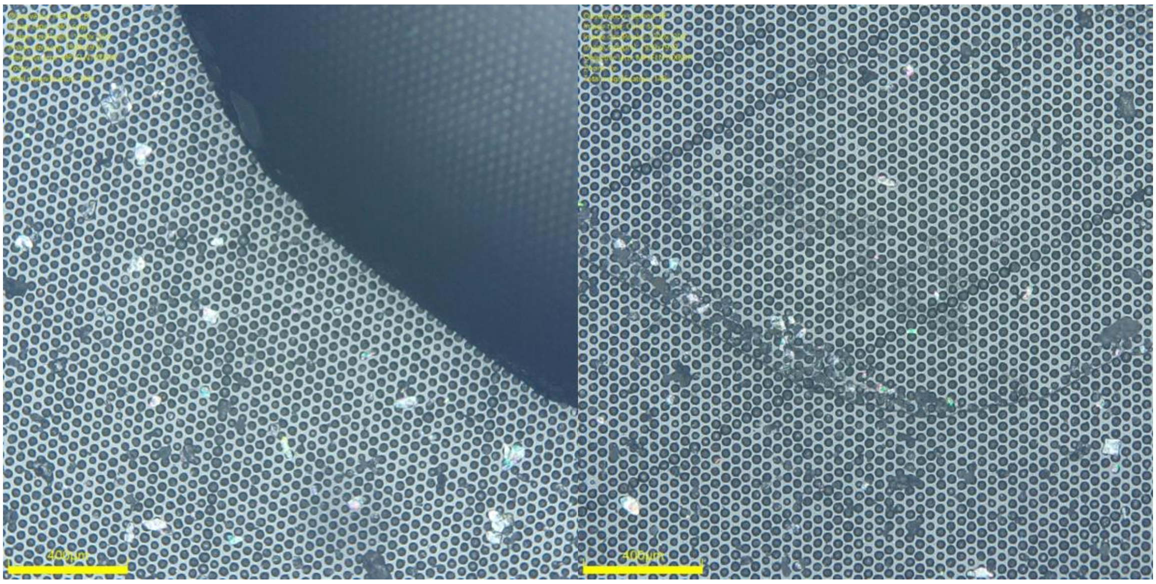

Figure 6-47: Pitted glass with no nanopillars, the droplet had a high contact angle and evaporated when the glass was put on a hot plate. Sand particles remain where in areas that were covered by the droplet. Thus, the high contact angle droplet was not very effective at displacing fine sand.

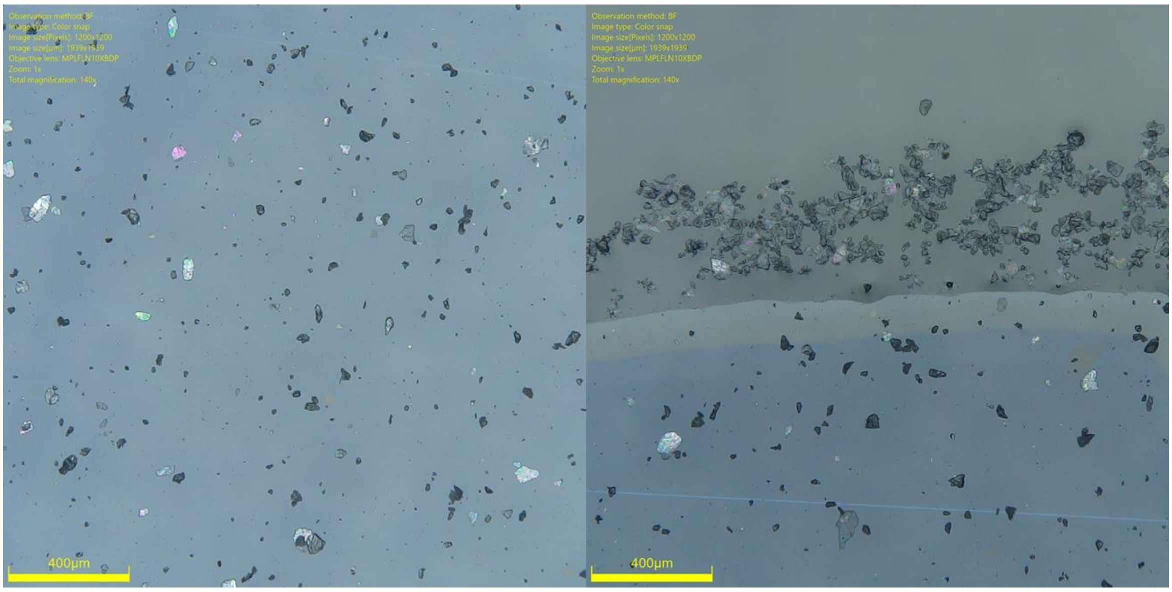

Figure 6-48: Flat glass with the extra small nanoscale pillars. This sample was superhydrophilic, As can be seen there are no sand particles remaining outside the edge of the wetted area which demonstrates effective self-cleaning.

7.9 CONCLUSIONS

To conclude, the hierarchically textured surfaces with both microscale pits and nanopillars displayed super hydrophilic behaviour which is desirable for self-cleaning provided there is plenty of humidity or rain in the environment that the technology is employed. This is the opposite of what was originally intended which was to form a superhydrophobic surface inspired by the lotus leaf structure.

While some of the textured surfaces had a higher contact angle than ordinary glass none of them could be classed as superhydrophobic. It is likely that further tuning of the micro and nano features would achieve a superhydrophobic surface. Achieving this on glass without the aid of a functionalized surface of organic chemicals is desirable for outdoor applications where UV radiation will eventually degrade these surfaces. The sand adhesion tests gave favourable results although even finer particles should have been used to test the limits of these surfaces.

7.10 REFERENCES

(1) Soiling Losses – Impact on the Performance of Photovoltaic Power Plants. **2023**.

(2) Jones, R. K.; Baras, A.; Saeeri, A. A.; Al Qahtani, A.; Al Amoudi, A. O.; Al Shaya, Y.; Alodan, M.; Al-Hsaien, S. A. Optimized Cleaning Cost and Schedule Based on Observed Soiling Conditions for Photovoltaic Plants in Central Saudi Arabia. *IEEE J. Photovolt.* **2016**

(3) Fernández Solas, Á.; Riedel-Lyngskær, N.; Hanrieder, N.; Norde Santos, F.; Wilbert, S.; Nygard Riise, H.; Polo, J.; Fernández, E. F.; Almonacid, F.; Talavera, D. L.; Micheli, L. Photovoltaic Soiling Loss in Europe: Geographical Distribution and Cleaning Recommendations. *Renew. Energy* **2025**

(4) Micheli, L.; Muller, M. An Investigation of the Key Parameters for Predicting PV Soiling Losses. *Prog. Photovolt. Res. Appl.* **2017**

(5) Jiang, C.-S.; Moutinho, H. R.; To, B.; Xiao, C.; Simpson, L. J.; Al-Jassim, M. M. Long-Lasting Strong Electrostatic Attraction and Adhesion Forces of Dust Particles on Photovoltaic Modules. *Sol. Energy Mater. Sol. Cells* **2020**

(6) Hossain, M. I.; Ali, A.; Bermudez Benito, V.; Figgis, B.; Aïssa, B. Anti-Soiling Coatings for Enhancement of PV Panel Performance in Desert Environment: A Critical Review and Market Overview. *Mater. Basel Switz.* **2022**

(7) Tanner, K.; Molina-Menor, E.; Latorre-Pérez, A.; Vidal-Verdú, À.; Vilanova, C.; Peretó, J.; Porcar, M. Extremophilic Microbial Communities on Photovoltaic Panel Surfaces: A Two-year Study. *Microb. Biotechnol.* **2020**

(8) Shirakawa, M. A.; Zilles, R.; Mocelin, A.; Gaylarde, C. C.; Gorbushina, A.; Heidrich, G.; Giudice, M. C.; Del Negro, G. M. B.; John, V. M. Microbial Colonization Affects the Efficiency of Photovoltaic Panels in a Tropical Environment. *J. Environ. Manage.* **2015**

(9) Wang, R.; Li, Q.; Zhou, N.; Chang, C.; Guo, Z.; Li, J. Effect of Wind Speed on Aggregate Size Distribution of Windblown Sediment. *Aeolian Res.* **2019**

(10) Zhou, L.; Li, Z.; Huang, B.; Pu, O. Wind Tunnel Test of Sand Particle Size Distribution along Height in Blown Sand. *Sustainability* **2024**

(11) *Quantifying Soiling Loss Directly from PV Yield - National Renewable Energy Laboratory*. https://research-hub.nrel.gov/en/publications/quantifying-soiling-loss-directly-from-pv-yield-2

(12) Ilse, K.; Micheli, L.; Figgis, B. W.; Lange, K.; Daßler, D.; Hanifi, H.; Wolfertstetter, F.; Naumann, V.; Hagendorf, C.; Gottschalg, R.; Bagdahn, J. Techno-Economic Assessment of Soiling Losses and Mitigation Strategies for Solar Power Generation. *Joule* **2019**

(13) Chow, T. S. Wetting of Rough Surfaces. *J. Phys. Condens. Matter* **1998**

(14) (PDF) A Personal Desktop Liquid-Metal Printer as a Pervasive Electronics Manufacturing Tool for Society in the Near Future. *ResearchGate* **2024**.

(15) Wetting. *Wikipedia Commons*; 2025.

(16) Nishimoto, S.; Bhushan, B. Bioinspired Self-Cleaning Surfaces with Superhydrophobicity, Superoleophobicity, and Superhydrophilicity. *RSC Adv.* **2012**

(17) Drelich, J.; Chibowski, E. Superhydrophilic and Superwetting Surfaces: Definition and Mechanisms of Control. *Langmuir* **2010**

(18) Bhushan, B.; Jung, Y. C. Natural and Biomimetic Artificial Surfaces for Superhydrophobicity, Self-Cleaning, Low Adhesion, and Drag Reduction. *Prog. Mater. Sci.* **2011**

(19) Ebert, D.; Bhushan, B. Wear-Resistant Rose Petal-Effect Surfaces with Superhydrophobicity and High Droplet Adhesion Using Hydrophobic and Hydrophilic Nanoparticles. *J. Colloid Interface Sci.* **2012**

(20) He, G.; Zhou, C.; Li, Z. Review of Self-Cleaning Method for Solar Cell Array. *Procedia Eng.* **2011**, *16*, 640–645. https://doi.org/10.1016/j.proeng.2011.08.1135.

(21) Son, J.; Kundu, S.; Verma, L. K.; Sakhuja, M.; Danner, A. J.; Bhatia, C. S.; Yang, H. A Practical Superhydrophilic Self Cleaning and Antireflective Surface for Outdoor Photovoltaic Applications. *Sol. Energy Mater. Sol. Cells* **2012**

(22) Mondal, B.; Mac Giolla Eain, M.; Xu, Q.; Egan, V. M.; Punch, J.; Lyons, A. M. Design and Fabrication of a Hybrid Superhydrophobic–Hydrophilic Surface That Exhibits Stable Dropwise Condensation. *ACS Appl. Mater. Interfaces* **2015**

(23) A Hybrid Hydrophobic-Hydrophilic Coating with Combined Anti-Reflective and Anti-Soiling Properties. *DuraMAT*.

(24) Aslam, A.; Ahmed, N.; Qureshi, S. A.; Assadi, M.; Ahmed, N. Advances in Solar PV Systems; A Comprehensive Review of PV Performance, Influencing Factors, and Mitigation Techniques. *Energies* **2022**

(25) Hassan, G.; Yilbas, B. S.; Al-Sharafi, A.; Al-Qahtani, H. Self-Cleaning of a Hydrophobic Surface by a Rolling Water Droplet. *Sci. Rep.* **2019**

(26) Li, H.; Zhang, Y.; Gu, X. S.; Qi, H.; Yu, J.; Zhuang, J. Study on the Shear Stress and Interfacial Friction of Droplets Moving on a Superhydrophobic Surface. *Colloids Surf. Physicochem. Eng. Asp.* **2022**

(27) *Contact Angle Goniometer*. Ossila. https://www.ossila.com/products/contact-angle-goniometer

(28) Church, M. J. Grain Size and Shape. In *Sedimentology*; Springer: Berlin, Heidelberg, 1978; pp 544–554

8 CONCLUSIONS AND FUTURE WORK

8.1 INITIAL GOALS AND ALTERATIONS

The initial objective of this research was to develop a patterned surface for solar panels capable of efficiently collecting light over a defined angular range corresponding to typical solar positions based on tilt, orientation, and latitude. Early designs, such as sawtooth and fish-scale patterns, aimed to enhance light trapping while incorporating self-cleaning properties to prevent the accumulation of dust, sand, and biological growth. Initially, the choice of surface material was open, allowing consideration of scalable polymer-based solutions such as roll-to-roll nanoimprint lithography on polycarbonate.

A computational approach, using COMSOL ray tracing and MATLAB solar models, guided the initial phase of the research. However, two key findings led to a shift in focus. Firstly, simulations demonstrated that in northern latitudes, the prevalence of diffuse light from cloud cover and atmospheric scattering required a broader angular acceptance than initially anticipated. This suggested that omnidirectional antireflection structures, such as pitted or microlens geometries, would be more effective. Secondly, concerns over UV degradation, delamination, and intrinsic optical limitations of polymer coatings, such as their higher refractive index compared to glass, indicated that a direct modification of the glass surface was a more viable long-term approach.

Following this shift, laser-based patterning of glass was attempted using an excimer laser. However, challenges arose due to power degradation between gas refills and inadequate focusing optics. Alternative approaches, such as weak acid leaching of tempered glass, were explored. These were limited by their dependence on microcrack formation for pattern nucleation, meaning the process was only effective on tempered glass due to its highly stressed surface that readily formed these cracks. The use of tempered glass imposed limitations, as the glass samples could not be diced to smaller dimensions without fracturing. A review of various glass patterning techniques identified hydrofluoric acid (HF) wet etching as the most suitable option, given the available laboratory resources. Soda lime glass was selected over fused silica to maintain relevance to commercial solar modules. In hindsight, beginning with fused silica could have facilitated better control over etch uniformity due to the absence of interfering ions such as Ca^{2+} and Na^{+}. Once the desired patterns were developed in fused silica, the focus could have shifted to the more challenging task of patterning soda lime glass.

For nanoscale structuring, a self-assembled silver dewetting mask was employed to produce hierarchical textures via dry etching. This approach leveraged existing ICP etching capabilities, eliminating the need for complex lithographic steps. Alternative strategies, such as spin-coating porous SiO_2 coatings, were considered but presented challenges in achieving uniform deposition on microscale pits. Specifically, coating the reverse slopes of the pits using spin coating would have been difficult. A promising technique involved co-sputtering zinc and silica, followed by selective etching of zinc to form a graded-index porous SiO_2 layer. This method offered tunable porosity but required further optimization to balance mechanical durability and optical performance.

The project also explored superhydrophobic coatings as a potential anti-soiling measure. However, experimental findings and literature indicated that superhydrophilic surfaces could provide equal or superior self-cleaning properties under conditions of regular rainfall or high humidity. Additionally, superhydrophilic surfaces were less dependent on precise feature dimensions and leveraged the intrinsic hydrophilic nature of glass. By achieving extreme contact angles through geometric modification of the glass surface, the use of fluoropolymer or other chemical coatings—which are susceptible to UV degradation—was avoided.

8.2 CONCLUSIONS

Hierarchically structured glass surfaces were successfully fabricated and demonstrated improvements in both optical and self-cleaning performance. The patterned glass achieved a 3% increase in light transmission under normal incidence, out of a theoretical maximum improvement of 4%. Additionally, pitted glass structures exhibited superior incidence angle modifiers, enhancing light capture at oblique angles compared to unpatterned glass.

The fabricated surfaces also functioned as effective anti-glare coatings, with high optical haze levels reducing specular reflection. While microscale pits alone did not significantly alter the water contact angle, their combination with nanoscale pillars resulted in superhydrophilic behavior, as confirmed by contact angle measurements. The self-cleaning performance of the superhydrophilic glass was evidenced by efficient water-mediated removal of sand particles. This performance compared favorably with both unmodified glass and microscale-patterned glass lacking nanoscale features.

However, nanoscale pillar structures did not contribute to improved light transmission as initially expected. Their optical response exhibited strong wavelength dependence, leading to unintended scattering losses, particularly in the blue spectral range. These losses could potentially be mitigated by optimizing pillar dimensions to better align with the solar spectrum. Another possible contributing factor to these losses is the presence of fluoropolymer residue from the dry etching step. Due to time constraints and limited access to the ICP etching tool, this aspect could not be thoroughly investigated.

A noteworthy finding was that bowl-shaped wet-etched pits exceeded initial expectations in terms of optical performance while also exhibiting lower surface roughness due to shorter etch durations. Extended etch times (50–85 minutes) resulted in increased surface roughness, attributed to non-uniform delamination of the chromium mask and the formation of insoluble salts such as calcium fluoride and sodium fluoride. Additionally, Ca^{2+} and Na^{+} ions in the glass acted as localized etch inhibitors[1], leading to pattern irregularities. To address this, a denser array of smaller pits could be employed to reduce etch times and minimize surface roughness. However, this approach is constrained by mask fabrication limitations, as excessively small chromium/photoresist mask holes hinder HF diffusion and reduce the etch rate. Enhancing HF mixing within the photoresist holes through forced convection may improve the etching process, though this was not pursued due to safety considerations. Furthermore, the resolution of the Heidelberg laser write head imposes constraints on the minimum achievable hole size in the photoresist.

8.3 FUTURE WORK

To further enhance this technology, several refinements are recommended. The wet etching process could be improved by employing a denser pit array and reducing etch duration, thereby preserving optical benefits while minimizing surface roughness. The nanoscale structuring process could also be refined by optimizing the metal dewetting mask and precisely controlling etch duration to improve spectral performance. Alternative nanoscale coatings, such as porous SiO_2 or moth-eye structures, could be investigated to achieve superior antireflective properties.

Future coatings should incorporate selective transmission and reflection characteristics to optimize overall performance. Ideally, coatings should transmit wavelengths above the semiconductor bandgap while reflecting infrared light to reduce thermal losses. Reflecting ultraviolet radiation is also advantageous, as UV light contributes disproportionately to heating while generating minimal useful photocurrent due to recombination and thermalization of excess carrier energy[2].

Durability testing of the hierarchical pitted glass samples is recommended. The microscale pits may serve to protect the fragile nanoscale pillars from abrasive particles such as sand or brush bristles[3]. One relevant accelerated aging test involves applying different grades of felt to the glass surface using a rotary tool (e.g., Dremel) under controlled pressure and rotation speed[4]. Realistic durability tests, such as sand impingement tests, should also be conducted[5].

Ultimately, hierarchical structures must balance optical performance with mechanical durability. For real-world photovoltaic applications, these surfaces must be robust, chemically stable, and economically viable.

8.4 SCALABILITY

While the fabrication techniques employed in this study are not currently suitable for large-scale commercial deployment, potential pathways for scalability exist. The primary limitation in the current process lies in the photoresist patterning step, which required approximately one hour to process a 1.2×1.2 mm² sample. Roll-to-roll lithography offers a promising route for high-throughput manufacturing by directly patterning resist layers on a continuous substrate. Additionally, the nanopillar deposition process could be replaced with more cost-effective alternatives such as TiO_2 nanoparticle coatings[6,7].

Economic feasibility remains a critical consideration. As demonstrated in Chapter 3, the production cost of the patterned surface must remain below €7 per module to be commercially viable. Future research should explore further cost reductions through scalable fabrication techniques and the use of alternative materials.

8.5 Other projects

In parallel with the primary research on hierarchical antireflective surfaces, I contributed to several related solar energy projects. One such project involved collaboration with Anandhi Paritiban on the development of low-cost solar thermal collectors utilizing a honeycomb polycarbonate layer to suppress convective heat losses. My contributions included optical measurements of angular transmittance and an economic assessment of the proposed design.

Another collaborative effort with Erik Soderholm and Sayuj Sasidharan focused on the development of an optimized heat exchanger for passive convective cooling of solar modules. This project involved computational fluid dynamics simulations and the attachment of physical cooling fins to the rear surface of solar panels. My role included setting up schlieren imaging to visualize convective flow patterns.

A more substantial side project involved efforts to fabricate ultrathin Schottky solar cells. These devices aimed to overcome absorption limitations associated with thin active layers by incorporating a Fabry-Pérot resonance cavity at the rear side. Such ultrathin devices offer advantages including reduced material consumption, minimized carrier recombination due to short diffusion paths, and potential for hot carrier extraction. The active layer material used was hydrogenated amorphous silicon, deposited via magnetron sputtering. Challenges encountered included hydrogen blistering in the metal contacts, quantum tunneling due to ultrathin junctions, and device shorting caused by fabrication defects. These issues were systematically addressed, resulting in successful diode formation; however, the devices exhibited negligible photovoltaic efficiency. As this work was beyond the scope of the main thesis and resource-intensive, it was eventually discontinued.

8.6 Final remarks

Porous silica anti-reflection coatings are present on nearly all of these modules and allows the manufacturer to claim a higher efficiency for their product despite the rapid degradation rate of the AR coating. The next generation of AR coatings should be significantly more durable and focus more on anti-soiling properties, solar panels typically have manufacturer warranties of 25 years, and the AR coating should ideally last for a similar timespan. Reduction of dust adhesion is particularly important as this is the main source of soiling in dry arid climates which are also the regions that have high solar insolation.

The solar PV industry is enormous and produces tens of thousands of square kilometres of solar PV modules every year and the total number of modules is growing by over 30% per year as mentioned in chapter 1. Thus, any solution must be low cost and scalable to justify the potentially high capital cost of retooling for the solar glass industry. This project, by focusing on all glass fabrication rather than polymer coating of the glass modules aimed to address the durability issue. Hierarchical structures also enhance the scratch resistance of fragile AR surfaces such as porous silica or moth-eye structures. The project demonstrates that contact angle and reflection properties can both be altered at the same time through glass patterning.

The specific focus on anti-reflection over a broad range of angles is relatively rare in the literature but the MATLAB simulations chapter shows the significance of glancing angle losses, all new AR coating designs should consider the incidence angle modifier and not just the normal incidence reflection. The samples in this project also supressed glare without reducing transmission which is beneficial as it allows solar panels to be placed in locations were previously the glare problem was a concern.

8.7 References

(1) Iliescu, C.; Jing, J.; Tay, F. E. H.; Miao, J.; Sun, T. Characterization of Masking Layers for Deep Wet Etching of Glass in an Improved HF/HCl Solution. *Surf. Coat. Technol.* **2005**

(2) Perrakis, G.; Tasolamprou, A. C.; Kenanakis, G.; Economou, E. N.; Tzortzakis, S.; Kafesaki, M. Ultraviolet Radiation Impact on the Efficiency of Commercial Crystalline Silicon-Based Photovoltaics: A Theoretical Thermal-Electrical Study in Realistic Device Architectures. *OSA Contin.* **2020**

(3) Law, A. M.; Jones, L. O.; Walls, J. M. The Performance and Durability of Anti-Reflection Coatings for Solar Module Cover Glass – a Review. *Sol. Energy* **2023**

(4) Law, A. M.; Bukhari, F.; Jones, L. O.; Abbas, A.; Walls, J. M. Testing the Abrasion Resistance of Porous SiO2 Anti-Reflection Coatings for Solar Cover Glass. In *2022 IEEE 49th Photovoltaics Specialists Conference (PVSC)*; 2022

(5) Miller, D. C.; Muller, M. T.; Simpson, L. J. *Review of Artificial Abrasion Test Methods for PV Module Technology*; NREL/TP-5J00-66334; National Renewable Energy Lab. (NREL), Golden, CO (United States), 2016

(6) Purcar, V.; Răditoiu, V.; Dumitru, A.; Nicolae, C.-A.; Frone, A. N.; Anastasescu, M.; Răditoiu, A.; Raduly, M. F.; Gabor, R. A.; Căprărescu, S. Antireflective Coating Based on TiO2 Nanoparticles Modified with Coupling Agents via Acid-Catalyzed Sol-Gel Method. *Appl. Surf. Sci.* **2019**

(7) Padmanabhan, N. T.; John, H. Titanium Dioxide Based Self-Cleaning Smart Surfaces: A Short Review. *J. Environ. Chem. Eng.* **2020**

9 APPENDIX 1: MATLAB MODEL

Key parts of the Matlab code are shown below. As can be seen the initial 28 lines of code create the array of daily energy losses (Eloss) as well as the total energy incident on the panel (Etot). The panel tilt and orientation is then defined in degrees and then converted to radians. The latitude is then set as 55 degrees North and then converted to radians. The refractive indices of glass and air are then set for use in the Fresnel equations later.

StabilityTest.m | DiffuseIrradianceross1.m | Dublin(Eoin).m | +

```
1  %%%%%%%%%%%%%%%% DUBLIN %%%%%%%%%%%%%%%%%%%%%%%
2
3
4
5
6  %Spring equunox  day 79
7  %Summer solstice day 172
8  %Autumn Equinox  day 265
9  %Winter solstice day 355
10 clear all;
11 th1dit=0;
12 Eloss=zeros(1,365);
13 Etot=zeros(1,365);
14
15 %Solar Geometry
16 tiltd=10; %panel tilt
17 th1d=180; %panel azimuth degree... (0=North... 180=South
18 ph1d=90-tiltd;  %panel elevtion degree.... (90-tilt)
19
20 tilt=tiltd*3.14/180;
21 th1=th1d*3.14/180;%azumith of panel in radians
22 ph1=ph1d*3.14/180; %elvation of panel normal in radians
23 %
24 latd=55;
25 latr=latd*3.14/180;
26
27 n1=1; %refrative index of air
28 n2=1.5; %refractive index of glass
```

The next part of the script creates a matrix of Sun declination angle (delta in degrees dd in radians) for every hour of every day of the year (365 x 24 matrix).

```
N=350; % day number
H=1;% add hour numer here

nit=0;
for N=1:365
    nit=nit+1;
    hit=0;
    for H=1:24
        hit=hit+1;
delta(nit,hit)=asin(0.39795*cos((0.98563*(N-173)*3.14/180)));
dd=delta*180/3.14;
```

The azimuth "Az" and elevation angles "aa" are then calculated using the hour angle "w" and the latitude angle "latr" (latr is the latitude in radians). Values where the Sun is below the horizon are set to zero using the if statements in lines 56 and 61.

```
47 %alpha and hour angle.
48 %w=15*(H-12);
49 w(nit,hit)=15*(H-12);
50
51 aa(nit,hit)=asin(sin(delta(nit,hit)).*sin(latr)+cos(delta(nit,hit)).*cos(w(nit,hit).*3.14/180).*cos(latr));
52 Az(nit,hit)=acos((sin(delta(nit,hit)).*cos(latr)-cos(delta(nit,hit)).*cos(w(nit,hit)*3.14./180).*sin(latr))./(cos(aa(nit,hit))));
53
54 aa_degrees=aa*180/3.14;
55
56 if aa(nit,hit)<=0
57     aa(nit,hit)=0;
58 end
59
60
61 if w(nit,hit) <= 0
62 Azvec(nit,hit)=Az(nit,hit);
63 elseif w(nit,hit)>0
```

The azimuth and elevation angles are then converted into spherical coordinates using theta for azimuth and phi for elevation. "th1" and "ph1" refer to the direction the solar panel is facing while "th2" and "ph2" are for the Sun position. The dot product of the panel vector and the Sun vector is then used to get the incident angle (ang) used in the Fresnel equations.

```
th2= Azvec(nit,hit);
ph2= aa(nit,hit);

%convert both vectors to carthesian
[x1,x2,x3]=sph2cart(th1,ph1,1);  %spherical coords in matlab written as azimuth, elevation then radius
[y1,y2,y3]=sph2cart(th2,ph2,1);

xvec=[x1,x2,x3];
yvec=[y1,y2,y3];

%get dot product
dp=dot(xvec,yvec);

%incident angle is the angle between vectors i.e. the acos of this
ang=acos(dp);
angd=ang*180/3.14;
th_inc(nit,hit)=ang;
```

The next part of the script applies the Fresnel equations for a given angle of incidence. The total reflection is the average of the s and p reflections as the sunlight is assumed to be non-polarized.

```
%reflectivity calculation
ref(nit,hit)=sqrt(1-(n1/n2).*sin(th_inc(nit,hit)).^2);

if th_inc(nit,hit)>=3.14/2
    Rs(nit,hit)=1;
    Rp(nit,hit)=1;
    Rtot(nit,hit)=1;
else

Rs(nit,hit)= real((n1.*cos(th_inc(nit,hit))-n2.*ref(nit,hit))./(n1*cos(th_inc(nit,hit))+n2.*ref(nit,hit))).^2;
Rp(nit,hit)= real((n1.*ref(nit,hit)-n2.*cos(th_inc(nit,hit)))./(n1*ref(nit,hit)+n2.*cos(th_inc(nit,hit)))).^2;
Rtot(nit,hit)=(Rs(nit,hit)+Rp(nit,hit))/2;
end
```

Now that the angle of incidence of the direct sunlight relative to the solar panel has been calculated as well as the percentage of light reflected off the panel surface the next step is to calculate the intensity of the incident sunlight which varies both by day and hour due to the changing air mass that the sunlight must pass through. AMM refers to the air mass while Si is the attenuated intensity of Sunlight as a function of air mass. Sm2 corrects for the projection of the sunlight on an inclined plane which reduces the incident sunlight intensity when the Sun is not orthogonal to the face of the solar panel.

```
AMM(nit,hit)=(1./cos((3.14/2)-aa(nit,hit)));
Si(nit,hit)=1353*exp(-0.357*(AMM(nit,hit)).^0.678); %
Sm2(nit,hit)=real(Si(nit,hit).*cos(th_inc(nit,hit)));
```

The energy collected is the incident solar irradiance “Sm2” minus the reflected light and then multiplied by the solar panel efficiency (22% was chosen as the efficiency, no temperature loss coefficient is accounted for as panel temperature was not calculated in this model). Below are several calculations for annual reflection and low light losses which can all be derived from the previous calculations.

```
%Electrical irradiance generated with reflection and low irradiance losses
%%units = Wm-2
Powt(nit,hit)=ne(nit,hit).*real(Sm2(nit,hit).*(1-Rtot(nit,hit)));
%Electrical Power generated with just low irradiance losses.
Powt2(nit,hit)=ne2(nit,hit).*real(Sm2(nit,hit));
%Electrical Power generated with just reflection losses.
Powt3(nit,hit)=0.22.*real(Sm2(nit,hit).*(1-Rtot(nit,hit)));
%Electrical Power generated with no losses
Powt4(nit,hit)=real(Sm2(nit,hit));


%total electrical energy collected per day
Ecoll(nit)=sum(Powt(nit,:)/1000);%kWhm-2
Etot(nit)=sum(Sm2(nit,:)/1000); %kWhm-2
Pc(nit)=(Ecoll(nit)./Etot(nit))*100;

%Annual energy collected with reflection and low light loss
Ean=sum(Ecoll); %kWhm-2
Eantot=sum(Etot); %kWhm-2
PCan=real((Ean./Eantot)*100);
```

The Matlab model did not account for clouds and only used a simplified isotropic diffuse irradiance model. For more completeness real world weather data from Solcast was imported and applied to the model.

```
%isotropic diffuse horizontal irradiance(IDI)
DHIdata = importdata("C:\Users\Administrator\Downloads\DHIData.xlsx");
IDI=DHIdata.*(1+a*cos(tiltd))./2;
IDI_new =  IDI(:,2:366); %factorng out titles in data table
IDI_new_transposed = IDI_new.'; %transposing matrix
%I need to make IDI a function of hour or day potentially
IDIsum = sum(IDI_new);

%Simple Sandia Sky Diffuse Model
GHIdata = importdata("C:\Users\Administrator\Downloads\GHI.xlsx");
GHIdatanew = GHIdata.data;
GHIdata_transposed = GHIdatanew.';
%SSDI(nit,hit) = GHIdatanewnewJan1.*(0.012*th_inc(nit,hit)*(1-cos(tiltd))./2);

%DNI Data
DNIdata = importdata("C:\Users\Administrator\Downloads\DNI.xlsx");
DNIdatanew = DNIdata(:,2:366)
DNIdata_transposed = DNIdatanew.';
```

10 APPENDIX 2: COMSOL RAY TRACING

Parameterization: The COMSOL ray tracing models all involved a light source called the "Sun" and a glass block. What varied between models was the geometry of the patterned top surface of the glass block. The lengths and angles of the top pattern features were parameterized so that the size, spacing and tilt angles could be varied in a parametric sweep in order to find the optimal feature dimensions. The below figure shows the parametrized features for a 3D sawtooth pattern as well as the pitted glass pattern.

Parameters

Name	Expression	Value
H	0.3	0.3
W	1	1
L	10	10
SunAngle	45[deg]	0.7854 rad
Array	10	10

Parameters

Name	Expression	Value
PoreRadius	1	1
SunAngle	60[deg]	1.0472 rad

Left: 3D sawtooth parameters, H is height, W is width, L is Length, Sun Angle is the rotational angle of the light source and array is how many times the pattern repeats. Right: Pitted glass parameters, PoreRadius is the size of the pits relative to the spacing of the pit centres, thus PoreRadius of 1 is where the edges of the pits touch each other while a lower PoreRadius value represents under etching and a higher value represents over etching.

Geometry: Making the patterned surface involved describing one unit of the pattern (including the tilt of the feature) and then copying that unit to form an array with a given spacing. Shown below are the steps required to make the sawtooth pattern.

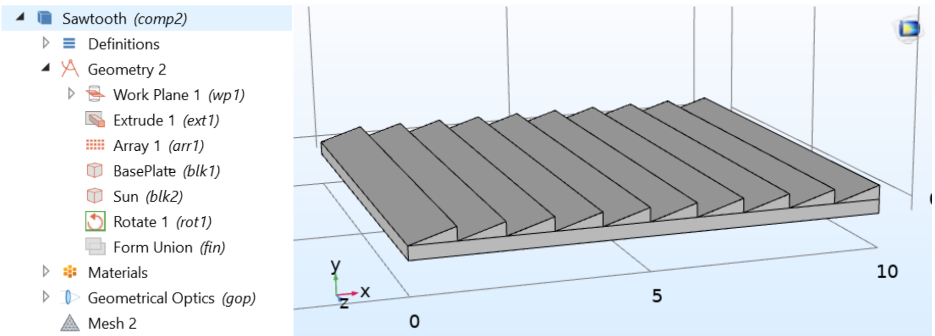

Firstly, a right-angle triangle is made in the work plane, then the triangle is extruded to make a 3D object, the object is then repeated 10 times using Array. The BasePlate represents the glass block. The Sun is then generated and rotated so that it always faces its centre of rotation which is set as the centre of the top surface of the glass block.

For the pitted glass model, it was necessary to create two arrays of pits which were offset from each other, alternately a unit cell of two pits could have been made and this patten repeated in an array.

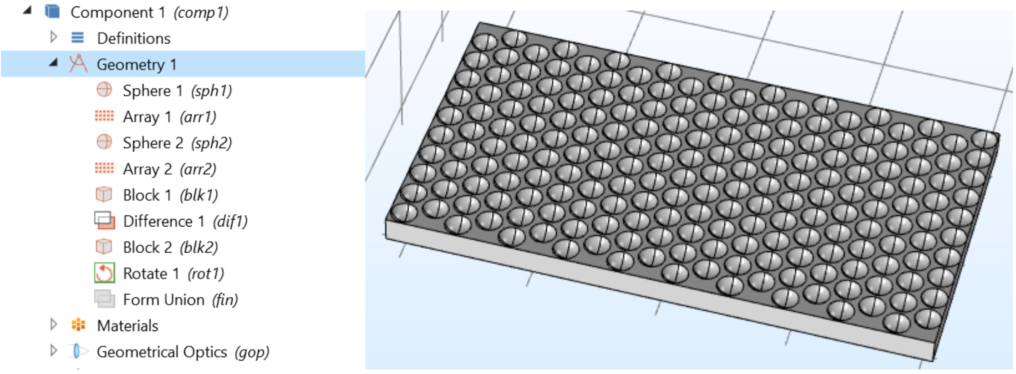

Two offset arrays of spheres were made to form a hexagonal pattern. The glass block was then formed such that the bottom half of the spheres overlapped with the glass block. The difference step was then used to subtract the spheres from the glass block leaving a pitted surface remaining.

Wall Conditions: The sides of the glass block were made reflective so that rays that would escape though the sides would remain in the glass block, this was considered suitable as a real solar module is over 1.5 m^2 in area and thus light escaping the glass though the sides would be negligible. The bottom of the glass block was given a freeze condition so any ray that reached the bottom surface of the glass block was considered to be successfully transmitted through the glass block. The rays were set as monochromatic and the real refractive index “n” of the glass was set to 1.5 while the imaginary part “k” was set to zero. Thus, the effects of optical dispersion as well as absorption in the glass were not accounted for in this model. Below is an example of the wall conditions.

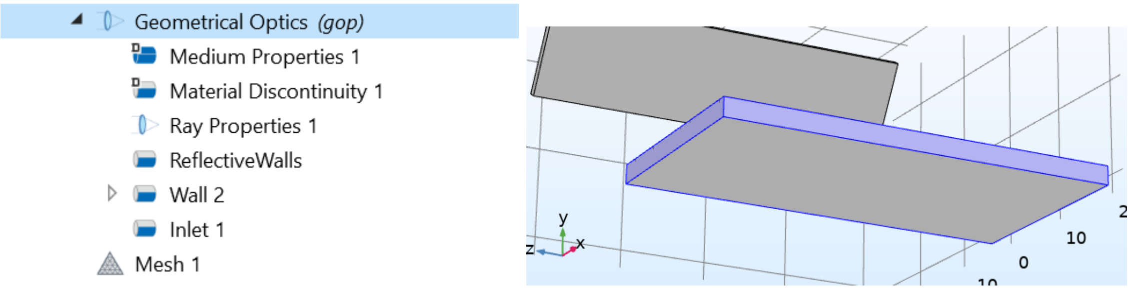

The side walls with reflective boundary conditions are highlighted. The bottom surface has a freeze condition for incident rays.

Study and Results: The study was set as a parametric sweep where SunAngle as well as at least one other parameter was varied. The SunAngle was increased in steps of 10 degrees with graduations getting smaller as the glancing limit was reached near 90 degrees. A boundary probe at the bottom of the glass block was set to accumulate the collected ray power. After running the simulation, the total collected ray power was evaluated at the final timestep.

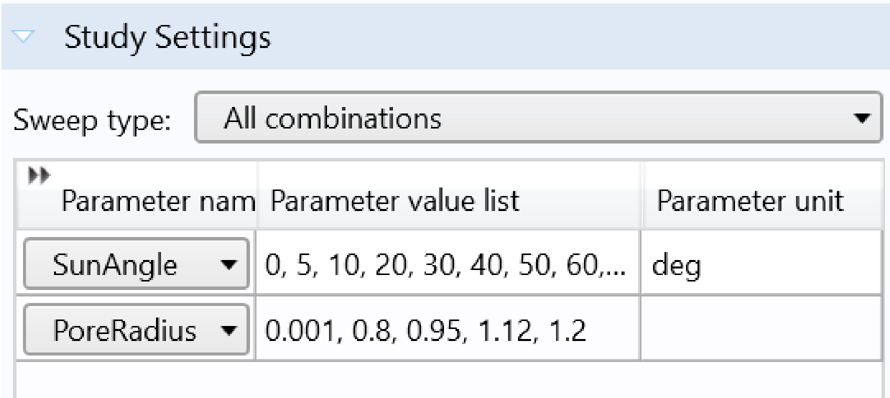

An example of a parametric sweep for a pitted glass pattern. PoreRadius 0.001 was the control measurement as it closely approximates to a flat surface, thus the pitted glass could be compared to flat glass in the same simulation.